

221

Topics in Current Chemistry

Editorial Board:

A. de Meijere · K.N. Houk · H. Kessler

J.-M. Lehn · S.V. Ley · S.L. Schreiber · J. Thiem

B.M. Trost · F. Vögtle · H. Yamamoto

Springer

Berlin

Heidelberg

New York

Barcelona

Hong Kong

London

Milan

Paris

Tokyo

Contrast Agents I

Magnetic Resonance Imaging

Volume Editor: Werner Krause

With contributions by

E. Brücher, R. B. Clarkson, J. A. Davies, J. F. Desreux,
L. Frullano, C. F. G. C. Geraldès, H. Gries, L. Helm,
V. Jacques, A. E. Merbach, J. A. Peters, N. Richardson,
J. Rohovec, D. D. Schwert, E. Tóth



Springer

The series *Topics in Current Chemistry* presents critical reviews of the present and future trends in modern chemical research. The scope of coverage includes all areas of chemical science including the interfaces with related disciplines such as biology, medicine and materials science. The goal of each thematic volume is to give the non-specialist reader, whether at the university or in industry, a comprehensive overview of an area where new insights are emerging that are of interest to a larger scientific audience.

As a rule, contributions are specially commissioned. The editors and publishers will, however, always be pleased to receive suggestions and supplementary information. Papers are accepted for *Topics in Current Chemistry* in English.

In references *Topics in Current Chemistry* is abbreviated *Top. Curr. Chem.* and is cited as a journal.

Springer WWW home page: <http://www.springer.de>
Visit the TCC home page at <http://link.springer.de/series/tcc/>
or <http://link.springer-ny.com/series/tcc/>

ISSN 0340-1022

ISBN 3-540-42247-1

Springer-Verlag Berlin Heidelberg New York

Library of Congress Catalog Card Number 74-644622

This work is subject to copyright. All rights are reserved, whether the whole or part of the material is concerned, specifically the rights of translation, reprinting, reuse of illustrations, recitation, broadcasting, reproduction on microfilms or in any other ways, and storage in data banks. Duplication of this publication or parts thereof is only permitted under the provisions of the German Copyright Law of September 9, 1965, in its current version, and permission for use must always be obtained from Springer-Verlag. Violations are liable for prosecution under the German Copyright Law.

Springer-Verlag Berlin Heidelberg New York
a member of BertelsmannSpringer Science+Business Media GmbH

<http://www.springer.de>

© Springer-Verlag Berlin Heidelberg 2002
Printed in Germany

The use of general descriptive names, registered names, trademarks, etc. in this publication does not imply, even in the absence of a specific statement, that such names are exempt from the relevant protective laws and regulations and therefore free for general use.

Cover design: Friedhelm Steinen-Broo, Barcelona; MEDIO, Berlin
Typesetting: Fotosatz-Service Köhler GmbH, 97084 Würzburg

SPIN: 10784892 02/3020 ra – 5 4 3 2 1 0 – Printed on acid-free paper

Volume Editor

Prof. Dr. Werner Krause

International Project Management Therapeutics

Schering AG

13342 Berlin, Germany

E-mail: werner.krause@schering.de

Editorial Board

Prof. Dr. Armin de Meijere

Institut für Organische Chemie

der Georg-August-Universität

Tammannstraße 2

37077 Göttingen, Germany

E-mail: ameijer1@uni-goettingen.de

Prof. Dr. Horst Kessler

Institut für Organische Chemie

TU München

Lichtenbergstraße 4

85747 Garching, Germany

E-mail: kessler@ch.tum.de

Prof. Steven V. Ley

University Chemical Laboratory

Lensfield Road

Cambridge CB2 1EW, Great Britain

E-mail: svl1000@cus.cam.ac.uk

Prof. Dr. Joachim Thiem

Institut für Organische Chemie

Universität Hamburg

Martin-Luther-King-Platz 6

20146 Hamburg, Germany

E-mail: thiem@chemie.uni-hamburg.de

Prof. Dr. Fritz Vögtle

Kekulé-Institut für Organische Chemie

und Biochemie der Universität Bonn

Gerhard-Domagk-Straße 1

53121 Bonn, Germany

E-mail: voegtle@uni-bonn.de

Prof. K. N. Houk

Department of Chemistry and Biochemistry

University of California

405 Hilgard Avenue

Los Angeles, CA 90024-1589, USA

E-mail: houk@chem.ucla.edu

Prof. Jean-Marie Lehn

Institut de Chimie

Université de Strasbourg

1 rue Blaise Pascal, B.P.Z 296/R8

67008 Strasbourg Cedex, France

E-mail: lehn@chimie.u-strasbg.fr

Prof. Stuart L. Schreiber

Chemical Laboratories

Harvard University

12 Oxford Street

Cambridge, MA 02138-2902, USA

E-mail: sls@slsiris.harvard.edu

Prof. Barry M. Trost

Department of Chemistry

Stanford University

Stanford, CA 94305-5080, USA

E-mail: bmtrost@leland.stanford.edu

Prof. Hisashi Yamamoto

School of Engineering

Nagoya University

Chikusa, Nagoya 464-01, Japan

E-mail: j45988a@nucc.cc.nagoya-u.ac.jp

Topics in Current Chemistry Now Also Available Electronically

For all customers with a standing order for Topics in Current Chemistry we offer the electronic form via LINK free of charge. Please contact your librarian who can receive a password for free access to the full articles by registration at:

<http://link.springer.de/orders/index.htm>

If you do not have a standing order you can nevertheless browse through the table of contents of the volumes and the abstracts of each article at:

<http://link.springer.de/series/tcc>

<http://link.springer-ny.com/series/tcc>

There you will also find information about the

- Editorial Board
- Aims and Scope
- Instructions for Authors

Preface

Magnetic Resonance Imaging (MRI) is a rapidly growing field in diagnostic medicine. In radiology, MRI has revolutionized the diagnosis of numerous types of illnesses. The clinical utility of MRI became visible exactly at the same time when for the classic radiological discipline, x-ray imaging, a revolution took place, i.e. at the advent of computed tomography (CT) in the 1970s. At that time, a new and infant method such as MRI was not considered necessary in face of the significant improvement observed for CT. Nonetheless, MRI not only was able to catch up with CT, but in many diagnostic areas, such as first observed for the detection and characterization of brain tumors, rapidly passed by CT.

This progress, however, was only possible due to the concomitant development and use of MRI contrast agents, which contributed significantly to the improvement of images. At the early times of MRI, it was predicted that for this modality the use of contrast agents was not necessary at all due to the excellent quality of unenhanced images. It was commonly accepted that in no case would the extent of contrast-enhanced procedures exceed 10%. Today, more than 30% of all MRI diagnoses use contrast enhancement.

The first type of contrast agents was similar in its characteristics and its function to that of compounds used for x-ray imaging, i.e. they were extracellularly distributed and were excreted exclusively via the kidneys. For a long time, the only available contrast agent was Gd-DTPA. Accordingly, the term "gadolinium" has been used synonymously for MRI contrast agent by most of the radiologists.

Further development proceeded in analogy to that observed for x-ray contrast agents twenty years earlier. After the ionic DTPA, nonionic compounds emerged. After the open-chain structures, macrocyclic substances were developed.

All these agents had in common that they were extremely useful for the delineation of anatomy and of anatomical deviations from normal, i.e. for "static" images. Later on, it was recognized that, in addition, albeit to a limited extent, they were also useful for functional measurements. This was possible by using their pharmacokinetics, particularly their kinetics of distribution. Now the function of blood distribution systems could be investigated. This includes both the heart and the blood vessels. However, regarding the heart, machine technology lagged behind for a long time. The acquisition times were too long to allow for a conclusive diagnosis of the functioning of the heart. Significant improvements have been achieved recently.

However, whereas for the x-ray techniques development has not proceeded past extracellular compounds, for MRI the next stage of development has already

been reached, tissue-specific contrast agents that accumulate in specific tissues and organs and allow for an improved diagnosis of these body regions. The first tissue that could be targeted was the liver. Contrast agents that accumulate in this organ are now available to the radiologists.

The search for new MRI contrast agents is an actively pursued field of research both in industry and in academia. Recently, an excellent monograph has been published by E. Tóth and A. Merbach. Most of the authors of that volume agreed to participate in an updated book on MRI contrast agent research demonstrating the rapid progress in their respective areas.

The first chapter of this new monograph summarizes extracellular MRI contrast agents, both the currently available products and those in development including those characteristics most relevant for their efficacy and tolerability, such as relaxivity, hydrophilicity, osmolality, viscosity, LD₅₀ and their pharmacokinetics. Additionally, the synthetic routes to these compounds are described. Gadolinium-containing chelates consist of a plethora of isomers, which are able to convert into each other in aqueous solutions. This phenomenon is detailed in the second chapter where the different configurations and conformations of lanthanide complexes are dealt with, both for presently available agents and for new, targeted compounds that are able to recognize different regions of interest or different body conditions including areas with modified pH value.

Relaxivity is the key determinant for the efficacy of lanthanide chelates. The design of improved contrast agents is only possible on the basis of an in-depth understanding of the underlying principles. The third chapter gives an extensive introduction into the theory and the determination of relaxivity data, which will enable the reader to better utilize further optimization efforts.

Since free lanthanide ions are very toxic, the stability of chelates have to be considered as a key factor influencing the tolerability of gadolinium-based MRI contrast agents. The fourth chapter describes molecular moieties, influences of the solution and potential components of body fluids affecting the kinetic stability of the agents. For the presently available substances, which are rapidly excreted, kinetic stability has a different impact than for future, potentially long-circulating compounds or agents that accumulate in body sites. For these new agents, the impact of stability will gain even more in importance.

An overview on new research ideas is given in chapter 5 where for example blood-pool agents based on macromolecular derivatives or agents imaging gene expression are described. Other targets include temperature, pH, ions and enzymes that may influence the signal of these types of contrast agents.

Data on non-gadolinium based compounds are summarized in chapters six and seven describing both tissue-specific and blood-pool agents.

MRI presently is fostering its position in radiology and in life sciences in general. The reasons are not only its lack of ionizing radiation or use of radioisotopes but rather the great wealth of information gained, which is unsurpassed by other modalities. Contrast agents have contributed a significant proportion to this information and will increase to do so in the future.

Contents

Extracellular MRI Contrast Agents Based on Gadolinium	
H. Gries	1
Structures of MRI Contrast Agents in Solution	
L. Frullano, J. Rohovec, J. A. Peters, C.F.G.C. Geraldès	25
Relaxivity of MRI Contrast Agents	
E. Tóth, L. Helm, A. E. Merbach	61
Kinetic Stabilities of Gadolinium(III) Chelates Used as MRI Contrast Agents	
E. Brücher	103
New Classes of MRI Contrast Agents	
V. Jacques, J. F. Desreux	123
Non-Gadolinium-Based MRI Contrast Agents	
D.D. Schwert, J. A. Davies, N. Richardson	165
Blood-Pool MRI Contrast Agents: Properties and Characterization	
R. B. Clarkson	201
Author Index Volumes 201–221	237
Subject Index	245

Contents of Volume 211

Bioorganic Chemistry of Biological Signal Transduction

Volume Editor: Herbert Waldmann

ISBN 3-540-67746-1

Protein Tyrosine Kinase Inhibitors as Therapeutic Agents

A. Levitzki

Peptidomimetic SH2 Domain Antagonists for Targeting Signal Transduction

G. Müller

Biophysical Characterization of the Ras Protein

J. Kuhlmann, C. Hermann

Ras-Farnesyltransferase-Inhibitors as Promising Anti-Tumor Drugs

H. Waldmann, M. Thutewohl

Phosphatidylcholine-Preferring Phospholipase C from *B. cerus*.

Function, Structure, and Mechanism

P.J. Hergenrother, S. F. Martin

Photoaffinity Labeling in Biological Signal Transduction

G. Dormán

Extracellular MRI Contrast Agents Based on Gadolinium

H. Gries

Schering AG, Contrast Media Research, Muellerstrasse 178, 13342 Berlin, Germany

E-mail: gabriele.seeger@schering.de

A summary of the development of extracellular MRI contrast agents during the last twenty years is given. Focal points are chemistry, physico-chemical properties and pharmacokinetic behaviour of gadolinium complexes. The synthesis of acyclic and macrocyclic ligands is described, particularly of derivatives of the ligands DTPA and DOTA. Stability, relaxivity and formulations of the gadolinium complexes are issues of special interest as well as their toxicological and clinical aspects. An outlook on the future development of clinically useful extracellular MRI contrast agents is provided.

Keywords. Extracellular MRI contrast agents, gadolinium complexes with acyclic and macrocyclic ligands, Gd-DTPA Gd-DOTA derivatives of Gd-DO3A, $[\text{Na}_2\text{Gd}_2(\text{OHEC})]$, oligomeric gadolinium complexes, Nitroxyles

1	Introduction	2
2	Metal Chelates as MRI Contrast Agents	3
2.1	Gadolinium Complexes	4
2.2	Chelates with Acyclic Ligands	4
2.2.1	Gadolinium-DTPA	4
2.3	Gadolinium-DTPA-Diamides	6
2.4	Gadolinium Chelates with Macrocyclic Ligands	7
2.4.1	Gd-DOTA	7
2.5	Derivatives of Gd-DO3A	9
2.6	$[\text{Na}_2\text{Gd}_2(\text{OHEC})]$	14
2.7	Oligomeric Complexes	14
3	Nitroxyles	18
4	Formulations of Extracellular Gadolinium Contrast Agents	19
4.1	Physico-Chemical Properties	19
4.1.1	Relaxivity	19
4.1.2	Hydrophilicity	20
4.1.3	Osmolality	21
4.2	Toxicology and Pharmacokinetics	22
5	References	23

1

Introduction

Extracellular MRI and X-ray contrast agents are characterized by their pharmacokinetic behaviour. After intravascular injection their plasma-level time curve is characterized by two phases. The agents are rapidly distributed between plasma and interstitial spaces followed by renal elimination with a terminal half-life of approximately 1–2 hours. They are excreted via the kidneys in unchanged form by glomerular filtration.

Extracellular water-soluble contrast agents to be applied for X-ray imaging were introduced into clinical practice in 1923. Since that time they have proved to be most valuable tools in diagnostics. They contain iodine as the element of choice with a sufficiently high atomic weight difference to organic tissue. As positive contrast agents their attenuation of radiation is higher compared with the attenuation of the surrounding tissue. By this contrast enhancement X-ray diagnostics could be improved dramatically.

In 2,4,6-triiodobenzoic acid derivatives iodine is firmly bound. Nowadays diamides of the 2,4,6-triiodo-5-acylamino-isophthalic acid like iopromide (Ultravist, Fig. 1) are used as non-ionic (neutral) X-ray contrast agents in most cases [1].

About twenty years ago magnetic resonance imaging (MRI) has been introduced as a new technique. The physical basis of MRI is totally different from that of X-ray imaging. Whereas for the latter the absorption of X-rays is the decisive factor, it is the influence on the relaxation rate of the protons in the body water that induces the efficacy of the method. Consequently, the chemical nature of MRI contrast agents has to be totally different from that of the iodinated X-ray contrast agents. Furthermore the agent itself is not visible in MRI but only its effect on protons in its immediate neighborhood can be monitored. In MRI, a magnetic field is applied to the region of interest which is subsequently modulated by a radio pulse. The change in distribution of the magnetic moments of the protons from random to directed and their return to normal constitutes the MRI signal. MRI contrast agents are able to affect this return to normal called relaxation by shortening particularly the relaxation time T1 (see below). As a result, the signal intensity is increased improving the imaging. However, in the early days it was rather questionable whether contrast agents at all could be of any benefit for the user of the new technique since MRI signals depend on a wide range of parameters.

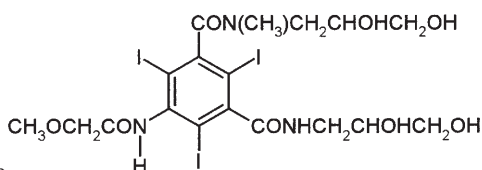


Fig. 1. Iopromide

2 Metal Chelates as MRI Contrast Agents

A compound that is able to influence the relaxation times of water protons has to be paramagnetic. In the Periodic System paramagnetic ions are to be found amongst the transition metals and the rare earth metals (lanthanides). However, it was well known, that the free ions of heavy metals are toxic. Lanthanide ions form soluble complexes with ligands such as phospholipids, amino acids and proteins that are present in plasma. The liver and the skeleton are the major sites of accumulation of free metal ions. Uptake in the liver is mediated by the hepatocytes [2].

The challenge was to render the metal ions safe without impairing their paramagnetic properties. This problem could successfully be solved by the complexation of the metal ions with suitable ligands.

Many heavy metal ions are able to produce metal-ligand complexes (metal chelates) that are very stable. As an acceptor the cation forms coordinate bonds with electron-donating ligands. All d-, s-, and p-metal ions can form a great variety of complexes. There are two coordination spheres surrounding the central metal ion. The primary coordination sphere consists of ligands directly bound to the cation possibly completed by electrostatically bound solvent molecules. The number of ligands in this sphere is called the coordination number. It depends mainly on the size of the central metal ion, steric interactions between the coordinating groups and electronic interactions. Ligands having only one point of attachment to the cation are called “monodentate” (derived from the Latin “dens” for tooth). Ligands having several points of attachment are called “polydentate” ligands. Well known examples of polydentate ligands are aminopolycarboxylic acids like ethylenediaminetetra-acetic acid (EDTA: Fig. 2a) and diethylenetriaminepenta-acetic acid (DTPA: Fig. 2b).

These ligands are frequently used as metal ion traps to bind undesired metal ions, e.g. in formulations of X-ray contrast agents. Chelated cations may associate electrostatically with anionic compounds and with solvent molecules by weak interactions. This results in the formation of an outer coordination sphere. Instead of the term “complex” the term “chelate” is very frequently used meaning that the metal ion is covered by the ligand like a claw (“chela”: word from the Greek for claw).

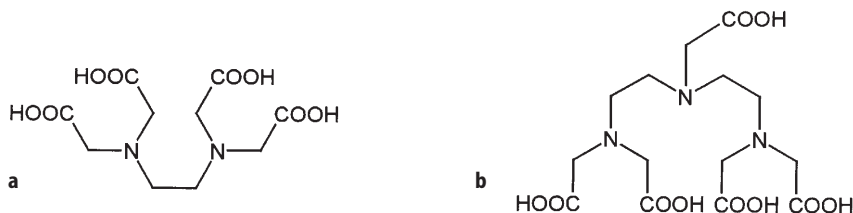


Fig. 2. a EDTA, b DTPA

For the use as a contrast agent the stability of the complex in vivo is most important. It depends significantly on the thermodynamic stability defined by Eq. (1).

$$K(\text{therm}) = \frac{[ML]}{[M][L]} \quad (1)$$

Most frequently the $\log K(\text{therm})$ -values of the complexes are used. They have been compiled in special compendia [3, 4]. A variety of approaches for the measurement of stability constants is available. However, thermodynamics alone is an insufficient predictor of the behaviour of the complexes in the organism. Other features have to be considered, particularly the stability of the aqueous solution under the physiological conditions at pH 7.4 which is characterized by the selective stability constant $K(\text{sel})$ that can be calculated from $K(\text{therm})$ [5]. Normally $K(\text{sel})$ is lower than $K(\text{therm})$. Expectedly, the toxicity of the chelate correlates best with $K(\text{sel})$.

Furthermore, the kinetic stability which refers to the rate of dissociation of the central metal ion from the complex must be considered for a possible interaction with endogenous ions in the organism (Zn, Ca, Mg, phosphate etc.).

Pharmacological and toxicological studies have shown that demetallation can occur in vivo with deposition of free metal ions in bone and liver especially in situations where the chelate has a long residence time in the body. This is the case with non-extracellular chelates like organ-specific contrast agents or with intravascular compounds such as polymers.

2.1

Gadolinium Complexes

All currently available extracellular contrast agents are gadolinium chelates. This rare earth metal ion exhibits the strongest effect of all elements on the longitudinal relaxation time T1. The ligands of these chelates belong to two different types of structure: Acyclic (open-chain) compounds and macrocyclics.

2.2

Chelates with Acyclic Ligands

2.2.1

Gadolinium-DTPA

Gd-DTPA (gadopentetate, Magnevist) is a good example of a “chelate”, because the metal ion is covered by the polydentate ligand like a claw (Fig. 3).

The central metal ion has nine coordination sites. It is attached to the three nitrogen atoms and to five carboxylate moieties (oxygen atoms). A single water molecule is able to coordinate at the vacant ninth site resulting in a strong enhancement of the water proton relaxation rate. The chelate can be described as a distorted capped square antiprism according to X-ray analysis [6].

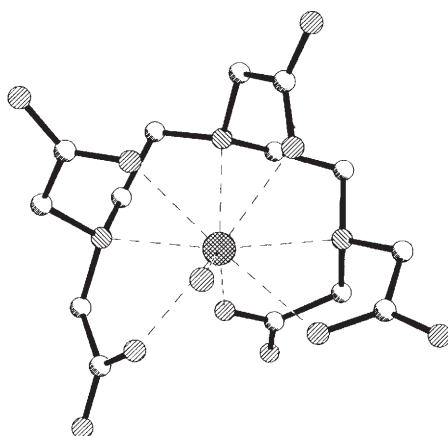


Fig. 3. X-ray structure of $\text{Gd-DTPA} (\text{H}_2\text{O})_2^{2-}$, top view (hydrogen atoms are omitted for clarity)

Table 1. Acute intravenous toxicity in rats

Generic name	LD50 (mmol/kg) body weight	References
Gadopentetate	8	[65]
Gadoterate	18	[30]
Gadodiamide	25	[17]
Gadoteridol	<15	[29]
Gadobutrol	25	[17]

Its di-meglumine salt is freely soluble in water and the stability of the aqueous solution is remarkably high. The $\log K(\text{therm})$ was determined as 22.2 [7] and $\log K(\text{sel})$ is calculated as 18.1 at pH 7.4 [8]. Surprisingly enough, the acute intravenous toxicity LD_{50} in rats is approx. 8 mmol/kg body weight (Table 1).

Thus the toxicity of Gd-DTPA is more than tenfold lower than the toxicity of the gadolinium ion and the ligand DTPA, respectively. Fortunately, the relaxivity of the chelate remained high enough to give an excellent contrast enhancement. The first clinical trials were conducted at the end of 1983 in the Department of Radiology of the Free University of Berlin by Professor R. Felix [9] and at the Hammersmith Hospital in London by Professor R. Steiner [10]. Since the first approval by regulatory authorities in the United States and in Germany in 1988 a wealth of diagnostic results has been accumulated in millions of patients worldwide. Its safety profile is very well established with a remarkably low incidence of adverse events [11–13]. Numerous reports indicate the diagnostic utility of Gd-DTPA enhancement for MRI assessments in the Central Nervous System (CNS), of disruptions of the blood brain barrier, of renal functions, inflammatory lesions, neoplasms, myocardial ischemia and many other indications. The risk of adverse reactions when the agent is administered intravenously even up to doses of 0.3 mmol/kg is low. No difference in the incidence of

adverse reactions following bolus injections with Gd-DTPA as opposed to slow infusions has been observed.

Special formulations have been developed to visualize the gastrointestinal tract (see below). Magnevist has also been applied successfully as an X-ray contrast agent in patients who were allergic to iodine because of the attenuation of X-rays by the gadolinium ion [14].

2.3

Gadolinium-DTPA-Diamides

Analogous to the development of the non-ionic X-ray contrast agents many years ago neutral chelates have been synthesized to reduce the osmotic pressure of the aqueous solutions. However, for MRI, injection volumes are used that are much smaller than for X-ray contrast agents. That means that the osmolality of the solutions is of minor importance for MRI contrast agents. The increase in blood osmolality after intravenous injection of up to 0.3 mmol/kg Gd-DTPA will not cause disturbance of the organism's osmotic balance.

Two extracellular contrast agents which contain neutral gadolinium chelates have entered the market: gadodiamide (Omniscan) (Fig. 4a) and gadoversetamide (Optimark) (Fig. 4b).

Both ligands are amides of DTPA and are obtained by treating the dianhydride of DTPA with the corresponding amine (methyl amine [15] and methoxyethylamine [16] respectively). These gadolinium complexes are freely soluble in water. As expected, the osmolality of the 0.5 molar solution of gadodiamide is lower (0.79 osmol/kg water) than that of the 0.5 molar solution of Gd-DTPA (gadopentetate) (Table 2) [17, 18].

Other parameters such as their physico-chemical properties, pharmacodynamics and the clinical application are very similar to the "ionic" agents gadopentetate and gadoterate [19].

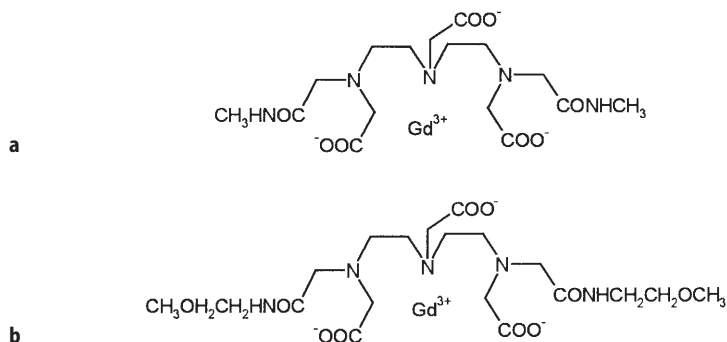


Fig. 4. a Gadodiamide (Omniscan). b Gadoversetamide (Optimark)

Table 2. Physico-chemical properties of formulations of gadolinium complexes

Generic name	Concentration (mol/l)	Osmolality (osmol/kg water)	Viscosity (cP)	References
Gadopentetate	0.5	1.96	2.9	[18]
Gadoterate	0.5	1.35	2.0	[29]
	1.0	4.02	11.3	[29]
Gadodiamide	0.5	0.79	1.4	[17, 18]
	1.0	1.90	3.9	[29]
Gadoteridol	0.5	0.63	1.3	[29]
	1.0	1.91	3.9	[29]
Gadobutrol	0.5	0.57	1.4	[17]
	1.0	1.39	3.7	[18]

2.4

Gadolinium Chelates with Macrocyclic Ligands

2.4.1

Gd-DOTA

A second class of MRI contrast agents contains ligands that are derivatives of the macrocyclic tetramine, 1,4,7,10-tetraazacyclododecane (cyclen). Gadoterate (Dotarem, Gd-DOTA, Scheme 3, formula 5) was the first macrocyclic gadolinium complex which has entered the market.

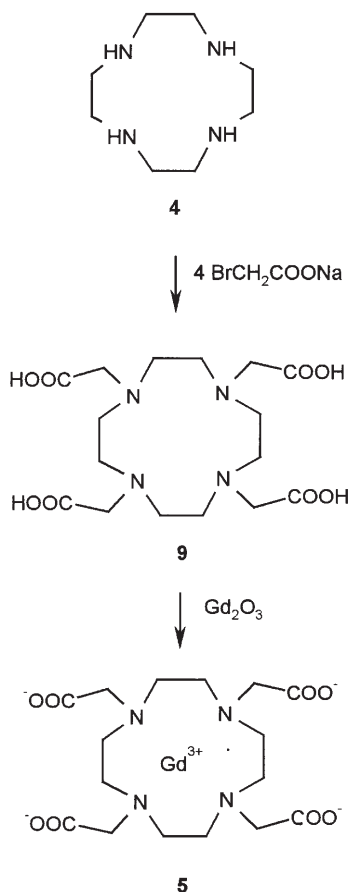
Several synthetic routes to cyclen as the starting material for the synthesis of gadoterate are available [20–26]. In Scheme 1 the cyclization of the tosylates **1** and **2** is performed in a high yield since the hydrocarbon segments between the hetero atoms are short, and relatively equal segments of the target macrocycle are condensed. After detosylation of **3** the cyclen **4** is obtained.

For the production of cyclen on a larger scale, the tetramerisation of N-benzylaziridine **6** seems to be preferential (Scheme 2).

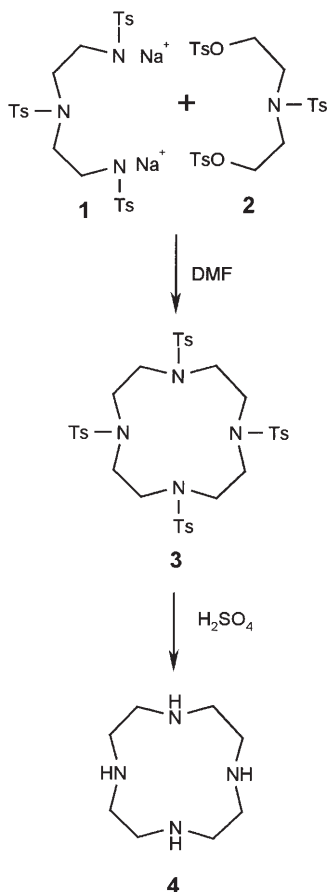
Tetrabenzylcyclen **7** has been prepared in nearly quantitative yield by refluxing a mixture of **6** and p-toluenesulfonic acid in alcohol for 6 hours. Debenzylation of **7** can be carried out by treatment with 10% Pd-C under hydrogen. Cyclen **4** is obtained in a high yield. Alkylation with chloro- or bromoacetic acid leads to the ligand DOTA **9** [25]. Subsequent complexation with gadolinium chloride or gadolinium oxide in the usual manner yields Gd-DOTA **5** (Scheme 3).

In the macrocyclic structure the metal binding site within the ligand is more encapsulated and the entropy is decreased upon metal incorporation. As a result the stability of the majority of macrocyclic metal chelates is higher than that of acyclic complexes (Table 3) [27, 28]. Generally the macrocyclic complexes exhibit a higher kinetic stability.

The formulations of Dotarem (Gd-DOTA) consist of aqueous solutions of gadoterate as its N-methylglucamine salt in concentrations of 0.5 and 1.0 mol/l. The latter solution displays relatively high osmolality and viscosity (Table 2) [29].



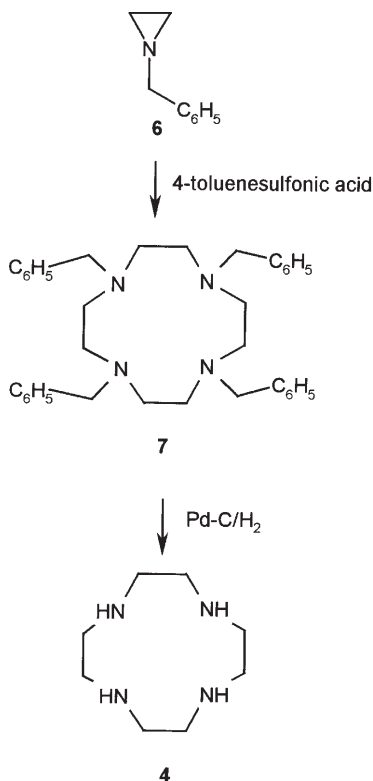
Scheme 3. Synthesis of gadoterate (Gd-DOTA) from cyclen



Scheme 1. Synthesis of Cyclen by cyclization

Table 3. Thermodynamic stability constants and relaxivities in water at 20 MHz and 40 °C of commercially available gadolinium chelates

Generic name	log K (therm)	References	1/T1 relaxivity (l/mmol ⁻¹ s ⁻¹)	References
Gadopentetate	22.2	[7]	3.8	[17]
Gadoterate	24.7	[27, 28]	3.5	[53]
Gadodiamide	16.9	[8]	3.9	[53]
Gadoteridol	23.8	[7]	3.7	[53]
Gadobutrol	21.8	[33]	3.6	[17]



Scheme 2. Synthesis of cyclen by tetramerisation

The LD₅₀ after intravenous injection in rats is approx. 18 mmol/kg (Table 1) [30].

Pharmacological behaviour and clinical use of Dotarem correspond to the acyclic extracellular agents.

2.5

Derivatives of Gd-DO3A

In analogy to the development of non-ionic open-chain metal chelates, neutral macrocyclic gadolinium chelates have also been synthesized. Two of them have been launched as extracellular MRI contrast agents: gadobutrol (Gadovist) (Fig. 5b) and gadoteridol (ProHance) (Fig. 5c). Both are derivatives of 1,4,7-tricarboxymethyl-1,4,7,10-tetraazacyclododecane (DO3A), (Fig. 5a) [31, 32].

There are several routes leading to derivatives of the key compound DO3A starting from cyclen. For example gadobutrol **10** can be synthesized via the route outlined in Scheme 4 [30].

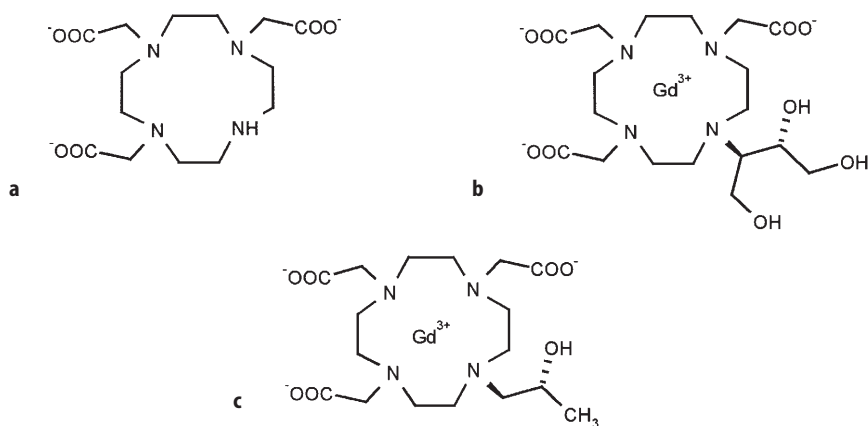
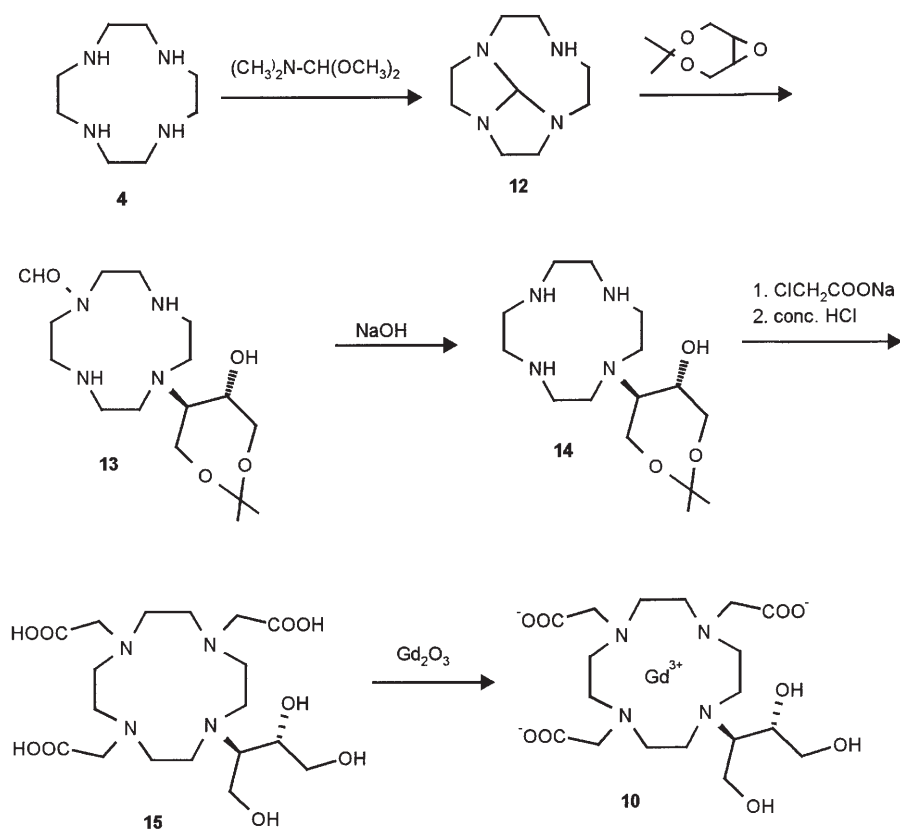


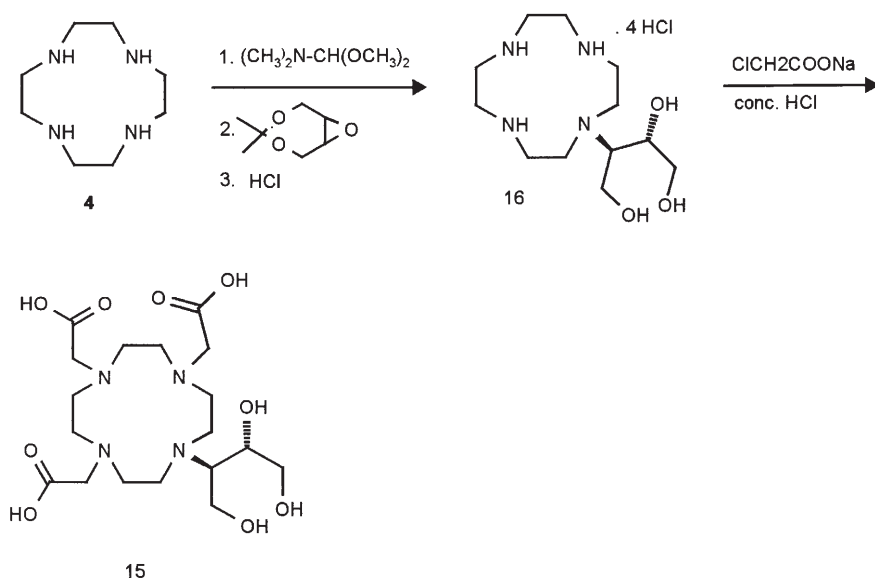
Fig. 5. a DO3A, b gadobutrol (Gadovist), c gadoteridol (ProHance)



Scheme 4. Synthesis of Gadobutrol

The first step is the treatment of cyclen **4** in toluene with dimethylformamide dimethyl acetal giving the tricyclic compound 1,4,7,10-tetraazatricyclo [5.5.1.0] tridecane **12**, which without further purification is reacted with 4,4-dimethyl-3,5,8-trioxabicyclo [5.1.0] octane yielding an intermediate which without isolation gives the formyl derivative **13** in a 73 % yield upon solvolysis. Spectroscopic investigations indicate the formation of the 1,7-disubstituted isomer; the 1,4-disubstituted product is not observed. Presumably, the steric hindrance imposed by the substituted dioxepanyl ring prevents the formation of the 1,4-isomer. Alkaline treatment of **13** removes the formyl group and results in the formation of the mono-substituted cyclen derivative **14** in a 93 % yield. Alkylation of **14** with chloroacetic acid sodium salt in water at pH 9–10 gives the ligand DO3A-butrol **15**. For purification, an acidic solution of **15** is adsorbed on a cation-exchange column. Elution with 2 M aqueous ammonia provides the purified ligand, which is isolated and crystallized on treatment with methanol.

For the preparation of gadobutrol **10** on a larger scale the approach described in Scheme 5 is preferred [25].



Scheme 5. Synthesis of the ligand butrol

Thus, in analogy to the above outlined procedure cyclen is converted to **12** and without isolation reacted with 4,4-dimethyl-3,5,8-trioxabicyclo [5.1.0] octane to give the formyl derivative **13** which also without isolation is treated with aqueous hydrochloric acid under heat. Under these conditions both the formyl group is removed and the dioxepanyl ring gives rise to the free butrol side chain yielding the monosubstituted cyclen derivative in the form of its tetrahydrochloride **16**. The overall yield for this reaction sequence is about 81%

based on cyclen. Similar to the conversion of **14** to **15** (Scheme 4), **16** is reacted with chloroacetic acid to give **15** (yield 65 %).

The ligand contains two chiral carbons at C13 and C14 (numbering adopted from Fig. 6) and thus represents a racemic mixture of (13R,14S)- and (13S,14R)-DO3A-butrol. For clarity, only one enantiomer is shown in Scheme 4 and Scheme 5.

The final step of the synthesis of 1,4,7-tris(carboxymethyl)-10-(1-hydroxymethyl)-2,3-dihydroxypropyl)-1,4,7,10-tetraazacyclododecanato gadolinium (gadobutrol **10**), the complexation of **15** with Gd_2O_3 is accomplished by the same procedure described for the production of gadopentetate (see below).

Analogously the calcium complex of **15** is obtained with CaCO_3 in an aqueous suspension. This compound is used as an additive in the pharmaceutical formulation.

Gadobutrol is a neutral and highly stable compound. However, its thermodynamic stability constant ($\log K(\text{therm}) = 21,8$ in 0.1 M KCl) [33] is nearly two orders of magnitudes lower compared with both Gd-DTPA and Gd-DOTA (Table 3). This is not unexpected since it is generally accepted that the hard Lewis acid Gd(III) is more tightly bond to negatively charged atoms rather than to neutral ones. A comparison of the stabilities of gadobutrol and gadoteridol shows that the introduction of additional hydroxyl groups in one of the side chains decreases the stability (Table 3). The lower thermodynamic stability of gadobutrol is without any consequence for its use in patients, since the complex exhibits excellent kinetic stability. In this connection it was of interest to determine the dissociation rates of these clinically used macrocyclic complexes. They were studied spectrophotometrically at pH 3.2–5.3 following the exchange reactions with Eu(III). The dissociation rate of gadobutrol proved to be about ten times lower than that of gadoteridol, which might be due to the bulkier 1-(hydroxymethyl)-2,3-dihydroxypropyl side chain of **10** compared with the 2-hydroxypropyl group of the latter [31].

In Fig. 6 a graphical presentation of gadobutrol (**1**) showing the atomic numbering scheme is given. The nine-coordinated Gd(III) has the four nitrogens of the aza crown, three oxygens of each of the three carboxylic groups, and one oxygen of the 1-(hydroxymethyl)-2,3-dihydroxypropyl side chain in its primary coordination sphere. In related compounds, the ninth coordination atom usually is the oxygen of a water molecule. In this structure, however, the ninth coordination partner surprisingly is a carboxylate oxygen provided by a further centrosymmetrically related complex molecule. The geometry of the coordination polyhedron can be approximated by a monocapped square antiprism.

From a structural point of view a number of different isomers could be present. In principal the three different hydroxyl groups in the ligand are able to interact with the central metal ion thus giving rise to three different constitutional isomers. The stereochemistry of the different configurational isomers of gadobutrol is best described in view of the stereochemistry of the parent compound Gd-DOTA. In this complex chirality results from the restriction of free rotation around the bonds of the ligand caused by the inclusion of the central metal ion. Thus four stereoisomers are generated upon complexation of Gd(III) by DOTA.

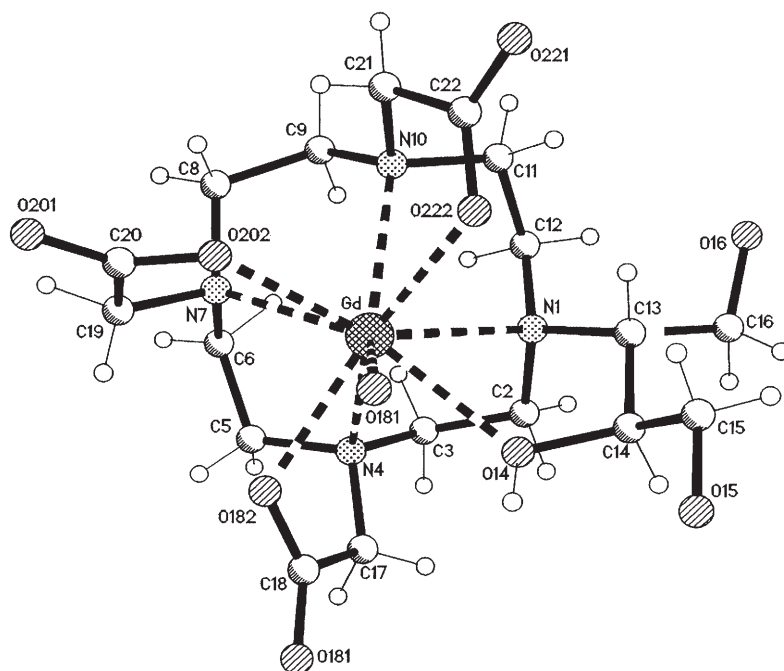


Fig. 6. Structure of Gadobutrol in the crystal showing the “cap atom” 0181

In gadobutrol, the replacement of one of the acetic acid groups of Gd-DOTA by the chiral 1-(hydroxymethyl)-2,3-dihydroxypropyl group gives rise to a diastereomatic differentiation of the four stereoisomers. Therefore, for each of the three possible constitutional isomers four diastereomers have been taken into account, thus, generating 12 diastereomers and a total of 24 stereoisomers. In the HPLC chromatogram of an aqueous solution of gadobutrol, however, it is rather probable that it contains only one diastereomer.

Following the procedures described above, the other neutral macrocyclic extracellular contrast agent, gadoteridol (ProHance), (Fig. 5.3) can be produced in an analogous way [32]. As an additive, the calcium salt of the calcium chelate of the ligand (calteridol) is used in the pharmaceutical formulation, prepared by treatment of the ligand 1,4,7-triscarboxymethyl-10-(2-hydroxypropyl)-1,4,7,10-tetraazacyclododecane with an aqueous suspension of CaCO_3 [34].

The LD_{50} of gadoteridol after intravenous injection has been determined as $<15 \text{ mmol/kg}$ (in rats), the LD_{50} of gadobutrol is as approx. 25 mmol/kg showing higher tolerability of the latter chelate (Table 1).

Both chelates have been launched as extracellular contrast agents using doses up to 3 mmol/kg body weight. Both can be formulated as 1.0 molar aqueous solutions with acceptable viscosity (Table 2). These highly concentrated agents are useful in fast dynamic studies such as brain perfusion and fast magnetic resonance angiography (MRA).

2.6

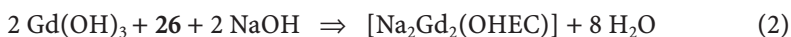
[Na₂Gd₂(OHEC)]

A point of special interest with respect to the design of new extracellular contrast agents is (i) slowing down of the molecular tumbling of the complexes in order to achieve enhanced proton relaxivity by increasing the ligand bulk and (ii) binding of more than one gadolinium to the monomeric ligand for this purpose. To achieve this effect the ligand 1,4,7,10,14,17,20,23-octaazacyclohexacosane-1,4,7,10,14,17,20,23-octaacetic acid ("H₈OHEC") has been synthesized [35]. The preparation of the macrocyclic octaamine **24** follows a modification of the well known procedure for the synthesis of 1,4,7,10,13,16,19,22-octaazacyclotetracosane by Richman and Atkins [36]. The reaction sequence for the synthesis of the ligand is shown in Scheme 6.

The critical step is the detosylation of the protected amines. Satisfactory yields (50% up to 75%) are obtained by heating the tosylated compounds in concentrated sulfuric acid (3 h, 110°C) or in a mixture of glacial acetic acid and concentrated sulfuric acid (3 h, 110°C). Varying amounts of water-insoluble side products are formed during the treatment with sulfuric acid which can be easily removed. The amount of these precipitated side products increases upon increasing the duration of treatment.

Carboxymethylation of the octaamine with *tert*-butylbromoacetate, followed by hydrolysis gives high yields of the octaacetic ligand **26**. The carboxymethylation requires careful control of the stoichiometry and the reaction conditions. Otherwise, mixtures of quaternary products are formed.

The dinuclear Gd(III) complex has been obtained by treating the ligand with gadolinium oxide, Gd₂O₃, or with gadolinium hydroxide, freshly prepared from the chloride or triflate under basic conditions (pH adjusted to 8.5 with NaOH) in aqueous solution according to equation (2):



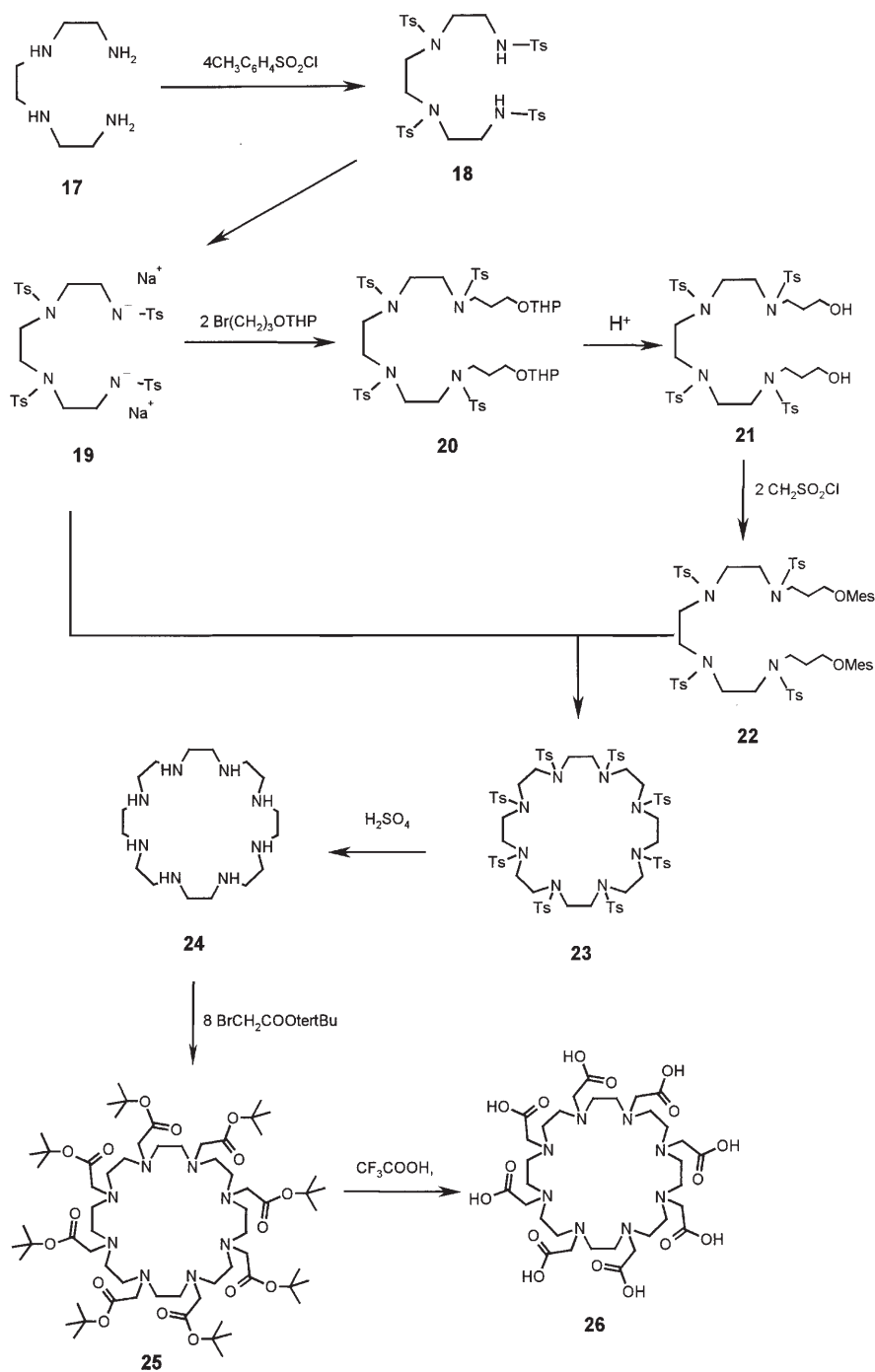
Yield: 52% as a white powder which was stable and highly soluble in water.

Mass spectrometry unambiguously showed complexation of two cations per ligand molecule.

2.7

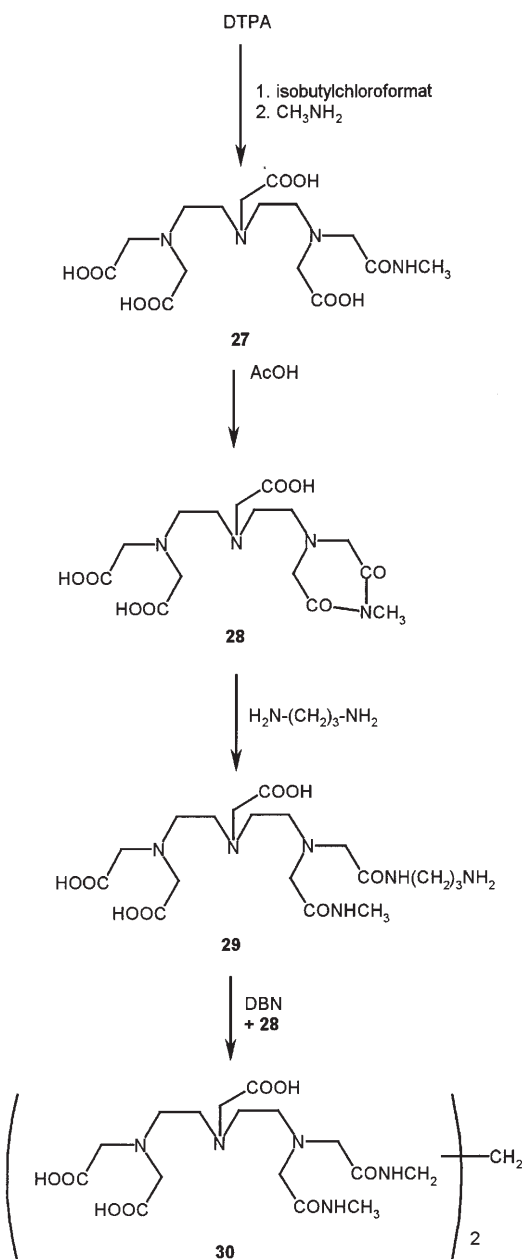
Oligomeric Complexes

A further approach to achieve enhanced proton relaxivity by binding of more than one lanthanide ion per chelant molecule has been realized by synthesizing acyclic and macrocyclic oligomers of DTPA and DOTA as ligands [37]. The process of preparation of such compounds comprises the steps of (i) obtaining from a polycarboxylate monochelant starting compound an activated polycarboxylate containing one or more reactive groups, e.g. imide, amide, anhydride or other activated carboxyl groups (ii) forming an amide or ester linkage between said activated compound and a polyamine or polyol linking compound thereby to obtain a chelant-linker compound, and (iii) forming an amide or ester link-

**Scheme 6.** Synthesis of the ligand H₈OHEC

age between said chelate-linker compound and a second activated polycarboxylate compound to obtain an oligomeric chelant.

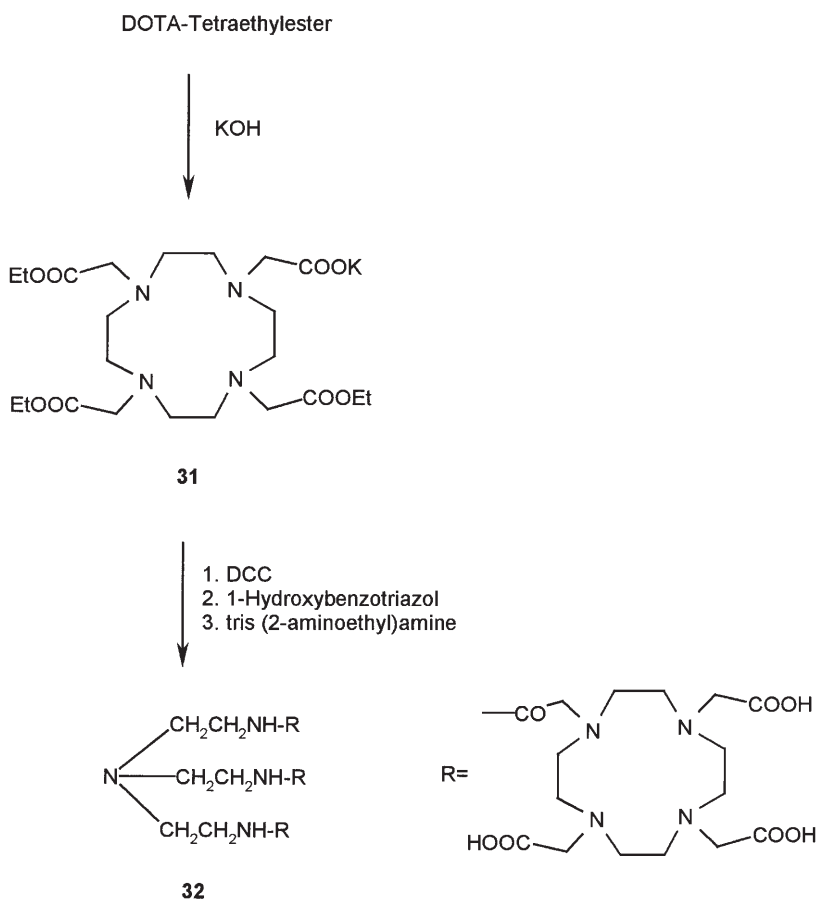
The synthesis of a dimeric DTPA is outlined in Scheme 7.



Scheme 7. Synthesis of a dimeric DTPA ligand

The first step follows a modification of the well known procedure of Krejcarek and Tucker [38] yielding the monomethylamide of DTPA **27**. After dehydration with glacial acetic acid the monomethylimide **28** has been obtained as an activated polycarboxylate compound. Subsequent reaction with 1,3-diaminopropane yielded the DTPA-mono(methyl-propylamino)amide Hydrochloride **29**. The reaction of **29** with **28** afforded the dimeric ligand **30**.

The synthesis of the trimeric macrocyclic chelant **32** is outlined in Scheme 8.



Scheme 8. Synthesis of the trimeric ligand TREN(DOTA)₃ nonaacid

Starting with the tetraethyl ester of DOTA the potassium salt of the triester **31** has been obtained by a partial saponification. To the solution of this compound in anhydrous tetrahydrofuran dicyclohexylcarbodiimide and 1-hydroxybenzotriazole has been added followed by tris(2-aminoethyl)amine. Subsequent hydrolysis of the ester groups yielded the nonaacid **32**.

Neutral bis- and tris-gadolinium complexes of the oligomeric ligands have been obtained in the usual manner with gadolinium oxide and the corresponding dysprosium complexes by reaction with dysprosium oxide. The latter might be useful as X-ray contrast agents.

In recent years a multitude of oligomeric lanthanide complexes has been published [39–41].

3 Nitroxyls

Besides the metal complexes there is another class of paramagnetic compounds which have been suggested as MRI contrast agents: the nitroxyls (nitroxides). These heterocyclic compounds are Stable Free Radicals characterized by a sterically hindered unpaired electron in a nitrogen-oxygen N-O[•]-bond. The most conspicuous role played by these compounds is that of a reporter group in the study of biological systems using electron spin resonance (ESR) spectroscopy (spin labeling). This technique was first introduced by McConnell [42]. It has rapidly evolved into a most powerful biophysical tool. For instance, nitroxyls have been used as *in vitro*-enhancers in proton-relaxation studies of protein configurations and membrane dynamics [43, 44]. Nitroxyls with an intracellular distribution might be selected to monitor redox potential and oxygen tension within the cell [44]. The proton relaxation efficacy of these compounds is much weaker than that of gadolinium complexes [45]. Nevertheless, they could potentially be useful as intracellular MRI contrast agents [46].

Two compounds of this structure type have been tested in preclinical studies as extracellular agents: (±) 2,2,5,5-tetramethylpyrrolidine-1-oxyl-3-carboxylic acid ("PCA", Fig. 7a) and N-(1-hydroxymethyl-2,3-dihydroxypropyl)- (±) 2,2,5,5-tetramethylpyrrolidine-1-oxyl-3-carboxamide ("NAT", Fig. 7b).

PCA was prepared by the method of Rozantsev and Krinitzkaya [47].

The synthesis of NAT was performed by reaction of the methylester of PCA with the acetone of 1,3,4-trihydroxybut-2-yl amine. After saponification with diluted sulfuric acid the neutral (non-ionic) compound NAT has been obtained [48].

Both compounds are freely soluble in water, PCA as sodium salt. The LD₅₀ of PCA after intravenous injection in rats has been determined as 15 mmol/kg, the LD₅₀ of NAT was even more favourable (as high as 25 mmol/kg). The relaxivity and the imaging capability have been studied. Both compounds revealed a

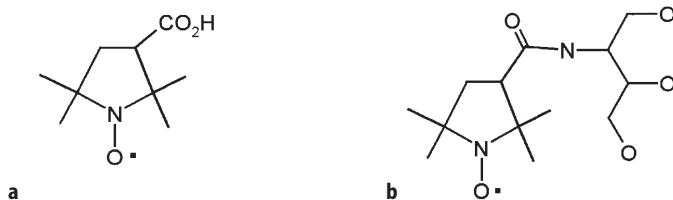


Fig. 7. a PCA; b NAT

pharmacological behaviour analogous to the extracellular gadolinium complexes and a remarkably high resistance to bio-reduction. However, in consideration of the minor paramagnetic efficacy no nitroxyl compound has been developed as extracellular MRI contrast agent in spite of the good preclinical results with NAT [49]. A possible use of them for performing electron spin resonance enhanced "Overhauser-MRI" in ultra-low field imaging up to 20 Gauss seems to be still under investigation [50].

4

Formulations of Extracellular Gadolinium Contrast Agents

4.1

Physico-Chemical Properties

4.1.1

Relaxivity

Relaxivity is described by the equations of Solomon [51] and Bloembergen [52]. A very simplified form is the equation (3) [53] where T_1 is the longitudinal relaxation time, k is a constant for a given metal, r is the distance between metal and proton and τ_c is the effective correlation time.

$$\frac{1}{T_1} = k \cdot \frac{1}{r^6} \cdot f(\tau_c) \quad (3)$$

The increase in relaxation rate is directly proportional to the concentration of the paramagnetic agent and to the square of its magnetic moment but inversely proportional to r^6 . Thus, a small increase in the interatomic distance causes a dramatic reduction in relaxation effects. At low concentrations of paramagnetic agents such as gadopentetate the enhancement of signal intensity by the increase of $1/T_1$ is usually the dominant effect whereas at high concentrations the decrease in signal intensity by the effect on T_2 is usually dominant. Thus, depending on the concentration, the signal intensity reaches a maximum before it decreases.

Enhancement of relaxation is also dependent on the effective correlation time τ_c which depends on molecular motion, on the rate of relaxation of the electron spins and on the exchange rate between free and bound water. τ_c is given by the equation (4).

$$\frac{1}{\tau_c} = \frac{1}{\tau_R} + \frac{1}{\tau_S} + \frac{1}{\tau_M} \quad (4)$$

where τ_M is the residence time of the water molecule in the first hydration sphere of the metal; τ_S is the electron correlation time and τ_R is the rotation correlation time. Only τ_R appears easily modifiable. Slowing down the rotation by increasing the molecular weight of the complex or by chelating the metal ion with bulky

ligands will result in an optimized rotational correlation time that could elicit relaxivities of up to 50 l/mmol/s. Low molecular weight gadolinium complexes such as gadopentetate, gadodiamide and gadoteridol exhibit very similar relaxivities of 3.5–3.8 l/mmol⁻¹/s⁻¹ (Table 3).

The magnetic field dependence of $1/T_1$ has been investigated in detail by the measurement of NMR dispersion (NMRD profiles) [54]. The studies have shown that the relaxivity of metal chelates varies with changes in magnetic field. In small metal chelates the relaxivity decreases with increasing field strength. However, this effect on low molecular weight gadolinium complexes at the field strength used in the clinical MRI (0.1–2 T), is relatively small.

Gadolinium and dysprosium, both elements of the lanthanide family, differ in the electronic occupancy of their f-shells. As a result, they are very similar chemically but very different magnetically. The relaxivity $1/T_1$ of Dy-DTPA is as low as ~ 0.1 l/mol⁻¹s⁻¹. However, dysprosium has a pronounced ability to influence transiently the residual magnetic susceptibility of tissues as it passes through. This effect of Dy-DTPA seems to be ideal for cerebral perfusion imaging and may be useful for the quantitation of partial occlusions and reperfusion.

4.1.2

Hydrophilicity

All the gadolinium complexes described above are highly soluble in water. The affinity of substances to water is called hydrophilicity. A high solubility in water correlates with a high hydrophilicity. The standard method of measuring this property is the determination of the partition coefficient. The compound is dissolved in buffer, then n-butanol or n-octanol is added. The mixture is vigorously shaken to allow the compound under investigation to reach an equilibrium concentration in n-butanol or n-octanol and buffer. The relative concentrations in the solvents are measured and the hydrophilicity is expressed as the corresponding coefficients. The extracellular gadolinium complexes are so hydrophilic that the concentrations in n-butanol are hardly measurable. The partition coefficients are lower (<0.01) than those of iodinated X-ray contrast agents.

The protein binding of compounds with such low partition coefficients is virtually non-existent as demonstrated by MRI and pharmacokinetic studies. The low protein binding of the extracellular gadolinium complexes currently used in clinical practice correlates very well with their excellent safety profile.

Standard formulations of the extracellular gadolinium complexes have a concentration of 0.5 mol/l. Gadobutrol and gadoteridol can be formulated even as 1.0-molar solutions with acceptable viscosity (Table 2).

These highly concentrated solutions are useful in fast dynamic studies such as brain perfusion and in magnetic resonance angiography (MRA) [56, 57].

As an example of a standard formulation, the preparation of a 0.5-molar solution of the pentamethylglutamine salt of gadopentetic acid (Magnevist) for parenteral application is given: 97.6 g (0.5 mol) of N-methylglucamine is dissolved under sterile conditions in 500 ml water for injection. After addition of 196.6 g (0.5 mol) of DTPA and 90.6 g (0.25 mol) of gadolinium oxide, Gd₂O₃, the batch is refluxed for two hours and the clear solution is brought to pH 7.2 by adding

another 97.6 g (0.5 mol) of N-methylglucamine. Then, a second solution of 197 mg (0.5 mmol) of DTPA and 488 mg (2.5 mmol) of N-methylglucamine in 100 ml water p.i. is added sterile to produce an overall volume of 1000 ml. The solution is finally ultrafiltered, placed in a vial and heat sterilized and is ready for parenteral use.

In this procedure the pentameglumine salt of the ligand DTPA was added to prevent any undesired release of the gadolinium ion from the chelate. Gadolinium-complex formulations normally contain a small amount of excess ligand either in its free or calcium-complexed form. As mentioned above, Pro-Hance (gadoteridol) contains calteridol, the calcium salt of the relatively weak calcium complex of the ligand for instance.

Special gadolinium-complex formulations were developed to visualize the gastrointestinal (GI) tract. An aqueous formulation of gadopentetate (1.0 mol/l) and mannitol (15 g/L) is clinically used especially to improve the delineation of pancreatic head and ventral outline. Because of the osmotic effect of mannitol, water is not absorbed from the GI tract. The recommended dose of the contrast agents is 100–1000 ml depending on the region of interest. Due to the paramagnetic effect of the gadolinium an intense signal on T₁-weighted sequences is obtained increasing the contrast of the bowel and improving the delineation of pathological structures. The problem of ghosting artefacts can be reduced by hyoscine-N-butyl-bromide (Buscopan).

Diluted Magnevist formulations are used in MR arthrography, MR cisternography and MR myelography [58–63]. Dilution with saline is necessary to avoid dominant T2 shortening effects. Optimal signal intensities have been observed after administration of solutions with a concentration between 0.5 and 1.0 mol/l.

4.1.3

Osmolality

The osmotic activity of a dissolved substance is characterized by its osmolarity and/or osmolality and the osmotic pressure. Osmolarity and osmolality are defined as follows:

$$\text{Osmolarity (osm/l solution)} = \text{g substance/L solution}$$

$$\text{Osmolality (osm/kg water)} = \text{g substance/ kg water}$$

The concentration in g/kg water is calculated from the specific gravity of the solution (usually measured at 20°C or 25°C) which is theoretically half of the value of the salt of an analogous ionic compound which has two ionic species.

The osmolality of a solution is proportional to the sum of the concentrations of the different molecular or ionic moieties contained in the solution. In the case of neutral structures, the osmolality is proportional to the concentration of the dissolved substance.

The osmotic activity is characterized further by the osmotic pressure of the aqueous solution which is defined as the force that must be applied to counterbalance the force arising from the flow of water across a semipermeable mem-

brane [64]. The following equation 5 applies approximately to the osmolality at 37°C (osm/kg water):

$$\frac{\text{Osmotic pressure (at 37°C)}}{25.4} \quad (5)$$

This simple relationship follows from the equation for the state of an ideal gas. In practice, deviations are frequently observed which are attributed to dissociation or association phenomena.

The development of low osmolar non-ionic X-ray contrast agents has resulted in a distinct reduction in the toxicity and the observed side-effects in patients. However, as already mentioned the osmotic activity of MRI contrast agents is less important in view of the smaller injection volumes which are used. All the formulations of extracellular gadolinium chelates are hypertonic when compared with blood. But the overall increase in osmolality after injection of even 0.3 mmol/kg body weight is insignificant. Osmolality-induced adverse reactions have been observed rarely not only because of the relatively small injection volumes but also because of the rapid dilution of the injected agent in the blood.

4.2

Toxicology and Pharmacokinetics

The major concern with the use of metal chelates *in vivo* is the potential release of the toxic heavy metal ion from the complex. However acute and subacute toxicity studies with gadopentetate and other extracellular gadolinium chelates have not elicited findings of any significant release of the metal in the organism. The chelation of the lanthanides drastically improves their tolerability profile and changes favourably their pharmacological behaviour. After intravenous administration in rats the gadolinium chloride and the ligand DTPA each displayed a LD₅₀ of about 0.5 mmol/kg body weight. The chelate, Gd-DTPA, as mentioned above displayed a LD₅₀ as high as about 8 mmol/kg. That means a more than tenfold increase of the margin of safety. The tolerance of the macrocyclic chelate gadobutrol was even better (LD₅₀: about 25 mmol/kg) (Table 1):

Very large doses of the commercially available agents would be required to reach the lethal dose in humans which is roughly 100 times higher than the diagnostic dose providing an excellent margin of safety for all commercially available extracellular MRI agents.

The extra-renal excretion of the extracellular gadolinium complexes is negligible and no significant absorption after enteral application has been observed. The elimination half-life depends on the glomerular filtration rate, and on the cardiovascular function. No significant differences between the gadolinium chelates have been observed, their terminal half-lives in blood are in the range of 15 to 75 minutes in animals and 1–2 h in humans [65–67].

Since the gadolinium chelates are unable to pass the intact blood brain barrier (BBB), they are very suitable for investigating any disturbances in this region of interest. They are particularly useful for increasing the detection rate of

metastases and small tumors and for tumor classification, the latter by allowing the differentiation of vital tumor tissue (BBB: well perfused and/or impaired or absent) from central necrosis and from surrounding oedema [68].

The pharmacokinetic parameters of the extracellular gadolinium chelates do not exhibit any dose dependency. The analysis of plasma and urine samples gave no evidence for any biotransformation of the compounds [69–71].

Pharmacokinetic results in humans have confirmed the favourable findings in animal studies. Thus the clinical use of extracellular gadolinium complexes as diagnostic tools in MRI has become routine practice in many fields of interest among others for diagnosing tumours, infections, inflammations and infarctions particularly in the Central Nervous System (CNS).

The combination of advanced imaging techniques tailored to the optimal efficacy of the extracellular gadolinium complexes will further improve the diagnostic potential of MRI in the future.

5 References

1. Sovak M (1984) (ed) Handbook of Experimental Pharmacology: Radiocontrast Agents vol 73 Springer Berlin Heidelberg New York Tokyo
2. Aeberhard A, Nizza P, Remy J (1962) *Int J Radiat Biol* 5: 217
3. Martell EM, Smith RM (1974) (eds) Critical Stability Constants Plenum Press New York London
4. Perrin DD (1979) Stability Constants of Metal Ion Complexes Pergamon Press Oxford New York Toronto Sidney Paris Frankfurt
5. Schwarzenbach G, Anderess G, Schneider W, Senn H (1955) *Helv Chim Acta* 38: 1147
6. Gries H, Miklautz H (1984) *Physiol Chem Phys Med NMR* 16: 111
7. Kumar K, Chang CA, Francesconi LC et al. (1994) *Inorg Chem* 33: 3567
8. Chang CA (1993) *Invest Radiol* 28: S21
9. Claussen C, Laniado M, Schoerner W, Felix R (1985) *Am J Neuroradiol* 6: 669
10. Carr DH, Brown J, Bydder GM (1984) *Lancet* 3: 484
11. Niendorf HP, Felix R, Laniado M et al. (1985) *Radiat Med* 3: 7
12. Niendorf HP, Al Hassan A, Clauss W, Cornelius I (1993) *Magn Reson Contrast Imaging* 2:12
13. Niendorf HP, Al Hassan A, Geens V, Clauss W (1994) *Invest Radiol* 29: S179
14. Kawano T, Ishijima H, Nakajima T, Aoki J, Endo K (1993) *Comput Ass Tomogr* 23: 939
15. Quay SC, US Patent 4,859,451 Paramagnetic contrast agents for MR Imaging
16. Moore DA, Wallace RA US Patent 5,137,711 Paramagnetic DTPA and EDTA alkoxyalkylamide complexes as MRI agents
17. Vogler H, Platzek J, Schumann-Giampieri G et al. (1995) *Eur J Radiol* 21: 1
18. Tweedle MF, Hagan JJ, Kumar K et al. (1991) *Magn Reson Imaging* 9: 409
19. Cacheris WP, Quay SC, Rocklage SM (1990) *Magn Reson Imaging* 8: 467
20. Richman JE, Atkins TJ (1974) *J Am Chem Soc* 96: 2268
21. Stetter H, Roos EE (1954) *Chem Ber* 87:566
22. Stetter H, Marx J (1957) *Justus Liebigs Ann Chem* 607: 59
23. Stetter H, Mayer KH (1961) *Angew Chem* 88: 760
24. Tsuboyama K, Tsuboyama S, Uzawa J, Kobayashi K, Sakurai T (1977) *Tetrahedron Lett* 52: 4603
25. Stetter H, Frank W (1976) *Angew Chem* 88: 760
26. Hansen GR, Burg TE (1968) *J Heterocycl Chem* 5: 305
27. Cabbiness DK, Margerum DW (1969) *J Am Chem Soc* 91: 6540
28. Clay RM, Corr S, Micheloni M, Paoletti P (1984) *Inorg Chem* 24: 3330

29. Tweedle MF (1992) *Invest Radiol* 27: 52
30. Doucet D, Meyer D, Bonnemain B et al. (1989) In: Runge VM (ed) *Enhanced Magnetic Resonance Imaging* The C.V. Mosby Company St.Louis Baltimore Toronto: p. 87
31. Platzek J, Blaszkiewicz P, Gries H, Luger P, Michl G, Mühler-Fahrnow A, Raduechel B, Suelzle D (1997) *Inorg Chem* 36: 6086
32. Dishino DD, Delaney EJ, Emswiler JE, Gaughan GT, Prasad JS, Srivastava SK, Tweedle MF (1991) *Inorg Chem* 30:1265
33. Toth E, Kiraly R, Platzek J, Raduechel B, Bruecher E (1996) *Inorg Chim Acta* 249: 191
34. Chang CA, Kumar K, Tweedle MF Eur Patent 0454078: Dual functioning excipients for metal contrast agents
35. Schumann H, Boettger UA, Zietzke K, Hemling H, Kociok-Koehn G, Pickardt J, Hahn FE, Zschunke A, Schiefner B, Gries H, Raduechel B, Platzek J (1997) *Chem Ber/ Reueil* 130:267
36. Atkins TJ, Richman JE (1978) *Organic Synthesis* 58:87
37. Love D, Dow WC, Himmelsbach RJ, Watson AD, Rocklage SM WO 91/05672: Multi-site metal chelating agents
38. Krejcarek GE, Tucker KL (1977) *Biochem Biophys Res Commun* 77: 581
39. Watson AD US Patent 5,914,095: Polychelants containing amide bonds
40. Gries H, Radüchel B, Speck U, Weinmann HJ Eur Patent 0255471: Makrocyclische Verbindungen
41. Krause W, Maier FK, Bauer M, Press W-R, Schumann-Giampieri G, Platzek J, Schmitt-Willich H WO 96/05167: Dimer DTPA derivatives and their metal complexes
42. Ohnishi S, McConnell HM (1965) *J Am Chem Soc* 87: 2293
43. Keana JFW (1978) *Chem Rev* 78: 37
44. Berliner LJ (1976 and 1979) *Spin labeling, theory and applications* Vol 1 and 2 Academic Press, New York
45. Lovin J, Wesbey GE, Engelstad BL (1984) *Invest Radiol* 19: S24
46. Swartz HM, Bennett H, Brown R et al. (1985) *Radiology* 157: 100
47. Rozantsev EG, Krinatzkaya LA (1985) *Tetrahedron* 21: 491
48. Gries H, Niedballa U, Weinmann H-J US Patent 4,925,652: Nitroxyl compounds, and diagnostic media based thereon useful for enhancing NMR imaging
49. Brasch RC, London DA, Wesbey GE et al. (1983) *Radiology* 147: 773
50. Leunbach I WO 93/02711: Use of persistent free-radicals in magnetic resonance imaging
51. Solomon I (1955) *J Chem Phys* 99: 559
52. Bloembergen N (1957) *J Chem Phys* 101: 572
53. Lauffer RB (1987) *Chem Rev* 87: 901
54. Koenig SH, Kellar KE (1995) *Magn Reson Med* 34: 227
55. Chang CA, Brittain HG, Telser J, Tweedle MF (1990) *Inorg Chem* 29: 4468
56. Kaufman JA, Geller SC, Petersen MJ (1994) *Am J Roentgeno* 163: 203
57. Prince MR, Narasimham DL, Stanley C (1995) *Vasc Surg* 21: 656
58. Di Chiro G, Knop RH, Girton ME (1985) *Radiology* 157: 373
59. Di Chiro G, Girton ME, Frank JA (1986) *Radiology* 160: 221
60. Baum H, Kuehnert A, Sundermayer R (1987) *Roentgenblätter* 40: 293
61. Hajek PC, Sartoris DJ, Gyls-Merin V (1990) *Invest Radiol* 25: 179
62. Chandnani VP, Ho C, Chu P (1991) *Radiology* 178: 557
63. Kramer J, Stiglbauer R, Engel A, Prayer L, Imhof H (1992) 16: 254
64. Lehninger AL (1975) *Biochemistry* 2nd ed Worth New York
65. Weinmann H-J, Press W-R, Gries H (1990) *Invest Radiol* 25: S49
66. Harpur ES, Worath D, Hals PA (1993) *Invest Radiol* 28: S28
67. Weinmann H-J, Gries H, Speck U (1989) In: Runge VM (ed) *Enhanced Magnetic Resonance Imaging*; The C.V. Mosby Company St.Louis Baltimore Toronto p. 74
68. Yamada K, Ushio Y, Hayakawa T (1982) *J Neurosurg* 57: 394
69. Weinmann H-J, Laniado M, Muetzel W (1984) *Physiol Chem Phys Med NMR* 16:167
70. Van Wagoner M, Worah D (1993) *Invest Rdiol* 28: S44
71. Staks T, Schumann-Giampieri G, Frenzel T (1994) *Invest Radiol* 29: 709

Structures of MRI Contrast Agents in Solution

Luca Frullano¹, Jan Rohovec², Joop A. Peters^{1,*}, Carlos F.G.C. Geraldes^{3,*}

¹ Laboratory of Applied Organic Chemistry and Catalysis, Delft University of Technology, Julianalaan 136, 2628 BL Delft, The Netherlands

* E-mail: j.a.peters@tnw.tudelft.nl

² Department of Inorganic Chemistry, Universita Karlova (Charles University), Albertov 2030, CZ-128 40 Prague 2, Czech Republic

³ Department of Biochemistry and Center of Neurosciences, Faculty of Science and Technology, University of Coimbra, Apartado 3126, 3000 Coimbra, Portugal

* E-mail: geraldes@ci.uc.pt

Contrast agents for magnetic resonance imaging are mainly Gd^{3+} complexes of octadentate polyaminopolycarboxylates and one water molecule in the first coordination sphere of the metal ion. Both the Ln^{3+} ion and the nitrogen atoms in these complexes may be chiral. Therefore, various isomers may occur for these complexes, which interconvert in aqueous solution. Here studies on the configurations and conformations of Ln^{3+} complexes of acyclic and cyclic ligands are reviewed. Furthermore, the structures of new generations of contrast agents that are able to target organs or to sense their biochemical environment are discussed. Molecular recognition is an important issue for these compounds.

Keywords. Lanthanide chelates, Chirality, Conformations, Molecular recognition, Dynamics

1	Introduction	26
2	Complexes of DTPA and Derivatives	27
2.1	DTPA and DTPA-Bisamides	27
2.2	DTPA Bisamides Incorporated in Macrocycles	30
2.3	Monosubstituted DTPA Derivatives	31
2.4	EGTA	33
2.5	TTHA	34
3	Complexes of Tripodal Hydroxypyridinonates	36
4	Complexes of Cyclen Type Compounds	36
4.1	DOTA and Derivatives	36
4.2	DO3A and Derivatives	41
4.3	DOTP	43
4.4	Phosphinates and Phosphonate Esters	45
4.5	Cationic Complexes	47
5	Targeted Contrast Agents	50
6	Responsive Contrast Agents	52
7	References	55

Abbreviations

CA	contrast agent for magnetic resonance imaging;
CSAP	monocapped square antiprism;
MRI	magnetic resonance imaging;
NMRD	nuclear magnetic relaxation dispersion
LIS	lanthanide induced shifts;
SAP	square antiprism;
TTP	tricapped trigonal prism

1

Introduction

Chelates of Gd^{3+} have found widespread application as contrast agents (CA's) for magnetic resonance imaging (MRI). The paramagnetic Gd^{3+} ion in these compounds has an enhancing effect on the relaxation rate of the water protons in its proximity, which may lead to an increase of the contrast in the images and a decrease of the recording time. Encapsulation of Gd^{3+} in a strongly chelating ligand is necessary, since the Gd^{3+} aquo ion is highly toxic, whereas the chelates are not. Thus an important requirement that a Gd^{3+} complex must meet for in vivo applicability is high stability, both thermodynamic and kinetic. Practically, this means that suitable ligands are generally octadentate. The chelating ligand preferably should leave enough space on the Gd^{3+} ion for coordination of water. The Gd^{3+} coordinated water exchanges with the bulk and as a result an overall contrast enhancement (reduction of the water proton relaxation rate) may be obtained. Currently, commercially available CA's are derivatives of: (i) DTPA (DTPA = diethylenetriamine-N,N,N',N'',N''-pentaacetate) and (ii) the macrocyclic ligand DOTA (DOTA = 1,4,7,10-tetraazacyclododecane-1,4,7,10-tetraacetate).

The overwhelming success of the CA's and the rapid development of the MRI technique have given rise to a continuing demand for new generations of CA's that are more effective and selective. Theory shows that the currently commercially available CA's are far from optimal with regard to relaxation enhancement. An improvement may be achieved via rational design of the ligands, which requires insight into the parameters that govern the relaxivity, r_1 (enhancement of the water proton relaxation rate, expressed in $\text{s}^{-1}\text{mM}^{-1}\text{Gd}^{3+}$). Extensive studies in this field have shown that each of these parameters is related to the solution structures and dynamics of the concerning complexes. Higher relaxivities may be achieved by, for example, (i) the design of the environment of the water coordination site, so that the water exchange rate will not limit the overall relaxivity ($\tau_m < T_{1m}$, with τ_m being the residence time of a water molecule in the first coordination sphere, and T_{1m} its proton longitudinal relaxation time), (ii) an increase of the molecular weight of the compounds, in order to increase the rotational correlation time, τ_R , or (iii) an increase of the rigidity of the complex, which gives rise to an increase of the electronic relaxation time of the Gd^{3+} ion, τ_{s0} . Furthermore, contrast improvements may be achieved by attaching substituents on the ligand such that higher organ or tissue specificity is obtained.

New generations of CA's are being developed that are reporters of their biochemical environment, allowing, for example, visualization of pH differences, oxygen concentrations, gene expression and therapeutic drug delivery. Molecular recognition and its translation into relaxivity are important issues in these studies.

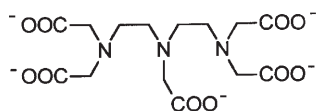
Here we overview the solution structures of lanthanide complexes of relevance to MRI, with a focus on the progress made during the last decade.

2

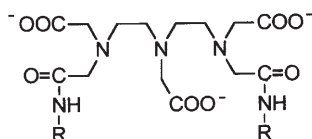
Complexes of DTPA and Derivatives

2.1

DTPA and DTPA-Bisamides



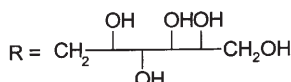
DTPA



DTPA-BMA

R = CH₃

DTPA-BGLUCA



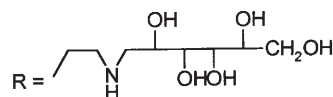
DTPA-BPA

R = CH₂-CH₂-CH₃

DTPA-BBA

R = CH₂-Ph

DTPA-BENGAALA



Structures 1

DTPA and all DTPA-bisamides reported up to now bind Ln³⁺ ions in a 8-coordinate fashion through the three N atoms of the diethylenetriamine backbone and five carboxylate and/or amide O-atoms, both in the solid and in solution. An inspection of crystal structures shows that diethylenetriamine moieties in these complexes always occur either in the $\lambda\lambda$ or in the $\delta\delta$ conformation [1, 2]. In these conformations, steric interactions are minimized. The coordination sphere is completed by one water molecule or, in some crystal structures, by the O-atom of a neighboring carboxylate group. In a recently reported low temperature (173 K) X-ray structure of K₂[Yb(DTPA)(H₂O)] second sphere waters were observed adjacent to the carboxylate oxygens [3]. The inner-sphere water is the most important source of the relaxivity of the corresponding Gd³⁺ complex, but the second sphere water molecules contribute significantly to it as well [3].

Solution structures have been extensively studied by NMR techniques [2] and by luminescence [4].

The ligation of Ln^{3+} by DTPA, DTPA-BPA, DTPA-BGLUCA, and DTPA-BEN-GALAA has been derived from Nd^{3+} -C distances as evaluated from Nd^{3+} -induced ^{13}C relaxation rate enhancements [5–8]. The distances obtained are in agreement with those observed in crystal structures of this class of compounds. ^1H NMR studies on various paramagnetic $[\text{Ln}(\text{DTPA})]^{2-}$ complexes [9, 10] and ^{13}C relaxation rate measurements on the diamagnetic $[\text{La}(\text{DTPA})]^{2-}$ confirm this mode of coordination [11]. A detailed X-ray absorption spectroscopy study of $[\text{Gd}(\text{DTPA})^{2-}]$ also showed that the local structure around the Gd^{3+} ion in aqueous solution is similar to that in crystals [12].

The inversion of the N-atoms in the diethylenetriamine backbone is precluded. The central N-atom is always chiral, since the ethylene bridges around it have different conformations (δ and λ). Furthermore, the two other N-atoms are chiral as well in the bisamides and chirality of the metal ion should be taken into account. DTPA derivatives with three chiral N-atoms can be wrapped around the Ln^{3+} ion in 16 different ways (8 diastereomeric pairs, see Fig. 1). In crystal structures of these compounds the Ln^{3+} coordination polyhedron can generally be best described as a tricapped trigonal prism (TTP). For $[\text{Ln}(\text{DTPA})]^{2-}$ $A_1 = A_2 = A_3 = B_1 = B_2$, and, consequently, only two enantiomers remain (1/1'). Analogously, it can be seen that the DTPA-bisamides can have 4 diastereomeric pairs.

Dynamic NMR studies [7–10] have shown that two exchange processes occur in these complexes: (i) Interconversion between the conformations of the ethylene bridges ($\delta\delta \rightleftharpoons \lambda\lambda$). This process can be achieved by a rearrangement in the coordination polyhedron and is characterized by a ΔG^\ddagger value between 49 and 57 kJ mol^{-1} . It should be noted that the shuffle in the coordination polyhedra converts 1 and 4 into their mirror images ($1 \rightleftharpoons 1'$ and $4 \rightleftharpoons 4'$), whereas 2 and 3 are converted into each others mirror images ($2 \rightleftharpoons 3'$ and $3 \rightleftharpoons 2'$). (ii) A relatively slow racemization of the terminal N-atoms ($\Delta G^\ddagger = 65\text{--}71 \text{ kJ mol}^{-1}$), requiring decoordination of the terminal N-atoms and their pending arms.

The NMR spectra of the paramagnetic DTPA-bisamide complexes show that the four diastereomeric pairs are populated in solution [7, 8]. NMR spectra of the diamagnetic complexes also show the presence of multiple isomers, although the number of NMR signals usually is lower than expected for four diastereomeric pairs [13–15]. This is probably due to superimposition of resonances or to rapid exchange between isomers on the NMR time scale. In the solid state DTPA-BBA has a *cis* configuration [14, 16], whereas all other Ln -DTPA-bisamide complexes occur in the *trans* configuration [17–19].

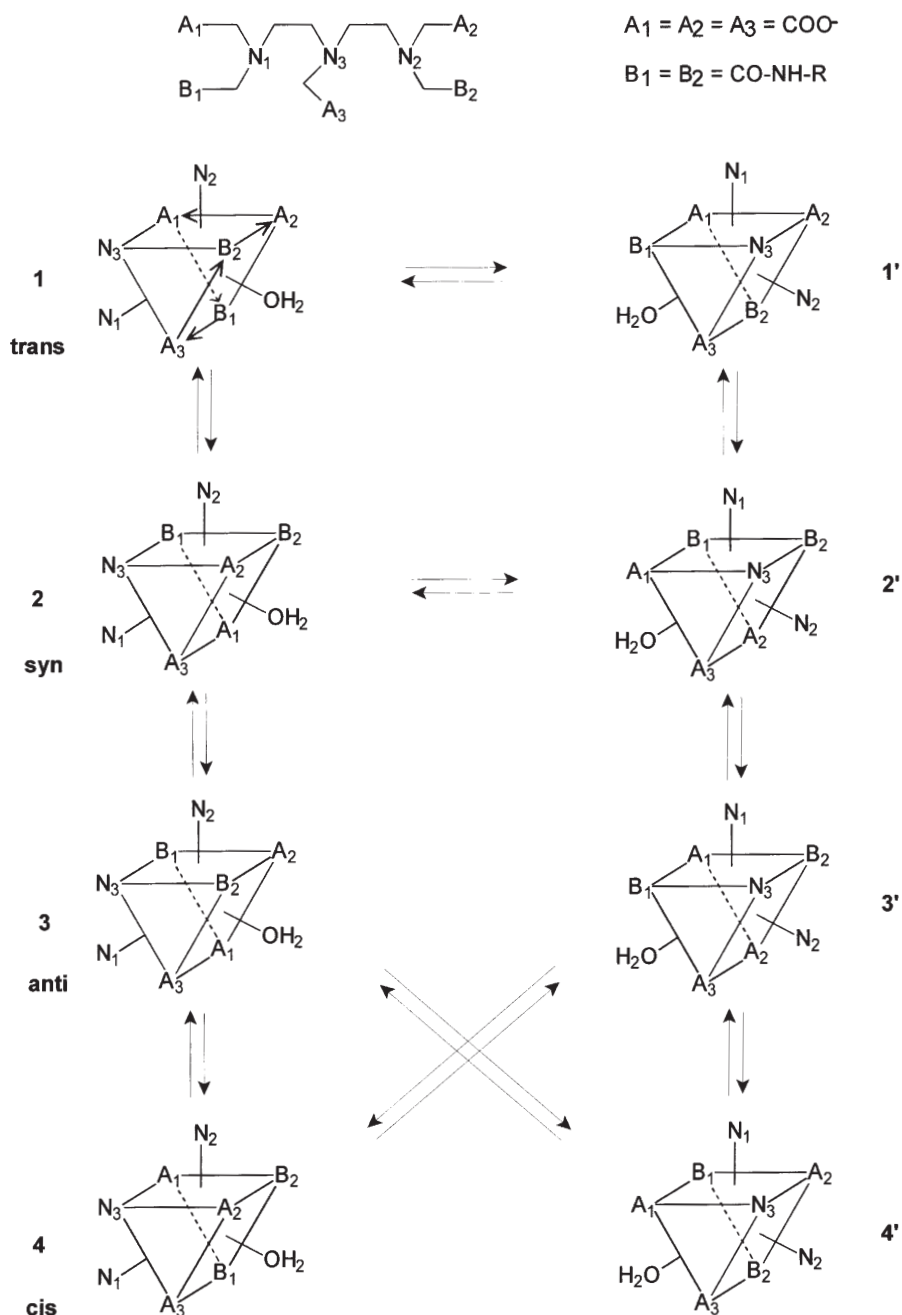
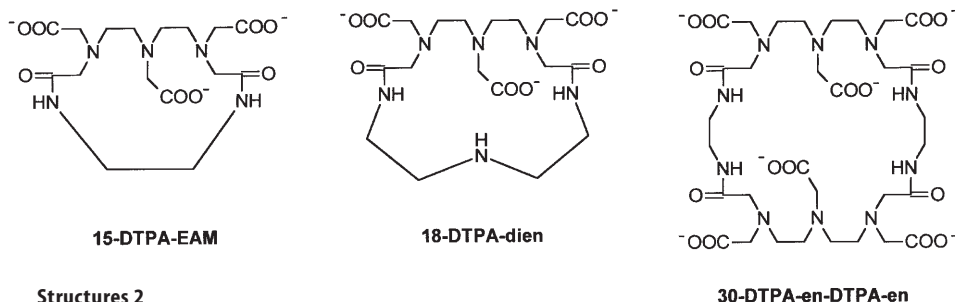


Fig. 1. Possible ways of wrapping a DTPA derivative around a Ln^{3+} ion in a TTP coordination polyhedron. Another set of mirror images is possible. For a monocapped square antiprism similar structures can be depicted. The shuffle in the coordination polyhedron related to the $\delta\delta/\lambda\lambda$ isomerization of the ethylene bridges is indicated with arrows in isomer 1

2.2

DTPA-Bisamides Incorporated in Macrocycles



Structures 2

30-DTPA-en-DTPA-en

In the crystal structures of the La^{3+} and Eu^{3+} complexes of $\text{Ln}(\text{18-DTPA-dien})$ oligomerization was observed [20]. The coordination of the Ln^{3+} ion by each DTPA unit, however, was similar to that in the linear bisamides. Vapor pressure osmometry indicated that oligomerization in solution does not occur under the conditions applied (0.2–0.5 M). Because of the constraints imposed by linking the two amide functions in the macrocycle, the isomers **1,1'** and **3,3'** depicted in Fig. 1 are sterically very unfavorable. In line with this, resonances for only two pairs of enantiomers were observed in the ^1H spectra of the $\text{Ln}(\text{18-DTPA-dien})$ complexes. The dynamic behavior showed that one pair was rather static, whereas the other was rapidly interconverting. The ΔG^\ddagger for the interconversion (65 kJ mol^{-1}) was about the same as those observed for the $\delta\delta \rightleftharpoons \lambda\lambda$ isomerization in other DTPA-derivatives. In the $\text{Ln}(\text{18-DTPA-dien})$ complex such an isomerization is only possible between mirror images **2** and **2'**. All other isomerizations require decoordination and, therefore, are much slower.

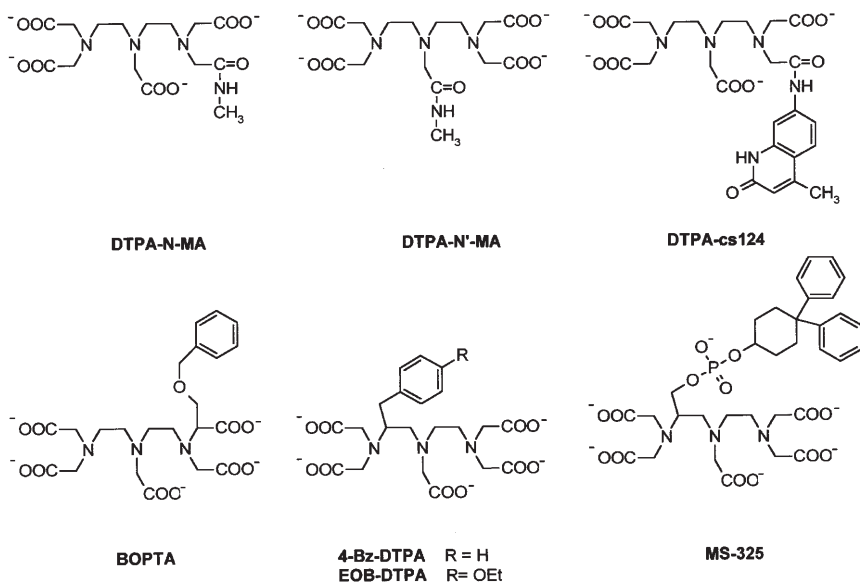
Similar species occur in solutions of Ln^{3+} complexes of a 30-membered macrocycle $\text{Ln}_2(\text{30-DTPA-en-DTPA-en})$ constructed of two DTPA units linked by two ethylenediamine bridges [21]. For the 15-membered macrocycle **15-DTPA-EAM**, however, only the equilibrium $\mathbf{2} \rightleftharpoons \mathbf{2}'$ was observed for the heavier Ln^{3+} ions [21]. Dy^{3+} induced ^{17}O NMR shifts showed that the hydration number of this complex is 0.8 ± 0.2 . A Eu^{3+} luminescence study indicated $q = 2.3 \pm 0.5$ for the corresponding Eu^{3+} complex at low concentration ($5 \mu\text{M}$) [22]. Usually, the results of the ^{17}O NMR method and luminescence are in good agreement with each other, and therefore it is assumed that the hydration number of the $\text{Ln}(\text{15-DTPA-EAM})$ complexes changes between Eu^{3+} and Dy^{3+} [21]. Unfortunately, the complexes of the lighter Ln^{3+} ions were insoluble under conditions required for NMR, probably due to the formation of dimeric complexes, similar to those observed in the solid state for various Ln^{3+} complexes of this ligand [23, 24]. The stoichiometries, hydration numbers, stabilities, conformations, and Eu^{3+} – Eu^{3+} distances of a series of Eu^{3+} complexes of amide based macrocycles, including **30-DTPA-en-DTPA-en** and **15-DTPA-EAM** have been studied in solution by Eu^{3+} luminescence and molecular mechanics [22]. From a single peak observed in the $^7\text{F}_0 \rightarrow ^5\text{D}_0$ excitation spectrum, it was concluded that a single isomeric form is

present in solution for all complexes. This is, however in conflict with the results of the NMR studies [20, 21]. Apparently, it is not possible to discriminate such closely related isomers with luminescence spectroscopy.

The complex formation of Eu(18-DTPA-dien) has been studied by laser-excited luminescence [25]. Immediately upon mixing the metal ion and the ligand, both the final complex and a long-lived intermediate were observed. It has been proposed that the intermediate is a “blind alley” in the reaction pathways. Based on the wavelength in the ${}^7F_0 \rightarrow {}^5D_0$ excitation spectrum and its excited lifetime (in H_2O and D_2O), it has been suggested that in the intermediate the ligand is coordinated to Eu^{3+} with three carboxylates (in up-down-up configuration with respect to the macrocycle), three amino nitrogen atoms, and a water molecule. Transformation of this intermediate into the final product requires some decomplexation, which explains the relatively low rate of this reaction.

2.3

Monosubstituted DTPA Derivatives



Structures 3

For Ln^{3+} complexes of DTPA-monoamides with the amide function on the central glycine moiety, similar isomers as in the parent system may be envisaged. This has been confirmed by a 1H NMR study of $[Ln(DTPA-N'-MA)]^-$ ($Ln = La, Lu$) [26]. Two AB multiplets were found for the acetate methylene, thus, the lifetime of $Ln-N$ bond is long on the NMR time scale. The ethane bridges in the coordinated ligand exist in two different conformations, which interconvert by wagging via an eclipsed transition state. Simulation of the 1H NMR spectrum leads to the conclusion that the two N-atoms on the bridge are in the gauche position, the dihedral angle between them is somewhat larger than 60° .

For Ln^{3+} complexes of DTPA derivatives with a single substituent at another position than the central glycine unit, the number of possible ways by which the ligand can be wrapped around a Ln^{3+} ion can be derived from Fig. 1. It should be taken into account that the interconversion between the $\delta\delta$ - and $\lambda\lambda$ -conformers of the triethylenediamine backbone does not result in interconversion of mirror images in this case. Therefore, a second set of isomers is possible which are mirror images of the first. Discrimination between pairs of mirror images is not possible by NMR and interconversion between them is expected to be extremely slow because it requires decoordination of at least seven of the eight donor sites of the ligand. The ^1H and ^{13}C NMR spectra of the less symmetrical $[\text{Ln}(\text{DTPA-N-MA})]^-$ are rich in signals and reveal the presence of at least three, presumably all four expected species in solution [26]. The intensities of the signals are different and probably the chemical shifts of the signals for two of the species are about the same.

A solid state Eu^{3+} complex of DTPA-cs124 was studied [27]. It was found that it is present as dimeric units, the carbostyryl moiety of one unit is bound to the lanthanide of the other unit via the quinolinone α -oxygen atom. In this case, no water molecule is coordinated directly to Eu^{3+} . This unusual behavior is ascribed to stacking properties of the carbostyryl unit and to the presence of the α -oxygen atom in a position advantageous for coordination.

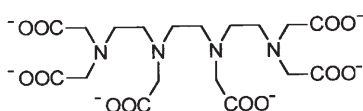
The ^{13}C NMR spectra of the La^{3+} and Lu^{3+} complexes of BOPTA display about 20 resonances in the aliphatic region at 60°C [28], which broaden upon lowering of the temperature. This suggests that a dynamic process is slowing down. It can be concluded that this compound occurs as at least two pairs of interconverting isomers [28]. In principle, the chirality in the benzyloxymethyl chain can give rise to doubling of the number of isomers, however, they are probably not observable in the NMR spectra of the diamagnetic La^{3+} and Lu^{3+} complexes due to small chemical shift differences between them. In the solid state structure of $\text{Na}_2[\text{Gd}(\text{BOPTA})]$, two enantiomeric forms (*trans*, see Fig. 1) occur in each unit cell [28].

Two diastereomeric $\text{Gd}(\text{S-EOB-DTPA})$ complexes have been isolated by preparative HPLC [29]. The interconversion between these complexes is very slow; the half-life time of one of the isomers of the Gd^{3+} complex is 13100 h at pH 9 and 25°C . At the thermodynamic equilibrium, the ratio of the isomers is 65:35. The first order rate constant for the interconversion between isomers is pH dependent, suggesting that the isomerization is an acid-catalyzed process similar to the dissociation of the complex. NMR studies on the two corresponding diamagnetic La^{3+} complexes gave no evidence for the presence of enantiomers that differ in the orientation of the acetate groups [29]. In principle, four isomers are possible for these systems, however two of them are mirror images of the other two and, therefore, discrimination by NMR is impossible. Dy^{3+} induced water ^{17}O shifts indicated that $q = 1.2$ for $\text{Dy}(\text{EOB-DTPA})^{2-}$ which is similar to $\text{Dy}(\text{DTPA})^{2-}$ [30, 31]. Relaxivity studies on the Gd^{3+} complexes of BOPTA [28], EOB-DTPA [30, 31], 4-Bz-DTPA [32] and MS-325 [33] indicated that the relaxivity of these compounds is higher than expected on the basis of the relevant correlation times. This may originate from a reduced distance between Gd^{3+} and the inner-sphere water protons (about 0.29 nm) as compared

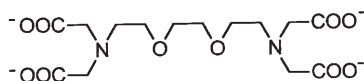
to the value usually reported for $\text{Gd}(\text{DTPA})^{2-}$ (0.31 nm) [31]. This shortening only concerns the Gd-H distance because similar Gd-O distances are found by crystallography for $\text{Gd}(\text{DTPA})^{2-}$ and $\text{Gd}(\text{BOPTA})^{2-}$ [28]. The apparent reduction of the Gd-H distance appears to be characteristic for Gd^{3+} complexes carrying substituents with aromatic groups at the ethylene bridge and is accompanied by a shortening of τ_M . Normal distances were obtained from simulations of ^1H NMRD data of the Gd^{3+} complexes of DTPA-bis(benzylamide) and DTPA-bis(benzylester) [32]. This effect may be attributed to a true reduction of the Gd-H distance or to a reorganization of the second hydration shell by the hydrophobic group [32]

2.4

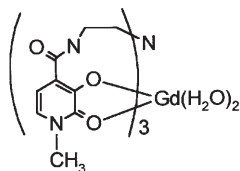
EGTA



TTHA



EGTA



$\text{Gd}[(\text{TREN-Me-3,2-HOPO})(\text{H}_2\text{O})]$

Structures 4

The crystal structures of the $[\text{Nd}(\text{EGTA})]^-$ and $[\text{Er}(\text{EGTA})]^-$ complexes are different, showing a 10- and 9-fold coordination, respectively [34]. The coordination polyhedron for $[\text{Nd}(\text{EGTA})(\text{H}_2\text{O})]^-$ can be described as a bicapped square antiprism, where the two N-atoms are in the capping positions. The two square faces, linked by the diether bridge, are formed by two O-atoms of adjacent acetate arms, one O-atom belonging to the ether bridge and an O-atom of either water or a carboxylate of an adjacent molecule. By contrast, the coordination cage of the complex $[\text{Er}(\text{EGTA})(\text{H}_2\text{O})]^-$ in the solid state can be described by a TTP with the capping positions occupied by the two N-atoms and by the inner sphere water molecule and the trigonal faces are formed both by one ether and by two carboxyl O-atoms.

The solution structure of the EGTA lanthanide complexes was investigated using the ^1H and ^{13}C NMR spectra of the various lanthanide complexes and the Lanthanide Induced Shift (LIS) for one of the acetate resonances for a series of Ln-EGTA complexes. The spectra of the lighter lanthanides up to Sm show five resonances in the ^1H spectrum and seven in the ^{13}C spectrum at room temperature. This pattern is consistent with a 10-coordinate structure characterized by a C_2 symmetry axis undergoing a fast rearrangement that averages the signals of

pairs of atoms. The most probable conformational change, which could determine such averaging, is the rotation around the central diether bridge that scrambles the acetate groups.

The heavier lanthanides, at room temperature, show ten resonances in the ^1H spectrum and seven in the ^{13}C spectrum, which is consistent with a 9-coordinated solution structure where all the atoms are magnetically inequivalent, and undergoing a fast rearrangement that averages signals of pairs of atoms. Such behaviour is explainable by the scrambling of the two carboxylate groups sitting on adjacent vertices of the two trigonal planes and connected by the edge opposite to the capping position occupied by the water molecule.

A thorough analysis of ^1H LIS data indicates the presence of a common structure for the lighter lanthanides, a change in structure near Eu, and probably another change between Tm and Yb. This view is supported by UV measurements that for the Ce^{3+} complex show the presence of two species which were assigned to the equilibrium between 9- and 10-coordinated complexes on the basis of the large ionic radius of Ce^{3+} , whereas the UV measurements for the Eu^{3+} complex show a single absorption band at 580 nm for the $^7\text{F}_0 \rightarrow ^5\text{D}_0$ transition, which was assigned to the 9-coordinate species. The last two members of the lanthanide series presumably adopt another structure, probably an 8-coordinate state without inner sphere water molecules.

The change in structure along the lanthanide series, going from La^{3+} to Lu^{3+} , can be ascribed to the decrease in ionic radius of the metal center which causes an increase of the rigidity and in the steric constraint on the water binding site [35, 36]. For this reason the 9-coordinate Gd complex shows a remarkably high water exchange rate.

2.5

TTHA

Two different coordination modes have been reported for various lanthanide complexes of TTHA in the solid state. Tenfold Ln^{3+} -coordination through the four N-atoms and six carboxylate O-atoms of TTHA has been observed for $[\text{La}(\text{HTTTHA})]^{2-}$ [37, 38] and $[\text{Nd}(\text{TTHA})]^{3-}$ [39]. The coordination polyhedron can be described as a distorted bicapped square antiprism with the terminal N-atoms of TTHA at the capping positions. However, for $[\text{Gd}(\text{HTTTHA})]^{2-}$ [37], $[\text{Dy}(\text{HTTTHA})]^{2-}$ [40], $[\text{Ho}(\text{TTHA})]^{3-}$ [41], and $[\text{Yb}(\text{TTHA})]^{3-}$ [42] the coordination number is nine. Here, one of the terminal carboxylates is not coordinated and the coordination polyhedron can be described as a TTP. In crystal structures of the Ln -TTHA complexes, the ethylene units in the triethylenetetraamine backbone occur exclusively in the $\lambda\lambda\delta$ and $\delta\delta\lambda$ conformations. The ethylenediamine bridge with the opposing conformation carries a carboxylate group that is characterized by a relatively long Ln-O binding distance (10-fold coordination) or that is not bound (9-fold coordination). The crystal structures of dimeric $[\text{Nd}_2(\text{TTHA})_2]^{6-}$ [43] and $[\text{Gd}_2(\text{TTHA})_2]^{6-}$ [44] complexes revealed both Ln^{3+} ions to be 9-coordinate in a TTP geometry. Each ligand molecule was bound via three N-atoms and six carboxylate O-atoms, two of which were coordinating the second Ln^{3+} ion. The fourth N-atom remains uncoordinated. In all reported

Ln-TTHA crystal structures no water molecules were found in the first coordination sphere of the metal ion.

Comparison of electronic absorption spectra of the Ln-TTHA complexes in the solid state and in solution has shown that the monomeric species with Ln³⁺ coordination numbers 10 and 9 also occur in solution for the light and heavy lanthanides, respectively [39, 41, 43]. In addition, these studies suggest the presence of another species with one uncoordinated N-atom for the Nd³⁺ and Eu³⁺ systems. Absorption spectra [39, 41, 43], luminescence [45] and ¹H Nuclear Magnetic Resonance Dispersion (NMRD) studies [46] have shown that oligomeric species also occur in solution, particularly below pH 5.

The change in coordination number along the lanthanide series is also demonstrated by the ¹H and ¹³C NMR spectra; aqueous solutions of [La(TTHA)]³⁻ [47, 48] and [Nd(TTHA)]³⁻ [49] at pH 6 and room temperature indicate a single species with an effective plane of symmetry bisecting the central C-C bridge of the TTHA ligand, whereas the spectra of the Lu³⁺ and Y³⁺ complexes are very complex. Upon cooling a sample of [Nd(TTHA)]³⁻ in D₂O-CD₃OD, the ¹³C NMR spectrum showed line-broadening and splitting of each peak into two new ones [49]. The ΔG^\ddagger value for the exchange process was determined to be 50 kJ mol⁻¹, which is in the same order of magnitude as that observed for the wagging process in [Ln(DTPA)]⁻ complexes. Nd-C distances evaluated from ¹³C NMR longitudinal relaxation rates confirm that the TTHA ligand is bound in a 10-coordinate fashion [49]. The binding of TTHA in this way makes the two central N-atoms chiral and, consequently, the ligand can be wrapped around the Ln³⁺ ion in two diastereomeric forms (*rac* and *meso*). The crystal structures reported up to now exhibit exclusively the racemic form. It is unlikely that this is also the predominant form in solution, the above described dynamic process leading to an effective plane of symmetry in the Ln³⁺ bound TTHA ligand would require an extensive decoordination of the ligand followed by inversion of the two central N-atoms and recoordination. It may be expected that such a process would be much slower than observed in the [Nd(TTHA)]³⁻ complex. Therefore, we assume that, in solution, the *meso* form predominates. A $\lambda\lambda\delta/\delta\delta\lambda$ isomerization of the ethylene bridges can then explain the time-averaged plane of symmetry in these complexes.

With the use of a 2D EXSY experiment on a [La(TTHA)]³⁻ sample, an exchange between the diastereotopic protons in the terminal acetate groups has been observed. The activation energy of this process is relatively high ($E_a = 69.6$ kJ) [48], which can be accounted for by a mechanism via decoordination of a terminal N(CH₂COO)₂ moiety, followed by inversion and recoordination.

In the 9-coordinate TTHA complexes of the heavier Ln³⁺ ions, the situation is more complex, since there also the terminal N-atom bearing the uncoordinated acetate moiety is chiral. ¹⁷O NMR [49, 50], luminescence [47, 51] and NMRD measurements [46] have shown that, for both 9- and 10-coordinate Ln(TTHA)³⁻ complexes, the inner coordination sphere of the metal ion is fully occupied by donating groups of the ligand, leaving no space for the coordination of water. Consequently, the water proton relaxation enhancement has no inner sphere contribution and the [Gd(TTHA)]³⁻ complex is not very suitable for application

as CA. It has been considered for many years as a model for the outer sphere contribution to the total relaxivity of acyclic polyaminocarboxylates [52], but at present, the outer sphere contribution is usually evaluated with the use of the Freed equations [53]. The negatively charged $[\text{Ln}(\text{TTHA})]^{3-}$ complexes have high affinity for metal ions, and particularly $[\text{Dy}(\text{TTHA})]^{3-}$ and $[\text{Tm}(\text{TTHA})]^{3-}$ have been shown to be good NMR shift reagents for Na^+ [54].

3

Complexes of Tripodal Hydroxypyridinonates

Raymond and coworkers have reported that the Gd^{3+} complex of the tripodant ligand TREN-Me-3,2-HOPO has promising potential for application as CA [55]. The X-ray structure of this complex shows that it is 8-coordinate. The organic ligand is coordinated in a hexadentate fashion through the hydroxypyridone O-atoms and two water molecules complete the coordination sphere. The relaxivity appears to be 2.5 times as high as that of $[\text{Gd}(\text{DTPA})]^-$. Although the organic ligand is only hexadentate, the thermodynamic stability of the complex is good ($\log \beta_{110} = 20.3$), which may be ascribed to some degree of preorganization and stability due to internal hydrogen bonds. The complex is more stable than $\text{Gd}(\text{DTPA-BMA})$ toward transmetallation with Zn^{2+} and Ca^{2+} . The solubility of this compound is too low for practical application, and, therefore, derivatives are being developed with substituents in the TREN moiety [56, 57], and by attaching two different HOPO chelators to TREN [58]. ^1H NMRD and ^{17}O NMR measurements on some of these compound confirmed the presence of two water molecules in the first coordination sphere of Gd^{3+} , which are in very fast exchange with the bulk water. A low barrier between the 8-coordinate ground state and 9-coordinate transition state in the associative exchange mechanism can explain the rapid exchange rates. The small difference in stability between 8- and 9-coordinate complexes of this type is supported by the occurrence of both coordination structures in a crystal of $\text{La}[\text{TREN-Me-3,2-HOPO}]$ [58].

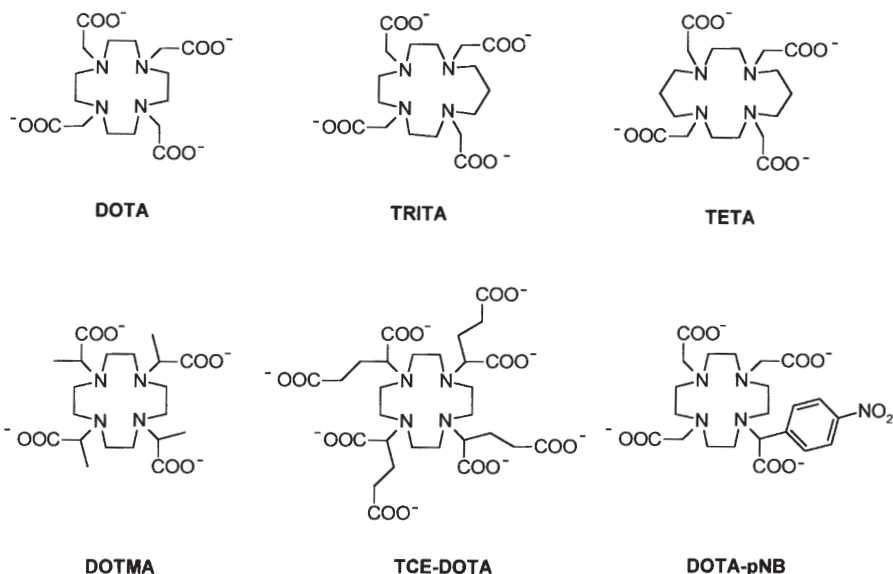
4

Complexes of Cyclen Type Compounds

4.1

DOTA and Derivatives

Ln^{3+} induced water ^{17}O shifts of $[\text{Ln}(\text{DOTA})]^-$ solutions show that the hydration number of the complexes is one across the lanthanide series [59]. The substantial pseudocontact contribution to its LIS indicated that this water ligand has a preferred location in the complex. Two sets of peaks have been observed in ^1H and ^{13}C NMR spectra of $[\text{Ln}(\text{DOTA})]^-$ complexes at room temperature showing the presence of two slowly interconverting structural isomers [60–63]. In the spectra of the paramagnetic complexes, one isomer has larger LIS values than the other. These structural features have been confirmed by luminescence studies [51, 64]. The temperature dependence of the ^1H and ^{13}C NMR spectral features of both the dia- and paramagnetic Ln^{3+} complexes indicates that the



Structures 5

12-membered macrocyclic ring is very rigid [60, 61]. The Ln^{3+} , too large to fit inside its internal cavity, is located outside of it, bound to the four N-atoms and the four carboxylate groups. All ethylene groups adopt an identical gauche conformation, either δ or λ , leading to one of two possible square [3333] conformations of the macrocyclic ring, whose interconversions are in part responsible for the dynamic phenomena observed in the NMR spectra at higher temperatures [60]. A structural description of both isomers in solution was carried out using 2D NMR techniques (COSY and EXSY) [62, 63]. Based on the similarity of the vicinal couplings in the ethylene bridges, it was concluded that the structure of the macrocyclic ring is the same in the two isomers and that their differences are in the layout of the acetate arms, through change of the four torsion angles Ln-N-C-COO . In both isomers, the coordination polyhedron is a capped square antiprism with two opposite parallel faces occupied by the ligand N (N_4 plane) and O (O_4 plane) donors and a water molecule at the capping position. The twist angle between the N_4 and O_4 planes (θ) is positive for one of the isomers (normal capped square antiprism, CSAP) and negative for the other (twisted or inverted CSAP) [61].

The relative concentrations of the two species depend on the size of the Ln^{3+} ion, temperature, pressure, and on the concentration of added inorganic salts [61–63]. While the twisted CSAP geometry is the isomer present with the higher percentage (“major” isomer) for the complexes of the larger cations, La^{3+} – Nd^{3+} , the CSAP geometry becomes the most stable for the smaller cations Sm^{3+} – Er^{3+} [61, 63]. In all these cases, the isomerization process is purely conformational, as shown by the near zero reaction volumes obtained by high-pressure NMR [63]. However, for the complexes of the smallest cations (Tm^{3+} – Lu^{3+}), the

large positive isomerization volumes obtained show that the “minor” isomer results from a fast water dissociation process superimposed on the conformational rearrangement leading to an 8-coordinate square antiprismatic geometry [63]. High concentrations of non-coordinating salts stabilize the twisted CSAP geometry relative to the CSAP due to preferential weak ion binding and water solvent stabilization of the former ligand geometry. Fluoride ions also preferentially replace the coordinated water in the first, more open, geometry [63].

The solution structure of the CSAP isomer is consistent with the X-ray structures of the Eu^{3+} [65], Gd^{3+} [66, 67], Y^{3+} [67] and Lu^{3+} [68] complexes of DOTA where $\theta \approx 39^\circ$. The solution structure of the twisted CSAP isomer is consistent with the X-ray structure of the La^{3+} complex of DOTA where $\theta \approx -22^\circ$ [69]. An EXAFS study confirmed that the local environments of Gd^{3+} are similar in solution and in crystals of $[\text{Gd}(\text{DOTA})]^-$ [12]. The similarity between the solid state and the solution structures of the two isomers was confirmed by the geometric dependence of the measured paramagnetic NMR shift and relaxation effects. There was an excellent agreement between the Yb^{3+} induced ^1H shifts (of the “major” isomer), which were assumed to be almost purely of pseudocontact origin, and shifts calculated from the X-ray structure of the Eu^{3+} complex, using an axial symmetry model, since that structure has a C_4 symmetry axis [60]. Starting from the structure of the “major” isomer, the torsion angle Ln-N-C-COO was altered stepwise until an optimal fit was obtained between calculated and observed LIS (^1H) for the “minor” isomer [61]. Distances between the Ln^{3+} ion and the ligand protons in the “major” isomer Tb^{3+} - Tm^{3+} complexes were evaluated by exploiting the magnetic field dependence of the Curie relaxation contribution, which gave excellent agreement with the values calculated for the CSAP X-ray structures [61, 70].

With the use of variable temperature ^{13}C NMR on the Nd^{3+} -complex and ^1H EXSY on the Yb^{3+} -complex, it was shown that exchange processes occur between the isomers [61]. A similar study with the Eu^{3+} and Yb^{3+} DOTA complexes led to the same conclusions [62]. The structure and dynamics of the $\text{Ln}(\text{DOTA})^-$ system are summarized in Fig. 2. The difference in the arrangements of the acetates, which leads to CSAP and twisted CSAP geometries for the two isomers that can be described with $\theta \approx 40^\circ$ for the CSAP geometry and $\theta \approx -20^\circ$ for the twisted CSAP geometry. Thus, there are four stereoisomers, two pairs of enantiomers, which can interconvert in solution by either cooperative ring inversion ($\delta\delta\delta\delta \rightleftharpoons \lambda\lambda\lambda\lambda$) or concerted acetate arm rotation ($\Delta \rightleftharpoons \Lambda$). Either process alone results in exchange between the CSAP and twisted CSAP geometries and both processes combined, either in succession or concerted, result in an exchange between enantiomeric pairs (see Fig. 2). A thorough quantitative analysis of variable temperature EXSY spectra of $[\text{Yb}(\text{DOTA})]^-$ has been carried out by completely solving the dynamic matrix [71]. It was shown that each species in the dynamic equilibrium is exchanging with all other species. The activation parameters (ΔG^\ddagger_{298}) for the enantiomerization, arm rotation and ring inversion processes in $[\text{Yb}(\text{DOTA})]^-$ were calculated, showing that, for this system, arm rotation is faster than ring inversion. This conclusion was confirmed by other ^1H EXSY and variable temperature ^{13}C NMR studies [60, 61, 68]. It reflects the high rigidity of the Ln^{3+} complexes of DOTA as compared to those of DTPA deriva-

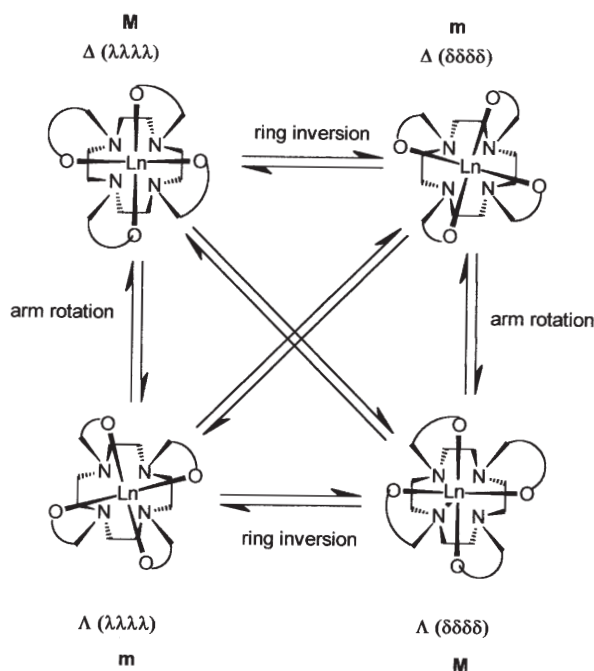


Fig. 2. Schematic representation of the structures and dynamics of $[\text{Ln}(\text{DOTA})]^-$ complexes, looking down along the Ln-water O bond. The water molecule is omitted for clarity

tives. Protonation of the $[\text{Ln}(\text{DOTA})]^-$ complexes in very acid medium slightly accelerates all the above ligand conformational dynamic processes but significantly decreases water exchange rates [72].

The solution structures of the Ln^{3+} complexes with the homologous tetracarboxylate ligands containing larger tetraaza macrocyclic moieties were elucidated in a similar way as described above for the DOTA complexes using NMR techniques [73, 74]. The complexes of the 14-membered system TETA, $\text{Ln}(\text{TETA})^-$, which contain no inner-sphere water, are also very rigid and undergo an exchange between two equivalent eight-coordinate dodecahedral geometries [73]. For the 13-membered system (TRITA), the macrocyclic backbone of $\text{Ln}(\text{TRITA})$ prefers a [12433] conformation [74].

In the case of α -substituted DOTA derivatives, the introduction of chiral centers at all four acetate arms of DOTA leads to further elements of chirality to consider in the corresponding Ln^{3+} complexes. The four stereogenic carbon centers at the acetate arms, with *R* or *S* configurations, generate six ligand stereoisomers: the two enantiomeric pairs *RRRR* and *SSSS*, *RSSS* and *SRRR*, and the two achiral diastereoisomers *RSRS* and *RRSS*. In the lanthanide complexes of a given ligand isomer there are the two further independent elements of chirality to consider, already present on the DOTA complexes, associated with the conformation of the NCCN chelate rings (δ or λ) and the helicity (Δ or Λ) of the acetate arms.

When the four chiral centers at the acetate arms of DOTA have equal configuration (*RRRR* or *SSSS*) four possible diastereoisomers may result upon chelation. However, the occurrence of only two isomers appears to be a general phenomenon of Ln^{3+} complexes of such DOTA derivatives. This is observed in $[\text{Ln}(\text{DOTMA})]^-$ complexes, where the configuration at each chiral carbon is *R* [75]. The ^1H NMR spectrum of $[\text{Yb}(\text{DOTMA})]^-$ and the high-resolution luminescence spectrum of the Eu^{3+} complex show only two species in solution [75], whose relative populations are temperature and solvent dependent [76]. The “major” isomer of the Yb^{3+} -complex has a structure corresponding to the “minor” isomer of $[\text{Yb}(\text{DOTA})]^-$ [71]. The isomerization process of $[\text{Yb}(\text{DOTMA})]^-$, like for $[\text{Yb}(\text{DOTA})]^-$ [63], involves exchange of a water molecule in the capping position of the CSAP coordination polyhedron, as shown by the sign of isomerization entropy values obtained by ^1H NMR [76]. Near-infrared circular dichroism (NIR CD) spectral studies of $[\text{Yb}(\text{DOTMA})]^-$ in solution provided an example of coupling chiroptical methods and paramagnetic NMR to study the absolute configuration of chiral lanthanide complexes [77].

The ligand tetracarboxyethyl DOTA derivative (TCE-DOTA) was synthesized as a mixture of the six stereoisomers defined by the absolute configuration of the four chiral carbons, *RRRR/SSSS* pair, *RSSS/SRRR* pair, *RSRS* and *RRSS*, which were separated, crystallized and their crystal structures determined [78, 79]. The crystal structures of the Eu^{3+} , Gd^{3+} and Tb^{3+} complexes of the TCE-DOTA (*RRRR*)/(*SSSS*) isomer are isostructural and consist of two co-crystallized enantiomers, the (*RRRR*) and (*SSSS*) complexes, with the same nine-coordinate CSAP geometry (twist angle averaging 38.5°) and opposite helicities [78, 79]. Thus, for an *R* configuration at carbon, the complex adopted a Λ (left-handed) arm helicity and a $(\delta\delta\delta\delta)$ chelate ring configuration. The (*SSSS*) enantiomer gave a Δ (right-handed) helicity and a $(\lambda\lambda\lambda\lambda)$ chelate ring configuration. A ^1H NMR study of the number of stereoisomers present in solution for each of the Eu^{3+} and Yb^{3+} complexes of the TCE-DOTA isomers was also carried out. The two diastereoisomers expected – CSAP (*M*) and twisted CSAP (*m*) are characterized by different dipolar shifts and are easily recognized by the NMR spectra. Two major isomeric species were observed for the (*RRRR*)-, (*RRRS*)- and [(*RSRS*)- $\text{Eu}(\text{TCE-DOTA})]^{5-}$ complexes in a relative ratio, *M/m* of 1:4, 2:1 and 4:1, respectively, compared with a *M/m* ratio of 4:1 for $[\text{Eu}(\text{DOTA})]^-$. For [(*RRSS*)- $\text{Eu}(\text{TCE-DOTA})]^{5-}$, only one (*M*) isomer is present in solution. For the (*RRRR*)- Eu complex, the major (*m*) isomer (not present in the crystal) must adopt a $\Lambda/(\lambda\lambda\lambda\lambda)$ configuration, while the minor (*M*) isomer possesses a $\Lambda/(\delta\delta\delta\delta)$ configuration. The absolute configuration of the stereogenic center at C is determining the left-handed helicity of the complex, so that neither the $\Delta/(\delta\delta\delta\delta)$ nor the $\Delta/(\lambda\lambda\lambda\lambda)$ complexes are present [79]. Two-dimensional ^1H EXSY spectra were recorded for the Eu^{3+} complexes of (*RRRR*)-, (*RRRS*)- and (*RSRS*)-(TCE-DOTA) at 293 K [79]. The EXSY spectrum of the (*RSRS*)- complex was very similar to that reported for $[\text{Eu}(\text{DOTA})]^-$ [60, 61, 71], consistent with relatively fast ring inversion and arm rotation on the NMR time scale. The EXSY spectra for the (*RRRR*)- and (*RRRS*)- complexes were much simpler, as no cross peaks were observed between corresponding axial proton resonances of the major and minor iso-

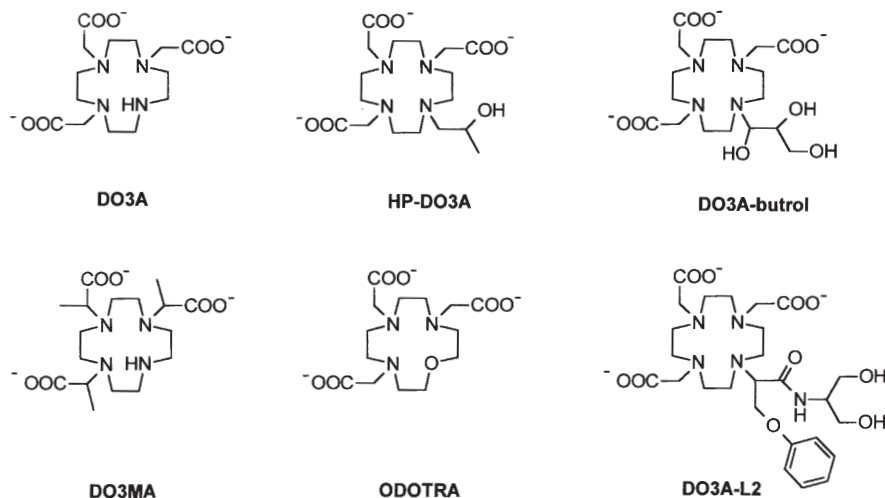
mers, indicating that concerted arm rotation was occurring two orders of magnitude more slowly than ring inversion.

The introduction of only one chiral center in DOTA by derivatizing one acetate α -carbon with a para-nitrophenyl group (DOTA-pNB) [80] also results in four possible diastereomers upon chelation. The Ho^{3+} and Yb^{3+} complexes of DOTA-pNB again give ^1H NMR spectra showing the presence of only two isomers. In these cases, like for some of the $[\text{Eu}(\text{TCE-DOTA})]^{5-}$ ligand isomers, ^1H EXSY has shown that the two isomers exchange through inversion of the macrocyclic ring, whereas no rearrangement of the acetate groups is observed. Thus, α -carbon derivatization drastically slows down the acetate arm rotation process so that ring inversion now becomes the faster isomerization process. The ring inversion results in an exchange between CSAP and twisted CSAP geometries of the same helicity while the arm rotation would lead to opposite helicities. The absence of the second process suggests that the configuration of the stereogenic center at carbon determines the least sterically hindered helical form of the complex. In fact, the crystal structures of the (RRRR) and (SSSS) TCE-DOTA Eu^{3+} complexes show that in both enantiomers the substituent is equatorially positioned, pointing away from the coordination cage [78, 79]. The same observation was made from the structural analysis of the LIS data for the $\text{Yb}(\text{DOTA-pNB})^-$ complex [80]. It is this preference for a particular helicity that reduces the number of diastereomers from four to two, in agreement with the NMR data for the DOTMA, TCE-DOTA and DOTA-pNB complexes [75–80].

Amphiphilic DO3A derivatives with long alkyl chains at the 10-N atom display micellar self-organization leading to an increase of τ_R , and therefore also of the relaxivity [81, 82].

4.2

DO3A and Derivatives



Structures 6

The success of $[\text{Gd}(\text{DOTA})]^-$ as a CA has initiated an intensive search for derivatives with improved properties, such as complexes of DO3A derivatives. The nonionic reagents $\text{Gd}(\text{HP-DO3A})$ and $\text{Gd}(\text{DO3A-butrol})$, in which one of the acetate groups of DOTA is replaced by a hydroxyalkyl group, have recently been introduced.

The crystal structures of the parent $\text{Gd}(\text{DO3A})$ [67] and of the $\text{Gd}(\text{DO3MA})$ [83] derivatives show the 9-coordinate Gd^{3+} to be bound by the ligands in a heptadentate fashion. The coordination geometry is CSAP for the DO3A ligand and both CSAP and twisted CSAP for the DO3MA ligand. The crystal structure of $\text{Gd}(\text{DO3A-L2})$ [84] shows the 9-coordinate Gd^{3+} bound by the ligand in an octadentate fashion, including the amide oxygen, and by one water molecule, in a CSAP geometry. In the crystal structures of the $\text{Ln}(\text{HP-DO3A})$ complexes ($\text{Ln} = \text{Gd}, \text{Y}$), the Ln^{3+} ion is again 9-coordinate, bound by the ligand in an octadentate fashion, including the hydroxyalkyl oxygen, and by one water molecule, with both the CSAP and twisted CSAP geometries present [85]. However, the similar $\text{Gd}(\text{DO3A-butrol})$ complex has the nine-coordinate Gd^{3+} exclusively in the twisted CSAP geometry [86].

The $[\text{Ln}(\text{DO3A})(\text{H}_2\text{O})_n]$ ($\text{Ln} = \text{Eu}, \text{Gd}$) chelates have been shown, by UV-visible spectrophotometry and ^{17}O NMR, to be present in solution in a hydration equilibrium ($n = 1, 2$), strongly shifted towards the bis-aqua species [87]. Among the various $\text{Ln}(\text{DO3A})$ derivatives, only $\text{Ln}(\text{HP-DO3A})$ was so far studied in solution [88]. Replacement of an acetate arm by a hydroxypropyl group, which contains a chiral carbon center, leads to eight possible stereoisomers (four pairs of enantiomers). A ^1H NMR study of $\text{Y}(\text{HP-DO3A})$ led to observation of exchange processes by ROESY spectra, which confirmed the presence of multiple isomeric species. Quantitative analysis of the cross-peaks in terms of the exchange dynamics gave the exchange rates of the various processes present. These have shown that the exchange of the methylene groups during ring inversion is faster than the exchange of pendant arms and the exchange of the hydroxypropyl pendant arm is faster than for the acetate arms. The two diastereoisomers found in the crystal structures of the Gd^{3+} and Y^{3+} complexes [85] are also found in solution and interconvert by ring inversion. Observation of an exchange process involving rearrangement of the acetate arms indicated that diastereomers of opposite helicities are present.

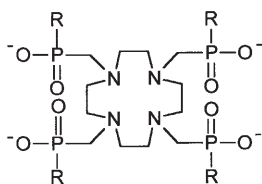
The crystal structure of the Gd^{3+} complex of ODOTRA (the analog of DO3A with the macrocyclic NH replaced by an ether oxygen) [89], shows that the Gd^{3+} ion is 9-coordinate, bound to three amine N-atoms, one ether O-atom, four carboxylate oxygens (one of which is bridging from a neighbor molecule in an infinite chain) and one water molecule with a twisted CSAP geometry.

Three DO3A derivatives, in which one of the acetate groups of DOTA was derivatized into an amide containing one or two negatively charged pendant phosphonate groups or a phosphonate and a carboxylate, were prepared and their Eu^{3+} and Yb^{3+} complexes were characterized in solution by ^1H and ^{31}P NMR [90]. All Yb^{3+} complexes occurred exclusively as the isomer of CSAP geometry, whereas the corresponding Eu^{3+} complexes were in a 3:1 CSAP to twisted CSAP isomeric ratio, quite similar to the parent $\text{Ln}(\text{DOTA})^-$ chelates [63]. In the complexes of the asymmetrically substituted ligands, the orientation of the sub-

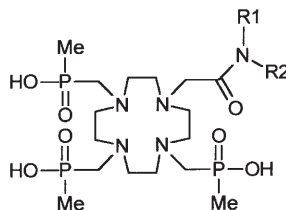
stituent generated two structural isomers and the consequent doubling of their NMR resonances. The Gd^{3+} chelates had reasonably high water relaxivities, resulting from an inner-sphere water molecule and a second-sphere water molecule entrapped between the inner-sphere water and the phosphonate or carboxylate substituent. The presence of the negatively charged pendant groups in the external surface of their Gd^{3+} chelates promoted the strong interaction with positively charged groups of polyaminoacids, such as polyornithine and polyarginine, leading to enhanced relaxivities.

4.3

DOTP



DOTP	R = O ⁻
DOTPME	R = OEt
DOTMB	R = OBu
F-DOTPME	R = OCH ₂ CF ₃
DOTMP	R = Me
DOTBuP	R = Bu
DOTPP	R = Ph
DOTBzP	R = CH ₂ Ph



DOTMP-MHBzA	R1 = H; R2 = CH ₂ Ph
DOTMP-MBMeA	R1 = R2 = Me
DOTMP-MBBzA	R1 = R2 = CH ₂ Ph
DOTMP-MPMeA	R1 = Ph; R2 = Me
DOTMP-MnaphMeA	R1 = 1-C ₁₀ H ₇ ; R2 = Me

Structures 7

The Ln^{3+} complexes of DOTP have been thoroughly investigated using multinuclear NMR techniques [90–92]. In these anionic complexes, the octadentate DOTP ligand coordinates the Ln^{3+} ions via the four N atoms of the macrocyclic ring and four phosphonate O atoms of the pendant arms. Four of the residual negative charges are localized on the phosphonate O-atoms that are directed away from the lanthanide coordination site with the fifth averaged over the bound O-atoms in the coordination cage. ¹⁷O NMR measurements of $[\text{Dy}(\text{DOTP})]^{5-}$ revealed that this complex lacks an inner-sphere water molecule [92]. The NMRD profile of $[\text{Gd}(\text{DOTP})]^{5-}$ shows, however a high relaxivity, which is consistent with the presence of a second hydration sphere with two water molecules and an outer-sphere which both contribute to the overall relaxivity [93]. The DOTP ligand coordinates the Ln^{3+} ions producing anionic complexes with various net charges. Potentiometric studies have indicated four protonation steps between pH 2 and 10 with $[\text{H}(\text{Ln}(\text{DOTP}))]^{4-}$ existing as the predominant species at pH 7.4 [94].

¹H and ¹³C NMR studies of the diamagnetic $[\text{La}(\text{DOTP})]^{5-}$ and $[\text{Lu}(\text{DOTP})]^{5-}$ complexes revealed a high degree of stereochemical rigidity in these compounds [91]. In addition, $[\text{Ln}(\text{DOTP})]^{5-}$ complexes possess a remarkable thermodynamic stability with long-lived coordinate bonds rendering them extremely

inert chelates. The solution structures of the whole paramagnetic series of $[\text{Ln}(\text{DOTP})]^{5-}$ complexes were studied by ^1H , ^{13}C , ^{31}P and ^{23}Na NMR as well as molecular mechanics calculations [91]. Structural analysis of the dipolar contribution to the LIS values and MMX force field calculations gave a square antiprismatic (SAP) arrangement of the ligand and suggested only minor structural changes throughout the Ln series [91]. An X-ray structure of the $[\text{Tm}(\text{DOTP})]^{5-}$ complex has been reported [95].

^{23}Na NMR studies with the $[\text{Tm}(\text{DOTP})]^{5-}$ complex revealed two possible binding sites for the Na^+ counteranions [94, 96]. One site (A), observed at low $\text{Na}^+ / [\text{Tm}(\text{DOTP})]^{5-}$ ratios, gave rise to an extremely large ^{23}Na LIS (≈ 420 ppm), indicating a binding position near the 4-fold symmetry axis. MMX calculations generated a model where the Na^+ ion interacts with one inner Ln-bound O atom and an axial O atom of an adjacent phosphonate group (dipolar angle $\theta = 26^\circ$). At high $\text{Na}^+ / [\text{Tm}(\text{DOTP})]^{5-}$ ratios, there is evidence for at least three sites of a second type (B) which impart significantly smaller bound shifts (≈ 160 ppm). An MMX model suggested that the Na^+ ions are associated with two unbound axial O-atoms of adjacent phosphonate groups with an average $\theta = 34^\circ$. The sign of the LIS for ^{23}Na in both cases indicate that the two binding sites are located within the positive shift cone. The magnitudes of the ^{23}Na LIS induced by $[\text{Ln}(\text{DOTP})]^{5-}$ complexes, in particular by $[\text{Tm}(\text{DOTP})]^{5-}$, are very large, most likely due to the formation of strong ion-pairs resulting from the increased negative charge on the DOTP complexes. Therefore, $[\text{Ln}(\text{DOTP})]^{5-}$ complexes have been successfully applied as shift reagents for separation of NMR signal degeneracy normally observed for intra- and extracellular compartments since they are impermeable to cell membranes. $[\text{Tm}(\text{DOTP})]^{5-}$ complexes have proven to be extremely effective shift reagents in perfused organs and in vivo [97–99].

Similar to other cyclen-based macrocycles (e.g. DOTA), two enantiomeric forms defined by a clockwise or counter-clockwise spiraling of the methylenephosphonate arms may be envisaged for $[\text{Ln}(\text{DOTP})]^{5-}$ complexes. However, unlike DOTA complexes, $[\text{Ln}(\text{DOTP})]^{5-}$ complexes are believed to exist in solution as one enantiomeric pair. An isomeric form of $[\text{Tm}(\text{DOTP})]^{5-}$ corresponding to the minor isomer observed for $[\text{Yb}(\text{DOTA})]^-$ (8-coordinate SAP geometry) was inferred by comparison of the paramagnetic ^1H shifts of the two species [94]. Although the coordination cage appears to be locked into a single conformation, variable temperature ^1H and ^{13}C NMR spectra suggest dynamic behavior related to the interconversion of the ethylenediamine chelate rings coupled with the concerted flipping motion of the arms. As a result, $[\text{Ln}(\text{DOTP})]^{5-}$ complexes exist as racemic mixtures in solution with the two enantiomers furnishing indistinguishable NMR signals at room temperature using conventional NMR techniques. Chiral NMR resolution, using the formation of diastereomeric adducts between the two enantiomers of $[\text{Ln}(\text{DOTP})]^{5-}$ and a chiral substrate, has provided indirect, albeit conclusive, evidence for the existence of these two enantiomers [100, 101]. The ion-pair interactions between lanthanide DOTP complexes and the chiral organic base, N-methyl-D-(-)-glucamine (Meg), were investigated by ^1H , ^{13}C and ^{31}P NMR spectroscopies [101]. Addition of Meg to a solution of $[\text{Eu}(\text{DOTP})]^{5-}$ lifted the signal degeneracy of the NMR spectra resulting in doubling of the corresponding signals. Similar spectral resolution in

the ^1H NMR spectrum of $[\text{Eu}(\text{DOTP})]^{5-}$ was achieved by addition of the chiral transition metal complex, (+)- $\text{Co}(\text{en})_3^{3+}$ [100]. In the ^{13}C and ^{31}P NMR spectra of mixtures of $[\text{Tm}(\text{DOTP})]^{5-}$ and the positively charged $[\text{La}(\text{S,S,S,S-THP})]^{3+}$ complex (see below), chiral resolution was observed due to the formation of diastereomeric 1:2 adducts ($\Delta\Delta\Delta$ and $\Delta\Delta\Lambda$) [102]. The formation of strong electrostatic interactions between lanthanide complexes and organic substrates, such as valeric acid, butanol, 1-adamantylamine, cyclen, and N-methyl-D-glucamine are well documented [103]. The ability of $[\text{Ln}(\text{DOTP})]^{5-}$ complexes to interact in this manner has been exploited to probe positively charged patches in protein surfaces.

4.4

Phosphinates and Phosphonate Esters

In principle, lanthanide complexes of alkyl- (phosphinates) or alkoxy- (phosphonate esters) DOTP derivatives may give rise to 32 stereoisomers, existing as 16 enantiomeric pairs, which are indistinguishable by NMR spectroscopy. The isomers originate from chiral elements inherent in these complexes, including the *R* or *S* configuration at each phosphorus and the helicity defined by the pendant arm orientations (Δ/Λ). Various Ln^{3+} complexes of phosphinate and phosphonate ester ligands derived from 1,4,7,10-tetraazacyclododecane (cyclen) have been described in the literature [104–107].

In the crystal structure of the $\text{La}(\text{DOTPP})^-$ complex, the phosphinate groups are orientated corresponding to a *RSRS* diastereoisomer [108], while for $\text{La}(\text{DOTBzP})^-$ [109] and $\text{Y}(\text{DOTMP})^-$ [106] only the (*RRRR*) and (*SSSS*) isomers were found in the solid state. All Ln^{3+} complexes of DOTBzP and DOTMP have the organic ligand bound in an octadentate fashion (4 N atoms of the cyclen ring and 4 phosphinate O-atom). The larger cations (e.g. La^{3+}) have an additional water molecule bound in the first coordination sphere, while for smaller metal ions such as Eu^{3+} and Gd^{3+} , no inner sphere water molecules were detected. The coordination geometry is similar for all phosphinate complexes studied and can be described by a (monocapped) SAP with a twist angle of about 25° (for DOTPP) or 29° (for DOTBzP , DOTMP). In aqueous solution various diastereoisomers can be formed, as described in the previous paragraph. Based on the integrals of the signals observed in the ^{31}P NMR spectrum, it was concluded that the *RRRR* isomer is the dominant species, which was a general feature for all ligands studied [110]. The abundance of the other isomers decreases with the number of *S*-oriented phosphinates. In a ^1H NMR study of the $\text{Yb}(\text{DOTBzP})^-$ complex only one set of signals was found in the spectrum, which corresponds to the minor isomer of the related DOTA complex. The sterically more demanding phosphinate group (in comparison to the acetate group) favors the SAP coordination geometry. The spectra of the $\text{Yb}(\text{DOTBzP})^-$ and the Y^{3+} and Eu^{3+} analogues, remained unchanged on temperature variations (from 278 to 353 K) indicating a highly rigid coordination cage. An LIS ^{31}P NMR study on the DOTBzP complexes, performed to test the isostructurality of the different Ln^{3+} complexes, indicated a slightly different structure for the smaller lanthanide ions (such as Ce^{3+} , Pr^{3+} , Nd^{3+}) compared to the ions in the middle and second

half of the series [110]. This phenomenon was explained by the presence of a bound water molecule present exclusively in the inner sphere of the complexes with the first elements of the series. This water molecule is not present in complexes with $\text{Ln}^{3+} = \text{Eu}^{3+} \rightarrow \text{Lu}^{3+}$, as confirmed by luminescence and relaxometry studies of the Eu^{3+} and Gd^{3+} complexes [106, 108–110]. The $\text{Ln}(\text{DOTPP})^-$ complexes did not show this irregularity [108] and can be considered as isostructural with an overall hydration number of $q = 0$.

NMRD studies of Gd^{3+} complexes of DOTPME and DOTPMB indicate $q < 1$ suggesting that the inner coordination sphere of these complexes is obstructed due to the steric encumbrance of the alkoxy substituents [104]. In a multinuclear NMR study of Ln^{3+} complexes ($\text{Ln} = \text{La}, \text{Gd}, \text{Dy}, \text{Tm}$ and Yb) with a fluorinated ethyl ester analog of DOTP (F-DOTPME), the ^{19}F NMR spectra reveal up to 16 resonances, which demonstrate that these complexes exist in aqueous solution as a mixture of stereoisomers [105]. $[\text{Gd}(\text{F-DOTPME})]^-$ afforded a water proton relaxivity typical of non-hydrated complexes. ^{17}O NMR of the Dy^{3+} complex confirmed the lack of a bound water molecule.

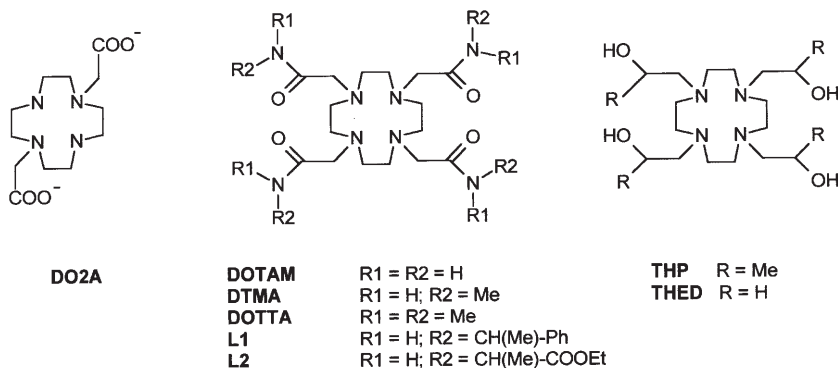
Structural studies have been described for a large number of lanthanide ($\text{Eu}, \text{Gd}, \text{Tb}$ and Yb) and Y complexes with macrocyclic ligands containing three phosphinate and one carboxamide arms [93, 111–115]. Among the 32 possible isomers which may exist, one stereoisomer predominates in aqueous solution, as verified by ^1H , ^{13}C and ^{31}P NMR spectroscopy. Luminescence studies with the Eu^{3+} and Tb^{3+} complexes are in agreement with the presence of one major isomer in aqueous solution. By comparison with crystal structures of the related tetra(benzylphosphinate) complexes and considering the steric requirements, it has been suggested that these complexes adopt the twisted SAP geometry. Spectral resolution of the ^{31}P NMR resonances was achieved by the addition of a chiral solvating agent (β -cyclodextrin) which demonstrated that the isomer is present as a 1:1 mixture of enantiomers [113]. Evaluation of the Curie contribution to the longitudinal relaxation rates of the ^{31}P resonances allowed for the determination of Yb-P distances in the $\text{Yb}(\text{DOTMP-MBBzA})$, $\text{Yb}(\text{DOTMP-MBMeA})$ and $\text{Yb}(\text{DOTMP-MHBzA})$ complexes [113]. The results suggest a certain distortion in the coordination polyhedron compared to the related tetra(benzylphosphinate) Y^{3+} complex [109]. The degree of distortion induced by the presence of the carboxamide substituent is dependent on the size of this group. Analysis of the variable temperature NMRD profiles indicates no coordinated water molecules in the Gd^{3+} complexes. Non-integral q values ($q < 1$) determined by luminescence measurements have been explained by the existence of a well defined ‘second hydration sphere’ promoted by the proximity of the amide carbonyl functionality which is capable of forming H-bonds with local water molecules [93].

Introducing a chiral center in the amide functionality renders all 32 potential isomers diastereomeric and thus discernable (in principle) by NMR spectroscopy. In practice, the lanthanide complexes formed (Eu, Gd and Tb) with macrocyclic monoamide tris(phosphinate) ligands bearing a chiral center on the amide group exist as only two non-interconverting diastereomers in a ratio of 2:1 and 4:1 for the α -phenylethyl and α -1-naphylethyl derivatives, respectively (DOTMP-MPMeA and DOTMP-MNaphMeA) [114]. The configuration at

the chiral carbon center (*R* or *S*) determines the helicity of the pendant arms and the conformation of the macrocyclic ring, as demonstrated by ^1H and ^{31}P NMR spectroscopy and circularly polarized luminescence studies. It was suggested that the major isomers observed in these complexes adopt a twisted SAP geometry with the P-Me groups projected away from the cyclen ring and an *RRR* or *SSS* configuration at phosphorus [114].

4.5

Cationic Macrocyclic Lanthanide Complexes



Structures 8

Neutral N-derivatized octadentate ligands based on cyclen (1,4,7,10-tetraazacyclododecane) form tripotential cationic complexes with the trivalent lanthanides [116–124]. The N-substituted tetraamide derivatives have proven useful in understanding the relationship between the solution structure of the Ln^{3+} complex and its water exchange rate, a critical issue in attaining optimal relaxation efficiency of CA's [125–131].

The solution structure and dynamics of the positively charged Ln^{3+} chelates containing the tetraaza dicarboxylate ligand DO2A [132], $[\text{Ln}(\text{DO2A})]^+$, have been studied by ^1H and ^{17}O NMR, relaxometry, UV-Vis and luminescence [133–135]. ^{17}O water shifts show that the number of inner-sphere water molecules replacing the two missing acetate arms of DOTA in the $[\text{Ln}(\text{DO2A})(\text{H}_2\text{O})_q]^+$ chelates changes from 3 to 2 along the Ln^{3+} series [134, 135]. One of the inner-sphere water molecules of the Eu^{3+} chelate hydrolyses at slightly basic pH with a pK_h of 8.1 ± 0.3 , as shown by luminescence [134]. The smaller extent of encapsulation of the Ln^{3+} ions by the DO2A ligand leads to a less rigid macrocyclic [3333] structure than in the DOTA chelates, as indicated by the ^1H NMR resonances of its CH_2 protons [133].

Detailed crystal and solution structure and dynamics studies have been reported for the Ln^{3+} complexes of the achiral tetraamide ligands DOTAM, DTMA and DOTTA. Crystal structures have been reported for $[\text{Eu}(\text{DOTAM})-(\text{H}_2\text{O})](\text{CF}_3\text{SO}_3)_3$ [117], $[\text{Gd}(\text{DTMA})(\text{H}_2\text{O})](\text{ClO}_4)_3$ [129] and $[\text{Dy}(\text{DTMA})-(\text{H}_2\text{O})](\text{PF}_6)_3$ [131]. The Ln^{3+} ion is 9-coordinate in the $[\text{Eu}(\text{DOTAM})(\text{H}_2\text{O})]^{3+}$,

[Gd(DTMA)(H₂O)]³⁺ and [Dy(DTMA)(H₂O)]³⁺ complexes, bound to four N atoms of the cyclen ring and four amide carbonyl O atoms and a coordinated water molecule. The coordination geometry at the Ln³⁺ site is a monocapped twisted SAP for the Eu³⁺ and Gd³⁺ complexes, but monocapped SAP for the Dy³⁺ complex. An X-ray study of [La(DOTAM)]³⁺ showed one cation in the asymmetric unit with an 8-coordinate La³⁺ ion [116]. The chiral complex possesses C₄ symmetry with the amide moieties arranged in a clockwise fashion producing a twisted SAP structure. In addition, an X-ray structure was reported for [La(DOTAM)(EtOH)(CF₃SO₃)](CF₃SO₃)₂ [117], where the La³⁺ ion was found to be 10-coordinate, producing an unusual 1, 5, 4 geometry. The six O atoms (four from the amidic arms, one from ethanol and one from the coordinated triflate anion) form a pentagonal pyramid with ethanol at the capping position. This pyramid is stacked base upon apex above a square pyramid made up of four N atoms from the macrocycle at the base and the La³⁺ ion at the vertex.

The solution structure and dynamics for the tetraamide Ln³⁺ complexes of DOTAM, DTMA and DOTTA have been extensively studied [116, 117, 120, 128–131]. These Ln³⁺ complexes may exist as two diastereomeric species in solution, similar to the Ln(DOTA) complexes. The ¹H NMR spectra of the corresponding Eu³⁺ complexes reveal the existence of major (M) and minor (m) isomers. For [Eu(DOTAM)]³⁺ and [Eu(DTMA)]³⁺ the major isomer (M) is defined by a SAP geometry, similar to [Eu(DOTA)]³⁺, with m/M isomer ratios of 0.25, 0.31 and 0.19, respectively [131], whereas the [Eu(DOTTA)]³⁺ has a m/M ratio of 2 with the predominant isomer having the twisted SAP geometry. These results indicate that a twisted SAP structure is preferred with increasing steric demand at the metal center, as found before for tetracarboxylate [75, 78, 79] and tetraphosphinate [109, 110] derivatives. The ratio of the two isomers for [Ln(DOTAM)]³⁺ complexes depends on temperature, solvent and the nature of the Ln³⁺ ion. Luminescence lifetime measurements of the DOTAM, DTMA and DOTTA Eu³⁺ complexes revealed the existence of one bound water molecule [127, 136]. ¹H NMR spectroscopy allowed for the direct observation of the bound water molecules for both isomers at low temperatures in dry CD₃CN [130, 131]. Direct observation of both isomers of [Eu(DOTAM)(H₂O)]³⁺ by ¹⁷O NMR allowed a quantitative study of water exchange rates and mechanism, including its role in the isomerization [137]. The water exchange rate on the m isomer is about 50 times faster than on M, and thus tends to dominate the overall value for the complex [130, 131, 137].

Variable temperature ¹H and ¹³C studies of [La(DOTAM)]³⁺ in CD₃CN revealed a high degree of structural rigidity for the chelate [117]. The ¹H NMR spectrum in D₂O closely resembles that in CD₃CN, but the complex is kinetically unstable and readily dissociates in water [116]. A detailed LIS study for 10 paramagnetic Ln³⁺ complexes of the corresponding N,N-diethylacetamido derivative in CD₃CN was carried out in conjunction with variable temperature ¹H and ¹³C NMR investigations of the diamagnetic La³⁺ complex [138]. NMR data established the existence of a single pair of enantiomers in solution. Molecular mechanics calculations combined with analysis of the LIS data determined a solution structure where the Ln³⁺ ion is eight-coordinate with the four N atoms

of the ring and four carbonyl O atoms at the vertices of a distorted square antiprism.

Lanthanide complexes of several chiral tetraamide ligands have been reported [121–124]. Four crystal structures have been reported for Eu^{3+} , Dy^{3+} and Yb^{3+} complexes of the (*R*)- and (*S*)-derivatives of the tetraamide $-\text{[CH}_2\text{C(O)NH-CH(Me)(Ph)]}_4$ -substituted ligand L_1 [121, 123, 124]. In each of these structures, the metal center is bound by four N atoms of the macrocycle and four amidic O atoms with a single water molecule in the capping position. The geometry of the coordination polyhedron varies from slightly distorted to regular CSAP with the chirality of the amide stereocenter ultimately determining the helicity of the complexes and the configuration of the macrocycle ring (with the (*R*)- and (*S*)-isomers producing the $\Delta(\delta\delta\delta\delta)$ and $\Delta(\lambda\lambda\lambda\lambda)$ configurations, respectively). The (*S*)-Eu and (*S*)-Dy complexes are isostructural. A crystal structure of the Eu^{3+} complex with the tetraamide (*S*)- $-\text{[CH}_2\text{C(O)NH-CH(Me)(CO}_2\text{Et)]}_4$ -derived cyclen, L_2 , shows a monocapped regular SAP geometry with the $\Delta(\lambda\lambda\lambda\lambda)$ absolute configuration [121].

Introducing a chiral center α to the amide N (δ to the ring N) imparts ample conformational rigidity to hinder pendant arm rotation. Solution NMR studies of the Eu^{3+} complexes of these enantiopure ligands in CD_3OD and D_2O show no evidence of exchange broadening (Δ/Δ interconversion) from 200 to 320 K, consistent with the presence of only one isomer having average C_4 symmetry [120, 123, 124]. The observed resonances in the ^1H NMR spectrum of a Yb^{3+} complex of tetraamide L_1 correspond closely to those obtained for the related chiral tetraphosphinate complexes, which exist exclusively as one diastereomer in solution having a twisted SAP geometry [124]. The ^1H NMR spectra in CD_3CN at -40°C showed a broad resonance corresponding to an Yb-bound water molecule [124]. The temperature and solvent effects on the ^1H NMR resonance of the bound water molecule and on the NIR-CD spectra of the Yb-*R* complex allowed to assess the effect of axial water ligation on the main magnetic and electronic properties of the Ln^{3+} (magnetic susceptibility anisotropy, crystal field parameters, absorption intensities) [139].

Lanthanide complexes of mono- and tetra-amide β -cyclodextrin derivatives of DOTA have been characterized [140]. The proton NMR spectra of the Eu^{3+} complexes in methanol- d_4 show that, while the tetra-amide complex occurs in solution exclusively as a C_4 -symmetry SAP structure, the mono-amide complex, with less than C_4 -symmetry, occurs predominantly as two SAP isomers ($\Delta/\lambda\lambda\lambda\lambda$ and $\Delta/\delta\delta\delta\delta$), with the presence of a small amount of the twisted SAP isomer. Luminescence and relaxivity measurements confirm that the Eu^{3+} , Tb^{3+} and Gd^{3+} complexes of the eight-coordinate mono-amide ligand possess one bound water molecule, while the tetra-amide complexes have $q = 0$. The relaxivity of the β -CD mono-amide Gd^{3+} complex is enhanced when non-covalently bound to a second Gd^{3+} complex bearing two phenyl moieties (MS-325, AngioMARKTM, EPIX/Mallinckrodt).

Additional cationic N-substituted amide complexes having mixed pendant groups have been reported [118, 119, 141].

The ^1H and ^{13}C NMR spectra of Ln^{3+} complexes formed with a single stereoisomer of THP having an *S*-configuration at all β -carbons (*S,S,S,S*-THP)

were investigated. In these (S,S,S,S)-THP complexes [142], the additional methyl group on the β -carbons adds four chiral centers, thus producing two diastereomers rather than an enantiomeric pair. ^1H and ^{13}C NMR spectra of La^{3+} and Lu^{3+} complexes of S,S,S,S-(–)-THP do not display the fluxional behavior as seen in $[\text{Ln}(\text{DOTA})]^-$ complexes over the temperature range from 18 to 100 °C, indicating the presence of only one diastereomer in solution. Molecular models suggest that a clockwise orientation of the pendant arms may be sterically favored. In the crystal structure of the racemic $[\text{Eu}(\text{THP})]^{3+}$ complex, the unit cell was shown to consist of two discrete $[\text{Eu}(\text{THP})(\text{H}_2\text{O})]^{3+}$ cations, which were diastereomers of each other, differing in the configuration at the chiral carbon (i.e. R,R,R,S versus S,S,S,R) and consequently the handedness of the helix. The THP ligand coordinated the Eu^{3+} ion through four N-atoms of the macrocycle and four hydroxyl O-atoms of the pendant arms with the ninth coordination site filled by a bound water molecule. The coordination geometry is best described as an inverted CSAP with an average twist angle of about 20°.

The ^1H NMR spectra of the related $[\text{La}(\text{THED})]^{3+}$ as a function of temperature reveal a dynamic process at room temperature similar to that observed for $[\text{Ln}(\text{DOTA})]^-$ complexes [143]. At ambient temperature, the ^{13}C NMR spectra (methanol- d_4) consists of two sharp resonances assigned to the pendant arms and one broad resonance attributed to the ethylene ring carbons, which sharpens as the fast exchange limit is approached (ca. 50 °C). Likewise, at –20 °C the broad resonance resolves into two peaks. The increased flexibility observed for $[\text{La}(\text{THED})]^{3+}$ as compared to DOTA complexes suggests that the pendant groups contribute to the structural rigidity of the macrocyclic ring.

5

Targeted Contrast Agents

The first generation of CA's are low molecular weight highly hydrophilic Gd^{3+} complexes, including $[\text{Gd}(\text{DTPA})]^{2-}$ and $[\text{Gd}(\text{DOTA})]^-$. Consequently, these compounds are distributed rather unselectively over the extracellular fluids. More efficient CA's are being developed that may be directed to targets of interest, thereby achieving higher local concentrations at lower dosages. Examples are CA's that are specific for organs, diseased tissue or that are able to recognize particular biochemicals. Usually, this is achieved by functionalization of the ligands in $[\text{Gd}(\text{DTPA})]^{2-}$ and $[\text{Gd}(\text{DOTA})]^-$ type complexes. For example, complexes of DTPA with lipophilic side chains ($[\text{Gd}(\text{BOPTA})]^{2-}$ and $[\text{Gd}(\text{EOB-DTPA})]^{2-}$, see above) have been introduced as hepatobiliary CA's and a macrocyclic Gd^{3+} complex with a perfluorinated side chain has been shown to accumulate in lymph nodes [144].

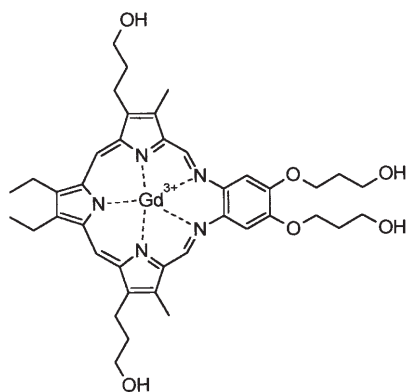
Covalent or non-covalent attachment of low-molecular weight Gd^{3+} chelates to polymers (e.g. dextrans, inulin, polylysine, polyornithine, HSA, and dendrimers [145–154]) or encapsulation of them in liposomes [155] may prolong their residence time in the cardiovascular system, rendering them amenable to applications in magnetic resonance angiography. High molecular weight compounds and liposomes have also shown potential as CA's for lymphography [156–160]. It has been demonstrated that binding of a chelate to a polymer has,

generally, no significant influence on the exchange rate of water between the complex and the bulk.

Several reports on potential tumor specific CA's based on conjugates of antibodies attached to conjugates of polymeric carriers and low molecular Gd^{3+} chelates have been reported [161–164].

An alternative approach has been suggested, which takes advantage of the negative charge of certain tumors. First positively charged poly(aminoacids) are selectively bound, which on their turn may serve as targets for a negatively charged Gd^{3+} chelate [90]. For this purpose, the interactions between polyornithine, polyarginine and negatively charged DO3A derivatives containing an additional pendant arm with phosphonate and carboxylate groups have been studied [90].

Another strategy for selective delivery of CA's at cancer cells exploits the intrinsic overexpression of sialic acid in them. Upon incubation of cancer cells with peracetylated N-levulinoylmannosamine the sialoside biosynthetic pathway affords N-levulinoyl sialic acid, the ketone group of which can be a target for an Gd^{3+} complex of an aminooxy-functionalized DTPA derivative [165].



Structures 9

$[\text{Gd}(\text{Tex})]^{2+}$

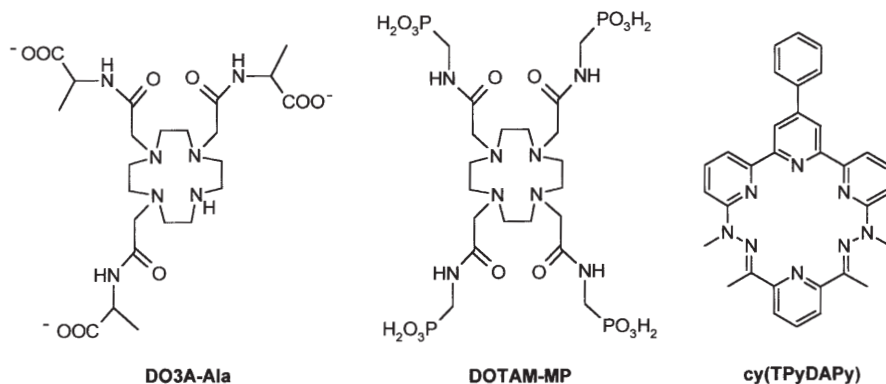
Lanthanide complexes of texaphyrin $[\text{Ln}(\text{Tex})]^{2+}$ have been shown to accumulate in tumors and atherosclerotic plaque and these compounds are being tested in photosensitized and radiation sensitized treatment of cancer and cardiovascular diseases [166]. Texaphyrin is an expanded porphyrin ligand with five N donor atoms. The crystal structure of the Gd complex shows that the cavity encompasses the Gd^{3+} ion almost ideally resulting in a high stability [167, 168]. The remaining axial positions are occupied by nitrate and methanol, both a 9- and a 10-coordinated Gd^{3+} occur. The solution structures of Ln-Tex complexes are similar as shown by analysis of lanthanide induced ^1H and ^{13}C NMR shifts in the Tex ligand [169, 170]. From an analysis of the NMRD curve of $[\text{Gd}(\text{Tex})]^{2+}$, it has been concluded that the water coordination number is 3.5 [171]. In combination with a relatively long rotational correlation time, this results in higher relaxivity compared to $\text{Gd}(\text{DTPA})^{2-}$ and $\text{Gd}(\text{DOTA})^{-}$ (3–4 times greater). Surprisingly, the relaxivity of $[\text{Gd}(\text{Tex})]^{2+}$ increases only slightly upon

mixing with 5% HSA. This might be ascribed to blocking for water coordination by an interaction between the complex and negatively charged groups of the protein. A similar effect has been observed recently upon interaction of Gd^{3+} complexes of DO3A derivatives [172].

In the presence of anions such as phosphate and oxalate, the relaxivity of $[\text{Gd}(\text{Tex})]^{2+}$ is considerably reduced revealing that these anions compete with water for binding to the Gd^{3+} ion [167, 171]. Most likely, texaphyrin complexes self-associate due to strong van der Waals interactions. UV-VIS studies suggest that the aggregates dissociate upon interaction with polyuronides (pectate, alginate), which probably act as polydentate polycarboxylate ligands for the $[\text{Gd}(\text{Tex})]^{2+}$ complexes [173].

6 Responsive Contrast Agents

A special category of targeted CA's is formed by those agents that are able to act as reporters of the biological environment where they are distributed through parameters as, for example, pH, partial oxygen pressure, degree of glycation of proteins, concentration of Ca^{2+} , and presence of enzymes.



Structures 10

Complexes that show a pH dependent relaxivity around physiological pH values are of particular interest since they may afford a way to distinguish tumor tissue ($\text{pH} = 6.9$) from healthy tissue ($\text{pH} = 7.4$). Protonation of a donor atom (O or N) can lead to competitive binding of a water molecule and thus affect the relaxivity. The development of a ligand exhibiting a pH dependent coordination number has not been successful so far [174], but is definitely a promising approach.

A Gd^{3+} complex of a hexaazamacrocyclic ligand, $\text{cy}(\text{TPyDAPy})$ [175] displays a pH dependent relaxivity in the range $6 < \text{pH} < 10$ which may be applied to study in vivo pH gradients. The relaxivity values measured varied from about $13 \text{ mM}^{-1} \text{ s}^{-1}$ ($\text{pH} < 6$) to $2 \text{ mM}^{-1} \text{ s}^{-1}$ ($\text{pH} = 11$). In previous studies these values

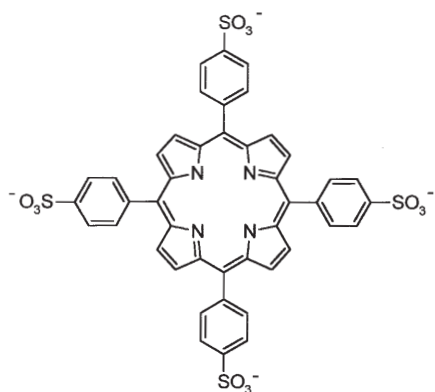
were measured for compounds with hydration numbers of $q = 2-3$ and for purely outer sphere complexes, respectively. This has been explained by the formation of an OH-bridged dimeric complex at higher pH values that indeed has no water molecules (or hydroxyl groups) bound in the first coordination sphere.

Sherry and coworkers have described a pH sensitive CA, Gd(DOTAM-MP)³⁺, that shows several pH jumps in its relaxivity between pH 3 and 8 [176]. NMR studies indicate that Ln³⁺ ion is bound by the four amide O-atoms and the four N-atoms of the cyclen backbone and that the first coordination sphere is completed by a water molecule. The phosphonate groups are not coordinated to the Ln³⁺ ion. The unique pH dependence of the relaxivity of the Gd³⁺ complex is ascribed to the protonation of the (uncoordinated) phosphonate groups. It is suggested that the H-bonding network created by protonation of the phosphonates provides a catalytic pathway for exchange of the water protons between the complex and the bulk.

A conjugate of a poly(aminoacid) and a DO3A chelate [177] has been reported to have a pH dependent relaxivity. Here, this originates from conformational changes of the poly(aminoacid) carrier as the pH varies from 4 to 8, which affect overall and local rotational motions in the macromolecule.

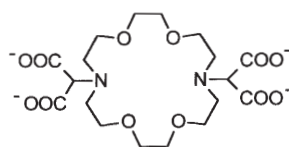
The interaction of hydrogen carbonate with the metal ion in a macrocyclic tetraazatriamide complex, Gd(DO3-Ala), under ambient conditions prevents any water molecule from directly binding to the paramagnetic center [122, 178]. In more acidic medium (pH < 6), the hydrogen carbonate ion will be protonated and displaced by two water molecules resulting in an increase of the relaxivity. Therefore, this reagent responds both to pH and to pHCO₃. ¹H NMR studies on the corresponding Eu³⁺ complex showed that the binding of HCO₃⁻ is accompanied by a conformational rearrangement from square antiprism to twisted-square antiprism.

CA's responsive to pO₂ can be imagined with chelates of metals that can switch between two redox states. The principle has been demonstrated for the system [Mn^{II/III}(TPPS)]^{4/3+} [179]. The relaxivity of Mn^{III} is dominated by the elec-

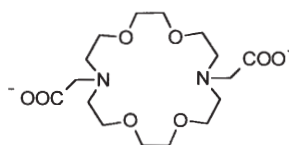


Structures 11

TPPS

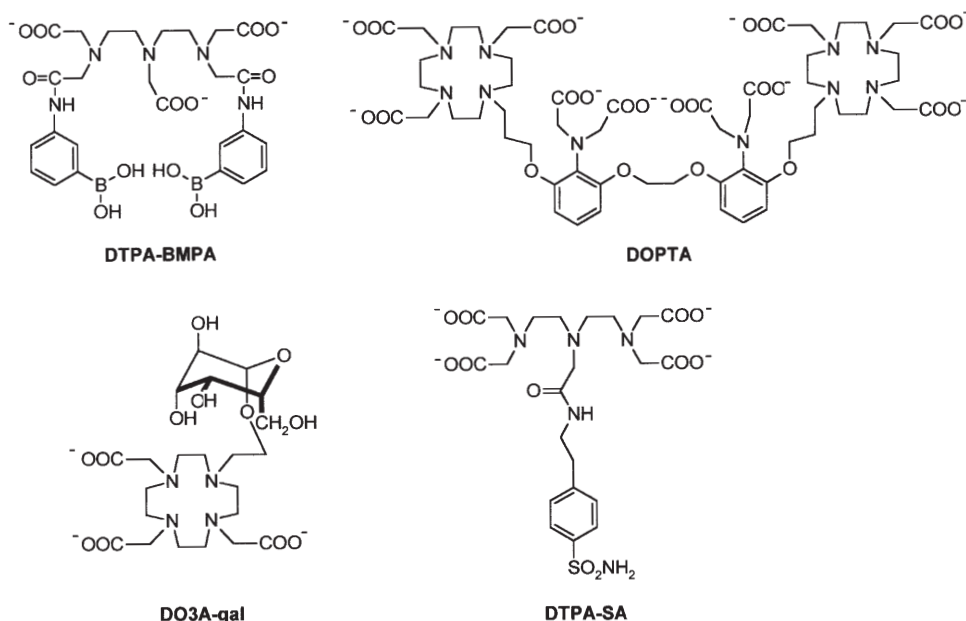


ODDM



ODDA

tronic relaxation time and that of Mn^{II} by the rotational correlation time. Upon slowing down the molecular tumbling by inclusion of the complex in poly- β -cyclodextrin, the relaxivity difference between the Mn^{II} and Mn^{III} state was sufficient for a response to pO_2 . Within the lanthanide series, the $\text{Eu}^{\text{II}}/\text{Eu}^{\text{III}}$ couple would be suitable for this purpose, since Eu^{II} is isoelectronic with Gd^{III} and has good relaxation enhancing properties [180, 181]. The redox stability of $[\text{Eu}^{\text{II}}(\text{DTPA})(\text{H}_2\text{O})]^{3-}$ is too low for practical applications, but the thermodynamic and redox stabilities of Eu^{II} complexes of ODDA and ODDM are higher [182]. ^{17}O NMR and ^1H NMRD measurements have shown that these complexes have one and no inner sphere water molecule, respectively [182]. The data suggest that optimal relaxivities may be obtained upon attaching the chelate to slowly rotating macromolecules, which would open routes to redox responsive CA's.



Structures 12

Aime and coworkers described the targeting properties of $\text{Gd}(\text{DTPA-BMPA})$ [183]. High levels of glucose in blood serum can induce a nonenzymatic glycation of albumin. Binding of the boronic functions of $\text{Gd}(\text{DTPA-BMPA})$ to the *syn*-diol moieties of the fructosamine residues in glycated albumin [184] induces an enhancement of the water proton relaxation rate as a consequence of the increased rotational correlation time τ_R . In this way it is possible to map the glycation level of proteins in the blood [183]. Unexpectedly, the $\text{Gd}(\text{DTPA-BMPA})$ complex also showed a strong interaction with unglycated oxygenated human hemoglobin [185]. This interaction involves formation of coordinative $\text{N} \rightarrow \text{B}$ bonds at two histidine residues of different β -chains of the peptide. The

interaction of the Gd^{3+} complex with hemoglobin was site specific, and results in a conformational switch (from the low-affinity T to the high-affinity R state) in the tetrameric protein. Highly selective interaction for T-state hemoglobin was also shown for $[\text{Gd}(\text{DOTP})]^{5-}$ [186].

Meade and coworkers reported a calcium sensitive CA, $\text{Gd}_2(\text{DOPTA})$ [187]. The ligand consists of two DO3A units that are linked via an EGTA type spacer carrying two aromatic iminoacetate groups. In the absence of Ca^{2+} , these iminoacetate functions are coordinating the Gd^{3+} ions, which are then not accessible for water. However, in the presence of Ca^{2+} , these carboxylate groups will rearrange to bind it. Consequently, two coordination sites on each of the Gd^{3+} ions are vacant for binding of water molecules resulting in an increase of the relaxivity from 3.26 to $5.76 \text{ mM}^{-1} \text{ s}^{-1}$. The interference of Ca^{2+} binding with Mg^{2+} or H^+ was determined to be minimal within physiological pH ranges. This compound offers a large and reliable change in relaxivity upon exposure to Ca^{2+} .

The first enzyme reporting CA described in the literature was $\text{Gd}(\text{DO3A-gal})$, a DOTA type ligand in which one of the acid groups is replaced by a galactose moiety [188]. This galactose moiety blocks the metal ion for water binding. The enzyme β -galactosidase cleaves off the sugar unit to form $[\text{Gd}(\text{DOTA})]^-$, where the inner sphere of Gd is accessible again for coordination of a water molecule. It was demonstrated that the change in hydration number from 0 to 1, resulting in a 20% increase in the measured water T_1 values, was indeed due to the enzymatic cleavage of the galactose residue. The $\text{Gd}(\text{DO3A-gal})$ agent has been applied for the in vivo visualization of gene expression by MRI [189, 190].

The complex $[\text{Gd}(\text{DTPA-SA})]^-$, which has a sulfonamide function at the central glycine unit of DTPA has been proposed as a CA targeting the enzyme carbon anhydrase [191]. The complex shows a strong interaction with this enzyme ($K = 15,000 \text{ M}^{-1}$), supposedly through the catalytic Zn^{2+} ion and the active site.

7

References

1. Caravan P, Ellison JJ, McMurry TJ, Lauffer LB (1999) *Chem Rev* 99:2293
2. Peters JA, Zitha-Bovens E, Corsi DM, Geraldes CFGC (2001) In: Merbach AE, Tóth É (eds) *The chemistry of contrast agents in medical magnetic resonance imaging*. Wiley, New York, Ch 8
3. Hardcastle KI, Botta M, Fasano M, Digilio G (2000) *Eur J Inorg Chem* 971
4. Bruce JJ, Lowe MP, Parker D (2001) In: Merbach AE, Tóth É (eds) *The chemistry of contrast agents in medical magnetic resonance imaging*. Wiley, New York, Ch 11
5. Peters JA (1988) *Inorg Chem* 27:4686
6. Geraldes CFGC, Urbano AM, Alpoim MC, Hoefnagel MA, Peters JA (1991) *Chem Commun* 656
7. Geraldes CFGC, Urbano AM, Hoefnagel MA, Peters JA (1993) *Inorg Chem* 32:2426
8. Lammers H, Maton F, Pubanz D, van Laren MW, van Bekkum H, Merbach AE, Muller RN, Peters JA (1997) *Inorg Chem* 36:2527
9. Jenkins BG, Lauffer RB (1988) *J Magn Reson* 80:328
10. Jenkins BG, Lauffer RB (1988) *Inorg Chem* 27:4730
11. Aime S, Botta M (1990) *Inorg Chim Acta* 177:101
12. Bénazeth S, Purans J, Chalbot M-C, Kim Nguyen-van-Duong M, Nicolas L, Keller F, Gaudemer A (1998) *Inorg Chem* 37:3667

13. White, DH, deLearie LA, Dunn TJ, Rizkalla EN, Imura H, Choppin GR (1991) *Invest Radiol* 26:S229
14. Aime S, Benetollo F, Bombieri G, Colla S, Fasano M, Paoletti S (1997) *Inorg Chim Acta* 254:63
15. Rizkalla EN, Choppin GR, Cachet W (1993) *Inorg Chem* 32:582
16. Bligh SWA, Chowdhury AHMS, McPartlin M, Scowen IJ, Bulman RA (1995) *Polyhedron* 14:567
17. Konings MS, Dow WC, Love DB, Raymond KN, Quay SC, Rocklage SM (1990) *Inorg Chem* 29:1488
18. Ehnebom L, Pedersen BF (1992) *Acta Chem Scand* 46:126
19. Wang Y-M, Cheng T-H, Sheu R-S, Chen I-T, Chiang MY (1997) *J Chin Chem Soc (Tapei)* 44:123
20. Franklin SJ, Raymond KN (1994) *Inorg Chem* 33:5794
21. Bovens E, Hoefnagel MA, Boers E, Lammers H, van Bekkum H, Peters JA (1996) *Inorg Chem* 35:7679
22. Frey ST, Chang CA, Carvalho JE, Varadarajan A, Schultze LM, Pounds KL, Horrocks, WDeW Jr (1994) *Inorg Chem* 33:2882
23. Inoue MB, Inoue M, Muñoz IC, Bruck MA, Fernando Q (1993) *Inorg Chim Acta* 209:29
24. Inoue MB, Inoue M, Fernando Q (1994) *Acta Crystallogr Cryst Struct Commun* C50:1037
25. Wu SL, Franklin SJ, Raymond KN, Horrocks, WDeW Jr (1996) *Inorg Chem* 35:162
26. Sarka L, Bányai I, Brücher E, Király R, Platzek J, Radüchel, Schmitt-Willich H (2000) *J Chem Soc, Dalton Trans* 3699
27. Selvin PR, Jancarik J, Li M, Hung L-W (1996) *Inorg Chem* 35:700
28. Uggeri F, Aime S, Anelli PL, Botta M, Brochetta M, DeHaën C, Ermondi G, Grandi M, Paoli P (1995) *Inorg Chem* 34:633
29. Schmitt-Willich H, Brehm M, Ewers ChLJ, Michl G, Müller-Fahrnow A, Petrov O, Platzek J, Radüchel B, Sülzle D (1999) *Inorg Chem* 38:1134
30. Vander Elst L, Maton F, Laurent S, Muller RN (1997) *Acta Radiol* 38 (S412):135
31. Vander Elst L, Maton F, Laurent S, Seghi F, Chapelle F, Muller RN (1997) *Magn Reson Med* 38:604
32. Laurent S, Vander Elst L, Houzé S, Guérit N, Muller RN (2000) *Helv Chim Acta* 83:394
33. Muller RN, Radüchel B, Laurent S, Platzek J, Piérart C, Mareski P, Vander Elst L (1999) *Eur J Inorg Chem* 1949
34. Schauer CK, Anderson OP (1989) *J Chem Soc Dalton Trans* 185
35. Aime S, Barge A, Borel A, Botta M, Chemerisov S, Merbach AE, Müller U, Pubanz D (1997) *Inorg Chem* 36:5104
36. Aime S, Botta M, Nonnato A, Terreno E, Anelli PL, Uggeri F (1995) *J Alloys Compd* 225:274
37. Ruloff R, Prokop P, Sieler J, Hoyer E, Beyer L (1996) *Z Naturforsch* 51b:963
38. Wang R-Y, Li J-R, Jin T-Z, Xu G-X, Zhou ZY, Zhou XG (1997) *Polyhedron* 16:1361
39. Mondry A, Starynowicz P (1997) *Inorg Chem* 36:1176
40. Ruloff R, Prokop P, Sieler J, Hoyer E, Beyer L (1996) *Z Naturforsch* 51b:963
41. Mondry A, Starynowicz P (2000) *New J Chem* 24:603
42. Wang R-Y, Li J-R, Jin T-Z, Xu G-X, Zhou ZY, Zhou XG (1997) *Polyhedron* 16:2037
43. Mondry A, Starynowicz P (1998) *J Chem Soc Dalton Trans* 859
44. Chen D-F, Yang W-C, Yang R-Y, Jin T-Z (1997) *Huaxue Xuebao* 55:672
45. Brittain HG (1990) *J Coord Chem* 21:295
46. Chang CA, Brittain HG, Telser J, Tweedle MF (1990) *Inorg. Chem.* 29:4468
47. Holz RC, Horrocks WDeW Jr (1990) *Inorg Chim Acta* 171:193
48. Lee S-G (2000) *Magn Reson Chem* 38:820
49. Zitha-Bovens E, Vander Elst L, Muller RN, van Bekkum H, Peters JA (2001) to be published
50. Alpoim MC, Urbano AM, Geraldès CFGC, Peters JA (1992) *J Chem Soc Dalton Trans* 463
51. Bryden CC, Reilley CN (1982) *Anal Chem* 54:610

52. Geraldes CFGC, Urbano AM, Alpoim MC, Sherry AD, Kuan KT, Rajagopalan R, Maton F, Muller RN (1995) *Magn Reson Imaging* 13:401
53. Freed JH (1978) *J Chem Phys* 68:4034
54. Chu SC, Pike MM, Fossel ET, Smith, TW, Balschi JA, Springer CS (1984) *J Magn Reson* 56:33
55. Xu J, Franklin SJ, Whisenhunt WD Jr, Raymond KN (1995) *J Am Chem Soc* 117:7245
56. Johnson AR, O'Sullivan B, Raymond KN (2000) *Inorg Chem* 39:2652
57. Hajela S, Botta M, Giraudo S, Xu J, Raymond KN, Aime S (2000) *J Am Chem Soc* 122:11228
58. Cohen SM, Xu J, Radkov E, Raymond KN (2000) *Inorg Chem* 39:5747
59. Bryden CC, Reilley CC, Desreux JF (1981) *Anal Chem* 53:1418
60. Desreux JF (1980) *Inorg Chem* 19:1319
61. Aime S, Botta M, Ermondi G (1992) *Inorg Chem* 31:4291
62. Hoelt S, Roth K (1993) *Chem Ber* 126:869
63. Aime S, Botta M, Fasano M, Marques MPM, Geraldes CFGC, Pubanz D, Merbach AE (1997) *Inorg Chem* 36:2059
64. Albin M, Horrocks WdeW Jr, Liotta FJ (1982) *Chem Phys Lett* 85:61
65. Spirlet M-R, Rebizant J, Desreux JF, Loncin MF (1984) *Inorg Chem* 23:359
66. Dubost JP, Leger JM, Langlois MH, Meyer D, Schaefer M (1991) *CR Academie Sci Ser II Univers* 312:329
67. Chang CA, Francesconi LC, Malley MF, Kumar K, Gougoutas JZ, Tweedle MF, Lee DW, Wilson LJ (1993) *Inorg Chem* 32:3501
68. Aime S, Barge A, Botta M, Fasano M, Ayala JD, Bombieri G (1996) *Inorg Chim Acta* 246:423
69. Aime S, Barge A, Benetollo F, Bombieri G, Botta M, Uggeri F (1997) *Inorg Chem* 36:4287
70. Aime S, Barbero L, Botta M, Ermondi G (1992) *J Chem Soc Dalton Trans* 225
71. Jacques V, Desreux JF (1994) *Inorg Chem* 33:4048
72. Szilágyi E, Tóth É, Brücher E, Merbach AE (1999) *J Chem Soc Dalton Trans* 2481
73. Desreux JF, Loncin MF (1986) *Inorg Chem* 25:69
74. Ascenso JR, Delgado R, Fraústo da Silva JJR (1986) *J Chem Soc Dalton Trans* 2395
75. Brittain HG, Desreux JF (1984) *Inorg Chem* 23:4459
76. Di Bari L, Pintacuda G, Salvadori P (2000) *Eur J Inorg Chem* 75
77. Di Bari L, Pintacuda G, Salvadori P (2000) *J Am Chem Soc* 122:5557
78. Howard JAK, Kenwright AM, Moloney JM, Parker D, Woods M, Port M, Navet M, Rousseau O (1998) *Chem Commun* 1381
79. Woods M, Aime S, Botta M, Howard JAK, Moloney JM, Navet M, Parker D, Port M, Rousseau O (2000) *J Am Chem Soc* 122:9781
80. Aime S, Botta M, Ermondi G, Terreno E, Anneli PL, Fedeli F, Uggeri F (1996) *Inorg Chem* 35:2726
81. André JP, Tóth É, Fischer H, Seelig A, Mäcke HR, Merbach AE (2000) *Chem Eur J* 5:2977
82. Gløgdard R, Fossheim SL, Aasen AJ, Klaveness J (2000) *J Chem Soc, Perkin Trans 2* 1047
83. Kang SI, Ranganathan RS, Emswiler JE, Kumar K, Gougoutas JZ, Malley MF, Tweedle MF (1993) *Inorg Chem* 32:2912
84. Aime S, Anneli PL, Botta M, Fedeli F, Grandi M, Paoli P, Uggeri F (1992) *Inorg Chem* 31:2422
85. Kumar K, Chang CA, Francesconi LC, Dischino DD, Malley MF, Gougoutas JZ, Tweedle MF (1994) *Inorg Chem* 33:3567
86. Platzek J, Blaszkiewicz P, Gries H, Luger P, Michl G, Müller-Fahrnow A, Radüchel B, Sülzle D (1997) *Inorg Chem* 36:6086
87. Tóth É, Ni Dhubbghaill OM, Besson G, Helm L, Merbach AE (1999) *Magn Reson Chem* 37:701
88. Shukla RB (1995) *J Magn Reson Ser A* 113:196
89. Spirlet M-R, Rebizant J, Wang X, Jin T, Gilsoul D, Comblin V, Maton F, Muller RN, Desreux JF (1997) *J Chem Soc Dalton Trans* 497
90. Aime S, Botta M, Garino E, Crich SG, Giovenzana GB, Pagliarin R, Palmisano G, Sisti M (2000) *Chem Eur J* 6:2609

91. Geraldès CFGC, Sherry AD, Kiefer GE (1992) *J Magn Reson* 97:290
92. Ren J, Sherry AD (1996) *J Magn Reson B* 111:178
93. Aime S, Botta M, Parker D, Williams JAG (1996) *J Chem Soc Dalton Trans* 17
94. Sherry AD, Ren J, Huskens J, Brücher E, Tóth É, Geraldès CFGC, Castro MMCA, Cacheris WP (1996) *Inorg Chem* 35:4604
95. Paulus EF, Juretschke P, Lang J (1995) 3. Jahrestag der Deutschen Gesellschaft für Kristallographie, Darmstadt
96. Ren J, Sherry AD (1996) *Inorg Chim Acta* 246:331
97. Malloy CR, Buster DC, Castro MMCA, Geraldès CFGC, Jeffrey FMH, Sherry AD (1990) *Magn Reson Med* 15:33
98. Bansal N, Germann MJ, Seshan V, Shires III G T, Malloy CR, Sherry AD (1993) *Biochemistry* 32:5638
99. Seshan V, Germann MJ, Preisig P, Malloy CR, Sherry AD, Bansal N (1995) *Magn Reson Med* 34:25
100. Ren J, Springer CS, Sherry AD (1997) *Inorg Chem* 36:3493
101. Aime S, Botta M, Crich SG, Terreno E, Anelli PL, Uggeri F (1999) *Chem Eur J* 5:1261
102. Corsi DM, van Bekkum H, Peters JA (2000) *Inorg Chem* 39:4802
103. Carvalho RA, Peters, JA, Geraldès, CFGC (1997) *Inorg Chim Acta* 262:167
104. Geraldès CFGC, Sherry AD, Lázár I, Miseta A, Bogner P, Berenyi E, Sumegi B, Kiefer GE, McMillan K, Maton F, Muller RN (1993) *Magn Reson Med* 30:696
105. Kim WD, Kiefer GE, Huskens J, Sherry AD (1997) *Inorg Chem* 36:4128
106. Broan CJ, Jankowski KJ, Kataký R, Parker D, Randall AM, Harrison A (1990) *Chem Commun* 1739
107. Broan CJ, Jankowski KJ, Kataký R, Parker D, Randall AM, Harrison A (1991) *Chem Commun* 204
108. Rohovec J, Vojtišek P, Hermann P, Mosinger J, Zák Z, Lukeš I (1999) *J Chem Soc Dalton Trans* 3585
109. Aime S, Batsanov AS, Botta M, Howard JAK, Parker D, Senanayake K, Williams G (1994) *Inorg Chem* 33:4696
110. Aime S, Batsanov AS, Botta M, Dickins R, Faulkner S, Foster CE, Harrison A, Howard JAK, Moloney JM, Norman TJ, Parker D, Royle L, Williams JAG (1997) *J Chem Soc Dalton Trans* 3623
111. Parker D, Pulukkody KP, Norman TJ, Harrison A, Royle L, Walker C (1992) *Chem Commun* 1441
112. Pulukkody KP, Norman TJ, Parker D, Royle L, Broan CJ (1993) *J Chem Soc Perkin Trans 2* 605
113. Aime S, Botta M, Parker D, Williams JAG (1995) *J Chem Soc Dalton Trans* 2259
114. Aime S, Botta M, Dickins RS, Maupin CL, Parker D, Riehl JP, Williams JAG (1998) *J Chem Soc Dalton Trans* 881
115. Harrison A, Norman TJ, Parker D, Royle L, Pereira KA, Pulukkody KP, Walker CA (1993) *Magn Reson Imaging* 11:761
116. Morrow JR, Amin S, Lake CH, Churchill MR (1993) *Inorg Chem* 32:4566
117. Amin S, Morrow JR, Lake CH, Churchill MR (1994) *Angew Chem Int Ed* 33:773
118. Amin S, Voss Jr DA, Horrocks Jr WdeW, Lake CH, Churchill MR, Morrow JR (1995) *Inorg Chem* 34:3294
119. Amin S, Voss Jr DA, Horrocks Jr WdeW, Morrow JR (1996) *Inorg Chem* 35:7466
120. Chappell LL, Voss Jr DA, Horrocks Jr WdeW, Morrow JR (1998) *Inorg Chem* 37:3989
121. Dickins RS, Howard JAK, Lehmann CW, Moloney J, Parker D, Peacock RD (1997) *Angew Chem Int Ed* 36:521
122. Aime S, Barge A, Botta M, Howard JAK, Kataký R, Lowe MP, Moloney JM, Parker D, de Sousa AS (1999) *Chem Commun* 1047
123. Dickins RS, Howard JAK, Maupin CL, Moloney JM, Parker D, Riehl JP, Siligardi G, Williams JAG (1999) *Chem Eur J* 5:1095
124. Batsanov AS, Beeby A, Bruce JI, Howard JAK, Kenwright AM, Parker D (1999) *Chem Commun* 1011

125. Katakly R, Matthes KE, Nicholson PE, Parker D (1990) *J Chem Soc Perkin Trans* 2:1425
126. Carlton L, Hancock RD, Maumela H, Wainwright KP (1994) *Chem Commun* 1007
127. Dickins RS, Parker D, de Sousa AS, Williams JAG (1996) *J Chem Commun* 697
128. Aime S, Barge A, Botta M, Parker D, de Sousa AS (1997) *J Am Chem Soc* 119:476
129. Alderighi L, Bianchi A, Calabi L, Dapporto P, Giorgi C, Losi P, Paleari L, Paoli P, Rossi P, Valtancoli B, Virtuani M (1998) *Eur J Inorg Chem* 1
130. Aime S, Barge A, Botta M, de Sousa AS, Parker D (1998) *Angew Chem Int Ed* 37:2673
131. Aime S, Barge A, Bruce JI, Botta M, Howard JAK, Moloney JM, Parker D, de Sousa AS, Woods M (1999) *J Am Chem Soc* 121:5762
132. Kim WD, Kiefer GE, Maton F, McMillan K, Muller RN, Sherry AD (1995) *Inorg Chem* 34:2233
133. Huskens J, Torres D, Kovacs Z, André JP, Geraldes CFGC, Sherry AD (1997) *Inorg Chem* 36:1495
134. Chang CA, Chen Y-H, Chen HY, Shieh F-K (1998) *J Chem Soc Dalton Trans* 3243
135. Yerly F, Dunand F, Tóth E, Figueirinha A, Kovacs Z, Sherry AD, Geraldes CFGC, Merbach AE (2000) *Eur J Inorg Chem* 1001
136. Beeby A, Clarkson IM, Dickins RS, Faulkner S, Parker D, Royle L, de Sousa AS, Williams JAG (1999) *J Chem Soc Perkin Trans* 2:493
137. Dunand FA, Aime S and Merbach AE (2000) *J Am Chem Soc* 122:1506
138. Forsberg JH, Delaney RM, Zhao Q, Harakas G, Chandran R (1995) *Inorg Chem* 34:3705
139. Di Bari L, Pintacuda G, Salvadori, Dickins RS, Parker D (2000) *J Am Chem Soc* 122:9257
140. Skinner PJ, Beeby A, Dickins RS, Parker D, Aime S, Botta (2000) *J Chem Soc Perkin Trans* 2:1329
141. Parker D, Williams JAG (1995) *J Chem Soc Perkin Trans* 2:1305
142. Chin KOA, Morrow JR, Lake CH, Churchill MR (1994) *Inorg Chem* 33:656
143. Morrow JR, Chin KOA (1993) *Inorg Chem* 32:3357
144. Misselwitz B, Platzek J, Radüchel B, Oellinger JJ, Weimann H-J (1999) *Magn Reson Mat Phys Biol Med* 8:190
145. Lauffer RB, Brady TJ (1985) *Magn Reson Imaging* 3:11
146. Brasch RC (1991) *Magn Reson Med* 22:282
147. Rongved P, Klaveness J (1991) *Carbohydr Res* 214:315
148. Rebizak R, Schaefer M, Dellacherie E (1997) *Bioconj Chem* 8:605
149. Chu W-J, Elgavish GA (1995) *NMR in Biomed* 8:159
150. Spanoghe M, Lanens D, Dommissie R, van der Linden A, Alderweireldt F (1992) *Magn Reson Imaging* 10:13
151. Corot C, Schaefer M, Beauté S, Bourrinet SP, Zehaf S, Bénizé V, Sabatou M, Meyer D (1997) *Acta Radiol* S412:91
152. Rebizak, Schaefer, Dellacherie (1999) *Eur J Pharm Sci* 7:243
153. Aime S, Botta M, Crich SG, Giovenzana G, Palmisano G, Sisti M (1999) *Bioconj Chem* 10:192
154. Corsi DM, Vander Elst L, Muller RN, van Bekkum H, Peters JA (2001) *Chem Eur J* 7:64
155. Nævestad A, Fossheim SL, Fahlvik AK (1999) In: *Trends in Contrast Media*, Springer Heidelberg, p 171
156. Harika L, Weissleder R, Poss K, Papisov MI (1996) *Radiol* 198:365
157. Desser TS, Rubin DL, Muller H, McIntire GL, Bacon ER, Hollister KR (1999) *Acad Radiol* 6:112
158. Wisner ER, AhoSharon KL, Bennet MJ, Penn SG, Lebrilla CB Nantz MH (1997) *J Med Chem* 40:3992
159. Misselwitz B, Sachse A (1997) *Acta Radiol* 38:51
160. Fujimoto Y, Okuhata Y, Tyngi S, Namba Y, Oku N (2000) *Biol Pharm Bull* 23:97
161. Wiener EC, Konda S, Shadron A, Brechbiel M, Gansow O (1997) *Invest Radiol* 32:748
162. Curtet C, Maton F, Havet T, Slinkin M, Mishra A, Chatal J-F, Muller RN (1998) *Invest Radiol* 33:752
163. Konda SD, Aref M, Brechbiel M, Wiener EC (2000) *Invest Radiol* 35:50
164. Nunn AD, Linder K, Tweedle MF (1997) *Quart J Nucl Med* 41:155

165. Lemieux GA, Yarema KJ, Jacobs CL, Bertozzi CR (1999) *J Am Chem Soc* 121:4278
166. Sessler JL, Hemmi G, Mody TD, Murai T, Burell A, Young SW (1994) *Acc Chem Res* 27:43
167. Sessler JL, Mody TD, Hemmi GW, Lynch V (1993) *Inorg Chem* 32:3175
168. Sessler JL, Mody TD, Hemmi GW, Lynch V, Young SW, Miller RA (1993) *J Am Chem Soc* 115:10368
169. Lisokowski J, Sessler JL, Lynch V, Mody TD (1995) *J Am Chem Soc* 117:2273
170. Lisokowski J, Sessler JL, Mody TD (1995) *Inorg Chem* 34:4336
171. Geraldès CFGC, Sherry AD, Vallet P, Maton F, Muller RN, Mody TD, Hemmi G, Sessler JL (1995) *J Magn Reson Imag* 5:725
172. Aime S, Gianolio E, Terreno E, Giovenzana GB, Pagliarin R, Sisti M, Palmisano G, Botta M, Lowe MP, Parker D (2000) *J Biol Inorg Chem* 5:488
173. Synytsya A, Synytsya A, Král V, Volka K, ěopíková J, Sessler JL (2000) *J Chem Soc Perkin Trans 2* 1876
174. Aime S, Batsanov AS, Botta M, Howard JAK, Lowe MP, Parker D (1999) *New J Chem* 23:669
175. Hall J, Haner R, Aime S, Botta M, Faulkner S, Parker D, de Sousa AS (1998) *New J Chem* 22:627
176. Zhang S, Wu K, Sherry AD (1999) *Angew Chem Int Ed* 38:21
177. Aime S, Botta M, Crich SG, Giovenzana G, Palmisano G, Sisti M (1999) *Chem Commun* 1577
178. Bruce JJ, Dickins RS, Govenlock LJ, Gunnlaugsson T, Lopinski S, Lowe MP, Parker D, Peacock RD, Perry JJB, Aime S, Botta M (2000) *J Am Chem Soc* 122:9674
179. Aime S, Botta M, Gianolio E, Terreno E (2000) *Angew Chem Int Ed* 39:747
180. Caravan P, Merbach AE (1999) *J Am Chem Soc* 121:10403
181. Seibig S, Tóth É, Merbach AE (2000) *J Am Chem Soc* 122:5822
182. Burai L, Tóth É, Seibig S, Scopelliti R, Merbach AE (2000) *Chem Eur J* 6:3761
183. Aime S, Botta M, Dastrú W, Fasano M, Panero M, Arnelli A (1993) *Inorg Chem* 32:2068
184. Rohovec J, Maschmeyer Th, Aime S, Peters JA, to be published
185. Aime S, Digilio G, Fasano M, Paoletti S, Arnelli A, Ascenzi P (1999) *Biophys J* 76:2735
186. Aime S, Ascenzi P, Comoglio E, Fasano M, Paoletti S (1995) *J Am Chem Soc* 117:9365
187. Li W-H, Fraser SE, Meade TJ (1999) *J Am Chem Soc* 121:1413
188. Moats RA, Fraser SE, Meade TJ (1997) *Angew Chem Int Ed* 36:726
189. Jacobs RE, Ahrens ET, Meade TJ, Fraser SE (1999) *Trends Cell Biol* 9:73
190. Louie AY, Huber MM, Ahrens ET, Rothbacher U, Moats R, Jacobs RE, Fraser SE, Meade TJ (2000) *Nat Biotechnol* 18:321
191. Anelli PL, Bertini I, Fragai M, Lattuada L, Luchinat C, Parigi G (2000) *Eur J Inorg Chem* 625

Relaxivity of MRI Contrast Agents

Éva Tóth, Lothar Helm, André E. Merbach

Institut de chimie minérale et analytique, Ecole Polytechnique Fédérale de Lausanne, BCH,
1015 Lausanne, Switzerland

E-mail: eva.jakob-toth@epfl.ch

E-mail: lothar.helm@epfl.ch

E-mail: andre.merbach@epfl.ch

In the recent years Magnetic Resonance Imaging has evolved into one of the most powerful diagnostic techniques in medicine, in part thanks to the application of suitable contrast agents. The design of new, more efficient MRI contrast media requires the complete understanding of all factors and mechanisms that influence proton relaxivity, hence efficiency of Gd(III) complexes. In this chapter we give an overview of our current knowledge in this field by shortly surveying theory and citing the most illustrative examples. We discuss each of the underlying factors, including the possible ways of their determination. Most recent developments in the field of electron spin relaxation and outer sphere relaxivity have also been reviewed. The last part is devoted to the comparison of the isoelectronic Eu(II) and Gd(III) complexes, which can give insight into the relaxation mechanisms of paramagnetic lanthanides in general, and thus help design novel Gd(III) based agents.

Keywords. Proton relaxivity, Water exchange, Electron spin relaxation, Outer sphere relaxivity, Eu(II)

1	Introduction	62
1.1	Relaxivity	62
2	Inner Sphere Proton Relaxivity	64
2.1	Hydration Number and Gd-H Distance	66
2.2	Water and Proton Exchange	68
2.2.1	Determination of the Water Exchange Rate	68
2.2.2	Mechanism of the Water Exchange	70
2.2.3	Rate and Mechanism of Water Exchange on Gd(III) Chelates	70
2.2.4	Proton Exchange	79
2.3	Rotation	79
2.3.1	Techniques of Determining the Rotational Correlation Time	79
2.3.2	Internal Flexibility of Macromolecular Gd(III) Complexes. The Lipari-Szabo Approach	80
2.4	Electron Spin Relaxation	82
3	Outer Sphere Proton Relaxivity	85
4	Relaxivity and NMRD Profile	90
4.1	Analysis of NMRD Profiles	91
4.2	Relaxivity of Low Molecular Weight Gd(III) Complexes	91
4.3	Relaxivity of Macromolecular Gd(III) Complexes	92

5	Comparison of Gd(III) and Eu(II) Complexes in Relation to MRI	93
6	Conclusions	98
7	References	98

1

Introduction

The strong expansion of Magnetic Resonance Imaging (MRI) has induced the development of a new class of pharmacological products, called contrast agents, designed for administration to patients in order either to enhance the contrast between normal and diseased tissue or to indicate organ function or blood flow. Nowadays, around 30% of all MRI investigations use a contrast medium.

Contrast agents function by increasing the relaxation rate of water protons in the surrounding tissue, thanks to their paramagnetism. The majority of the currently used contrast agents are stable chelates of gadolinium(III). This trivalent lanthanide ion has the highest possible number (seven) of unpaired electrons which makes it the most paramagnetic among the stable metal ions. The slow relaxation of the Gd(III) electron spin is an additional favourable factor.

The goal of the present chapter is to discuss relaxation phenomena for Gd(III) chelates and to describe the various physico-chemical parameters which are related to their relaxivity, hence to their efficacy with regard to contrast agent applications for medical Magnetic Resonance Imaging. Due to the preponderance of Gd(III) based agents, we will not treat other, currently used or potential contrast media, such as paramagnetic particles [1] or hyperpolarized gases [2].

1.1

Relaxivity

The relaxation of solvent nuclei around a paramagnetic centre has been described by Solomon, Bloembergen and others [3–8]. The observed solvent relaxation rate, $1/T_{i,obs}$, is the sum of a diamagnetic term $1/T_{i,d}$, corresponding to the relaxation rate of the solvent nuclei without the paramagnetic solute, and a paramagnetic term $1/T_{i,p}$ which is the relaxation rate enhancement caused by the paramagnetic substance:

$$\frac{1}{T_{i,obs}} = \frac{1}{T_{i,d}} + \frac{1}{T_{i,p}} \quad i = 1, 2 \quad (1)$$

The paramagnetic contribution is linearly proportional to the concentration of the paramagnetic species, [Gd]:

$$\frac{1}{T_{i,obs}} = \frac{1}{T_{i,d}} + r_i [Gd] \quad i = 1, 2 \quad (2)$$

In principle, [Gd] should be expressed in molality (mol/kg solvent), however, for dilute solutions molarity is generally used (mol/L or in practice mmol/L). If the longitudinal relaxation rate of water protons is considered and the concentration of Gd is given in mM, the parameter r_1 is called proton relaxivity (its unity is $\text{mM}^{-1}\text{s}^{-1}$). Proton relaxivity directly refers to the efficiency of a paramagnetic substance to enhance the relaxation rate of water protons, thus to its efficiency to act as a contrast agent.

The paramagnetic relaxation of the water protons originates from the dipole-dipole interactions between the proton nuclear spins and the fluctuating local magnetic field caused by the unpaired electron spins of the paramagnetic substance. There are two main contributions to the overall paramagnetic relaxation rate enhancement thus to the overall proton relaxivity. The inner sphere contribution is due to the interaction between the Gd^{III} electron spins and the water protons in the first coordination sphere of the metal transmitted to the bulk via the chemical exchange of the inner sphere protons (Fig. 1). Bulk solvent molecules diffusing around the paramagnetic centre also experience the paramagnetic effect. The relaxation mechanism arising from this random translational diffusion is defined as outer sphere relaxation. The separation of the inner and outer sphere relaxation terms is thus based on the intra- and intermolecular nature of the interaction, respectively. Moreover, the theoretical approach to describe the two relaxation mechanisms is also different.

The total paramagnetic relaxation rate enhancement due to the paramagnetic agent is given as in Eq. (3), or expressed in relaxivities as in Eq. (4):

$$\left(\frac{1}{T_{i,p}}\right) = \left(\frac{1}{T_{i,p}}\right)^{\text{IS}} + \left(\frac{1}{T_{i,p}}\right)^{\text{OS}} \quad (3)$$

$$r_i = r_i^{\text{IS}} + r_i^{\text{OS}} \quad (4)$$

where IS and OS stand for inner and outer sphere, respectively.

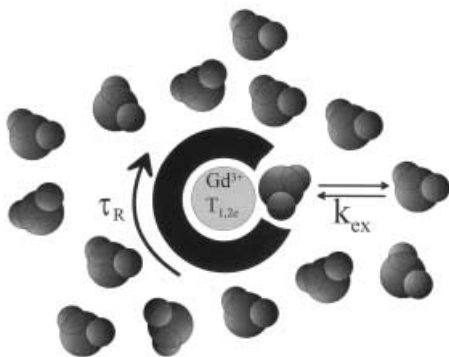


Fig. 1. A Gd(III) complex with one inner sphere water molecule, surrounded by bulk water. Inner sphere proton relaxivity is due to interactions between the Gd electron spin and the water protons on the inner sphere water. Outer sphere relaxivity arises from interactions between the Gd electron spin and bulk water protons. τ_R stands for the rotational correlation time of the molecule, k_{ex} for the water/proton exchange rate and $1/T_{1,2e}$ for the electron spin relaxation rates of the Gd(III)

Beside the inner sphere coordinated water, in a Gd(III) complex there can be solvent (water) molecules hydrogen-bonded to the ligand (usually to its carboxylate or phosphonate groups) or to the inner sphere water molecule. These water molecules can also contribute to the overall relaxivity, giving rise to a “second sphere” relaxation mechanism [9]. In terms of theory, this second sphere contribution is analogous to the inner sphere relaxation. Very often the second sphere contribution is difficult to separate and evaluate, thus it is neglected or simply taken into account as an increase in the outer sphere term. However, the augmentation of the second sphere relaxation term represents a possible route to increase the overall proton relaxivity of Gd(III) based MRI contrast agents.

For monomer Gd(III) complexes the inner and outer sphere mechanisms contribute more or less to the same extent to the overall paramagnetic relaxation enhancement. The development of high relaxivity contrast agents mainly involves increasing the inner sphere term, since the outer sphere contribution can hardly be modified. For the new generation macromolecular agents, therefore, the inner sphere relaxivity becomes much more significant (over 90% of total relaxivity).

2

Inner Sphere Proton Relaxivity

The inner sphere contribution to proton relaxivity results from the chemical exchange of the coordinated water protons with the bulk. The longitudinal and transverse inner sphere relaxation rates, $1/T_1$ and $1/T_2$, of the bulk solvent nuclei (the only observable NMR signal) are given by Eqs. (5) [10] and (6) [11]:

$$\left(\frac{1}{T_1}\right)^{\text{IS}} = \frac{cq}{55.5} \frac{1}{T_{1m} + \tau_m} = P_m \frac{1}{T_{1m} + \tau_m} \quad (5)$$

$$\left(\frac{1}{T_2}\right)^{\text{IS}} = \frac{P_m}{\tau_m} \frac{T_{2m}^{-2} + \tau_m^{-1} T_{2m}^{-1} + \Delta\omega_m^2}{(\tau_m^{-1} + T_{2m}^{-1})^2 + \Delta\omega_m^2} \quad (6)$$

where c is the molal concentration, q is the number of bound water nuclei per Gd (hydration number), P_m is the mole fraction of the bound water nuclei, τ_m is the lifetime of a solvent (water) molecule in the inner sphere of the complex (equal to the reciprocal water exchange rate, $1/k_{ex}$), $1/T_{1m}$ and $1/T_{2m}$ are the longitudinal and transverse proton relaxation rates in the bound water, and $\Delta\omega_m$ is the chemical shift difference between bound and bulk water.

The relaxation of bound water protons is governed by the magnetic field dependent dipole-dipole (DD) and scalar or contact mechanisms (SC). The dipole-dipole interaction is modulated by the reorientation of the nuclear spin – electron spin vector, by electron spin relaxation and by water (proton) exchange. The scalar interaction is influenced by electron spin relaxation and water exchange, and generally it represents a small, and for the longitudinal relaxation negligible contribution. The relaxation rates are generally expressed by the modified Solomon-Bloembergen equations:

$$\frac{1}{T_{im}} = \frac{1}{T_i^{DD}} + \frac{1}{T_i^{SC}} \quad i = 1, 2 \quad (7)$$

$$\frac{1}{T_1^{DD}} = \frac{2}{15} \frac{\gamma_I^2 g^2 \mu_B^2}{r_{GdH}^6} S(S+1) \left(\frac{\mu_0}{4\pi} \right)^2 \left[7 \frac{\tau_{c2}}{1 + \omega_s^2 \tau_{c2}^2} + 3 \frac{\tau_{c1}}{1 + \omega_I^2 \tau_{c1}^2} \right] \quad (8)$$

$$\frac{1}{T_1^{SC}} = \frac{2S(S+1)}{3} \left(\frac{A}{\hbar} \right)^2 \left(\frac{\tau_{e2}}{1 + \omega_s^2 \tau_{e2}^2} \right) \quad (9)$$

$$\frac{1}{T_2^{DD}} = \frac{1}{15} \frac{\gamma_I^2 g^2 \mu_B^2}{r_{GdH}^6} S(S+1) \left(\frac{\mu_0}{4\pi} \right)^2 \left[13 \frac{\tau_{c2}}{1 + \omega_s^2 \tau_{c2}^2} + 3 \frac{\tau_{c1}}{1 + \omega_I^2 \tau_{c1}^2} + 4\tau_{c1} \right] \quad (10)$$

$$\frac{1}{T_2^{SC}} = \frac{S(S+1)}{3} \left(\frac{A}{\hbar} \right)^2 \left(\frac{\tau_{e2}}{1 + \omega_s^2 \tau_{e2}^2} + \tau_{e1} \right) \quad (11)$$

In Eqs. (7–11), γ_I is the nuclear gyromagnetic ratio, g is the electron g factor, μ_B is the Bohr magneton, r_{GdH} is the electron spin – proton distance, ω_I and ω_s are the nuclear and electron Larmor frequencies, respectively ($\omega = \gamma B$, where B is the magnetic field), and A/\hbar is the hyperfine or scalar coupling constant between the electron of the paramagnetic center and the proton of the coordinated water. The correlation times that are characteristic of the relaxation processes are depicted as:

$$1/\tau_{ci} = 1/\tau_R + 1/T_{ie} + 1/\tau_m \quad i = 1, 2 \quad (12)$$

$$1/\tau_{ei} = 1/\tau_{ie} + 1/\tau_m \quad i = 1, 2 \quad (13)$$

where τ_R is the rotational correlation time or, more precisely, the reorientational correlation time of the metal – proton vector, and T_{ie} and T_{2e} are the longitudinal and transverse electron spin relaxation times of the metal ion.

The electronic relaxation rates, as described by Bloembergen, Morgan and McLachlan [12], also depend on the magnetic field. For Gd(III) complexes they are usually interpreted in terms of zero field splitting interactions (ZFS). The electronic relaxation rates can be described by the Eqs. (14–16), often called as the Bloembergen-Morgan theory of paramagnetic electron spin relaxation:

$$\left(\frac{1}{T_{1e}} \right)^{ZFS} = 2C \left(\frac{1}{1 + \omega_s^2 \tau_v^2} + \frac{4}{1 + 4 \omega_s^2 \tau_v^2} \right) \quad (14)$$

$$\left(\frac{1}{T_{2e}} \right)^{ZFS} = C \left(\frac{5}{1 + \omega_s^2 \tau_v^2} + \frac{2}{1 + 4 \omega_s^2 \tau_v^2} + 3 \right) \quad (15)$$

$$C = \frac{1}{50} \Delta^2 \tau_v \{ 4S(S+1) - 3 \} \quad (16)$$

Δ^2 is the mean square zero field splitting energy and τ_v is the correlation time for the modulation of the zero field splitting interaction. This modulation results

from the transient distortions of the complex. C can be expressed with the low-field limiting value of the electronic relaxation rate, τ_{s0} :

$$C = \frac{1}{10\tau_{s0}}; \quad \frac{1}{\tau_{s0}} = \frac{1}{5} \Delta^2 \tau_v \{4S(S+1) - 3\} = 12 \Delta^2 \tau_v \quad (17)$$

Equations (14–16) are only valid when $\tau_v^2 \Delta^2 \ll 1$ is fulfilled.

The combination of the modified Solomon-Bloembergen Eqs. (7–11) with the equations for electron spin relaxation (14–16) constitutes a complete theory to relate the observed paramagnetic relaxation rate enhancement to the microscopic properties, and it is generally referred as to Solomon-Bloembergen-Morgan (SBM) theory. Detailed discussions of the relaxation theory have been published [13, 14].

As we have seen above, a large number of parameters (proton exchange rate, $k_{ex} = 1/\tau_m$; rotational correlation time, τ_R , electronic relaxation times, $1/T_{1,2e}$; Gd – proton distance, r_{GdH} ; hydration number, q) influence the inner sphere proton relaxivity. If the proton exchange is very slow ($T_{1m} \ll \tau_m$), it will be the only limiting factor (Eq. (5)). If it is fast ($\tau_m \ll T_{1m}$), proton relaxivity will be determined by the relaxation rate of the coordinated protons, T_{1m} , which also depends on the rate of proton exchange, as well as on rotation and electronic relaxation. The optimal relationship is:

$$\frac{1}{T_{1m}} < \frac{1}{\tau_m} < \frac{1}{\tau_R}; \frac{1}{T_{1e}}$$

In order to visualize the effects of water exchange, rotation and electronic relaxation as well as of magnetic field on proton relaxivity, we have calculated proton relaxivities as a function of these parameters (Fig. 2). The relaxivity maximum is attained when the correlation time, τ_{cl} , equals the inverse proton Larmor frequency ($1/\tau_{cl} = 1/\tau_R + 1/\tau_m + 1/T_{1e} = \omega_I$). The most important message of Fig. 2 is that the rotational correlation time, proton exchange and electronic relaxation rates have to be optimized simultaneously in order to attain maximum relaxivities. If one or two of them have already an optimal value, the remaining parameter starts to become more limitative. The marketed contrast agents have relaxivities around 4–5 mM⁻¹ s⁻¹ contrary to the theoretically attainable values over 100 mM⁻¹ s⁻¹, which is mainly due to their fast rotation and slow water exchange.

2.1

Hydration Number and Gd-H Distance

All Gd(III) chelates approved for contrast agent application have one inner sphere water molecule. The inner sphere proton relaxivity is linearly proportional to the hydration number q (Eq. (5)), thus a higher q would result in increased relaxivities. However, ligands that leave space for more than one water molecule in the first coordination sphere form complexes of reduced stability,

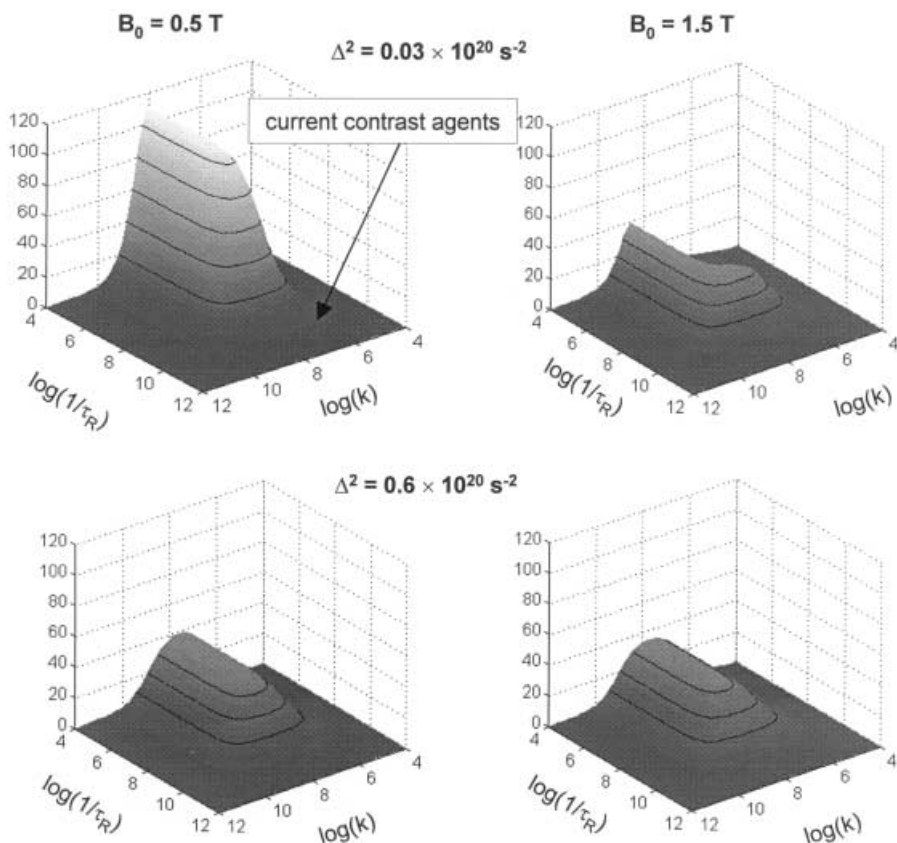


Fig. 2. Simulated inner sphere ^1H relaxivities as a function of the rotational correlation time, τ_R , and of the water exchange rate, k , at two different magnetic fields and two different electron spin relaxation rates ($T_{1e} = 2.9 \times 10^{-8} \text{ s}$ (top) and $2.9 \times 10^{-9} \text{ s}$ (bottom); τ_v has been fixed to $1 \times 10^{-12} \text{ s}^{-1}$)

therefore, due to toxicity concerns, this simple way of increasing the relaxivity is usually not realizable.

Information on the hydration state of the Gd(III) chelate in solution is indispensable for the analysis of its proton relaxivity. Several methods exist to determine q , though they are mostly applicable for other lanthanides than Gd(III). In the case of Eu(III) and Tb(III) complexes, the difference of the luminescence lifetimes measured in D_2O and H_2O can be related to the hydration number [15, 16]. For Dy(III) chelates, the lanthanide induced ^{17}O chemical shift of the bulk water is proportional to the hydration number [17]. Different hydration states of the same chelate may also coexist in solution giving rise to a hydration equilibrium. Such an equilibrium can be assessed by UV-Vis measurements on the Eu(III) complex [18–20]. These techniques have been recently discussed [21].

The Gd-H distance, r_{GdH} , which enters on the sixth power into the expression of inner sphere proton relaxivity, is a difficult parameter to obtain experimen-

tally. It is generally deduced from the Gd – coordinated water oxygen distance, however, this calculation is complicated by the fact that the tilt angle of the plane of the bound water molecule with respect to the Gd – O bond is not well defined in solution. Distance data on Gd(III) chelates in solution state are rather scarce. Solid state Gd – O distances can provide a good estimation for the solution case as well. Indeed, an X-ray absorption fine structure (XAFS) study found that Gd – O distances in aqueous solution were identical to the solid state values for $[\text{Gd}(\text{DOTA})(\text{H}_2\text{O})]^-$ and $[\text{Gd}(\text{DTPA})(\text{H}_2\text{O})]^{2-}$ (2.46 and 2.47 Å, respectively) [22]. Electron Spin Echo Envelope Modulation (ESEEM) measurements in frozen $[\text{Gd}(\text{EDTA})(\text{H}_2\text{O})_x]^-$ and $[\text{Gd}(\text{DTPA})(\text{H}_2\text{O})]^{2-}$ solutions gave rather short metal – deuterium distances [23].

The aqua ions have been more widely studied in solution. An X-ray diffraction (XRD) study in highly concentrated GdCl_3 aqueous solution resulted in 2.37 Å for the Gd – O distance [24]. Extended X-ray fine structure (EXAFS) measurements on lanthanide(III) perchlorate solutions revealed that the metal – oxygen distance changes along the series from 2.51 Å (Nd) to 2.31 Å (Lu) which is accompanied by a change in the hydration number (9.5 for Nd and 7.7 for Lu) [25]. This study reports $r_{\text{GdO}} = 2.41$ Å and $q = 7.6$ for $\text{Gd}^{3+}_{\text{aq}}$. A neutron scattering first order difference study with isotopic substitution in D_2O confirmed the change of coordination number from 9 for the light to 8 for the heavy lanthanides, with a hydration equilibrium at $\text{Sm}^{3+}_{\text{aq}}$ ($q = 8.5$) [26, 27]. Both lanthanide – oxygen and lanthanide – deuterium distances have been obtained: $r_{\text{LnO}} = 2.46$ and 2.50 Å and $r_{\text{LnD}} = 3.11$ and 3.03 Å for $\text{Sm}^{3+}_{\text{aq}}$ and $\text{Dy}^{3+}_{\text{aq}}$, respectively.

2.2

Water and Proton Exchange

The residence lifetime of protons, τ_m , plays a dual role in determining proton relaxivity. It modulates the efficiency of chemical exchange from the inner sphere of the metal to the bulk (Eq. 5), and it also contributes to the overall correlation time, τ_c , that governs the dipole-dipole interaction between the electron and nuclear spin (Eqs. 8 and 12). The exchange of coordinated water protons can occur either independently of the exchange of the entire water molecule, or via the exchange of the water molecule itself (or both). Thus the water exchange rate always represents a lower limit for the proton exchange rate. For the currently used Gd(III) based contrast agents the proton exchange rate is generally equal to the water exchange rate at physiological pH. On increasing the acidity or basicity of the solution, the proton exchange on the Gd(III) complex may become considerably faster than the water exchange due to acid- or base-catalyzed pathways [28, 29] (see below).

2.2.1

Determination of the Water Exchange Rate

The water exchange rate on a Gd(III) complex can be directly determined by variable temperature transverse ^{17}O relaxation rate measurements. The para-

magnetic transverse ^{17}O relaxation rate enhancement, $1/T_{2r}$, is related to the water residence time, τ_m and to the relaxation rate of the bound water, $1/T_{2m}$:

$$\frac{1}{T_{2r}} = \frac{1}{P_m} \left[\frac{1}{T_2} - \frac{1}{T_{2A}} \right] = \frac{1}{\tau_m} \frac{T_{2m}^{-2} + \tau_m^{-1} T_{2m}^{-1} + \Delta\omega_m^2}{(\tau_m^{-1} + T_{2m}^{-1})^2 + \Delta\omega_m^2} \quad (18)$$

where $1/T_2$ and $1/T_{2A}$ are the ^{17}O NMR relaxation rates of the paramagnetic solution, and of an external reference, respectively, and $\Delta\omega_m$ is the chemical shift difference between bound and bulk water. (The reference is a solution of an analogue diamagnetic Ln(III) complex of the same concentration and pH as the Gd(III) sample. For low molecular weight complexes of $\text{pH} = 4.0 - 6.5$, acidified water can also be used as reference). Outer sphere contributions to ^{17}O relaxation rates are negligible [30]. $\Delta\omega_m^2$ is also negligible compared to other terms in Eq. (18) which then simplifies to Eq. (19):

$$\frac{1}{T_{2r}} = \frac{1}{T_{2m} + \tau_m} \quad (19)$$

The transverse ^{17}O relaxation is principally modulated by a scalar mechanism [30], and its rate is expressed as:

$$\frac{1}{T_{2m}} \cong \frac{1}{T_{2sc}} = \frac{S(S+1)}{3} \left(\frac{A}{\hbar} \right)^2 \tau_{el} \quad \frac{1}{\tau_{el}} = \frac{1}{\tau_m} + \frac{1}{T_{1e}} \quad (20)$$

Although the scalar coupling constant, A/\hbar , does not vary much from one Gd(III) complex to another, it is advisable to determine its value from chemical shift measurements in each case in order to be able to calculate exact exchange rates.

The binding time ($\tau_m = 1/k_{ex}$) of water molecules in the inner sphere is assumed to obey the Eyring equation (Eq. (21)), where ΔS^\ddagger and ΔH^\ddagger are the entropy and enthalpy of activation for the exchange process, and k_{ex}^{298} is the exchange rate at 298.15 K.

$$\frac{1}{\tau_m} = k_{ex} = \frac{k_B T}{h} \exp \left\{ \frac{\Delta S^\ddagger}{R} - \frac{\Delta H^\ddagger}{RT} \right\} = \frac{k_{ex}^{298} T}{298.15} \exp \left\{ \frac{\Delta H^\ddagger}{R} \left(\frac{1}{298.15} - \frac{1}{T} \right) \right\} \quad (21)$$

Figure 3 shows a typical plot of the paramagnetic transverse ^{17}O relaxation rate enhancement versus the inverse temperature. At low temperatures the reduced transverse relaxation rates increase with temperature. In this *slow kinetic region* $1/T_{2r}$ is determined by the exchange rate, k_{ex} . At high temperatures, in the *fast exchange region*, the reduced transverse relaxation rates decrease with temperature and they are determined by the transverse relaxation rate of the coordinated water oxygen, $1/T_{2m}$.

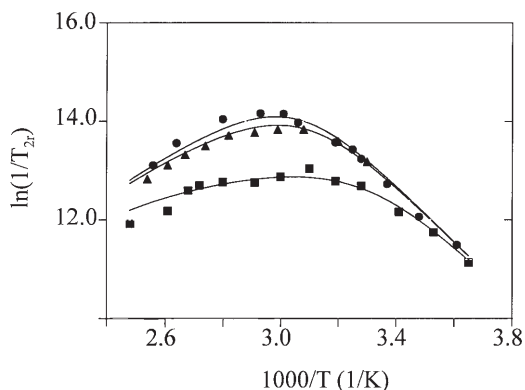


Fig. 3. Paramagnetic enhancement of the transverse ^{17}O relaxation rates as a function of the inverse temperature and of the magnetic field ($B = 1.41$ T (squares), 4.7 T (triangles) and 9.4 T (circles)), measured for $[\text{Gd}(\text{DTPA-BMA})(\text{H}_2\text{O})]$

2.2.2

Mechanism of the Water Exchange

The water exchange mechanism can be assessed by determining the activation volume, ΔV^\ddagger , from variable pressure ^{17}O transverse relaxation measurements [31]. The activation volume, defined as the difference between the partial molar volume of the transition state and the reactants, is related to the pressure dependence of the exchange rate constant through Eq. (22):

$$\frac{1}{\tau_m} = k_{\text{ex}} = (k_{\text{ex}})_0^T \exp \left\{ -\frac{\Delta V^\ddagger}{RT} P \right\} \quad (22)$$

where $(k_{\text{ex}})_0^T$ is the water exchange rate at zero pressure and temperature T . The exchange reaction is either slowed down or accelerated by increasing pressure when ΔV^\ddagger is positive or negative, respectively. A dissociative **D** mechanism is characterized by a greatly expanded transition state, thus by a large positive ΔV^\ddagger value. An associative **A** mechanism is described by a greatly contracted transition state, and by a large negative ΔV^\ddagger . Between these two extremes, the bond breaking and bond making both contribute to ΔV^\ddagger resulting in a continuum of interchange **I** mechanisms. On either side of **I** are the I_d and I_a mechanisms which are characterized by positive and negative ΔV^\ddagger values corresponding to a greater or smaller bond breaking contribution.

2.2.3

Rate and Mechanism of Water Exchange on Gd(III) Chelates

Although the water exchange rates on all, medically used Gd(III) chelates are similar (within the range of one order of magnitude), other Gd(III) complexes were found to have considerably lower (e.g. positively charged DOTA-amide derivatives) or considerably higher (e.g. the aqua ion) water exchange rates. In

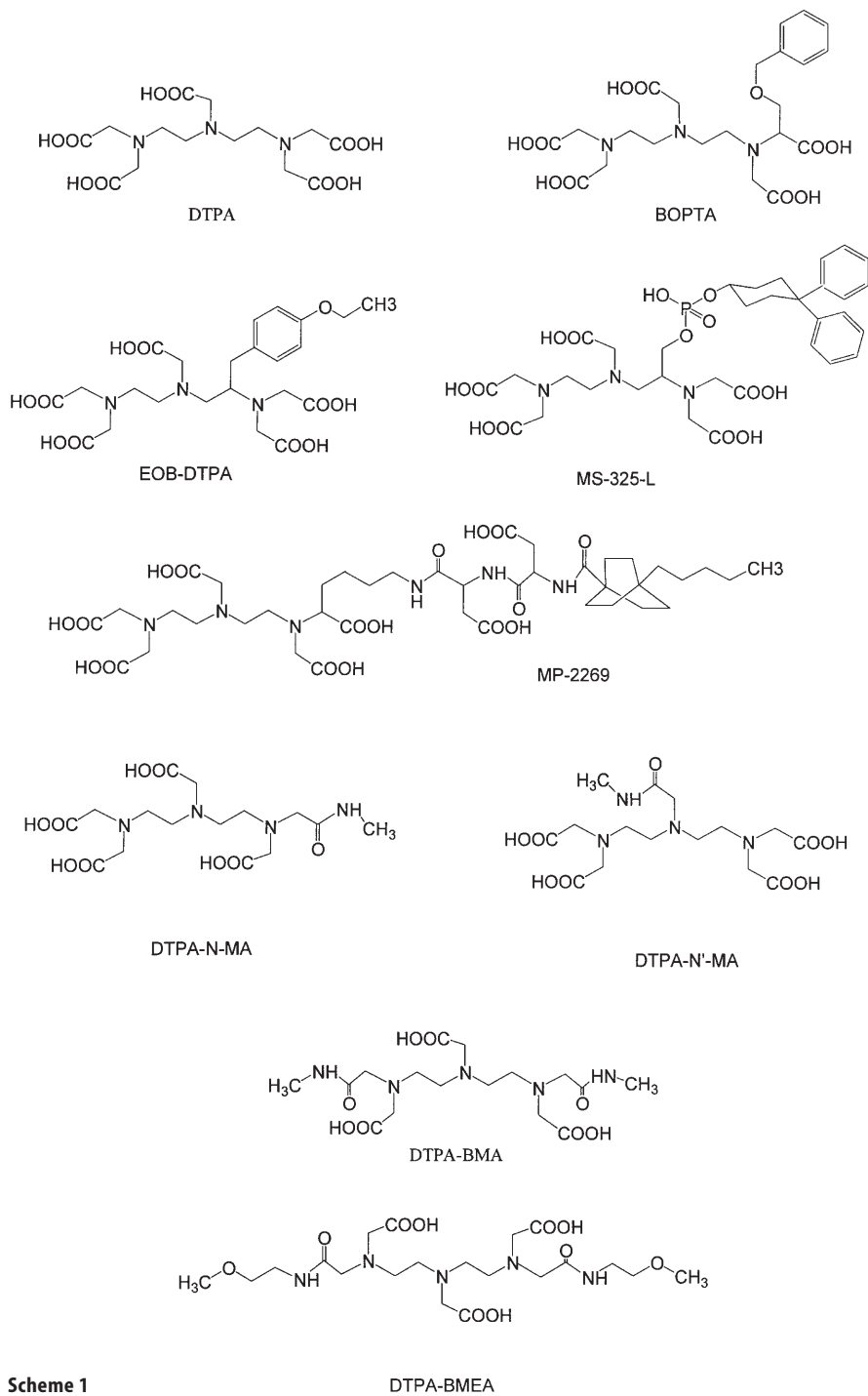
Table 1. Water exchange rates and activation volumes determined on small molecular weight Gd(III) chelates by ^{17}O NMR

Ligand	Coordinating unit	q	k_{ex}^{298} (10^6 s^{-1})	ΔV^\ddagger ($\text{cm}^3 \text{ mol}^{-1}$)	Mech.	Ref.
Aqua		1	804	– 3.3	A	55
DTPA	DTPA	1	3.30	+12.5	D	41
BOPTA	DTPA	1	3.45			67
EOB-DTPA	DTPA	1	3.60	+12.3	D	40
MP-2269	DTPA	1	4.20		D	50
DTPA-N-MA	DTPA-monoamide	1	1.30	+12.7	D	40
DTPA-N'-MA	DTPA-monoamide	1	1.90	+10.6	D	40
DTPA-BMA	DTPA-bisamide	1	0.45	+ 7.3	D	41
DTPA-BMEA	DTPA-bisamide	1	0.39	+ 7.4	D	39
DOTA	DOTA	1	4.1	+10.5	D	41
DO3A	DO3A	1.9	11			19
DO2A	DO2A	2.8	10			20
DOTASA	DOTA+COO [–]	1	6.3		I _d -D	63
DO3A-bz-NO ₂	DOTA-monoamide	1	1.6	+ 7.7	D	43
DOTA-C ₁₂	DOTA-monoamide +COO [–]	1	4.8		I _d -D	47
DOTAM	DOTA-tetraamide	1	0.053			58
PCTP-[13]		1	125			53
PCTP-[12]		1	170			54
PCTA-[12]		2	14			54
EGTA		1	31	+10.5	D	51
PDTA		2	102	– 1.5	I _a	55
TTAHA		2	8.6	+ 2.9	I _d	52
taci		2	11.0	–12.7	A	56

overall, water exchange rates on Gd(III) can vary by 4 orders of magnitude. Table 1 shows water exchange rates and activation volumes for some representative examples of monomer Gd(III) complexes.

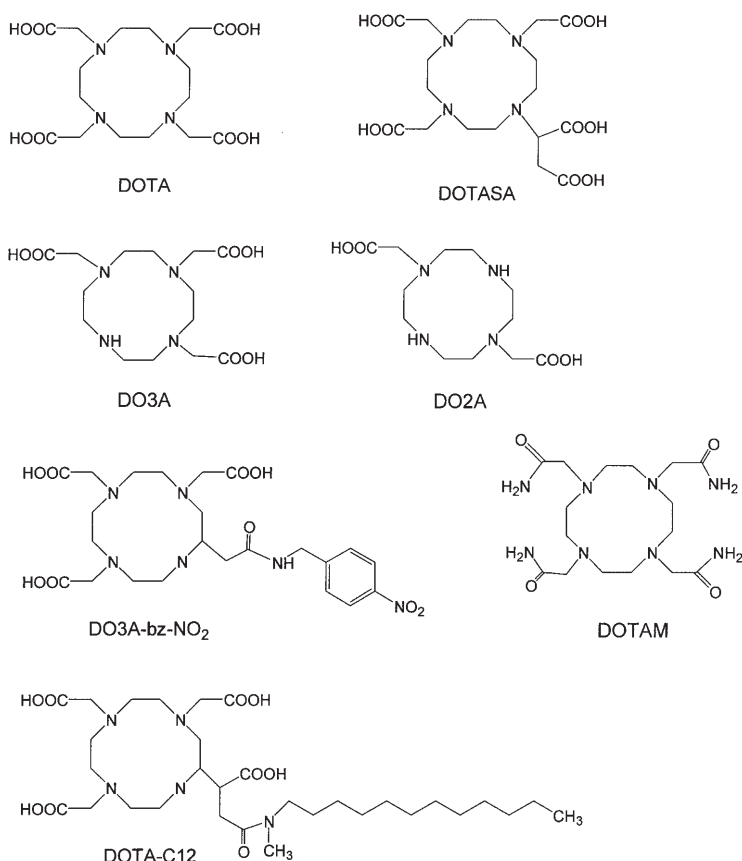
The rate and the mechanism of water exchange are closely related to the inner sphere solution structure of the complexes. This is nicely illustrated by the Ln(III) aqua ions. The decrease in the ionic radius from the beginning to the end of the series is accompanied by a decrease in the hydration number from nine to eight, with a hydration equilibrium for the middle of the series (Sm) [27]. The water exchange rates decrease by more than one order of magnitude between $[\text{Gd}(\text{H}_2\text{O})_8]^{3+}$ and $[\text{Yb}(\text{H}_2\text{O})_8]^{3+}$, whereas the mechanism remains associatively activated [32, 33]. Since $[\text{Gd}(\text{H}_2\text{O})_8]^{3+}$ is relatively close to a hydration equilibrium state (which was found for the almost neighbouring Sm), the activation energy needed for passing from the eight-coordinate reactant state to the nine-coordinate transition state is small, thus the water exchange rate is high.

The nine-coordinate Gd(III) poly(amino carboxylates) all have positive activation volumes as indicative of dissociatively activated water exchange, and much lower exchange rates in comparison to the Gd(III) aqua ion (Table 1). Several factors should be considered to rationalize the decreased water exchange rates. For many of these complexes only the coordination number of nine exists



Scheme 1

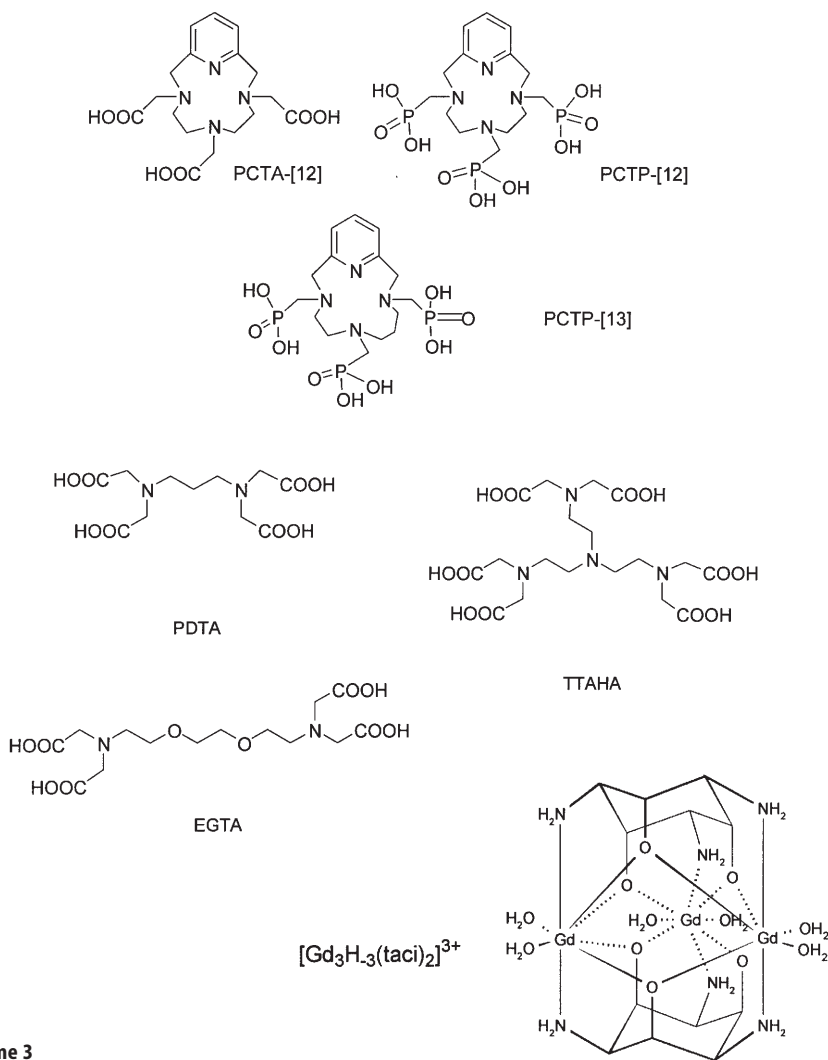
DTPA-BMEA



Scheme 2

all along the series [34–36]. Since the eight-coordinate transition state is relatively unstable, a high activation energy will be needed to reach the transition state in a dissociative process. The rigidity of the inner coordination sphere also plays a role. Whereas in the aqua ion the rearrangement of the flexible coordination sphere is easy, this rearrangement in poly(amino carboxylate) complexes needs higher energy. Moreover, the large charge density of the trivalent ion is a favourable factor in associatively activated water exchange for $[\text{Gd}(\text{H}_2\text{O})_8]^{3+}$, however, it is unfavourable in a dissociative activation mode.

Within one family of nine-coordinate Gd(III) poly(amino carboxylates), the replacement of a carboxylate donor by an amide group results in a decrease in the exchange rate by a factor of 3–4. This diminution has been equally found for linear (DTPA-type) [37–40] and macrocyclic (DOTA-type) chelates [41–43]. The decrease of the water exchange rate is in part explained in terms of steric crowding around the metal ion. Gd – amide oxygen distances are longer than Gd – carboxylate oxygen distances which results in a less crowded inner sphere for the amides (in solid state the average Gd – carboxylate oxygen distance in



Scheme 3

$\text{Na}_2[\text{Gd}(\text{DTPA})(\text{H}_2\text{O})]$ is 2.40 Å [44], the Gd – amide oxygen distance e.g. in the Gd(III) bis(benzylamide)-DTPA complex is 2.44 Å [45]). In dissociatively activated exchange processes the steric crowding is of primary importance: a tightly coordinating ligand pushes the water molecule to leave, thus favors the dissociative activation step. The significance of crowding at the water binding site was also demonstrated by an ^{17}O NMR study on the whole lanthanide series of DTPA-BMA complexes [46]. On progressing from the middle to the end of the series, the eight-coordinate transition state becomes more and more accessible since the radius of the lanthanide ion decreases, and the result is a large increase in the water exchange rate from $[\text{Eu}(\text{DTPA-BMA})(\text{H}_2\text{O})]$ to $[\text{Ho}(\text{DTPA-BMA})(\text{H}_2\text{O})]$.

Charge effects have also to be considered when comparing amide and carboxylate derivatives. A higher negative overall charge favors the leaving of the water molecule in a dissociative process, thus accelerates the exchange. Indeed, about 50% higher water exchange rate was found for the pentacarboxylate DOTA derivative $[\text{Gd}(\text{DOTA})(\text{H}_2\text{O})]^{2-}$ as compared to $[\text{Gd}(\text{DOTA})(\text{H}_2\text{O})]^-$ [47]. Analogously, the water exchange rate on $[\text{Gd}(\text{DOTA})(\text{H}_2\text{O})]^-$ decreases significantly with increasing extent of protonation, thus with decreasing negative charge, and at $[\text{H}^+] = 1.0 \text{ M}$ it is about ten times lower than in neutral media [48].

The water exchange rate is hardly affected by substituents which do not directly interfere in the inner coordination sphere. For instance, different bisamide DTPA-derivatives (DTPA-BMA, DTPA-BMEA, DTPA-BENGALAA, etc) have similar exchange rates [37, 39]. Similarly, substituents on the carbon backbone of the DTPA have little influence on the water exchange kinetics [30, 40, 49, 50].

Several complexes with not DTPA- or DOTA-derivative ligands have also been investigated. The nine-coordinate $[\text{Gd}(\text{EGTA})(\text{H}_2\text{O})]^-$ has a 10 times faster water exchange than $[\text{Gd}(\text{DTPA})(\text{H}_2\text{O})]^{2-}$ [51]. For the tripod $[\text{Gd}(\text{TTAHA})(\text{H}_2\text{O})_2]^{2-}$ the presence of two inner sphere water molecules decreases the stereoridity of the system which results in an increased water exchange rate compared to $[\text{Gd}(\text{DTPA})(\text{H}_2\text{O})]^{2-}$ [52]. Gd(III) complexes of some pyridin-based macrocycles have, in general, remarkably higher water exchange rates than that of the parent $[\text{Gd}(\text{DOTA})(\text{H}_2\text{O})]^-$ [53,54]. The exchange is particularly fast on the eight-coordinate phosphonate derivative $[\text{Gd}(\text{PCTP-12})(\text{H}_2\text{O})]$, probably due to an associatively activated mechanism. Among eight-coordinate complexes, $[\text{Gd}(\text{PDTA})(\text{H}_2\text{O})_2]^-$ has an is extremely fast water exchange with an associative interchange, I_a , mechanism [55]. The trimer $[\text{Gd}_3(\text{H}_3\text{taci})_2(\text{H}_2\text{O})_6]^{3+}$ undergoes a slightly slower water exchange than $[\text{Gd}(\text{PDTA})(\text{H}_2\text{O})_2]^-$, via a limiting A mechanism [56]. The lower exchange rate was attributed to the particularly rigid structure of this trimer complex which slows down the transition from the eight-coordinate reactant to the nine-coordinate transition state.

Water exchange on Gd(III) systems in hydration equilibrium has also been investigated. In aqueous solution, the $[\text{Gd}(\text{DO3A})(\text{H}_2\text{O})_{1,2}]$ and $[\text{Gd}(\text{DO2A})(\text{H}_2\text{O})_{2,3}]$ complexes are present as both eight- and nine-coordinate species [19, 20]. Since it is usually admitted that only the coordination numbers of 8 or 9 are available for Gd(III) in solution, nine-coordinate complexes exchange in dissociatively activated processes, thus via an eight-coordinate transition state, whereas eight-coordinate complexes exchange in associatively activated processes via a nine-coordinate transition state. The rate of the water exchange depends on the accessibility of the transition state. If a hydration equilibrium exists between eight- and nine-coordinate species ($[\text{GdL}(\text{H}_2\text{O})_n]$ and $[\text{GdL}(\text{H}_2\text{O})_{n+1}]$), one can expect the energy gap to be relatively small between them, i.e. between the nine-coordinate ground state and the eight-coordinate transition state (or the eight-coordinate ground state and the nine-coordinate transition state), which can consequently result in a fast exchange. Contrary to these expectations, for both $[\text{Gd}(\text{DO2A})(\text{H}_2\text{O})_{2,3}]^+$ ($k_{\text{ex}}^{298} = 10 \times 10^6 \text{ s}^{-1}$) and $[\text{Gd}(\text{DO3A})(\text{H}_2\text{O})_{1,2}]$ ($k_{\text{ex}}^{298} = 11 \times 10^6 \text{ s}^{-1}$) only a twofold gain is observed in the water exchange rate in comparison to $[\text{Gd}(\text{DOTA})(\text{H}_2\text{O})]^-$ ($k_{\text{ex}}^{298} = 4.8 \times 10^6 \text{ s}^{-1}$).

The reason is that, beside the favorable influence of the equilibrium state on increasing the water exchange rate, one has to consider the increased overall positive charge of the complex as a negative factor. The interplay of the opposite effects of the hydration equilibrium and of the increasing positive charge results in the limited water exchange gain. It has to be noted that a rigorous analysis of ^{17}O NMR data obtained on Gd(III) complexes in hydration equilibrium requires the use of the Kubo-Sack formalism which allows to treat correctly the system as a three-site exchange problem [57].

DOTA-type complexes exist in two diastereomeric forms (**m** and **M**) which may have remarkably different water exchange rates as found for $[\text{Eu}(\text{DOTAM})(\text{H}_2\text{O})]^{3+}$ [58, 59]. In this ^{17}O and ^1H NMR study performed in acetonitrile-water solvent, it was possible to detect the NMR signals of the coordinated water molecules in both isomers. In a general case, the observation of the bound water signal for Ln(III) poly(amino carboxylates) is not possible due to the fast exchange, and for Gd(III) complexes, to the slow electronic relaxation.

In the last few years several macromolecular systems have been studied by variable temperature and pressure ^{17}O NMR in order to determine the rate and mechanism of water exchange. The kinetic parameters characterizing the water exchange on some macromolecular Gd(III) complexes are presented in Table 2.

The rate and mechanism of water exchange have been found to be similar for different generations (gen. 3, 4 and 5) of PAMAM dendrimers functionalized with the same Gd(III) DO3A-monoamide chelate and for the monomer Gd(III) DO3A-monoamide complex itself [43]. This study gave the first experimental evidence that the attachment of a Gd(III) chelate to a dendrimer did not significantly influence the water exchange kinetics.

Linear copolymers of Gd(DTPA-bisamide) or Gd(EGTA-bisamide) units with poly(ethylene-glycol) (PEG) or polyalkyl $-(\text{CH}_2)_n-$; $n = 6, 10$ and 12) spacers also had water exchange kinetics similar to that of the corresponding monomer chelate [60–62]. An ^{17}O NMR study on the micellar system formed in aqueous solution of the amphiphilic DOTA-derivative $[\text{Gd}(\text{DOTA-C}_{12})(\text{H}_2\text{O})]$ also showed that the water exchange is not altered by the micellar structure [63].

Table 2. Water exchange rates and activation volumes measured on macromolecular Gd(III) chelates and on the corresponding monomer units by ^{17}O NMR

	Complex	k_{ex}^{298} (10^6 s^{-1})	ΔV^\ddagger ($\text{cm}^3 \text{ mol}^{-1}$)	Ref.
Dendrimers	$[\text{G3}(\text{N}\{\text{CS}\}\text{N-bz-Gd}\{\text{DO3A}\}\{\text{H}_2\text{O}\})_{23}]$	1.0	+3.1	43
	$[\text{G4}(\text{N}\{\text{CS}\}\text{N-bz-Gd}\{\text{DO3A}\}\{\text{H}_2\text{O}\})_{30}]$	1.3		43
	$[\text{G5}(\text{N}\{\text{CS}\}\text{N-bz-Gd}\{\text{DO3A}\}\{\text{H}_2\text{O}\})_{52}]$	1.5		43
Monomer unit	$[\text{Gd}(\text{DO3A-bz-NO}_2)(\text{H}_2\text{O})]$	1.6	+7.7	43
Linear polymers	$[\text{Gd}(\text{DTPA-BA})(\text{H}_2\text{O})(\text{CH}_2)_n]_x$ $n = 6$	0.43	+9.6	61
	$[\text{Gd}(\text{DTPA-BA})(\text{H}_2\text{O})(\text{CH}_2)_n]_x$ $n = 10$	0.66		61
	$[\text{Gd}(\text{DTPA-BA})(\text{H}_2\text{O})(\text{CH}_2)_n]_x$ $n = 12$	0.50		61
	$[\text{Gd}(\text{DTPA-BA})(\text{H}_2\text{O})\text{-PEG}]_x$	0.48	+9.2	60
Monomer unit	$[\text{Gd}(\text{DTPA-BMA})(\text{H}_2\text{O})]$	0.45	+7.3	41



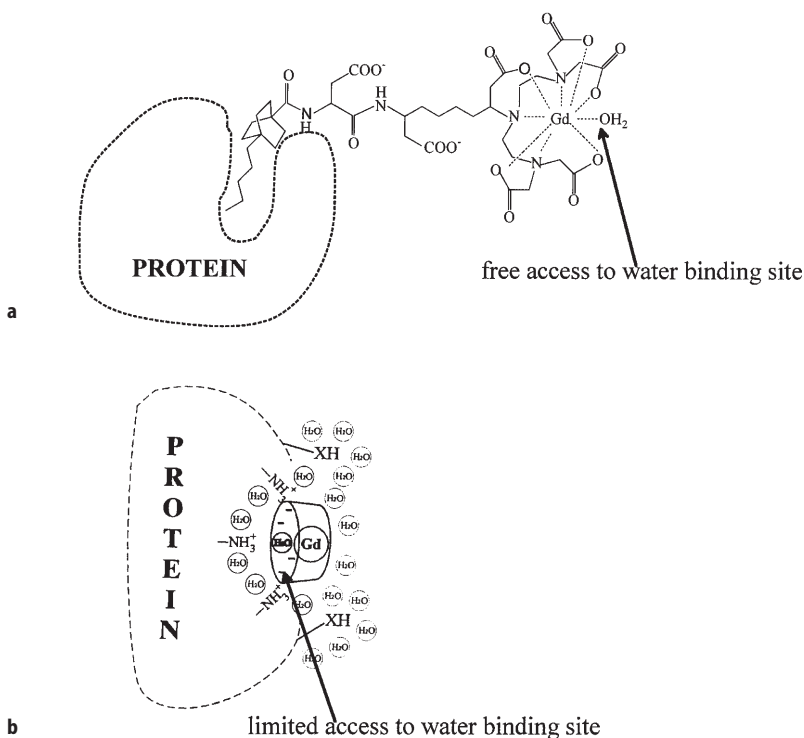


Fig. 4. Effect of protein binding on the water binding site. (a) The hydrophobic side chain of the ligand, bound to the protein is far from the Gd(III) chelate, thus protein binding does not influence water exchange. (b) The Gd(III) chelate is bound to the protein via electrostatic forces. The water binding site of the complex is partially blocked by the protein, thus the water exchange rate is diminished

Non-covalent binding to a protein, however, can influence the water exchange. Due to the interaction between the Gd(III) chelate and the protein the access to the water binding site can be limited, and consequently, the rate of water exchange significantly reduced. This scenario has been reported for Gd(PCTP-[13]) or MS-325 [53, 64, 65]. On the other hand, if there is a relatively large distance between the metal- and protein binding site of the ligand, the water exchange is not affected by the protein, as it was found for MP2269 (Fig. 4) [50].

In conclusion, the incorporation of Gd(III) complexes into macromolecular systems (dendrimers, linear polymers, micelles) does not significantly affect the water exchange kinetics, exceptions have only been found for few protein bound chelates.

2.2.4

Proton Exchange

So far we have considered the exchange of entire inner sphere water molecules. From the practical point of view of MRI contrast agent applications, it is the rate of proton exchange which is important since it determines the proton relaxivity. For the Gd(III) chelates used as MRI contrast agents, at physiological pH the proton exchange rate equals the water exchange rate. Proton exchange may become faster than water exchange in acidic or basic media due to H^+ or OH^- catalyzed processes. Several examples of H^+ or OH^- catalyzed prototropic exchange have been reported on Gd(III) complexes [28, 29, 49, 66]. The general form of the proton exchange rate is given as:

$$k = k_{ex}^{H_2O} + k^H[H^+] + k^{OH}[OH^-] \quad (23)$$

where $k_{ex}^{H_2O}$ is the water exchange rate as obtained from ^{17}O NMR measurements, and k^H and k^{OH} are the rate constants for the acid and base catalyzed prototropic exchange processes, respectively [67]. These rate constants can be assessed by pH-dependent 1H relaxometric studies [28], if the water exchange rate is known from ^{17}O NMR measurements. Since the water exchange rate on currently used, Gd-based MRI contrast agents is lower than the optimal value to attain high proton relaxivities, much effort is being made to accelerate proton exchange at physiological pH by displacing the domain of H^+ or OH^- catalysis.

2.3

Rotation

2.3.1

Techniques of Determining the Rotational Correlation Time

Most of the τ_R values reported for Gd(III) complexes in the literature have been obtained from proton relaxation measurements. However, as we have seen above, numerous factors influence proton relaxivity which often renders the determination of the rotational correlation time by relaxometry difficult and uncertain. Consequently, independent measurements of this parameter are often needed.

τ_R for spherical molecules can be estimated from the Debye-Stokes equation (Eq. 24):

$$\tau_R = \frac{4\pi\eta r_{eff}^3}{3k_B T} \quad (24)$$

Although usually the exact values of the effective radius, r_{eff} , and of the microviscosity, η , are not known, rotational correlation times for similar systems with different molecular weight can be well compared using this equation, supposing that the microviscosity and the density of the molecules are the same, thus the ratio of the r_{eff}^3 values can be expressed by the ratio of the molecular weights.

Nuclear relaxation of different nuclei other than the proton can also be used to determine the rotational correlation time. The longitudinal relaxation of the ^{17}O is governed by quadrupolar [68] and dipolar mechanisms [69], $1/T_{1q}$ and $1/T_{1d}$, respectively, both dependant on rotation:

$$\frac{1}{T_{1q}} = \frac{3\pi^2}{10} \frac{2I+3}{I^2(2I-1)} \chi^2 (1 + \eta^2/3) \left[0.2 \frac{\tau_R}{1 + \omega_I^2 \tau_R^2} + 0.8 \frac{\tau_R}{1 + 4\omega_I^2 \tau_R^2} \right] \quad (25)$$

$$\frac{1}{T_{1d}} = \frac{2}{15} \frac{\gamma_I^2 g^2 \mu_B^2}{r_{\text{GdO}}^6} S(S+1) \left(\frac{\mu_0}{4\pi} \right)^2 \left[7 \frac{\tau_{c2}}{1 + \omega_S^2 \tau_{c2}^2} + 3 \frac{\tau_{c1}}{1 + \omega_I^2 \tau_{c1}^2} \right] \quad (26)$$

Here I is the nuclear spin, χ^2 is the quadrupolar coupling constant, η is an asymmetry parameter, r_{GdO} is the Gd–O distance, and τ_{ci} is defined by Eq. 12. The difficulty of this technique is that both the quadrupolar coupling constant and the Gd–O distance can only be estimated. However, rotational correlation times obtained from longitudinal ^{17}O relaxation rates can provide a good comparison for similar Gd(III) complexes. One advantage is that the rotational correlation time is measured directly on the Gd(III) complex. Furthermore, the τ_R determined in this way corresponds to the rotation of the Gd(III) – coordinated water oxygen vector which is probably analogous to the rotation of the Gd(III) – coordinated water proton, which, itself determines proton relaxivity.

The rotational correlation time can be directly obtained from ^{13}C or deuterium relaxation measurements on a diamagnetic analogue (Y(III), La(III) or Lu(III)) of the Gd(III) complex [38, 70–72]. One disadvantage is low sensitivity of ^{13}C or ^2D at natural abundance. Moreover, these methods do not measure the rotation of the metal – coordinated water vector, important from the practical point of view, and this may cause problems mainly in the case of large molecules.

EPR spectroscopy has been used to study rotation on vanadyl (VO^{2+}) analogues of Gd(III) chelates [73–76]. Vanadyl EPR line shapes are sensitive to rotation, they even allow for the distinction of isotropic and anisotropic motions. One concern about this technique is that substituting the trivalent Gd ion with the divalent vanadyl may modify the rotational dynamics of the complex.

Rotational correlation times determined by different methods are shown in Table 3.

2.3.2

Internal Flexibility of Macromolecular Gd(III) Complexes. The Lipari-Szabo Approach

The proton relaxivity of small molecular weight MRI contrast agents is mainly limited by fast rotation. This prompted the development of a wide variety of macromolecular agents to slow down rotation and thus increase relaxivity. Indeed, τ_R generally increases with increasing molecular weight. However, this increase is often much less than expected on the basis of the molecular weight due to the internal flexibility of the macromolecule. For instance, for certain linear polymers the proton relaxivity was found to be independent of the molecular weight. Since their relaxivity is limited by fast rotation, the invariance of the

Table 3. Comparison of rotational correlation times and proton relaxivities for low molecular weight and macromolecular Gd(III) complexes

	Ligand	τ_R^{298} /ps	M_w	r_1 /mM ⁻¹ s ⁻¹ (20 MHz; 37 °C)	Ref.
Monomers	aqua	41 ^a	301		41
	DTPA	58 ^a	563	4.02	41
		103 ^b			30
	EOB-DTPA	84 ^c	696	5.3	70, 113
		93 ^d			70
		178 ^b			40
	BOPTA	88 ^c	683	4.39	114
	DTPA-BMA	66 ^a	587	3.96	41
		167 ^b			
	MP-2269	139 ^a	1069	5.64	50
	DOTA	77 ^a	575	3.83	41
		90 ^b			
	PCTA-[12]	70 ^c	552	6.9 (25°C)	54
	PCTP-[12]	106 ^c	657	7.5 (25°C)	54
Linear polymers	[DTPA-BA-PEG] _x	232 ^a	20.2 kDa	6.31	60
	[DTPA-BA(CH ₂) _n] _x n = 6	801 ^b	19.4 kDa	9.8	61
	[DTPA-BA(CH ₂) _n] _x n = 10	$\tau_g = 2900^{b,e}$ $\tau_l = 460^f$	10.3 kDa	15.4	61
	[DTPA-BA(CH ₂) _n] _x n = 12	$\tau_g = 4400^{b,e}$			
	15.7 kDa	19.6 $\tau_l = 480^f$	61		
Dendrimers	[G3(N{CS}N-bz- {DO3A}) ₂₃]	580 ^b	22.1 kDa	14.6	43
	[G4(N{CS}N-bz- {DO3A}) ₃₀]	700 ^b	37.4 kDa	15.9	43
	[G5(N{CS}N-bz- {DO3A}) ₅₂]	870 ^b	61.8 kDa	18.7	43
Protein bound	PCTP-[13]-HSA	30 000 ^c	69 kDa	45.0	53
	MS-325-HSA	3–4000 ^c	69 kDa	48.9	64
		6–7000 ^d			
	MP-2269-BSA	1000 ^c	66 kDa	24.5	50

^a Determined from simultaneous analysis of NMRD and ¹⁷O T₁ data (the Gd-H distance, r_{GdH} , was fixed to 0.31 nm, and the Gd-O distance, r_{GdO} , was left variable (0.21–0.24 nm)).

^b Determined from ¹⁷O T₁ data (with the Gd-O distance, r_{GdO} , fixed to 0.25 nm).

^c Determined from NMRD data.

^d Determined by ²D NMR.

^e Global rotational correlation time.

^f Local rotational correlation time.

relaxivity reflects the invariance of the rotational correlation time [77, 78]. The rotational correlation time of these polymers is dominated by segmental motions which are independent of the molecular weight.

The flexibility of the linker group was found to be responsible for the much lower effective rotational correlation time, consequently lower relaxivity of many different types of macromolecular agents. For dendrimers loaded with

Gd(III) chelates, the relatively low relaxivity is the consequence of the flexibility of the linker group between the Gd(III) chelate and the rigid dendrimer molecule (slow water exchange is also limitative). Internal flexibility has been also proved for certain non-covalently bound Gd(III) chelate – protein adducts. The τ_R value determined for MP-2269 bound to bovine serum albumin is 1.0 ns, one order of magnitude lower than the rotational correlation time of the protein molecule [50].

Clarkson et al. investigated molecular dynamics of vanadyl-EDTA and DTPA complexes in sucrose solution or attached to PAMAM dendrimers by EPR [74, 75]. The motion-sensitive EPR data of the dendrimeric system have been fitted to an anisotropic model which is described by an overall spherical rotation combined with a rotation around the axis of the arm branching out of the central core. The motions around the axis of the branch connecting the chelate to the central core were found to be very rapid, whereas the overall tumbling was slow.

Recently the “model-free” Lipari-Szabo approach [79] has proved useful to describe rotational motion of macromolecular Gd(III) chelates, using longitudinal ^{17}O relaxation rates [61, 62]. Two kinds of motion are assumed to affect relaxation: a rapid, local motion which lies in the extreme narrowing limit and a slower, global motion. Provided they are statistically independent and the global motion is isotropic, the reduced spectral density function can be written as:

$$J(\omega) = \left(\frac{S^2 \tau_g}{1 + \omega^2 \tau_g^2} + \frac{(1 - S^2) \tau_l}{1 + \omega^2 \tau_l^2} \right) \quad \tau^{-1} = \tau_g^{-1} + \tau_l^{-1} \quad (27)$$

where τ_g is a correlation time for the global motion, common to the whole molecule, τ_l is the correlation time for the fast local motion, specific for the individual relaxation axis which is related to the motion of the Gd(III) chelate unit. The generalized order parameter, S , is a model-independent measure of the degree of spatial restriction of the local motion, $S = 0$ if the internal motion is isotropic; $S = 1$ if the motion is completely restricted.

The rotation of linear [Gd(III)DTPA-bisamide] – alkyl and [Gd(III)EGTA-bisamide] – alkyl copolymers have been analyzed with the Lipari-Szabo approach. These polymers form intramolecular micelle-like aggregates in aqueous solution, resulting in a relatively slow rotation and consequently high proton relaxivity. The local rotational correlation times were found to be similar for these polymers, whereas the global rotational correlation times were different and reflected their molecular weight. The difference in proton relaxivity could be interpreted with the different global rotational correlation times showing that, for these polymers, the overall motion also contributes to the relaxivity [61, 62].

2.4

Electron Spin Relaxation

The influence of the electron spin relaxation on the relaxivity of gadolinium based contrast agents is essentially governed by the decay of the electron spin magnetization in the direction parallel to the external magnetic field, described

by the longitudinal electronic relaxation time T_{1e} . This decay is too fast to be directly measured. Nevertheless the investigation of the transverse electronic relaxation, described by T_{2e} , may allow an estimation of T_{1e} within the framework of a given model.

The basic theory of the EPR line shape of Gd^{3+} complexes was proposed by Hudson and Lewis [80] who used a transient zero-field splitting (ZFS) as the main relaxation mechanism. The transverse electronic spin relaxation was described by four different relaxation times due to the superposition of four transitions with different intensities. For complexes with cubic symmetry Bloembergen and Morgan developed an approximate theory which led to the equations generally used in the context of electronic relaxation of Gd^{3+} complexes (Eqs. 14–16) [77]. A similar approximate treatment was used by Powell et al. [81] to describe temperature and magnetic field dependence of T_{2e} measured on several gadolinium complexes. To be able to extract parameters from a combined fit of ^{17}O NMR and EPR measurements a second relaxation mechanism was introduced, which was assumed to be independent from the observation frequency [37]. Already in 1974 Poupko et al. [82] discussed the factors which determine EPR line shapes and shifts of transition metal complexes in solution showing that the dynamic frequency shift can have pronounced effects. In 1996 Strandberg and Westlund [83] derived a closed analytical form of the line shape including the dynamic frequency shift and calculated theoretical NMRD profiles of $[Gd(H_2O)_8]^{3+}$ and some gadolinium chelates.

A systematic variable temperature (0–100°C), concentration and frequency (9.425, 75, 150 and 225 GHz) EPR study on three $Gd(III)$ compounds: $[Gd(H_2O)_8]^{3+}$, $[Gd(DOTA)(H_2O)]^-$ and $[Gd(DTPA-BMA)(H_2O)]$ in aqueous solution was analyzed using both peak-to-peak widths, ΔH_{pp} , and dynamic frequency shifts calculated from a theory involving numerical calculations using the full relaxation matrix similar to that proposed by Poupko and Strandberg [84]. In this, as well as in a more approximate treatment, valid only at very high magnetic field [85], the frequency independent relaxation term, sometimes attributed to the spin-rotation relaxation mechanism, had still to be included in the fitting procedure to get reasonable fits.

A general model for electronic relaxation of the Gd^{3+} $S = 7/2$ ion in various complexes in solution was presented by Rast et al. [86]. Contrary to the usual assumption, the electronic relaxation in their model is not only due to the effects of the transient zero field splitting, but is also strongly influenced by the static crystal field effect which is modulated by the random Brownian rotation of the complex. Experimental peak-to-peak widths of three gadolinium complexes could be well interpreted as a function of temperature and frequency using three static and one transient crystal field parameters. Moreover, their interpretation of experimental data did not require the addition of any field independent contribution to the line width like the spin-rotation mechanism.

An interesting finding for the aqua ion is that at X-band the static contribution is an order of magnitude larger than the transient one and in the high temperature range the experimental line widths follow the static part. On the contrary, for the 2 mm-band, the transient contribution to ΔH_{pp} is about 5 times larger (at low temperature) than the static one. The longitudinal relaxation func-

tion, calculated using adjusted parameters from transverse relaxation, shows a quasi mono-exponential decay, characterized by a single relaxation time T_{1e} .

Recently Rast et al. [87] proceeded a step further by adding the dynamic frequency shift to their theory and by fitting simultaneously full experimental EPR spectra as a function of temperature and frequency. It was shown that in the static crystal field mechanism, contrary to the usual global models involving only second-order terms, the fourth and sixth order terms can play a non-negligible role. The peak-to-peak distances, indicating the line width, and the apparent g-factor, indicating the central field, are only used as a comprehensive way to present the results because it is impossible to determine them in a simple way without introduction of uncontrollable errors. A complete line shape analysis overcomes this problem. Fig. 5 shows some examples of experimental spectra

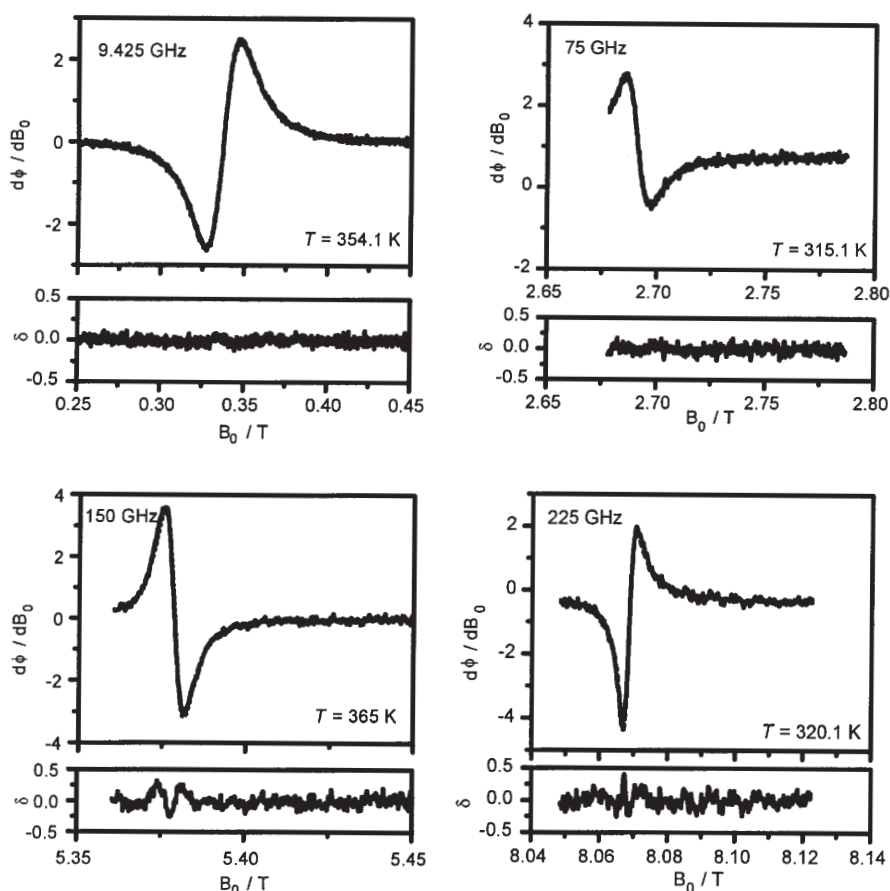


Fig. 5. Selected experimental (full line) and nearly identical underlying theoretical spectra (dotted line) for $[\text{Gd}(\text{H}_2\text{O})_8]^{3+}$ at fixed frequency and temperature values versus variable external magnetic field. The difference between experimental and theoretical line shape is shown on the bottom of each figure

and their counterparts calculated from the best-fitting model for the aqua-ion. The very good agreement of experimental spectra and their fitted counterparts for $[\text{Gd}(\text{H}_2\text{O})_8]^{3+}$ and $[\text{Gd}(\text{DOTA})(\text{H}_2\text{O})]^-$ clearly demonstrates the power of this approach. Despite the large amount of spectroscopic data, model parameters can be obtained on a modern personal computer within a few minutes. As already found in the first paper, the postulated spin rotation mechanism plays a negligible role and can be omitted. A limitation of the model can be the use of Redfield's approximation in the calculation of the line shape. This may be inadequate in the case of complexes with long rotation correlation times and at very low magnetic fields. The application of this recent theory in a combined fitting procedure of ^{17}O NMR, ^1H NMRD and EPR data is not straightforward and, moreover, needs EPR spectra over a wide range of frequencies and temperatures. Therefore, the common Bloembergen-Morgan theory will probably still be applied in the future to generate electron spin relaxation rates but one should be aware of its limitations and renounce to discuss the parameters τ_v and Δ^2 .

3 Outer Sphere Proton Relaxivity

The relaxivity induced by gadolinium chelates due to inner-sphere water molecules, r_1^{IS} , is well understood on the microscopic scale as can be seen from the above discussion. The contribution to the overall relaxation enhancement due to all other water molecules is normally summed up in the term r_1^{OS} , generally called the outer-sphere contribution. The interaction between the water proton nuclear spin I and the gadolinium electron spin S is supposed to be a dipolar intermolecular interaction whose fluctuations are governed by random translational motion. The corresponding relaxation rate, $1/T_1$, for unlike spins is given by Eq. (23) [88–90]

$$\frac{1}{T_1} = \frac{32\pi}{405} \left(\frac{\mu_0}{4\pi} \right)^2 \frac{N_A[M]}{dD} \gamma_I^2 \gamma_S^2 \hbar^2 S(S+1) [j_2(\omega_I - \omega_S) + 3j_1(\omega_I) + 6j_2(\omega_I + \omega_S)] \quad (23)$$

where N_A is Avogadro's constant, d is the closest distance of approach of spins I and S , D is the diffusion constant for relative diffusion and $[M]$ is the molar concentration of the metal bearing spin S . The spectral densities $j(\omega)$ are obtained from the Fourier transformation of the correlation function $g(t)$ which depends on the conditional probability for the relative diffusion of spins I and S , $P(\mathbf{r}_0|\mathbf{r}, t)$. This probability can be approximated as the solution of the Smoluchowski equation (Eq. 24): [90, 91]

$$\frac{\partial P(\mathbf{r}_0|\mathbf{r}, t)}{\partial t} = D \nabla \cdot \left[\nabla P(\mathbf{r}_0|\mathbf{r}, t) + \frac{1}{k_B T} P(\mathbf{r}_0|\mathbf{r}, t) \nabla U(r) \right] \quad (24)$$

\mathbf{r}_0 and \mathbf{r} are the separations of spins I and S at time 0 and t , respectively. $U(r)$ is the potential of averaged forces between the spin-bearing molecules and can be

obtained from the radial distribution function $g(r)$ by $\ln[g(r)] = -U(r)/k_B T$. Freed and others [91–93] showed that an analytical expression for $1/T_1$ exists for the simplest case of a force-free model where $g(r)$ is a simple step function raising from 0 to 1 at a distance $r = d$. The spectral densities are given in this model by Eq. 25:

$$j_k(\omega) = \text{Re} \left\{ \frac{1 + z/4}{1 + z + 4z^2/9 + z^3/9} \right\} \quad (25)$$

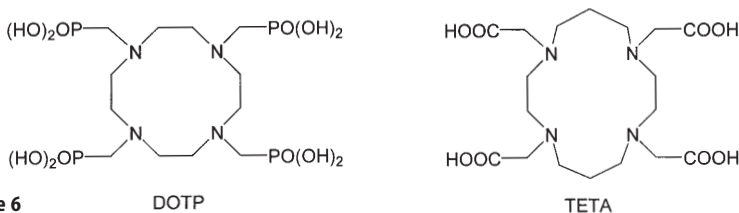
with $z = \sqrt{i\omega\tau + \tau/T_{ke}}$ and $\tau = d^2/D$; $k = 1, 2$

T_{ke} is the longitudinal or transverse electronic relaxation time.

A direct measurement of the relaxation enhancement of gadolinium chelates is only possible for complexes with no inner sphere (IS) water, complexes which are in general not interesting as contrast agents. An estimation of the outer sphere (OS) contribution of a complex with inner sphere water is sometimes obtained by replacing the chelating ligand by a similar one leading to complexes without IS-water as for example using the cyclic TETA to replace DOTA. This method can be dangerous as will be seen below. In most studies the outer sphere contribution is estimated using Eqs. 23–25 and setting the closest distance of approach, d , to a “reasonable value” as for example 3.6 Å. The relative diffusion constant D is the sum of the self-diffusion constants for the Gd-complex, D_s and for a water molecule, D_l . The parameter D which determines also the translational correlation time τ (Eq. 25), is either set to a value close to D_l (normally $D_l \gg D_s$ for large complexes) or fitted in the evaluation of the NMRD profiles. For ligands with phosphonate groups Aime et al. [94, 95] proposed the existence of a “second coordination sphere” formed by water molecules hydrogen bonded to the complex. Equation (4) has to be replaced by Eq. (26).

$$r_i = r_i^{IS} + r_i^{2nd} + r_i^{OS} \quad (26)$$

where r_i^{2nd} is the contribution from water molecules in the 2nd coordination sphere and r_i^{OS} accounts for the contribution from H₂O-molecules which diffuse in the proximity of the paramagnetic complex. Enforcing the interaction between functional groups of the chelating ligand and water molecules will lead to the formation of a well defined 2nd coordination sphere with several water molecules considerably bound in the proximity of the paramagnetic center. Through a careful choice of the hydrogen-bond-acceptor groups one may promote the formation of a strong interaction, increase the number of water molecules in the second shell and decrease their average distance from the Gd-center



Scheme 6

[9]. Clarkson [96] showed in a combined EPR and NMRD study using VO^{2+} and Gd^{3+} that for TTHA the second sphere contribution can be substantial (over 30%).

Experimental data on the structure and dynamics of water molecules in the vicinity of Gd^{3+} chelates are very difficult to obtain. Molecular dynamics (MD) simulation, however, can give direct access to these properties and allow estimation of outer sphere relaxivity. The interaction between polyamino-carboxylate and polyamino-phosphonate complexes of Gd^{3+} with the surrounding water is essentially given by the electrostatic interaction and the van der Waals repulsion of the atoms [97]. The electrostatic potential of the molecular surface can be obtained from quantum mechanical calculations using the Merz-Kollman method [98] and the atomic repulsion from classical force-field parameters. The electrostatic potential on the surface of complexes with cyclic ligands (as for example DOTA, TETA or DOTP) shows that these can be split into two regions, one hydrophilic (containing the carboxylates/phosphonates) and one hydrophobic (containing the macrocycle) [97] (Fig. 6). From a classical molecular dynam-

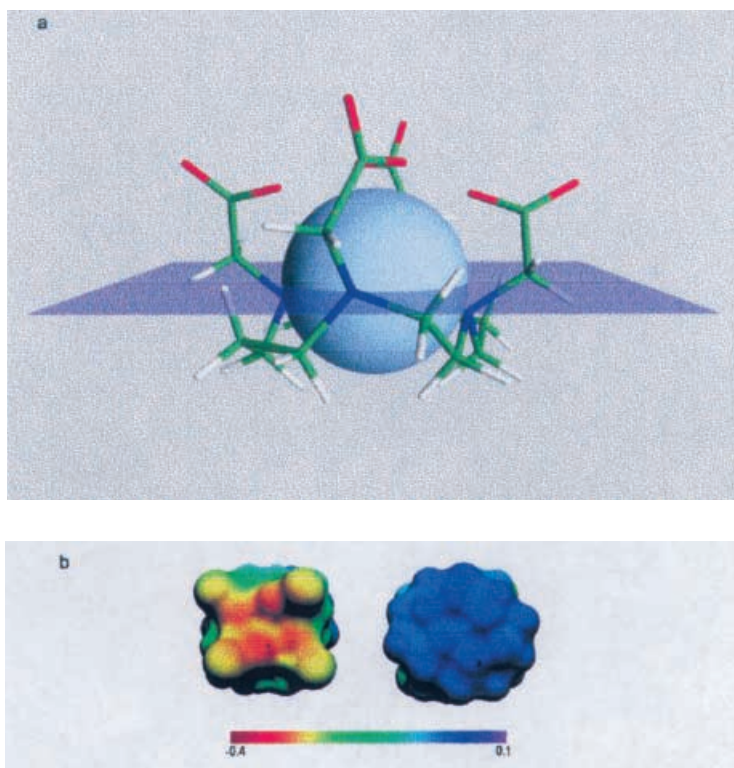


Fig. 6. **a** Model of $[\text{Gd}(\text{teta})]^-$, and division of the surrounding space into hydrophilic (above) and hydrophobic (below) hemispheres. **b** Electrostatic potential [au] at the molecular surface of $[\text{Gd}(\text{teta})]^-$ in the hydrophilic (carboxylate, left) and hydrophobic (macrocycle, right) regions

ics simulation one can distinguish water molecules in both regions. The radial distribution functions (rdf) of water around carboxylate oxygen atoms, $g_{\text{OO}}(r)$ and around N atoms from the ring, $g_{\text{NO}}(r)$ show marked differences (Fig. 7). Around the hydrophilic COO^- a sharp peak in the rdf for both water hydrogen (H_W) and water oxygen (O_W) is observed. The closer H_W peak indicates hydrogen bonds between water and the carboxylate O atoms. However, no preferred orientation is apparent around the N atoms in the ring (Fig. 7). The smooth rise of $g(r)$ from 0 to 1 at a distance of $\sim 4 \text{ \AA}$ indicates a shielding on the N atoms by the shear volume of the neighboring macrocyclic C and H atoms and there is essentially no difference between H_W and O_W distribution. The “second coordination shell” is clearly not a complete shell covering the whole surface of the complex but there is a number of water molecules (2 to 8) bound to functional groups of the ligand.

The average lifetime of water molecules in the second coordination shell can be obtained from the MD simulation and was found to be in the range of 20–25 ps for the poly(amino-carboxylate) complexes and 56 ps for the polyamino-phosphonate based $[\text{Gd}(\text{DOTP})]^{5-}$ [97]. These residence times are long if compared to those of second sphere water around the aqua ions of lan-

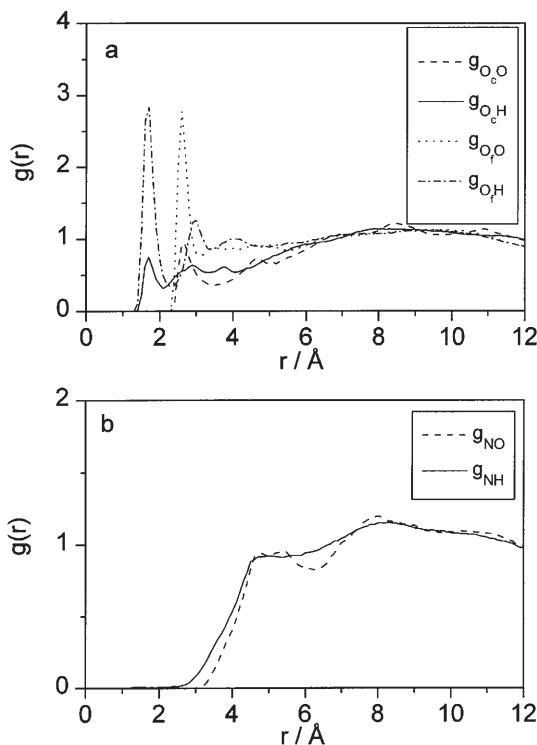


Fig. 7. The rdf around carboxylate O atoms (top) and N atoms (bottom) of $[\text{Gd}(\text{teta})]^-$. A distinction is made between O atoms bonded to the metal ion (O_c) and free O atoms (O_f)

thanide ions (~ 12 to 18 ps [99]) but they are short if compared to water around the inert $[\text{Cr}(\text{H}_2\text{O})_6]^{3+}$ complex (>120 ps [100]).

The MD simulations show that second shell water molecules exist and are distinct from freely diffusing bulk water. Freed's analytical force-free model can only be applied to water molecules without interacting force relative to the Gd-complex, it should therefore be restricted to water molecules without hydrogen bonds formed. Freed's general model [91, 92] allows the calculation of NMRD profiles if the radial distribution function $g(r)$ is known and if the fluctuation of the water-proton – Gd vector can be described by a translational motion. The potential of mean force in Eq. 24 is obtained from $U(r) = -k_B T \ln[g(r)]$ and the spectral density functions have to be calculated numerically [91, 97].

Gd-complexes of TETA and DOTP have no inner sphere water molecule and therefore the NMRD profiles reflect directly the second- and outer-sphere relaxivity accessible also from calculations based on the molecular dynamics simulations (Fig. 8). The experimental NMRD profile of $[\text{Gd}(\text{TETA})]^-$ could be reproduced by drastically changing the electronic relaxation parameters from those

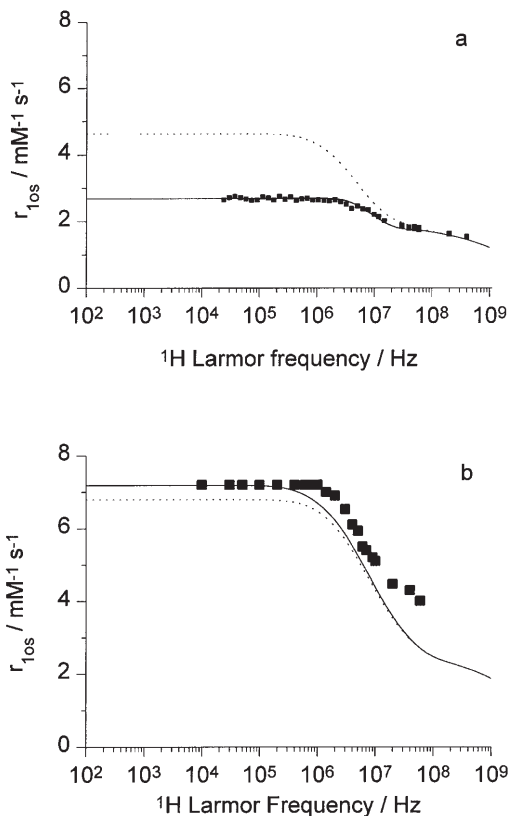


Fig. 8. NMRD profile of $[\text{Gd}(\text{teta})]^-$ (top) and $[\text{Gd}(\text{dotp})]^{5-}$ (bottom); \cdots , profiles incorporating the electron relaxation parameters determined by Powell et al. for $[\text{Gd}(\text{dota})(\text{H}_2\text{O})]^-$

of $[\text{Gd}(\text{DOTA})(\text{H}_2\text{O})]^-$. EPR measurements indicate that the electron spin relaxation of $[\text{Gd}(\text{TETA})]^-$ is indeed extremely fast, with a linewidth ten times as high as the DOTA complex. This shows that using a chemically similar chelating ligand (TETA versus DOTA) to estimate the non-inner sphere relaxivity can be dangerous. The NMRD profile calculated for $[\text{Gd}(\text{DOTP})]^{5-}$ at low magnetic field is only 6% too low compared to the experimental one from Aime et al. [94]. At higher magnetic fields deviations become more systematic. This discrepancy can originate from the inadequacy of the model of relaxation through translational diffusion [97]. The residence time observed for this complex (56 ps) is no longer negligible with respect to the usual rotational correlation time of such complexes (60–80 ps [41]). Thus a purely translational diffusive motion might not be strictly valid in this case.

4

Relaxivity and NMRD Profiles

Measuring the relaxation rates of an abundant nucleus in a large magnetic field range is called relaxometry. A relaxometry profile is a plot of nuclear magnetic relaxation rates, usually $1/T_1$, as a function of the Larmor frequency or the magnetic field on a logarithmic scale (Figs. 8, 9). This plot is also called a Nuclear Magnetic Relaxation Dispersion (NMRD) curve. Whereas the measurement of relaxation rates is a routine task at higher magnetic fields (>1 MHz proton Larmor frequency, 0.023 T), at lower fields the dramatic decrease in sensitivity sets a practical limit. NMRD profiles of paramagnetic solutions show, however, very often interesting features at frequencies below 1 MHz. This led to the development of a special experimental technique using fast cycling of the magnetic field [101–103].

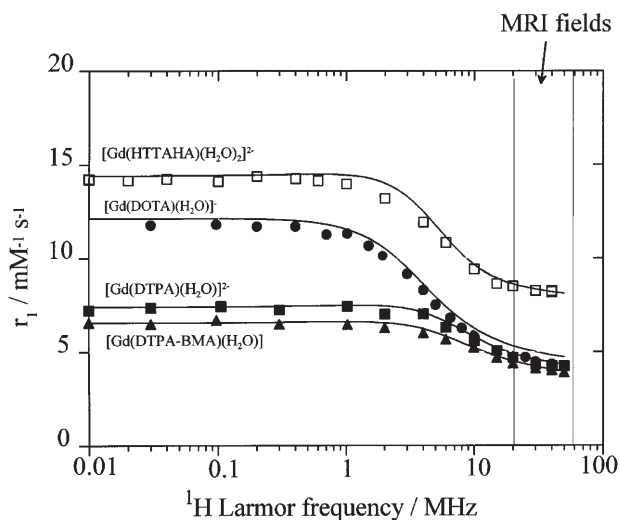


Fig. 9. Typical NMRD profiles of low molecular weight Gd(III) complexes

4.1

Analysis of NMRD Profiles

Proton relaxivities are influenced by numerous physical-chemical parameters. NMRD can be of great help in determining these parameters and indeed has played a central role in the development of our understanding of proton relaxivity. However, the underlying complexity represents an important drawback: the many influencing parameters can be ill-defined by the – sometimes featureless – NMRD curves. In certain cases it is possible to separate these parameters to some extent, since they affect the profile at different magnetic fields. For instance, electronic relaxation usually dominates inner sphere relaxivity at low field, whereas rotation becomes more significant at higher fields. However, an accurate interpretation of NMRD profiles can only be made by reference to independent information from other techniques. EPR and ^{17}O NMR have proved useful as probes for a number of the parameters of importance to proton relaxivity. EPR line widths give direct access to transverse electronic relaxation rates. ^{17}O NMR relaxation rates and chemical shifts permit estimates of the number of inner sphere water molecules, the rotational correlation time, the longitudinal electronic relaxation rate, and most importantly, this technique allows accurate determination of the water exchange rate. Since the results of the three techniques, EPR, ^{17}O NMR and NMRD, are influenced by a number of common parameters, in some cases (mainly for low molecular weight chelates) it is reasonable to subject them to a simultaneous least-squares fitting procedure [41]. This will allow a more reliable determination of the set of parameters governing proton relaxivity, provide a more stringent test of the relaxation theories applied to the three techniques, and permit a validation of current models for the dynamics in paramagnetic solutions.

Variable temperature data can be useful, and assuming physically reasonable exponential or Eyring behaviour for the different correlation times, rather than fitting independent values at each temperature has also proved helpful in the analysis. The temperature dependence of the NMRD profiles gives some indication on what parameter limits the relaxivity, especially at high fields. Rotation and water exchange, the two main limiting parameters, lead to opposite temperature behaviour of the relaxivity: when rotation is the principal factor governing relaxivity, the r_1 values decrease with increasing temperature, whereas an exchange limitation results in an opposite temperature effect.

4.2

Relaxivity of Low Molecular Weight Gd(III) Complexes

NMRD profiles of low molecular weight Gd(III) complexes with one inner sphere water can be typified by that of the commercialized agents, $[\text{Gd}(\text{DTPA})(\text{H}_2\text{O})]^{2-}$, $[\text{Gd}(\text{DTPA-BMA})(\text{H}_2\text{O})]$ or $[\text{Gd}(\text{DOTA})(\text{H}_2\text{O})]^-$ and have the general form as shown in Fig. 9. For these low molecular weight agents, the relaxivity is limited by fast rotation, especially at high frequencies (>10 MHz). As a consequence, the high field relaxivities of the three agents are practically the same, since their rotational correlation time is also very similar. According-

ly, the one order of magnitude lower water exchange rate of $[\text{Gd}(\text{DTPA-BMA})(\text{H}_2\text{O})]$ has no influence on the high field relaxivities. The different low field relaxivities reflect the remarkably slower electronic relaxation of the symmetric $[\text{Gd}(\text{DOTA})(\text{H}_2\text{O})]^-$ as compared to the linear chelates, which has no more influence at higher fields due to the dispersion of the electronic relaxation term. The inner and outer sphere relaxivity terms contribute more or less to the same extent to the overall effect. Consequently, doubling the inner sphere contribution by using a bishydrated chelate such as $[\text{Gd}(\text{TTAHA})(\text{H}_2\text{O})_2]^{2-}$, one increases the overall relaxivity by 50% (Fig. 9).

4.3

Relaxivity of Macromolecular Gd(III) Complexes

Macromolecular Gd(III) chelates are widely investigated as MRI contrast agents. In addition to the potential increase in relaxivity due to their slower rotation, they have an extended lifetime in the blood pool allowing for magnetic resonance angiography applications. Several approaches have been tested to increase the molecular weight. Generally, two main groups of macromolecular agents are distinguished based on the covalent or non-covalent nature of the binding between the monomeric agent and the macromolecule. Covalent binding may involve conjugation of functionalized Gd(III) chelates to polymers, dendrimers, or biological molecules, or synthesis of poly(amino carboxylate) containing copolymers. Non-covalent binding is first of all represented by protein-bound chelates.

When the rotation of the Gd(III) chelate is substantially slowed down, one observes the typical “high field” peak around 20–60 MHz in the NMRD profiles. As an example, Fig. 10 shows the effect of non-covalent protein binding on the relaxivity: under the experimental conditions applied, the small molecular weight chelate MP2269 is totally bound to bovine serum albumin which results in an increase in the rotational correlation time, and consequently in proton relaxivity [50].

For several macromolecular systems, the increase in proton relaxivity was much less than expected solely on the basis of the increased molecular weight, due to their internal flexibility. Typical examples can be taken from linear polymers [77, 78]. Dendrimers are more rigid systems, with the additional advantage of being almost monodisperse, which can be a great advantage for biomedical applications [104]. Gd(III) chelates can be conjugated to the surface groups of the molecule, whose number is increasing with increasing generation. For their relaxivity, a key issue – beside the sufficiently rapid water exchange – is the right choice of the linker group between the macromolecule and the Gd(III) complex. This has to be rigid enough so that the slow rotation of the rigid dendrimer molecule is transmitted to the surface chelate itself. Relaxivities up to $36 \text{ mM}^{-1} \text{ s}^{-1}$ (20 MHz; 23 °C) have been reported for dendrimeric Gd(III) complexes [105].

The analysis of ^{17}O NMR and NMRD data on Gd(DO3A-monoamide) functionalized dendrimers (generations 5, 4 and 3) as well as on Gadomer 17 has shown that, beside fast rotation, slow water exchange also limits proton relaxivity [43, 106]. These results show that high molecular weight complexes like these

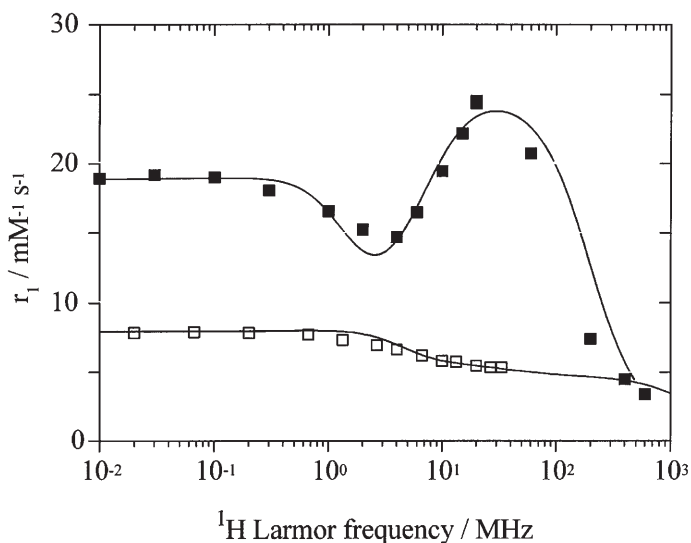


Fig. 10. Effect of non-covalent protein binding on proton relaxivity: NMRD profiles obtained for the small molecular weight Gd(III) complex, MP2269 (empty squares) and for its fully bound protein adduct (filled squares) at $t = 37^\circ\text{C}$. The high field peak in the NMRD profile of the protein-bound chelate is the consequence of slow rotation

dendrimers have rotational correlation times that are long enough for the water exchange to influence the overall relaxivity. Therefore, beside slowing down rotation, a further improvement in the efficiency of the contrast agents can only be achieved with higher water exchange rates.

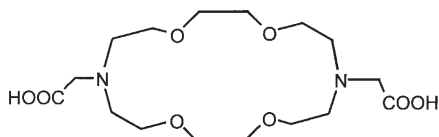
5

Comparison of Gd(III) and Eu(II) Complexes in Relation to MRI

Eu(II) has seven unpaired electrons in an ^8S ground state, thus it is isoelectronic with Gd(III). There are two main aspects which have recently prompted the studies on Eu(II) chelates in relation to MRI contrast agents. The first is the interest in $\text{Eu}^{\text{III}}/\text{Eu}^{\text{II}}$ systems as potential redox responsive relaxometric probes. Current developments in MRI aim the visualization of the physical-chemical state of tissues. The oxygen partial pressure, $p\text{O}_2$, is particularly significant in metabolic processes of cells as well as in many pathologies (ischemic diseases, strokes, tumours). The simplest design of a $p\text{O}_2$ responsive, MRI contrast agent is based on metal complexes whose metal ion can be reduced or oxidized depending on the biological environment, and the two oxidation forms have different relaxation properties. Thus the two redox states influence the proton relaxation of the surrounding protons in a different extent, resulting in different image intensities. The adducts formed between $\text{Mn}^{\text{III}}/\text{Mn}^{\text{II}}$ tpps complexes and poly- β -cyclodextrine have been recently reported to have considerably different

relaxivities depending on the redox state of the metal, itself determined by the partial oxygen pressure of the solution [107] (tpps = 5,10,15,20-tetrakis-(p-sulfonatophenyl porphinate). The $\text{Eu}^{\text{III}}/\text{Eu}^{\text{II}}$ system can also be considered as a candidate for imaging the redox state of the biological environment, since for Eu^{II} , being isoelectronic with Gd^{III} , one can expect relatively high proton relaxivities, whereas Eu^{III} is a very poor relaxing agent.

Eu^{II} complexes also offer a good possibility to investigate the effect of large changes in water exchange and electronic relaxation on the proton relaxivity in comparison to the corresponding Gd^{III} analogues. Indeed, it is rather difficult to considerably increase water exchange rate, or even more problematic to substantially influence electron spin relaxation on Gd^{III} poly(amino carboxylates). Substituting the metal to a fast exchanging one with modified electronic properties can provide valuable information in this respect. For example, it has been proposed for Gd^{III} compounds with long rotational correlation times that electronic relaxation may become a limiting factor for proton relaxivity at medium fields (20 MHz). So far, this has not been observed for $\text{Gd}(\text{III})$ chelates. Studying the analogous europium(II) complexes can help better understand the different mechanisms governing proton relaxivity of paramagnetic metal complexes in general, and in particular design more efficient contrast agents for medical MRI. With these perspectives in mind, some Eu^{II} poly(amino carboxylate) complexes have been recently investigated and compared to the Gd^{III} analogues [108–111]. The ligands studied involve DTPA and DOTA, the chelating agents of two commercial contrast media, as well as some other macrocyclic compounds.



Scheme 7

ODDA

The control of the Eu^{II} redox stability is certainly a key issue for an eventual MRI contrast agent application. With the exception of cryptate complexes of Eu^{II} such as $\text{Eu}^{\text{II}}(2.2.2)^{2+}$ and $\text{Eu}^{\text{II}}(2.2.1)^{2+}$, the complexation with poly(amino carboxylates) diminishes the redox stability of the Eu^{II} state, as compared to the aqua ion (some representative redox potentials are: -0.63 V ($\text{Eu}(\text{H}_2\text{O})_8^{2+}$); -0.21 V ($\text{Eu}(2.2.2)^{2+}$); -0.82 V (EuODDA); -1.00 V (EuTETA^{2-}); -1.18 V (EuDOTA^{2-}); -1.35 V (EuDTPA^{3-})) [111, 112]. Macrocyclic ligands that match in size with the larger Eu^{II} ion have a stabilizing effect of the reduced state, whereas carboxylate coordinating groups seem to be unfavorable in this respect.

On the Eu^{II} aqua ion $[\text{Eu}(\text{H}_2\text{O})_8]^{2+}$ itself, similarly to $[\text{Gd}(\text{H}_2\text{O})_8]^{3+}$, the water exchange is a limiting associative process, and has the highest rate ever measured by magnetic resonance (Table 4). Chelation of Gd^{III} by poly(amino carboxylates) usually results in a substantial decrease in the water exchange rate accompanied by a changeover of the mechanism. Contrary to this, the water exchange on nine-coordinate Eu^{II} poly(amino carboxylates) is only slightly

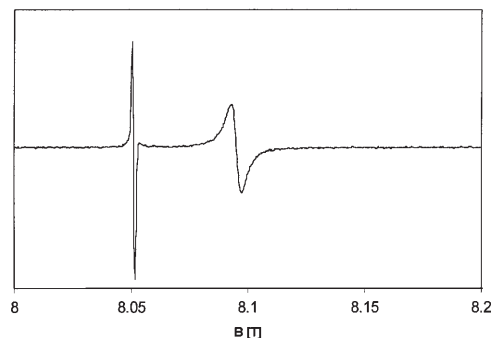
Table 4. Water exchange rates and activation volumes of Eu(II) complexes in comparison to the Gd(III) analogue compounds. All values have been obtained from variable temperature ^{17}O NMR data

	$k_{\text{ex}}^{298}/10^9 \text{ s}^{-1}$	$\Delta V^\ddagger/\text{cm}^3 \text{ mol}^{-1}$	Mechanism	Ref.
$\text{Gd}(\text{H}_2\text{O})_8^{3+}$	0.8	-3.3	I_a	41
$[\text{Gd}(\text{DTPA})(\text{H}_2\text{O})]^{2-}$	0.0033	+12.5	D	41
$[\text{Gd}(\text{DOTA})(\text{H}_2\text{O})]^-$	0.0041	+10.5	D	41
$[\text{Gd}(\text{ODDA})(\text{H}_2\text{O})]^+$	0.0093	0.0	I	115
$[\text{Eu}^{\text{II}}(\text{H}_2\text{O})_8]^{2+}$	4.4	-11.3	A	108
$[\text{Eu}^{\text{II}}(\text{DTPA})(\text{H}_2\text{O})]^{3-}$	1.3	+4.5	I_d	109
$[\text{Eu}^{\text{II}}(\text{DOTA})(\text{H}_2\text{O})]^{2-}$	2.4	-	-	115
$[\text{Eu}^{\text{II}}(\text{ODDA})(\text{H}_2\text{O})]$	0.43	-3.9	I_a	110

slowed down as compared to the Eu^{II} aqua ion. Due to the lower charge and larger ionic radius, the charge density is significantly smaller on Eu^{II} than on Gd^{III} . In a dissociatively activated exchange, the rate determining dissociation of the metal – water O bond will be much easier for a metal with low charge density such as Eu^{II} . The longer metal – coordinated water distance in Eu^{II} chelates (evidenced by X-ray structures) is also favorable for the fast water exchange. Interestingly, on the nine-coordinate $[\text{Eu}^{\text{II}}(\text{ODDA})(\text{H}_2\text{O})]$ the water exchange proceeds via an associatively activated interchange (I_a) mechanism. The crystal structures show that the water coordinating site, located on the hydrophobic side of the complex, is much more open in the ODDA than e.g. in the DTPA complex, thus $[\text{Eu}^{\text{II}}(\text{ODDA})(\text{H}_2\text{O})]$ can accommodate a second water molecule in the inner sphere without the preceding departure of the leaving water molecule, which leads to an associative activation mode. In general, the water exchange rate on Eu^{II} complexes is in the optimal range to attain maximum relaxivities according to the simulations (Fig. 2), provided the rotation of the molecule is also controlled by using rigid macromolecules.

The other parameter which influences proton relaxivity and which can be considerably different for Eu^{II} and Gd^{III} is electron spin relaxation. In contrast to Gd^{III} , the EPR spectra of Eu^{II} show hyperfine coupling with the two Eu nuclei of a nuclear spin of 5/2. The hyperfine structure becomes more apparent at high frequencies as shown in Fig. 11. In the case of Gd^{III} , no hyperfine structure is observed even at high magnetic field, since the two isotopes with non-zero nuclear spin have relatively low γ and low abundance. For the Eu^{II} poly(amino carboxylate) complexes studied the linewidths are considerably larger than for the aqua ion, indicating a higher electron spin relaxation rate. Based on the few examples studied so far, it seems that the formation of Eu^{II} poly(amino carboxylate) complexes results in faster electronic relaxation as compared to the aqua ion. It is in contrast to Gd^{III} chelates, where, in general, electron spin relaxation is slower on the complexes than on the aqua ion itself (at least at magnetic fields important for magnetic resonance imaging).

^{155}Gd	$I = 3/2$	14.7 %	$\gamma = -0.83 \times 10^7 \text{ T}^{-1}\text{s}^{-1}$
^{157}Gd	$I = 3/2$	15.7 %	$\gamma = -1.08 \times 10^7 \text{ T}^{-1}\text{s}^{-1}$
$^{154}\text{Gd}, ^{156}\text{Gd}, ^{158}\text{Gd}, ^{160}\text{Gd}$		$I = 0$	69.6 %



^{151}Eu	$I = 5/2$	47.82%	$\gamma = 6.55 \times 10^7 \text{ T}^{-1}\text{s}^{-1}$
^{153}Eu	$I = 5/2$	52.18%	$\gamma = 2.94 \times 10^7 \text{ T}^{-1}\text{s}^{-1}$

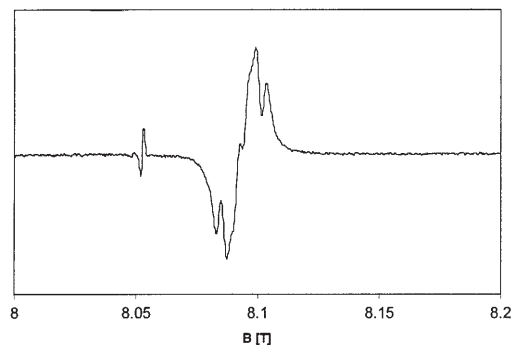


Fig. 11. Typical high frequency (225 GHz, 8.1 T) EPR spectra of $[\text{Gd}(\text{H}_2\text{O})_8]^{3+}$ ($c = 0.080 \text{ M}$) and $[\text{Eu}(\text{H}_2\text{O})_8]^{2+}$ ($c = 0.176 \text{ M}$). The low field peak belongs to a,g-bisdiphenylene-b-phenylal-lyl, used as g factor reference

The proton relaxivity of Eu^{II} and Gd^{III} complexes also reflects the differences in water exchange and electronic relaxation. It is well known that for the Gd^{III} aqua ion and for monomer Gd^{III} poly(amino carboxylates) fast rotation limits proton relaxivity at imaging fields (20–60 MHz proton Larmor frequency). The analysis of the NMRD profiles of the Eu^{II} aqua ion (Fig. 12) revealed that beside rotation (as for $[\text{Gd}(\text{H}_2\text{O})_8]^{3+}$), fast water exchange, which is already faster than the optimal value (see Fig. 2) also becomes a limiting parameter. For the Eu^{II} chelates, the water exchange rate is in the optimal range to obtain maximum relaxivities. Since these are low molecular weight chelates, the limiting factor is fast rotation. However, for $[\text{Eu}^{\text{II}}(\text{DTPA})(\text{H}_2\text{O})]^{3-}$, fast electronic relaxation also limits proton relaxivity, even at imaging fields (20–60 MHz). By increasing the rotational correlation time, the limiting effect of electronic relaxation would evidently become much more important. This could mean that fast electron spin

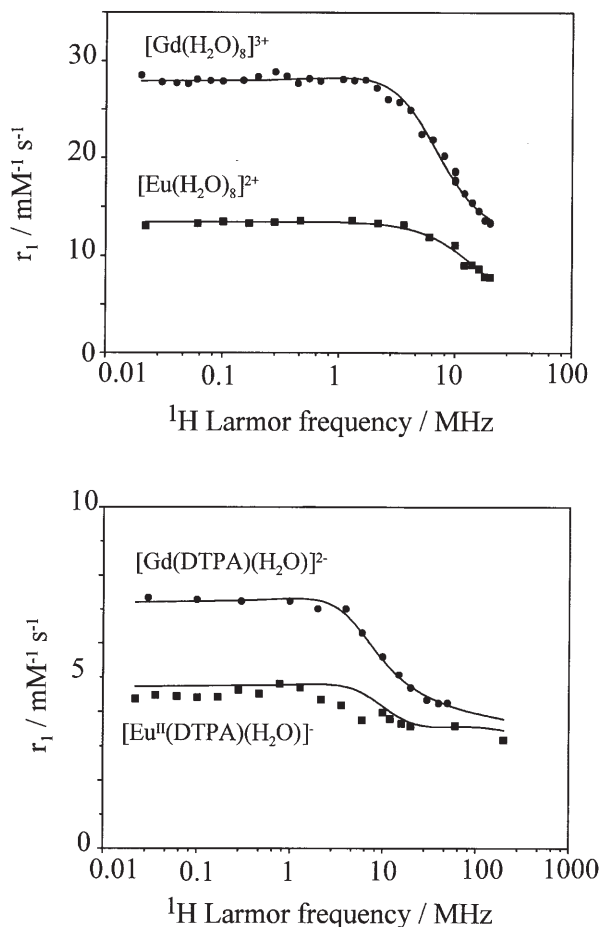


Fig. 12. Comparison of NMRD profiles for Eu^{II} and Gd^{III} complexes. $T = 298 \text{ K}$

relaxation can be an obstacle to the potential application of Eu^{II} chelates as contrast agents in magnetic resonance imaging. However, preliminary EPR experiments on other Eu^{II} complexes indicate that this unfavourable property is not general.

At the present stage, the *in vivo* applicability of Eu^{II} complexes as MRI redox reporters remains questionable, mainly due to the difficulties in controlling the reduced state. Efforts are focused on the synthesis of new water soluble macrocyclic ligands with matching cavity size for Eu^{2+} in order to ensure high thermodynamic and redox stability of the Eu^{II} chelate.

6

Conclusions

The proton relaxivity, thus the efficiency of Gd(III) based MRI contrast agents is influenced by a large number of parameters. The development of high relaxivity contrast agents requires the simultaneous control and optimization of all these parameters, most importantly the optimization of water (proton) exchange rate and rotation, the two factors that limit relaxivity of current contrast agents. The knowledge accumulated in this area during the recent years gives us hope to be able to increase water exchange rate by appropriate modification of the chelates which also ensure non-toxicity, as well as to increase rotational correlation time by using rigid macromolecules. Our understanding of the electron spin relaxation and of the second and outer sphere relaxation mechanisms will also contribute to the design of more powerful MRI contrast agents.

Acknowledgement. The authors are grateful to the Swiss National Science Foundation and the Office for Education and Science (OFES) for their financial support. The work discussed here was partly carried out in the frame of the EC COST D18 Action "Lanthanide Complexes in Biology and Medicine".

7

References

1. Muller RN, Roch A, Colet J-M, Ouakssim A, Gillis P (2001) Particulate Magnetic Contrast Agents. In: Merbach AE, Toth E (eds) *The Chemistry of Contrast Agents in Medical Magnetic Resonance Imaging*. Wiley, Chichester, p 417
2. Kauczor H, Surkau R, Roberts T (1998) *Eur. Radiology* 8:820
3. Bloembergen N, Purcell EM, Pound RV (1948) *Phys Rev* 73:678
4. Solomon I (1955) *Phys Rev* 99:559
5. Solomon I, Bloembergen N (1956) *J Chem Phys* 25:261
6. Bloembergen N (1957) *J Chem Phys* 27:572
7. Bloembergen N, Morgan LO (1961) *J Chem Phys* 34:842
8. Connick RE, Fiat DJ (1966) *Chem Phys* 44:4103
9. Botta M (2000) *Eur J Inorg Chem* 399
10. Swift TJ, Connick RE (1962) *J Chem Phys* 37:307
11. Luz Z, Meiboom S (1964) *J Chem Phys* 40:2686
12. McLachlan AD (1964) *Proc R Soc London A* 280:271
13. Kowalewski J, Nordenskiöld L, Benetis N, Westlund P-O (1985) *Progr NMR Spectrosc* 17:141
14. Kowalewski J (1996) In: Grant DM, Harris RK (eds) *Encyclopedia of NMR* Wiley, Chichester, p 3456
15. Horrocks WD Jr, Sudnick DR (1979) *J Am Chem Soc* 101:334
16. Parker D, Williams JAG (1996) *J Chem Soc Dalton Trans* 3613
17. Alpoim MC, Urbano AM, Geraldes CFGC, Peters JA (1992) *J Chem Soc Dalton Trans* 463
18. Graeppi N, Powell DH, Laurenczy G, Zékány L, Merbach AE (1994) *Inorg Chim Acta* 235:311
19. Tóth É, Ni Dhubhghaill OM, Besson G, Helm L, Merbach AE (1999) *Magn Res Chem* 37:701
20. Yerly F, Dunand FA, Tóth É, Figueirinha A, Kovács Z, Sherry AD, Geraldes CFGC, Merbach AE (2000) *Eur J Inorg Chem* 1001

21. Merbach AE, Toth E (2001) (eds) *The Chemistry of Contrast Agents in Medical Magnetic Resonance Imaging*. John Wiley & Sons, Chichester
22. Bénazeth S, Purans J, Chalbot MC, Nguyen-van-Duong MK, Nicolas L, Keller F, Gaudemer A (1998) *Inorg Chem* 37:3667
23. Clarkson RB, Hwang JH, Belford RL (1993) *Magn Res Med* 29:521
24. Steele ML, Wertz DL (1976) *J Am Chem Soc* 98:4424
25. Yamaguchi T, Nomura M, Wakita H, Ohtaki H (1988) *J Chem Phys* 89:5153
26. Cossy C, Barnes A, Enderby JE, Merbach AE (1989) *J Chem Phys* 90:3254
27. Cossy C, Helm L, Powell DH, Merbach AE (1995) *New J Chem* 19:27
28. Aime S, Barge A, Botta M, Parker D, De Sousa AS (1997) *J Am Chem Soc* 119:4767
29. Aime S, Botta M, Fasano M, Paoletti S, Terreno E (1997) *Chem Eur J* 3:1499
30. Micskei K, Helm L, Brücher E, Merbach AE (1993) *Inorg Chem* 32:3844
31. Lincoln SF, Merbach AE (1995) *Adv Inorg Chem* 42:1
32. Cossy C, Helm L, Merbach AE (1989) *Inorg Chem* 28:2699
33. Cossy C, Helm L, Merbach AE (1988) *Inorg Chem* 27:1973
34. Peters JA (1988) *Inorg Chem* 27:4686
35. Rizkalla EM, Choppin GR, Cacheris W (1993) *Inorg Chem* 32:582
36. Geraldies CFGC, Sherry AD, Cacheris WP, Kuan K-T, Brown RD III, Koenig SH, Spiller M (1988) *Magn Res Med* 8:191
37. Gonzalez G, Powell DH, Tissières V, Merbach AE (1994) *J Phys Chem* 98:53
38. Lammers H, Maton F, Pubanz D, Van Laren MW, Van Bekkum H, Merbach AE, Muller RN, Peters JA (1997) *Inorg Chem* 36:2527
39. Tóth É, Connac F, Helm L, Adzamli K, Merbach AE (1998) *Eur J Inorg Chem* 2017
40. Tóth É, Burai L, Brücher E, Merbach AE (1997) *J Chem Soc Dalton Trans* 1587
41. Powell HD, Ni Dhubbghaill OM, Pubanz D, Helm L, Lebedev Y, Schlaepfer W, Merbach AE (1996) *J Am Chem Soc* 118:9333
42. Tóth É, Vauthey S, Pubanz D, Merbach AE (1996) *Inorg Chem* 35:3375
43. Tóth É, Pubanz D, Vauthey S, Helm L, Merbach AE (1996) *Chem Eur J* 2:1607
44. Gries H, Miklautz H (1984) *Physiol Chem Phys Med NMR* 16:105
45. Bligh SWA, Chowdhury AHMS, McPartlin M, Scowen IJ, Bulman RA (1995) *Polyhedron* 14:567
46. Pubanz D, Gonzalez G, Powell DH, Merbach AE (1995) *Inorg Chem* 34:4447
47. André JP, Maecke HR, Tóth É, Merbach AE (1999) *J Biol Inorg Chem* 4:341
48. Szilágyi E, Tóth É, Brücher E, Merbach AE (1999) *J Chem Soc Dalton Trans* 2481
49. Aime S, Crich SG, Gianolio E, Terreno E, Beltrami A, Uggeri F (1998) *Eur J Inorg Chem* 1283
50. Tóth É, Connac F, Helm L, Adzamli K, Merbach AE (1998) *J Biol Inorg Chem* 3:606
51. Aime S, Barge A, Borel A, Botta M, Chemerisov S, Merbach AE, Muller RN, Pubanz D (1997) *Inorg Chem* 36:5104
52. Ruloff R, Muller RN, Pubanz D, Merbach AE (1998) *Inorg Chim Acta* 275–276:15
53. Aime S, Botta M, Crich SG, Giovenzana G, Pagliarin R, Piccinini M, Sisti M, Terreno E (1997) *J Biol Inorg Chem* 2:470
54. Aime S, Botta M, Crich SG, Giovenzana G, Pagliarin R, Sisti M, Terreno E, (1998) *Magn Res Chem* 36:S200
55. Micskei K, Powell DH, Helm L, Brücher E, Merbach AE (1993) *Magn Res Chem* 31:1011
56. Tóth É, Helm L, Merbach AE, Hedinger R, Hegetschweiler K, Jánossy A, (1998) *Inorg Chem* 37:4104
57. (a) Kubo RJ (1954) *Phys Soc Jpn* 9:888
(b) Sack RA (1958) *Mol Phys* 1:163
(c) Reeves LW, Shaw KN (1970) *Can J Chem* 48:3641
58. Aime S, Barge A, Bruce JI, Botta M, Howard JAK, Moloney JM, Parker D, De Sousa AS, Woods M (1999) *J Am Chem Soc* 121:5762
59. Dunand AF, Aime S, Merbach AE (2000) *J Am Chem Soc* 122:1506
60. Tóth É, van Uffelen I, Helm L, Merbach AE, Ladd D, Briley-Saebo K, Kellar KE (1998) *Magn Res Chem* 36:S125

61. Tóth É, Helm L, Kellar KE, Merbach AE (1999) *Chem Eu J* 5:1202
62. Dunand F, Tóth É, Hollister R, Merbach AE (2001) *J Biol Inorg Chem* 6:247
63. André JP, Tóth É, Maecke HR, Merbach AE (1999) *Chem Eur J* 5:2977
64. Muller RN, Radüchel B, Laurent S, Platzek J, Pierart C, Mareski P, Vander Elst L (1999) *Eur J Inorg Chem* 1949
65. Aime S, Chiaussa M, Digilio G, Gianolio E, Terreno E (1999) *J Biol Inorg Chem* 4:766
66. Aime S, Barge A, Botta M, Howard JAK, Kataký R, Lowe MP, Moloney JM, Parker D, de Sousa AS (1999) *Chem Commun* 1047
67. Aime S, Botta M, Fasano M, Terreno E (1999) *Accounts of Chem Res* 32:941
68. Halle B, Wennerstrom H (1981) *J Magn Res* 44:89
69. Banci L, Bertini I, Luchinat C (1991) in *Nuclear and Electron Relaxation VCH, Weinheim*, p. 95.
70. Vander Elst L, Maton F, Laurent S, Seghi F, Chapelle F, Muller RN (1997) *Magn Reson Med* 38:604
71. Aime S, Nano R (1998) *Invest Radiol* 23:S264
72. Vander Elst L, Laurent S, Muller RN (1998) *Invest Radiol* 33:828
73. Chen JW, Auteri FP, Budil DE, Belford RL, Clarkson RB (1994) *J Phys Chem* 98:13452
74. Chen JW, Clarkson RB, Belford RL (1996) *J Phys Chem* 100:8093
75. Wiener EC, Auteri FP, Chen JW, Brechbiel MW, Gansow OA, Schneider DS, Clarkson RB, Lauterbur PC (1996) *J Am Chem Soc* 118:7774
76. Chen JW, Belford RL, Clarkson RB (1998) *J Phys Chem A* 102:2117
77. Vexler VS, Clement O, Schmitt-Willich H, Brasch RC (1994) *J Magn Reson Imaging* 4:381
78. Desser T, Rubin D, Muller H, Qing F, Khodor S, Zanazzi Y, Ladd D, Wellons J, Kellar K, Toner J, Snow R (1994) *J Magn Reson Imaging* 4:467
79. a. Lipari G, Szabo A (1982) *J Am Chem Soc* 104:4546
b. Lipari G, Szabo A (1982) *J Am Chem Soc* 104:4559
80. Hudson A, Lewis LWE (1970) *Trans Faraday Soc* 66:1297.
81. Powell DH, Merbach AE, González G, Brücher E, Ottaviani MF, Köhler K, von Zelewsky A, Grinberg OY, Lebedev YS (1993) *Helv Chim Acta* 76:2129
82. Poupko R, Baram A, Luz Z (1974) *Mol Phys* 27:1345
83. Strandberg E, Westlund P-O (1996) *J Mag Reson A* 122:179
84. Borel A, Tóth É, Helm L, Jánosy A, Merbach AE (2000) *Phys Chem Chem Phys* 2:1311
85. Clarkson RB, Smirnov AI, Smirnova TI, Kang H, Belford RL, Earle K, Freed JH (1998) *Mol Phys* 96:1325
86. Rast S, Fries HP, Belorizky E (2000) *J Chem Phys* 113:8724
87. Rast S, Borel A, Helm L, Belorizky E, Fries HP, Merbach AE (2001) *J Am Chem Soc* 123:2637
88. Abragam A (1961) *The Principles of Nuclear Magnetism*. Oxford University Press, Oxford.
89. Fries PH, Belorizky E (1978) *J Phys (Paris)* 39:1263
90. Albrand JB, Taieb MC, Fries PH, Belorizky E (1983) *J Chem Phys* 78:5809
91. Hwang L-P, Freed JH (1975) *J Chem Phys* 63:1975
92. Freed JH (1978) *J Chem Phys* 68:4034
93. Polnaszek CF, Bryant RG (1984) *J Chem Phys* 81:4038
94. Aime S, Botta M, Terreno E, Anelli PL, Uggeri F (1993) *Magn Reson Med* 30:583
95. Aime S, Botta M, Crich SG, Giovenzana G, Pagliarin R, Piccinini M, Sisti M, Terreno E (1997) *J Biol Inorg Chem* 2:470
96. Chen JW, Belford RL, Clarkson RB (1998) *J Phys Chem A* 102:2117
97. Borel A, Helm L, Merbach AE (2001) *Chem Eur J* 7:600
98. Besler BH, Merz KMJ, Kollman PA (1990) *J Comput Chem* 11:431
99. Kowall T, Foglia F, Helm L, Merbach AE (1996) *Chem Eur J* 2:285
100. Bleuzen A, Foglia F, Furet E, Helm L, Merbach AE, Weber J (1996) *J Am Chem Soc* 118:12777
101. Noack F (1986) *Prog Nucl Magn Reson Spectrosc* 18:171
102. Koenig SH, Brown RD (1990) *Prog Nucl Magn Reson Spectrosc* 22:487

103. Kimmich R (1997) NMR Tomography, Diffusometry, Relaxometry, Springer, Berlin
104. Zeng F, Zimmerman SC (1997) Chem Rev 97:1681
105. Bryant LH Jr, Brechbiel MW, Wu C, Bulte JWM, Herynek V, Frank JA (1999) J Magn Reson Imaging 9:348
106. Nicolle G, Tóth É, Schmitt-Willich H, Sülzle D, Radüchel B, Merbach AE, *submitted*.
107. Aime S, Botta M, Gianolio E, Terreno E (2000) Angew Chem Int Ed 39:747
108. Caravan P, Tóth É, Rockenbauer A, Merbach AE (1999) J Am Chem Soc 121:10403
109. Seibig S, Tóth É, Merbach AE (2000) J Am Chem Soc 122:5822
110. Burai L, Tóth É, Seibig S, Scopelliti R, Merbach AE (2000) Chem Eur J 6:3761
111. Tóth É, Burai L, Merbach AE (2001) Coord Chem Rev in press
112. Yee EL, Gansow OA, Weaver MJ (1980) J Am Chem Soc 102:2278
113. Weinmann HJ, Schuhmann-Giampieri G, Schmitt-Willich H, Vogler H, Frenzel T, Gries H (1991) Magn Res Med 22:233
114. Uggeri F, Aime S, Anelli PL, Botta M, Brochetta M, de Haen C, Ermondi G, Grandi M, Paoli P (1995) Inorg Chem 34:633
115. Burai L, personal communication

Kinetic Stabilities of Gadolinium(III) Chelates Used as MRI Contrast Agents

Ernö Brücher

University of Debrecen, Department of Inorganic and Analytical Chemistry, 4010 Debrecen, Hungary

E-mail: ebrucher@delfin.klte.hu

Equilibrium calculations indicate that the Gd^{3+} chelates used as contrast agents in MRI may partly dissociate in the body fluids. However, the results of the kinetic studies point to the proton, Cu^{2+} and Zn^{2+} assisted dissociation of Gd^{3+} complexes being slow at $\text{pH} > 5$. The excretion of these contrast agents from the body is relatively fast so that the system is far from the equilibrium and the extent of in vivo dissociation is very low.

The rate constants, characterizing the dissociation of Gd^{3+} chelates, used to compare the kinetic stabilities, are about 10^3 times lower for the macrocyclic DOTA derivative complexes than for the complexes of the open-chain DTPA derivatives. The rigid structure of ligands is highly important for the inertness of the complexes. The use of functional groups in the ligands, possessing donor atoms of lower basicity (e.g. amide, phosphinate or phosphonate ester), result in significantly lower stability constants, but the kinetic stability of complexes is practically not influenced. Substituents, attached to the diethylenetriamine backbone, increase the kinetic stability of the DTPA derivative complexes.

Keywords. Gadolinium, Contrast agents, Dissociation kinetics, Kinetic stability, Stability constants

1	Introduction	104
2	Chemical Properties of Gd^{3+} Chelates and Tolerance to them	105
2.1	The Ligands Used for the Complexation of Gd^{3+}	105
2.2	Equilibrium Properties and the Toxicity of Contrast Agents	106
3	Kinetic Properties of Gd^{3+} Chelates	110
3.1	Demonstration of Kinetic Stability of Gd^{3+} Chelates	111
3.2	Kinetic Stabilities of Gd^{3+} Complexes with DTPA and its Derivatives	113
3.3	Kinetic Stabilities of Gd^{3+} Complexes of DOTA and DOTA Derivative Ligands	117
4	Conclusions	120
5	References	121

1

Introduction

During the last decade, magnetic resonance imaging (MRI) has become a powerful clinical modality in diagnostic medicine. MRI was initially introduced as a noninvasive diagnostic tool, but certain clinical problems necessitated the use of exogenous materials, called contrast agents (CAs), which increase the difference between the signals of the normal and the diseased tissues. The intensities of MRI signals depend on the proton density and on the longitudinal ($1/T_1$) and transverse relaxation rates ($1/T_2$) of the protons (mainly water protons). The contrast-enhancing agents are paramagnetic compounds, which increase the relaxation rates of protons in the body; the most effective ones of which are Gd^{3+} , Fe^{3+} and Mn^{2+} . These metal ions have a half-filled d^5 (Fe^{3+} and Mn^{2+}) or f^7 (Gd^{3+}) electron shell and relatively long electron spin relaxation times ($\sim 10^{-9}$ s). Since the aqua-metal ions are toxic, they are used in the form of chelate complexes which are well tolerated [1]. In clinical investigations, practically only the chelates of Gd^{3+} are used at present, and we shall therefore limit our discussion to the chemical properties of the complexes of Gd^{3+} . The ligands used for the complexation of Gd^{3+} are the open-chain DTPA, the macrocyclic DOTA and their derivatives (Scheme 1).

The Gd^{3+} chelates used as CAs are administered into the body, and accordingly the requirements for their clinical use are very rigorous. The most important conditions to be met are the lack of toxicity, rapid excretion, high water solubility, a high relaxation effect, high thermodynamic and kinetic stabilities and specific *in vivo* distribution [2].

In recent years, a number of chelate complexes of lanthanides have been proposed for use in other fields of medical diagnosis and therapy. The complexes of Gd^{3+} and some heavier lanthanides with the ligands used as MRI CAs are investigated as potential CAs in radiography [3]. The complexes formed with certain radioactive isotopes, e.g. ^{153}Sm , are used in pain palliation therapy in patients with metastatic bone cancer [4, 5], while the complexes of ^{90}Y , attached to monoclonal antibodies or certain proteins, are proposed for use in the treatment of cancer [5–7].

For the application of lanthanide complexes in medical diagnosis and therapy, a general requirement is that the ion Ln^{3+} and the ligand should remain associated while the complex is in the body, i.e. their dissociation should be minimal, since the free ligand and Ln^{3+} are toxic. For the dissociation to be negligible, the complexes must be kinetically inert under physiological conditions. Since the complexation properties of the lanthanide ions and Y^{3+} are quite similar, it is of interest to compare the results obtained as concerns the kinetic behavior of Gd^{3+} complexes with those known for the complexes of other lanthanides and Y^{3+} .

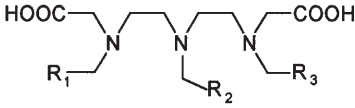
2

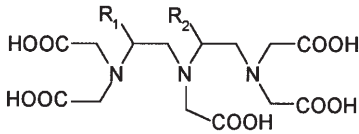
Chemical Properties of Gd^{3+} Chelates and Tolerance to them

2.1

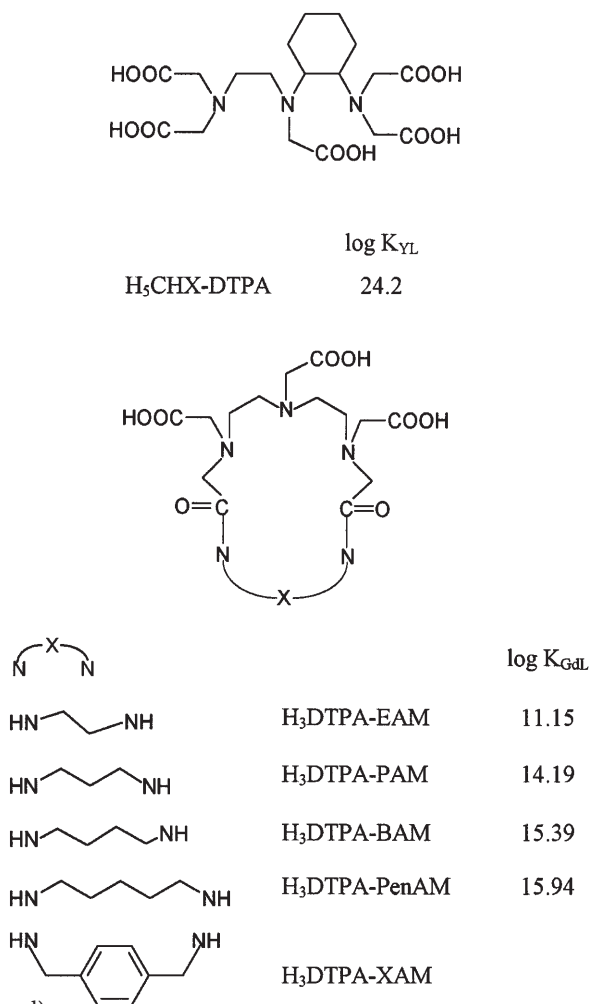
The Ligands Used for the Complexation of Gd^{3+}

As mentioned earlier, for safety reasons the Gd^{3+} chelates used as CAs in MRI must have high thermodynamic and kinetic stabilities. Since the chemical bonds in the complexes of lanthanides are predominantly ionic in nature, highly stable complexes are formed only with multidentate ligands. The ligands (H_nL) used in the commercial and potential CAs are practically all octadentate and all eight of their donor atoms are coordinated to Gd^{3+} [2, 8]. The coordination number of Gd^{3+} in these complexes is 9 and the ninth coordination site being occupied by a water molecule. The protons of this molecule in the first coordination sphere of Gd^{3+} rapidly relax and the fast exchange of this H_2O with the bulk water results in transfer of the paramagnetic effect of Gd^{3+} to the surrounding water protons. The most important ligands used for the complexation of Gd^{3+} are presented in Scheme 1, where the stability constants ($\log K_{GdL}$) are also given ($K_{ML} = [ML]/[M] \cdot [L]$).

			$\log K_{GdL}$
$R_1 = R_2 = R_3 = -COOH$		H_5DTPA	22.46
$R_1 = R_3 = -CONHMe$	$R_2 = -COOH$	$H_3DTPA-BMA$	16.85
$R_1 = R_3 = -CONHCH_2CH_2OMe$	$R_2 = -COOH$	$H_3DTPA-BMEA$	16.84
$R_2 = -CONHMe$	$R_1 = R_3 = -COOH$	$H_4DTPA-N'-MA$	19.94
$R_3 = -CONHMe$	$R_1 = R_2 = -COOH$	$H_4DTPA-N-MA$	19.37

			$\log K_{GdL}$
$R_1 = -BzOEt$	$R_2 = -H$	$H_5EOB-DTPA$	23.46
$R_1 = -BzNO_2$	$R_2 = -H$	$H_5PNP-DTPA$	21.5
$R_1 = -BzNO_2$	$R_2 = -Me$	$H_5PNPM-DTPA$	22.5

Scheme 1. Formulas of the ligands



Scheme 1 (continued)

Under physiological conditions ($\text{pH} = 7.4$) complexes with a 1:1 metal to ligand ratio are present: $\text{GdL}^{(n-3)-}$. At pH values lower than 3–4, protonated complexes GdHL can be formed. The protonation constants (K_{MHL}) of the highly stable complexes are in general low, with $\log K_{\text{GdHL}}$ less than 2.5 ($K_{\text{MHL}} = [\text{MHL}] / [\text{M}] \cdot [\text{H}^+]$).

2.2

Equilibrium Properties and the Toxicity of Contrast Agents

The complex-forming ligands listed in Scheme 1 and also their Gd^{3+} complexes are generally hydrophilic. The exceptions are those ligands and complexes which possess lipophilic groups (e.g. Gd(EOB-DTPA)^{2-} [9, 10], Gd(BOPTA)^{2-}

in order to diminish this problem, neutral CAs with lower osmolalities were also developed (Gd(DTPA-BMA), Gd(HP-DO3A) and Gd(DO3A-Bu)) [8]. The hyper-tonic effect of solutions of CAs is considered to be one of the important factors that results in the toxicity of Gd^{3+} chelates. This is a particularly important factor in animal experiments, when the acute LD_{50} values (the lethal doses causing the death of 50% of the treated animals) are determined by increasing the amount of CAs administered to the animals.

In clinical investigations, the dosage of the CAs is 0.1–0.3 mmol/kg body weight [2, 8]. Since the LD_{50} values in mice and rats are ~ 0.3 – 0.5 mmol/kg for $GdCl_3$, 0.15 mmol/kg for MEG_3H_2DTPA and 10 mmol/kg for $MEG_2[Gd(DTPA)]$ [2], it is clear how important it is that the Gd^{3+} and the ligand remain associated to the maximal extent in the body before excretion. The LD_{50} values also indicate that the presence of free Gd^{3+} and free ligand is probably the most important factor in the toxicity of the CAs. Free Gd^{3+} and free ligand are formed on the dissociation of the Gd^{3+} chelates; high thermodynamic stability and in particular kinetic inertness of the complexes are therefore of the utmost importance.

The high safety of Gd^{3+} -containing compounds plays a crucial role in the widespread use of CAs in MRI investigations. As concern this safety, the high stability constants of Gd^{3+} chelates is an important demand, though attempts to find a relationship between the stability constants and the toxicity of CAs have failed. Studies on acute toxicity have been carried out with animals, when the dosages of CAs used to determine the LD_{50} values were much larger than in clinical human investigations. The results of animal experiments with ^{153}Gd -radio-labeled Gd^{3+} chelates indicated a small amount of residual Gd in the bodies of the animals even 7–14 days after the i.v. injection [14–16]. This retention of Gd^{3+} is a result of the dissociation of Gd^{3+} chelates. The extent of dissociation was found to be larger for the complexes formed with the open-chain DTPA and its derivatives than with the macrocyclic DOTA and its derivatives [15–16]. A few clinical events have also been reported, when the effects of free Gd^{3+} were detected in human investigations [18].

To explain the behavior of Gd^{3+} chelates and for a better understanding of their in vivo fate, it is necessary to know the equilibrium properties of the CAs in the plasma. Since the human plasma is a very complicated system, where a huge number of metal ions and ligands can form complexes of different types, a simplified plasma model must be used in order to approximate to the equilibrium situation, including the speciation of Gd^{3+} .

The in vivo dissociation of Gd^{3+} chelates can result from exchange reactions involving endogenous metal ions and ligands. Cacheris et al. used an eight-component plasma model for biospeciation calculations and found that of the endogenous ions, Zn^{2+} , Cu^{2+} and Ca^{2+} , Zn^{2+} is the most important in effecting the release of Gd^{3+} from its chelates [17]. They assumed that the extent of dissociation of Gd^{3+} chelates is determined by the selectivity of the ligand for Gd^{3+} over Zn^{2+} . The stability constants indicated that the selectivity of the ligand DTPA-BMA ($10^{4.8}$) was significantly higher than that of DTPA ($10^{3.8}$) or EDTA ($10^{0.4}$). This high selectivity of DTPA-BMA presumably plays a decisive role in the safety of Gd(DTPA-BMA) [17]. However, the selectivity values calculated from the experimental data obtained by Puttagunta et al. in a study of the exchange reac-

tions between the Gd^{3+} chelates and Zn^{2+} citrate are significantly lower and unfavorable for DTPA-BMA [18]. The cause of this contradiction is probably the inappropriate nature of the equilibrium model. Cacheris et al. neglected the formation of binuclear complexes [17]. The stability constant of $\text{Zn}_2(\text{DTPA})^-$ is $\log K_{\text{Zn}_2\text{L}} = 4.48$ [19], while that for $\text{Gd}_2(\text{DTPA})^+$ is only $\log K_{\text{Gd}_2\text{L}} = 1.3$ [20]. The octadentate DTPA-BMA presumably also forms a binuclear complex of higher stability with Zn^{2+} (the coordination number of Zn^{2+} is 6, while that of Gd^{3+} in these complexes is 9). The formation of more stable complexes Zn_2L decreases the selectivity of the ligand for Gd^{3+} over Zn^{2+} .

On the basis of a computer model developed with the use of 7 metal ions, 40 ligands and about 5000 complexes [21], Jackson et al. carried out speciation calculations involving Gd^{3+} and the ligand DTPA [22]. The concentration of free Gd^{3+} at pH = 7.4 in the presence of 1×10^{-3} M $\text{Gd}(\text{DTPA})^{2-}$ was as low as 2.4×10^{-13} M. Unfortunately, the concentrations of other Gd^{3+} -containing species were not reported. However, the presence of 1×10^{-3} M $\text{Gd}(\text{DTPA})^{2-}$ resulted in significant alterations in the species distribution of Cu^{2+} , Zn^{2+} and Fe^{3+} , indicating that the concentrations of the citrate, glutamate, threoninate, transferrin and lactate complexes of Gd^{3+} were relatively high [22].

By using a simplified plasma model, in which only the competition between Gd^{3+} and Zn^{2+} was considered, Sarka et al. made a species distribution calculation for the DTPA complexes [20]. The ligands involved in the model have relatively high affinities for Gd^{3+} (0.1 mM) and/or Zn^{2+} (0.05 mM). These ligands were as follows: DTPA (0.1 mM), Gly (representing all the simple α -amino acids, 1.0 mM), Asp (0.07 mM), His (0.08 mM), Cys (0.04 mM), succinate (0.04 mM), lactate (2.0 mM) and citrate (0.1 mM) [21]. In the assumed equilibrium system, 90.7% of Gd^{3+} was in the form $\text{Gd}(\text{DTPA})^{2-}$, and 9.2% as $\text{Gd}(\text{cit})$. For Zn^{2+} , the predominant species were $\text{Zn}(\text{Cys})$ (45.3%), $\text{Zn}(\text{His})$ (17.8%), $\text{Zn}(\text{cit})$ (12.4%), $\text{Zn}(\text{DTPA})^{3-}$ (17.9%) and $\text{Zn}_2(\text{DTPA})$ (1.24%) [20]. These equilibrium data indicate the partial transmetallation of Gd^{3+} from $\text{Gd}(\text{DTPA})^{2-}$ by Zn^{2+} . The displaced Gd^{3+} is present in the form of $\text{Gd}(\text{cit})$. These equilibrium calculations suggest that the amount of Gd^{3+} displaced from $\text{Gd}(\text{DTPA})^{2-}$ would be very large. However, the results of both human and animal biodistribution studies indicate a significantly lower extent of Gd^{3+} displacement. In animal experiments with ^{153}Gd - and ^{14}C -labeled Gd^{3+} complexes, the whole-body retention of ^{153}Gd 7–14 days after the injection was in general lower than 1% of the injected dose [15, 16, 23]. The residual ^{153}Gd was somewhat larger than 1% only for $\text{Gd}(\text{DTPA-BMA})$ [15, 16]. Tweedle et al. also found that the complexes of the macrocyclic ligands $\text{Gd}(\text{DOTA})^-$ and $\text{Gd}(\text{HP-DO3A})$ led to lower amounts of whole-body residual ^{153}Gd than in the cases of the complexes of open-chain ligands, $\text{Gd}(\text{DTPA})^{2-}$ and $\text{Gd}(\text{DTPA-BMA})$ [15, 16].

In a human experiment, Puttagunta et al. studied the amounts of Cu^{2+} and Zn^{2+} excreted in the urine before and after the administration of CAs. They found increases in the urinary Cu^{2+} and Zn^{2+} concentrations after the injection of CA, presumably as a result of the displacement of Gd^{3+} from the Gd^{3+} complex by Cu^{2+} and Zn^{2+} . However, 3 h after the injection, the amounts of excreted Cu^{2+} and Zn^{2+} were low, totalling only 0.38% and 0.09% of the injected dosage (~ 7 mmol) of $\text{Gd}(\text{DTPA-BMA})$ and $\text{Gd}(\text{DTPA})^{2-}$, respectively [24]. These exper-

imental results also indicate that the amount of Gd^{3+} retained in the body is very low, and in fact much lower than predicted by equilibrium calculations. This contradiction is not a real one, since the calculations based on the values of the stability constants predict only the possibility of the exchange reactions between the metal ions. These exchange reactions are relatively slow and, if the rapid excretion of the Gd^{3+} chelates from the body (the half-time of excretion is 6, 20 and 90 min for mice, rats and humans, respectively) is taken into account, it is clear that the system is far from equilibrium. Numerous experimental data demonstrate that a knowledge of the kinetic stabilities of Gd^{3+} chelates is more important for the characterization of the *in vivo* stability than a knowledge of the equilibrium constants. In the following section we discuss parameters characterizing the rates of the exchange reactions of Gd^{3+} chelates.

3

Kinetic Properties of Gd^{3+} Chelates

The substitution reactions of the complexes of trivalent lanthanides are generally rapid, in contrast with the reactions of the inert transition metal(III) complexes (e.g. Cr^{3+} , Co^{3+} and Rh^{3+}), and can be studied only by relaxation methods. The first relatively slow substitution reactions, which could be followed by a conventional technique were observed for the complexes $\text{Ln}(\text{EDTA})^-$ in 1958 [25]. In the following two decades, the kinetics of metal-exchange reactions were investigated in detail for several Ln^{3+} -polyaminopolycarboxylate complexes, such as $\text{Ln}(\text{EDTA})^-$, $\text{Ln}(\text{HEDTA})$, $\text{Ln}(\text{DCTA})^-$ and $\text{Ln}(\text{DTPA})^{2-}$ [26–32]. The results of these studies indicated that, in the pH range ~4–6, the metal-exchange reactions occur through dissociation of the monoprotonated complexes LnHL and the diprotonated complexes LnH_2L , followed by a fast reaction between the free ligand and the exchanging metal ion. Exchange reactions also take place by direct attack of the exchanging metal on the complex, when a binuclear intermediate (LnLM) is formed and the functional groups of the ligand are transferred stepwise from the Ln^{3+} to the attacking ion. The exchange reactions were assumed to be slow, because both the dissociation and the transfer of the multidentate ligand occur through the consecutive breaking of several Ln^{3+} -ligand bonds [32, 33].

The results and experience that have accumulated from studies of the exchange reactions of the aminopolycarboxylates of different lanthanides are very useful in the assessment of the kinetic stabilities of the Gd^{3+} chelates. In the body fluids where the CAs are administered, the Gd^{3+} chelates are surrounded by various endogenous metal ions and ligands. Some of these metal ions can react with the Gd^{3+} chelate by displacing Gd^{3+} in a metal-metal exchange reaction:



The free Gd^{3+} formed in the metal ion-assisted dissociation of the Gd^{3+} chelate will react with some of the endogenous ligands with the formation of Gd^{3+} complexes (Gd^{3+} -citrate, Gd^{3+} -glutamate, etc.). In principle, the endogenous

ligands (A) may also react with the Gd^{3+} chelate in a ligand-ligand exchange reaction, when a new Gd^{3+} complex is formed:



The free ligand L will react with some of the endogenous metal ions, e.g. with Ca^{2+} , and the CaL complex formed may excrete through the kidneys. The probability of the ligand-exchange reactions is very low, because for ligand exchange to occur the attacking ligand must form a ternary complex (GdLA) with the Gd^{3+} chelate, but it has been found that such ternary complexes are practically not formed with the important endogenous ligands (e.g. citrate) [34].

After the importance of the kinetic stability of the Gd^{3+} chelates was realized, a number of authors studied the kinetic properties of such complexes. Some of these studies were performed in order to demonstrate the inertness (or lability) of the complex of interest, while in other works the kinetic parameters were also determined. In the following, we shall present first the results of certain qualitative studies, which experimentally prove the importance of the kinetic stability of Gd^{3+} chelates. Since the kinetics of dissociation of complexes formed with the open-chain and macrocyclic ligands differ quite considerably, we shall discuss the kinetic properties of the complexes formed with DTPA and its derivatives and with DOTA and its derivatives in separate sections.

3.1

Demonstration of Kinetic Stability of Gd^{3+} Chelates

In the course of the development of CAs, the question of the stability of Gd^{3+} chelates in the serum has often been raised. Besides, the possibility of the metal and ligand-assisted dissociation of Gd^{3+} complexes, which was mentioned above, the formation of precipitates of $\text{Gd}(\text{PO}_4)$ and $\text{Gd}_2(\text{CO}_3)_3$ was additionally assumed to be possible [2]. The concentration of phosphate (0.38 mM) and particularly carbonate ions (24.5 mM) in the plasma is relatively high [21], while the solubilities of $\text{Gd}(\text{PO}_4)$ and $\text{Gd}_2(\text{CO}_3)_3$ are very low. Many experimental data and also the calculations carried out by Cacheris et al. indicate the stability of the clinically used CAs in the serum [17, 22]. However, Magerstadt et al. observed a decrease in the concentration of $\text{Gd}(\text{DTPA})^{2-}$ in the serum at 37°C , while the concentration of the more inert $\text{Gd}(\text{DOTA})^-$ remained practically unchanged. They assumed the formation of a precipitate of GdPO_4 [35].

The formation of the precipitate of GdPO_4 was used by Tweedle et al. to compare the relative kinetic stabilities of several Gd^{3+} chelates [36]. In a solution of $[\text{GdL}] = [\text{HCO}_3^-] = 25 \text{ mM}$ and $[\text{HPO}_4^{2-}] + [\text{H}_2\text{PO}_4^-] = 66 \text{ mM}$ at $\text{pH} = 7$, the complexes formed with DTPA, DOTA, HP-DO3A and DO3A proved to be stable for at least 10 min, whereas a few per cent of Gd^{3+} was precipitated from $\text{Gd}(\text{EDTA})^-$, as detected with radioactive ^{153}Gd . In the presence of 25 mM Cu^{2+} or 25 mM Zn^{2+} , the Gd^{3+} complexes formed with the macrocyclic ligands were found to be stable, but about 25–35% and 60–90% of the Gd^{3+} , respectively, was precipitated from $\text{Gd}(\text{DTPA})^{2-}$ and $\text{Gd}(\text{EDTA})^-$. These results indicate the higher kinetic stabilities of $\text{Gd}(\text{DOTA})^-$, $\text{Gd}(\text{HP-DO3A})$ and $\text{Gd}(\text{DO3A})^-$. From

the complexes $\text{Gd}(\text{DTPA})^{2-}$ and $\text{Gd}(\text{EDTA})^-$ a significant amount of Gd^{3+} was replaced by Cu^{2+} or Zn^{2+} in 10 min, which formed a precipitate of GdPO_4 [36].

Puttagunta et al. studied the extent of the „double“ exchange reactions between the complexes $\text{Gd}(\text{DTPA})^{2-}$, $\text{Gd}(\text{DTPA-BMA})$, $\text{Gd}(\text{HP-DO3A})$, $\text{Gd}(\text{EDTA})^-$ and Zn^{2+} -citrate at pH = 7.4 [37]. The concentrations of these complexes was as high as 20 mM. After 4 h, there was no reaction between $\text{Gd}(\text{HP-DO3A})$ and Zn^{2+} -citrate, while from $\text{Gd}(\text{DTPA})^{2-}$, $\text{Gd}(\text{EDTA})^-$ and $\text{Gd}(\text{DTPA-BMA})$ about 35%, 50% and 75% of the Gd^{3+} was replaced by Zn^{2+} . The sequence of kinetic stability was found to be $\text{Gd}(\text{HP-DO3A}) \gg \text{Gd}(\text{DTPA})^{2-} > (\text{Gd}(\text{DTPA-BMA}) > \text{Gd}(\text{EDTA})^-$. It was also established that the ligand-exchange reaction between $\text{Gd}(\text{DTPA-BMA})$ and DTPA or EDTA was relatively rapid. The results further indicate that the kinetic stability of the Gd^{3+} complex formed with the macrocyclic HP-DO3A is significantly higher than those of the complexes of the open-chain ligands [37].

The rates of dissociation of Gd^{3+} chelates used or proposed as CAs are generally low at pH = 7.4. The complexes dissociate much faster in acidic solutions, when the proton-assisted dissociation predominates. In order to compare the kinetic stabilities of complexes, some authors suggest use of the first-order rate constants (k_{obs}) obtained in 0.1 M HCl or HClO_4 solution. Wedeking et al. compared the acid-assisted dissociation rates (k_{obs}) of several acyclic and cyclic Gd^{3+} complexes with the long term (14 days) deposition of Gd in the whole body of mice [15]. They found an inverse proportionality between the dissociation rates (k_{obs}) and the total residual Gd, i.e. the lower the dissociation rate, the less the residual Gd found in the bodies of the mice [15]. The (k_{obs}) values determined by Wedeking et al. and other authors for several Gd^{3+} and Y^{3+} complexes are shown in Table 1.

Table 1. Dissociation rates k_{obs} (s^{-1}) of the Gd^{3+} complexes in 0.1 M HCl and 0.1 M HClO_4

Complex	k_{obs} (s^{-1})	k_{obs} (s^{-1})	Ref.
	25 °C, I = 1.0 M	37 °C, I = 1.0 M	
$\text{Gd}(\text{EDTA})^-$	1.4×10^2		[15]
$\text{Gd}(\text{DTPA})^{2-}$	1.2×10^{-3}		[15]
$\text{Gd}(\text{DTPA-BMA})$	$> 2 \times 10^{-2}$		[15]
$\text{Y}(\text{DTPA})^{2-}$	144		[38]
$\text{Y}(\text{CHX-DTPA})^{2-}$	0.75		[38]
$\text{Y}(\text{PNP-DTPA})^{2-}$	37.5		[38]
$\text{Gd}(\text{DO3A})^-$	2.3×10^{-3}		[15]
$\text{Gd}(\text{DOTA})^-$	2.1×10^{-5}	3.2×10^{-6}	[15, 39]
$\text{Gd}(\text{HP-DO3A})$	6.3×10^{-5}		[15]
$\text{Y}(\text{DOTA})^-$		1.5×10^{-5}	[39]
$\text{Gd}(\text{DOTMO})^-$		1×10^{-5}	[39]
$\text{Gd}(\text{DOTBzP})^-$		2.4×10^{-5}	[39]
$\text{Gd}(\text{DOTBuP})^-$		3.7×10^{-5}	[39]
$\text{Gd}(\text{DOTPP})^-$		7.8×10^{-5}	[39]
$\text{Y}(\text{DOTMP})^-$		2.1×10^{-5}	[39]
$\text{Gd}(\text{DOTEP})^-$	6.4×10^{-6}		[40]

The data presented in Table 1 indicate the significantly higher kinetic stabilities of the Gd^{3+} and Y^{3+} complexes with the macrocyclic ligands. In this respect, it is interesting that the complexes formed with the cyclen derivative ligands, containing pendant acetate or methylenephosphinate groups, behave similarly. The rate constants (k_{obs}) are $\sim 10^{-5}$ – 10^{-6} s^{-1} (the only exception is $\text{Gd}(\text{DO3A})$).

The extents of inertness of the Gd^{3+} and Y^{3+} complexes formed with DTPA differ considerably. On the basis of detailed kinetic studies, the k_{obs} values reported for $\text{Y}(\text{DTPA})^{2-}$ seem to be more reliable, while the rate constant found for $\text{Gd}(\text{DTPA})^{2-}$ is too low [20, 43].

The k_{obs} values obtained for the Y^{3+} complexes with some DTPA derivative ligands indicate that substitution in the diethylenetriamine backbone increases the inertness of the complex [38].

The Gd^{3+} complex MS-325 formed with a diphenylcyclohexyl derivative of DTPA, proved to be kinetically more stable than $\text{Gd}(\text{DTPA})^{2-}$ in a metal-exchange reaction with Zn^{2+} [41].

3.2

Kinetic Stabilities of Gd^{3+} Complexes with DTPA and its Derivatives

The results of kinetic studies up to the mid-1970 s on the metal and ligand-exchange reactions of the transition metal(II, III) and lanthanide(III) complexes with the open-chain polyaminopolycarboxylate ligands were surveyed by Margerum et al. [33]. These results in general show an inverse relationship between the stability constants and the rates of the substitution reactions of the complexes, i.e. the thermodynamically more stable complexes exhibit higher kinetic stabilities. For the $\text{Ln}(\text{III})$ -polyaminopolycarboxylates, only the kinetics of metal-metal exchange reactions were investigated, most often the isotopic-exchange reactions of the complexes $\text{Ln}(\text{EDTA})^-$ [25–30]. These exchange reactions take place predominantly through the proton-assisted dissociation of the complexes, and the reactions involving direct attack of the exchanging metal ions play only a minor role. The coordination number of Ln^{3+} is 8 or 9. In the complexes of the hexadentate EDTA or CDTA therefore, there are no free functional groups, and the formation of binuclear intermediates, which plays an important role in the direct substitution reactions, occurs with very low probability. The situation is a little different for the complexes $\text{Ln}(\text{DTPA})^{2-}$. The stability constants of $\text{Ln}(\text{DTPA})^{2-}$ as a function of the atomic numbers, exhibit a maximum at around Dy and Ho, which was explained in terms of an increase in steric hindrance between the functional groups. This finding and the two negative charges on $\text{Ln}(\text{DTPA})^{2-}$ increase the probability of the metal-exchange reactions occurring by direct attack of the exchanging metal ion.

The rates of the exchange reactions between several complexes $\text{Ln}(\text{DTPA})^{2-}$ ($\text{Ln} = \text{La}, \text{Nd}, \text{Gd}, \text{Ho}$ and Lu) and Eu^{3+} have been studied by spectrophotometry on the charge-transfer band of Eu^{3+} [20, 31]. Similar studies were carried out with the Gd^{3+} complexes of some other DTPA derivatives: DTPA-BMA, DTPA-N-MA and DTPA-N'-MA. The progress of the exchange reactions between the complexes and Eu^{3+} and Cu^{2+} was followed by spectrophotometry, while when Zn^{2+} was used as exchanging ion, the longitudinal relaxation rates of water pro-

tons were measured. In the kinetic studies, the concentration of the exchanging metal ion (M^{z+}) was generally significantly higher than the concentration of the complexes LnL ; hence, the exchange reaction (1) proceeded to completeness and could be regarded as a pseudo-first-order reaction. The rate of the exchange is directly proportional to the total concentration of the complex:

$$-\frac{d[GdL]_t}{dt} = k_p \cdot [GdL]_t \quad (3)$$

where k_p is a pseudo-first-order rate constant.

The k_p values calculated from the experimental data increase with increase of the H^+ concentration: $k_p = k'_0 + k'_1 \cdot [H^+] + k'_2 \cdot [H^+]^2$. From this dependence of k_p on $[H^+]$, it seems probable that the exchange reactions can take place through the dissociation of protonated complexes. The protonated complexes $GdHL$ are formed in equilibrium reactions. The protonation occurs on a carboxylate group, but the proton can be transferred to a nitrogen and the dissociation of this protonated intermediate is much faster than the spontaneous (or H_2O -assisted) dissociation of the complex GdL .



The presence of the term $k'_2 \cdot [H^+]^2$ indicates the importance of a reaction pathway in which the exchange occurs with the assistance of one more proton:

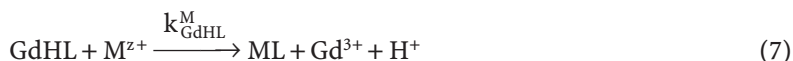


The free ligands formed ($H_nL^{(5-n)-}$) are in protonation equilibrium and react very rapidly with the exchanging metal M^{z+} with the formation of ML .

The increases in k'_0 and k'_1 with increasing concentration of M^{z+} demonstrate the importance of the reactions occurring by direct attack of the exchanging metal ion on the complex GdL and protonated complex $GdHL$:



On the attack of the exchanging metal, a binuclear complex is formed, in which the functional groups are transferred stepwise to the metal ion M^{z+} . The exchange may also occur by direct reaction of the exchanging metal ion with the protonated (partly unwrapped) complex:



When the reaction pathways (4), (5), (6) and (7) are taken into account, the rate of the exchange reaction can be expressed as

$$-\frac{d[\text{GdL}]_t}{dt} = k_{\text{GdHL}} \cdot [\text{GdHL}] + k_{\text{GdHL}}^{\text{H}} \cdot [\text{GdHL}] \cdot [\text{H}^+] + k_{\text{GdLM}} \cdot [\text{GdLM}] + k_{\text{GdHL}}^{\text{M}} \cdot [\text{GdHL}] \cdot [\text{M}^{z+}] \quad (8)$$

Since the total concentration of the complex, $[\text{GdL}]_t$, is $[\text{GdL}] + [\text{GdHL}] + [\text{GdLM}]$, from the equations defining the stability constants of the protonated and binuclear complexes and Eq. (3), the rate constant k_p can be expressed as follows [20, 31]:

$$k_p = \frac{k_1 \cdot [\text{H}^+] + k_2 \cdot [\text{H}^+]^2 + k_3^{\text{M}} \cdot [\text{M}^{z+}] + k_4^{\text{M}} \cdot [\text{M}^{z+}] \cdot [\text{H}^+]}{1 + K_{\text{GdHL}} \cdot [\text{H}^+] + K_{\text{GdLM}} \cdot [\text{M}^{z+}]} \quad (9)$$

where $k_1 = k_{\text{GdHL}} \cdot K_{\text{GdHL}}$, $k_2 = k_{\text{GdHL}}^{\text{H}} \cdot K_{\text{GdHL}}$, $k_3^{\text{M}} = k_{\text{GdLM}} \cdot K_{\text{GdLM}}$, $k_4^{\text{M}} = k_{\text{GdHL}}^{\text{M}} \cdot K_{\text{GdHL}}$. Since the protonation constants of the complexes are ~ 100 [20], the second term in the denominator of Eq (9), $K_{\text{GdHL}} \cdot [\text{H}^+]$, can be neglected at about $\text{pH} > 4$. The rate constants were calculated by fitting the k_p values to Eq. (9). The rate constants k_1 , k_2 and k_3 are presented in Table 2. The stability constants of binuclear complexes (K_{GdLM}) are ~ 10 – 30 . The values of the rate constant k_4^{M} are relatively low and the term $k_4^{\text{M}} \cdot [\text{M}^{z+}] \cdot [\text{H}^+]$ in Eq. (9) is of lower importance, particularly at $\text{pH} > 5$.

The rate constants k_1 and k_2 furnish information on the role of the proton-assisted dissociation of the Gd^{3+} complexes. However, under physiological conditions the H^+ concentration is very low and the rate of proton-assisted dissociation is therefore also very low. The k_1 values obtained for the DTPA derivative complexes do not differ considerably. Only the k_1 value characterizing the dissociation of $\text{Gd}(\text{DTPA-BMA})$ is larger, but, because of the relatively low protonation constant value ($K_{\text{GdHL}} < 2$ [43]), the concentration of the protonated complex $\text{Gd}(\text{HDTPA-BMA})^+$ is also low, and thus the rate of dissociation of $\text{Gd}(\text{DTPA-BMA})$ is comparable with those of the other DTPA derivative complexes.

Under physiological conditions, the exchange reactions with the endogenous Zn^{2+} and Cu^{2+} are of higher significance in the dissociation of the Gd^{3+} chelates. The rates of the exchange reactions increase with increasing concentrations of Cu^{2+} and Zn^{2+} and at about $\text{pH} > 4.5$, when the k_p values are much higher than those in the reactions with Eu^{3+} , the rates are independent of the H^+ concentration. These findings show that under such conditions the exchange reactions occur predominately via the direct attack of Cu^{2+} and Zn^{2+} on the complexes. In this case, only the reaction pathway given by Eq. (6) is effective and the relationship expressed by Eq. (9) simplifies to Eq. (10):

$$k_p = \frac{k_3^{\text{M}}}{1 + K_{\text{GdHL}} \cdot [\text{M}^{z+}]} \quad (10)$$

The parameters k_3^{M} calculated by fitting the k_p values to Eq. (10) are presented in Table 2. A comparison of the rate constants reveals that the k_3^{Cu} values are ~ 10 – 80 times higher than the k_3^{Zn} values, i.e. Cu^{2+} is the more effective in the direct reaction with the Gd^{3+} complexes formed with DTPA and its derivatives.

Table 2. Rate constants characterizing the proton and metal ion-assisted dissociation of the Gd^{3+} complexes formed with DTPA derivative ligands (25 °C)

	$k_1 (\text{M}^{-1} \text{s}^{-1})$	$k_2 (\text{M}^{-2} \text{s}^{-1})$	$k_3^{\text{Eu}} (\text{M}^{-1} \text{s}^{-1})$	$k_3^{\text{Cu}} (\text{M}^{-1} \text{s}^{-1})$	$k_3^{\text{Zn}} (\text{M}^{-1} \text{s}^{-1})$	Ref.
DTPA	0.58	9.7×10^4	4.9×10^{-4}	0.93	5.6×10^{-2}	[20]
DTPA-BMA	12.7			0.62	7.8×10^{-3}	[43]
DTPA-N-MA	1.5	5.2×10^4	3.8×10^{-4}	1.9	3.2×10^{-2}	[43]
DTPA-N'-MA	1.6	2.5×10^4	3.2×10^{-3}	0.63	8.2×10^{-2}	[43]
DTPA-BMEA	8.6					[42]
DTPA-EAM	1.2×10^{-1}	1.3×10^5		1.30		[44]
DTPA-PAM	3.9×10^{-2}	1.2×10^5		1.27		[44]
DTPA-XAM	3.6×10^{-2}	1.2×10^5		1.27		[44]
DTPA-BAM	2.0×10^{-2}	1.2×10^5		1.24		[44]
DTPA-PenAM	1.5×10^{-2}	1.2×10^5		1.20		[44]

It is somewhat surprising that the exchange reactions of $\text{Gd}(\text{DTPA-BMA})$, which has the lowest stability constant, occur more slowly with both Cu^{2+} and Zn^{2+} than the reactions of the thermodynamically more stable complexes. This suggests that the presence of an iminodiacetate group in the coordinated ligand may play an important role in the exchange reactions involving direct attack of Cu^{2+} or Zn^{2+} . The functional groups of the ligands are transferred stepwise to the attacking ion and the formation of a binuclear intermediate, in which an iminodiacetate group is coordinated to the Cu^{2+} or Zn^{2+} , may have a rate-controlling role in the exchange reactions. However, the k_3^{Eu} values obtained for $\text{Gd}(\text{DTPA})^{2-}$, $\text{Gd}(\text{DTPA-N-MA})^-$ and $\text{Gd}(\text{DTPA-N'-MA})^-$ are significantly lower than k_3^{Cu} and k_3^{Zn} (Table 2), while the stability constants of the iminodiacetate (IMDA) complexes of Zn^{2+} ($\log K_{\text{ZnL}} = 7.24$) and Eu^{3+} ($\log K_{\text{EuL}} = 6.73$) are similar (The stability of Cu^{2+} -IMDA is larger: $\log K_{\text{CuL}} = 10.57$ [19]). This contradiction can be interpreted since the Zn^{2+} -N bond in Zn^{2+} -IMDA is stronger than the Eu^{3+} -N bond in Eu^{3+} -IMDA, and thus the transfer of the further functional groups to the Zn^{2+} occurs with higher probability.

The rate of proton-assisted dissociation of $\text{Gd}(\text{DTPA-BMEA})$, studied by Rothermel et al., does not differ considerably from that of $\text{Gd}(\text{DTPA-BMA})$ (Table 2), indicating that the kinetic stabilities of the complexes of the different DTPA-bis(amide) derivatives are similar [42].

The rates of the exchange reactions between some macrocyclic DTPA-bis(amide) derivatives and Cu^{2+} were studied by Choi et al. [44]. The rate law determined in the pH range 4–5 was similar to that obtained for $\text{Ln}(\text{DTPA})^{2-}$ [20, 31]. The rate constants, compared in Table 2, do not exhibit a significant change on variation of the ring size. The rate of proton-assisted dissociation (k_1) increases weakly with increasing ring size, but the contributions of the reactions proceeding through the formation of diprotonated complexes (k_2) do not depend on the ring size. This is the case with the k_3^{Cu} values characterizing the exchange reactions involving direct attack of Cu^{2+} on the Gd^{3+} complexes. The difference between the rate constants obtained for the complexes of macrocyclic and open-chain DTPA derivatives is larger in the case of the k_1 values. This

shows that the proton-assisted dissociation of the macrocyclic complexes is slower than that of the complexes of the open-chain DTPA-BMA. However, it is surprising that the rate constants k_2 and k_3^M of the complexes of the open-chain and macrocyclic ligands are very similar, indicating that the use of macrocyclic ligands does not have any appreciable advantage over the linear DTPA-bis(amide) derivatives.

3.3

Kinetic Stabilities of Gd^{3+} Complexes of DOTA and DOTA Derivative Ligands

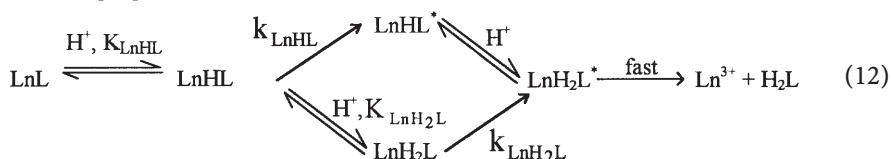
The complexation properties of the macrocyclic, spider-like tetraaza-tetraacetate ligand DOTA were found by Desreux to be very unique [45]. The stability constants of the complexes $Ln(DOTA)^-$ are very high and both the formation and dissociation rates are unusually low. The behavior of the $DOTA^-$ analogous ligands containing at least three acetate and three or four methylene-phosphonate or methylene-phosphinate groups is very similar, and a number of new derivatives have been synthesized and investigated in order to develop new CAs.

The kinetic stabilities of the Gd^{3+} complexes have been studied in acidic solutions, since the rates of dissociation are unmeasurably low at $pH \approx 7$. The kinetic inertness of the complexes of DOTA and its derivatives is attributed to the rigidity of the 12-membered chelate ring structure. However, the complexes are thermodynamically unstable at about $pH < 2$, because of the high first two protonation constants of the ligands, and the rates of proton-assisted dissociation can be studied in 0.01–1.0 M acid [39, 46–49]. Through the use of solutions containing the Gd^{3+} complex at high concentration (e.g. 0.1 M), the rates of metal-exchange reactions between the complex and another Ln^{3+} (e.g. Eu^{3+}) or Cu^{2+} can be studied even in the pH range 3–5 [50–52]. Under pseudo-first-order conditions (a large excess of the Gd^{3+} complex over the exchanging metal ion, or a high concentration of the acid), the rate of dissociation of the complex can be expressed with Eq. (3). In the H^+ concentration range 10^{-5} – 10^{-1} M, the first-order rate constants k_p are directly proportional to the H^+ concentration and do not depend on the concentration of the exchanging metal ion. In this case, the k_p can be expressed as follows:

$$k_p = k_0 + k_1 \cdot [H^+] \quad (11)$$

where k_0 is characteristic of the spontaneous dissociation of the complex GdL . The rate constant k_1 , expresses the rate of proton-assisted dissociation of the complex, which presumably occurs through the formation and rate-determining dissociation of the monoprotonated complex $GdHL$. The values of k_0 , are generally very low, and can be determined only with relatively high error; many authors regard these values as negligibly small. However, at physiological pH some reported k_0 values make a larger contribution to the dissociation rate in Eq. (11) than the term $k_1 \cdot [H^+]$. The rate constants obtained for the Gd^{3+} and some other Ln^{3+} complexes are presented in Table 3. The protonation constants of the complexes (K_{LnHL}) are also shown; these determine the concentrations of the dissociable protonated species.

At H^+ concentrations higher than about 0.2 M, Eq. (11) does not describe the dependence of the dissociation rates, since k_p exhibits saturation behavior [47, 48, 50]. At these higher H^+ concentrations, the monoprotonated complexes $LnHL$ predominate, because the protonation constant values (K_{LnHL}) are ~ 20 – 200 (Table 3). The saturation behavior of the $[H^+]$ vs. k_p plots is presumably a result of the accumulation of the protonated complexes. On the basis of the rate law derived and the experimental data obtained in more acidic solutions, the assumed acid-catalyzed dissociation mechanism can be depicted in a reaction scheme [50]:



A similar, but somewhat simpler mechanism was proposed to interpret the dissociation of the complexes $Ln(\text{NOTA})$ ($\text{H}_3\text{NOTA} = 1,4,7\text{-triazacyclononane-1,4,7-triacetic acid}$) [53]. Scheme (12) has been used to interpret of the rate data obtained for the dissociation of $\text{Eu}(\text{DOTA})^-$ and various DO3A-derivative complexes of Gd^{3+} and other lanthanides [47, 48, 50].

In the dissociation of the Ln^{3+} complexes, the formation of protonated species plays an important role. It has generally been assumed that, similarly to the protonation of the complexes formed with the open-chain polyaminopolycarboxylate ligands, the proton is attached to a carboxylate oxygen, when a free carboxyl group is formed and the number of coordinated functional groups decreases by one. In the complexes of the macrocyclic ligands, however, the effect of protonation is different. $^1\text{H-NMR}$ studies have revealed that, in the complexes $\text{Ln}(\text{DOTA})^-$, through the formation of the protonated species $\text{Ln}(\text{HDOTA})$, the proton is attached to a noncoordinated oxygen of a carboxylate group and thus the coordination sphere does not change [54]. However, the instability of this protonated complex somehow increases: the proton can probably be transferred to a ring nitrogen (with very low probability) and from this protonated intermediate (LnHL^*), the Ln^{3+} can dissociate. This reaction step is probably assisted by the attachment of a second proton, and the diprotonated intermediate formed (LnH_2L^*) dissociates rapidly. The dissociation of the complexes through the formation of the monoprotonated intermediate, LnHL^* occurs mainly below a H^+ concentration of 0.2 M. If the acidity of the solutions is higher than this, the diprotonated complexes LnH_2L can be formed in higher concentration; these may then rearrange to the diprotonated intermediate LnH_2L^* , and the dissociation occurs.

From reaction scheme (12), the rate of dissociation given by Eq. (3) and the total concentration of the Ln^{3+} complexes, $[\text{LnL}]_t = [\text{LnL}] + [\text{LnHL}] + [\text{LnH}_2\text{L}]$, with the equations defining the protonation constants K_{LnHL} and K_{LnH_2L} ($K_{LnH_2L} = [\text{LnH}_2\text{L}]/[\text{LnHL}] \cdot [H^+]$), the first-order rate constant is expressed as follows [50]:

$$k_p = \frac{k_{LnHL} \cdot K_{LnHL} \cdot [H^+] + k_{LnH_2L} \cdot K_{LnHL} \cdot K_{LnH_2L} \cdot [H^+]^2}{1 + K_{LnHL} \cdot [H^+] + K_{LnHL} \cdot K_{LnH_2L} \cdot [H^+]^2} \quad (13)$$

Equation (13) describes the relationship between the dissociation rates and $[H^+]$ in a broad range of concentrations. At $[H^+] < 10^{-2}$ M, the second term in the numerator and the second and third term in the denominator can be neglected, when $k_p = k_{LnHL} \cdot K_{LnHL} \cdot [H^+] = k_1 \cdot [H^+]$, i.e. in Eq. (11) $k_1 = k_{LnHL} \cdot K_{LnHL}$. The rate constants k_1 and k_{LnH_2L} obtained for some complexes are presented in Table 3. The protonation constants K_{LnH_2L} are very low and can not be determined experimentally. The K_{LnH_2L} values can be calculated from the kinetic data, but are quite uncertain. Since the dissociation of Gd^{3+} complexes at high H^+ concentrations is of no practical significance, the K_{LnH_2L} values are not presented in Table 3.

The rate data obtained for the dissociation reactions, presented in Table 3, show that the complexes formed with DOTA and its derivatives are kinetically very stable. At $[H^+] < 0.1$ M, practically only the reaction pathway characterized by the rate constant k_{LnHL} or k_1 is important. The rate constants k_1 , presented in Table 2 for the DTPA derivative and in Table 3 for the DOTA derivative complexes, can be compared directly. This comparison shows that the k_1 values of the DOTA and DOTA derivative complexes are about four orders of magnitude lower than those of the complexes of the open-chain DTPA derivatives. The only exceptions are the complexes of DO3A, which dissociate approximately 10^2 – 10^3 times faster than the other DOTA derivative complexes. The k_1 values of $GdDO3A$ and $Y(DO3A)$ are comparable with those of the Gd^{3+} complexes of the macrocyclic DTPA derivatives. The lower kinetic stabilities of the DO3A complexes are probably a result of the presence of the secondary nitrogen in the ligand. This nitrogen atom can be much more easily protonated than the

Table 3. Rate constants characterizing the proton-assisted dissociation of the DOTA and DOTA derivative complexes (25°C)

Complex	K_{LnHL}	k_1 ($M^{-1}s^{-1}$)	k_{LnH_2L} (s^{-1})	Ref.
$Gd(DOTA)^-$	634 [47] 141 [59] 200 [58]	0.84×10^{-5} 2.0×10^{-5} (37°C) 3.64×10^{-5} (37°C)		[46] [50] [49]
$Gd(DO3A)$	115	2.6×10^{-2a} $1.17 \times 6 \times 10^{-2}$	1.93×10^{-2}	[48] [51]
$Gd(HP-DO3A)$	240 12	2.6×10^{-4}	1.66×10^{-3}	[48] [52]
$Gd(DO3A-Bu)$	13	2.8×10^{-5}		[52]
$Gd(HL-DO3A)$	110		1.9×10^{-3}	[48]
$Gd(HIP-DO3A)$	170	3.4×10^{-3}	6.4×10^{-2}	[48]
$Y(DOTA)^-$	20	2.3×10^{-4} (37°C)		[39]
$Eu(DOTA)^-$	63	1.4×10^{-5}	6.2×10^{-4}	[50]
$Ce(DOTA)^-$		8×10^{-4}		[57]
$Y(DO3A)$		5.2×10^{-2}		[51]
$Gd(DOTP)^{5-}$	1.7 ^b	5.4×10^{-4}		[56]
$Gd(DOTP-MB)$	1.9	2.1×10^{-4}		[56]

^a Calculated from the reported K_{LnHL} and k_{LnHL} values.

^b The protonation constant is defined for the reaction $GdH_4L + H^+ = GdH_5L$ because $Gd(DOTP)^{5-}$ forms thermodynamically stable complexes $Gd(H_iDOTP)$ ($i = 1, 2, 3, 4$). The protonated complex GdH_5L is presumably the dissociable species.

nitrogens in the other cyclen derivative ligands, which leads to the dissociation of the complex. This finding indicates that the attachment of functional groups to all four ring nitrogens of the cyclen is of high importance for the high kinetic stability of the complexes formed.

Table 3 demonstrates that the kinetic stability of Gd(DO3A-Bu) is about 10 times higher than that of Gd(HP-DO3A). The donor atoms of the two ligands are similar. The higher kinetic stability of Gd(DO3A-Bu) may result from the bulkiness of the “butrol” group. This group contains three alcoholic OH groups, which may restrict the rearrangement and dissociation of the protonated complex to a higher degree than does the hydroxypropyl group in Gd(HP-DO3A) [52].

Parker and coworkers have synthesized a number of tetraaza-tetra-methylenephosphinate ligands. The kinetic stabilities of the complexes of these ligands with Gd³⁺ and Y³⁺ are comparable with those of the DOTA complexes [39, 55]. The kinetic stabilities of Gd(DOTP)⁵⁻ and Gd(DOTP-MB)⁻ are a little lower, but the k_1 values obtained for the proton-assisted dissociation of the two complexes are similar. This result is surprising, because the stability constant of Gd(DOTP-MB) ($\log K_{\text{GdL}} = 12.3$) is more than ten orders of magnitude lower than that of Gd(DOTP)⁵⁻ [56]. The high kinetic stabilities of the complexes formed with the cyclen derivatives containing phosphinate or phosphonate-ester (DOTP-MB) functional groups are a consequence of the low basicity of the oxygen donor atoms. Because of this low basicity, the protonation constants of the complexes are also very low and consequently the concentrations of the dissociable protonated complexes and hence the rates of dissociation are also relatively low.

4

Conclusions

Studies on the kinetic stabilities of Gd³⁺ chelates have generally not been in the limelight of the research and development of CAs. In this field, the main directions have involved the increase of the relaxivity values and the synthesis of organ-specific Gd³⁺ chelates. To achieve these aims, the CAs are bound either covalently or noncovalently to macromolecules (e.g. proteins) which exhibit higher relaxivities, because of their slower rotation. The Gd³⁺ complexes formed with bifunctional chelators are conjugated to macromolecules (e.g. monoclonal antibodies or their fragments) capable of binding to certain receptor sites in diseased tissues. The delivery of the macromolecular CAs in the intravascular space is much slower, and the residence time in the body is therefore much longer than that of the low molecular mass CAs. The slower excretion increases the possibility of in vivo dissociation and thus the significance of the higher kinetic stabilities of the covalently or noncovalently bound Gd³⁺ complexes.

The results of kinetic studies indicate that the kinetic stabilities can be increased through the use of more rigid ligands. It is probable that mainly macrocyclic ligands (e.g. DOTA) or possibly some more rigid DTPA derivatives (e.g. CHX-DTPA) will be used for the synthesis of macromolecules with attached Gd³⁺ complexes.

To characterize the kinetic stabilities of complexes, the rate constants should be used, determined for the exchange reactions occurring between the complexes and endogenous metal ions (e.g. Cu^{2+} and Zn^{2+}). Similarly to the equilibrium plasma models, the development of a kinetic model is needed for a better understanding of the relation between the extent of in vivo dissociation and the parameters characterizing the rates of dissociation, the rates of distribution in the extracellular space and the rates of excretion of the Gd^{3+} complexes.

Acknowledgement. The author wishes to thank the Hungarian National Science Foundation (OTKA T 025462) and the Schering A.G. (Berlin) for financial support.

5 References

1. Tweedle MF (1989) Relaxation Agents in NMR Imaging. In: Bünzli J-CG, Choppin GR (eds) Lanthanide Probes in Life, Chemical and Earth Sciences: Theory and Practice, Elsevier, Amsterdam, p. 129–179
2. Lauffer RB (1987) Chem Rev 99:2353
3. Yu S-B, Watson AD (1999) Chem Rev 87:901
4. Jarvis NN, Wagener JM, Jackson GE (1995) J Chem Soc Dalton Trans 2269
5. Volkert WA, Hoffman TJ (1999) Chem Rev 99:2269
6. Cox PL, Jankowski KJ, Katakly R, Parker D, Beeley NRA, Boyce BA, Eaton MAW, Millar K, Millican AT, Harrison A, Walker C (1989) J Chem Soc Chem Commun 797
7. Reichert DE, Lewis JS, Anderson CJ (1999) Coord Chem Rev 184:3
8. Caravan P, Ellison JJ, McMurry TJ, Lauffer RB (1999) Chem Rev 99:2293
9. Schuhmann-Giampieri G, Schmitt-Willich H, Press W-R, Negishi C, Weinmann H-J, Speck U (1992) Radiology 183:59
10. Schmitt-Willich H, Brehm M, Ewers ChLJ, Michl G, Müller-Fahrow A, Petrov O, Platzek J, Radüchel B, Sülzle D (1999) Inorg Chem 38:1134
11. Uggeri F, Aime S, Anelli PL, Botta M, Brochetta M, de Haën C, Ermondi G, Grandi M, Paoli P (1995) Inorg Chem 34:633
12. Parmelee DJ, Walovitch RC, Ouellet HS, Lauffer RB (1997) Invest Radiol 32:741
13. Weinmann HJ, Laniado M, Mützel W (1984) Physiol Chem Phys Med NMR 16:167
14. Weinmann HJ, Brasch RC, Press W-R, Wesbey GE (1984) AJR 142:619
15. Wedeking P, Kumar K, Tweedle MF (1992) Magn Reson Imaging 10:641
16. Tweedle MF, Wedeking P, Kumar K (1995) Invest Radiol 30:372
17. Cachetis WP, Quay SC, Rocklage SM (1990) Magn Reson Imaging 8:467
18. Puttagunta NR, Gibby WA, Puttagunta VL (1996) Invest Radiol 31:619
19. Martell AE, Smith KM (1974) Critical Stability Constants, vol. 1, Plenum Press, New York
20. Sarka L, Burai L, Brücher E (2000) Chem Eur J 6:719
21. May PM, Linder PW, Williams DR (1977) J Chem Soc Dalton Trans 588
22. Jackson GE, Wynchank S, Woudenberg M (1990) Magn Reson Med 16:57
23. Kasokat T, Urich K (1992) Arzneim-Forsch/Drug Res 42:869
24. Puttagunta NR, Gibby WA, Smith GT (1996) Invest Radiol 31:739
25. Betts RH, Dahlinger DG, Munro DM (1958) In: Exterman RC (ed) Radioisotopes in Scientific Research, vol. 2, Pergamon Press, Oxford, p. 326
26. Glentworth P, Wiseall B, Wright CL, Mahmood AJ (1968) J Inorg Nucl Chem 10:967
27. Brücher E, Szarvas P (1970) Inorg Chim Acta 4:632
28. Asano T, Okada S, Taniguchi S (1970) J Inorg Nucl Chem 32:1287
29. Ryhl T (1972) Acta Chem Scand 26:3955
30. D'Olieslager W, Choppin GR (1971) J Inorg Nucl Chem 33:127
31. Brücher E, Laurenczy G (1981) J Inorg Nucl Chem 43:2089

32. Brücher E, Laurenczy G (1983) *Inorg Chem* 22:338
33. Margerum DW, Cayley GR, Weatherburn DC, Pagenkopf GK (1978): Martell AE (ed) *Coordination Chemistry*, vol 2, ACS Monograph 174, American Chemical Society, Washington D.C., p. 1
34. Burai L, Hietapelto, Király R, Tóth É, Brücher E (1997) *Magn Reson Med* 38:146
35. Magerstadt M, Gansow OA, Brechbiel MW, Colcher D, Baltzer L, Knop RH, Girton ME, Naegele M (1986) *Magn Reson Med* 3:808
36. Tweedle MF, Hagan JJ, Kumar K, Mantha S, Chang CA (1991) *Magn Reson Imaging* 9:409
37. Puttagunta NR, Gibby WA, Puttagunta VL (1996) *Invest Radiol* 31:619
38. McMurry TJ, Pippin CJ, Wu C, Deal KA, Brechbiel MW, Mirzadeh S, Gansow OA (1998) *J Med Chem* 41:3546
39. Pulukkody KP, Norman TJ, Parker D, Royle L, Broan CJ (1993) *J Chem Soc Perkin Trans* 2:605
40. Lázár I, Sherry AD, Ramasamy R, Brücher E, Király R (1991) *Inorg Chem* 30:5016
41. Muller RN, Radüchel B, Laurent S, Platzek J, Piérart C, Mareski P, Vander Elst L (1999) *Eur J Inorg Chem* 1949
42. Rothermel GL, Rizkalla EN, Choppin GR (1997) *Inorg Chim Acta* 262:133
43. Sarka L, Burai L, Brücher E, to be published
44. Choi K-Y, Kim KS, Kim JC (1994) *Polyhedron* 13:567
45. Desreux JF (1980) *Inorg Chem* 19:1319
46. Wang X, Jin T, Comblin V, Lopez-Mut A, Merciny E, Desreux JF (1992) *Inorg Chem* 31:1095
47. Kumar K, Chang CA, Tweedle MF (1993) *Inorg Chem* 32:587
48. Kumar K, Jin T, Wang X, Desreux JF, Tweedle MF (1994) *Inorg Chem* 33:3823
49. Schwizer R, Fraser R, Maecke H, Siebold K, Funck R, Fried M (1994) *Magn Reson Med* 31:388
50. Tóth É, Brücher E, Lázár I, Tóth I (1994) *Inorg Chem* 33:4070
51. Cai H-Z, Kaden TA (1994) *Helv Chim Acta* 77:383
52. Tóth É, Király R, Platzek J, Radüchel B, Brücher E (1996) *Inorg Chim Acta* 249:191
53. Brücher E, Sherry AD (1990) *Inorg Chem* 29:1555
54. Szilágyi E, Tóth É, Brücher E, Merbach AE (1999) *J Chem Soc Dalton Trans* 2481
55. Broan CJ, Cox JPL, Craig AS, Kataky R, Parker D, Harrison A, Randall AM, Ferguson G (1991) *J Chem Soc Perkin Trans* 2:87
56. Burai L, Király R, Lázár I, Brücher E (2001) *Eur J Inorg Chem* 813
57. Brücher E, Laurenczy G, Makra Zs (1987) *Inorg Chim Acta* 139:141
58. Clarke ET, Martell AE (1991) *Inorg Chim Acta* 190:37
59. Burai L (1997) Thesis, University of Debrecen, Debrecen

New Classes of MRI Contrast Agents

Vincent Jacques, Jean François Desreux

Department of Coordination and Radiochemistry, University of Liège, Sart-Tilman B16,
4000 Liège, Belgium

E-mail: vjacques@ulg.ac.be

A very high spatial resolution and a so far unsurpassed ability in distinguishing soft tissues characterize magnetic resonance imaging (MRI). This imaging technique has therefore become one of the most important diagnosis tools available in medicine. Insufficient contrast is nevertheless a drawback of the technique in many instances, hence the need for contrast agents. A number of such substances have been developed and enjoy widespread use in hospitals around the globe. However, there remains a need for new and more selective contrast media that would allow a better delineation of diseases thus helping the radiologist in giving a more precise diagnosis. This chapter is devoted to these new types of contrast agents and provides an overview of new ideas and their applications as they appear in the recent literature. Examples are given of new blood-pool agents mostly based on macromolecular derivatives. Linking contrast agents to antibodies or other biologically relevant macromolecules may provide a way of highlighting regions of interest. Such compounds are also discussed. Very recent examples of *in vitro* and *in vivo* contrast agents for imaging gene expression will also be presented, as this appears to be of utmost importance for assessing gene delivery and gene expression in gene therapy applications and for studying developmental stages in embryology. Finally, MRI contrast agents are presented that react to variables in their environment. Temperature, pH, ions, enzymes are just a few of the parameters that may influence the response of these so-called smart contrast agents.

Keywords: Magnetic resonance imaging, Contrast agent, Smart, Targeting, Chelate

1	Introduction	125
1.1.	MRI and MRI Contrast Agents	125
1.2.	Relaxivity of Gadolinium(III) Chelates	126
2	Blood-Pool Contrast Agents	127
2.1	A Short Description	127
2.2	Three Ways to Blood-Pool Agents	128
2.2.1	Liposomal Contrast Agents	128
2.2.2	Particulate and Polymeric Contrast Agents	129
2.2.3	Non-Covalent Binding to Plasma Proteins	130
2.3	Remarks and New Approaches	131
3	Targeting MRI Agents	133
3.1	Scope and Limitations	133
3.2	Cell Surface Targeting	134

3.3	Receptor Targeting	135
3.3.1	Labeled Antibodies	135
3.3.2	Low Molecular Weight Targeting Species	138
3.4	Internalization: Fluid Phase and Receptor Mediated Endocytosis	141
3.5	Direct Imaging of Gene Expression	147
4	Smart Contrast Agents	148
4.1	Definition	148
4.2	Several Examples	149
4.2.1	Temperature Sensitive	149
4.2.2	pH Sensitive	150
4.2.3	Oxygen Pressure Responsive	153
4.2.4	Enzyme Responsive	155
4.2.5	Metal Ion Concentration Dependent	157
5	Concluding Remarks	160
6	References	160

List of Abbreviations

mAb	monoclonal antibody
CEA	carcinoembryonic antigen
CLIO	cross-linked dextran-coated iron oxide
DOTA	1,4,7,10-tetracarboxymethyl-1,4,7,10-tetraazacyclododecane
HSA	human serum albumin
MION	monocrystalline iron oxide nanoparticle
(M)PEG	(monomethoxy)polyethyleneglycol
MR	magnetic resonance
MRA	magnetic resonance angiography
MRI	magnetic resonance imaging
MTS	membrane translocating signal
P(D)L	poly-L(D)-lysine
mRNA	messenger RNA
rRNA	ribosomal RNA
(U)SPIO	(ultrasmall) superparamagnetic iron oxide
(h)TfR	(human) transferrin receptor

1

Introduction

1.1

MRI and MRI Contrast Agents

The high spatial resolution and an undisputed capacity for differentiating soft tissues have highly contributed to the widespread use of magnetic resonance imaging (MRI). The contrast of proton MR images depends essentially on three factors: the density of proton spins in a given volume and the longitudinal and transverse relaxation times T_1 and T_2 of these spins. T_1 - and T_2 -weighted images display the best contrast for soft tissues, as proton spin density is essentially invariant while relaxation times vary greatly from one tissue to the other. Lesions usually show up quite nicely. Nevertheless, there remains the possibility of poor contrast between healthy and damaged tissues due to a too small variation in relaxation times. In such cases, contrast agents play a beneficial role. Indeed, their influence on the relaxation times of proton spins has a marked effect on the signal intensity thereby increasing the contrast of the images and better delineating the damaged regions.

MRI contrast agents do not appear per se on MR images but affect longitudinal and transverse relaxation of the surrounding nuclei, mainly the water solvent protons. The addition of a contrast agent results in an increased relaxation rate of the surrounding nuclei that appear as a bright spot of increased intensity in T_1 -weighted images or as a region of decreased brightness in T_2 -weighted images. MRI contrast agents are thus classified as positive or negative, T_1 or T_2 , contrast agents. It should be noted that T_1 agents are usually preferred as a positive contrast enhancement is often more easily detected than a negative one. The effectiveness of a MRI contrast agent is usually measured in terms of relaxivity, i.e. the longitudinal or transverse relaxation rate of water protons observed for a millimolar solution of contrast agent. The relaxivity of a contrast agent can be influenced by several parameters that are briefly reminded below.

Some compounds have already received approval for clinical use and are currently used for recording the majority of MR images. Most of these MRI contrast agents are complexes of gadolinium(III) as this ion has a high magnetic moment and a long electronic relaxation time. However, this metal ion being toxic, its complexation is needed in order to ensure the innocuousness of the agent during its travel through the body of the patient. The formation of kinetically inert and thermodynamically stable complexes of Gd(III) has been demonstrated with chelating agents such as diethylenetriaminepentaacetic acid (DTPA) and 1,4,7,10-tetracarboxymethyl-1,4,7,10-tetraazacyclododecane (DOTA). Both chelates have received approval, as have some of their substituted derivatives (Fig. 1).

These contrast agents are all non-specific, even if their distribution in the body is far from homogeneous. Indeed, their efficacy in enhancing contrast stems only from their preferential distribution in the blood stream because they are all quite hydrophilic. There thus remains the need for new compounds of improved performances. Increased efficacy, exclusive blood distribution, target-

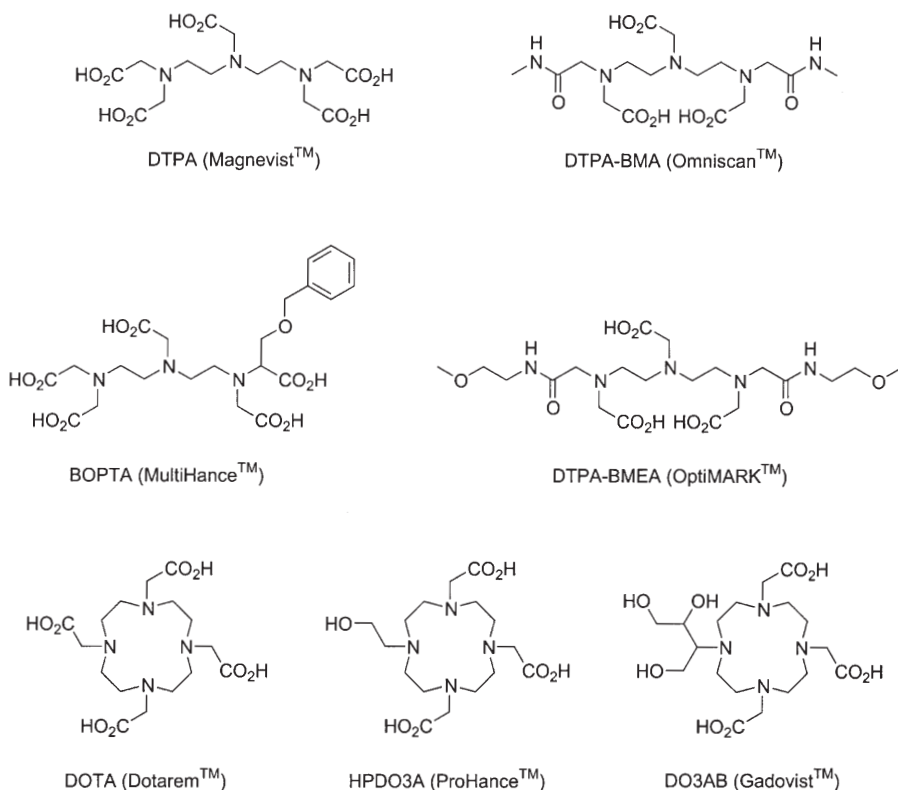


Fig. 1. Clinically approved MRI contrast agents (only the ligands are presented in the figure)

ing, sensing are some of the exciting properties of the new molecules developed during the last few years. The following pages are devoted to the description of major achievements in this ever-growing field of research.

1.2

Relaxivity of Gadolinium(III) Chelates

Several parameters have a strong influence on the relaxivity and this has been summed up in the well-known Solomon-Bloembergen-Morgan equations that are described elsewhere in this book. A short discussion of the parameters controlling the efficacy of a metal complex to enhance the longitudinal and/or axial relaxation rate of water protons is nonetheless needed here in order to gain some understanding of the rationale behind the design of new MRI gadolinium-based contrast agents.

As shown in Fig. 2, the Gd^{3+} ion enhances the relaxation rate of the protons of water molecules located at a distance r from the metal center in the first coordination sphere of the metal ion. The relaxivity is thus primarily affected by the hydration of the metal ion. Toxicity reasons however limit the maximum num-

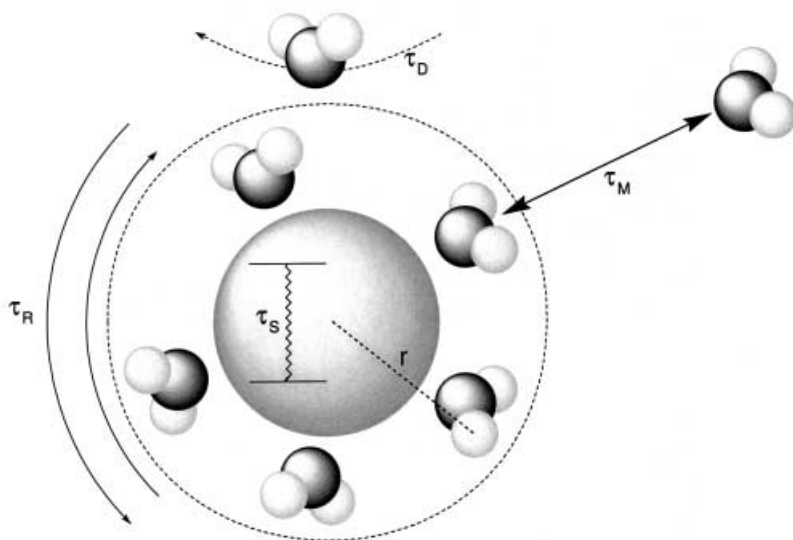


Fig. 2. Relaxivity of a T_1 contrast agent in water, influence of various parameters (see text)

ber of water molecules in this closest vicinity since the Gd^{3+} ion must be complexed to ensure its elimination from the body. Therefore a trade-off must be paid between efficacy and safety. The relaxivity is also strongly influenced by τ_m , the mean residence time of water molecules in the first coordination sphere. A maximum increase in the relaxation rate of high molecular weight chelates is indeed observed for an optimal exchange time between the bulk of the solvent and the first coordination sphere. Diffusion of water molecules near the metal chelate also accounts for a part of the relaxation rate enhancement. Finally, the tumbling rate of the relaxation inducing species also affects the relaxivity of a metal complex and is characterized by the rotational correlation time τ_r . At current imaging fields, slowly rotating chelates do indeed show much higher relaxivities than fast tumbling species.

2

Blood-Pool Contrast Agents

2.1

A Short Description

Noninvasive detection of vascular abnormalities is of the utmost importance in clinical imaging. Indeed, a lot of injuries and diseases manifest themselves through modifications of the vasculature [1, 2]. For example, abnormal angiogenesis (blood vessel growth) is observed in the development of most tumors. Embolism and atherosclerosis also manifest themselves through alterations of the blood vessels, namely through occlusions. Hemorrhage could also be detected noninvasively, which is crucial in injuries or in diseases such as ulcers [1].

Contrast-enhanced magnetic resonance angiography (MRA) could be an interesting alternative to conventional X-ray angiography, for both safety and financial considerations [3].

In order to efficiently image blood vessels, compounds need to stay in the circulation and should not redistribute in the interstitial space. High molecular weight species are therefore highly desirable as such compounds cannot be eliminated by glomerular filtration and do not permeate into the interstitial space [4]. Furthermore, due to longer rotational correlation times τ_r , high molecular weight contrast agents based on gadolinium are characterized by higher relaxivities. This constitutes a major impetus for the continued development of these compounds. Several methodologies have been developed for obtaining high molecular weight MRA contrast agents. A short description of these approaches is given below. The reader is referred to an entire chapter of this book that is devoted to their preparation and use. Using macromolecular agents does not proceed without drawbacks: these big molecules can elicit immunogenic responses as they are usually taken up by the reticulo-endothelial system. Moreover, the toxicity of these compounds might increase dramatically as their longer residence time makes them good candidates for cell uptake and processing.

2.2

Three Ways to Blood-Pool Agents

As suggested by A. Bogdanov [1], the blood vessels can be divided into three components, namely cells (particularly red blood cells), plasma proteins (essentially albumin, the major component) and solvent (water). MRA contrast agents that are being developed target one of these components.

2.2.1

Liposomal Contrast Agents

Red blood cells can be directly targeted but the amount of magnetic resonance contrast agent needed to achieve a good contrast is very high, meaning an altered cell function after labeling [5]. On the other hand, liposomal contrast agents have been obtained that mimic the behavior of circulating cells. Liposomes are vesicles built from a double layer of lipids encapsulating an aqueous cavity. They have the ability to transport substances in the lipid bilayer or the internal aqueous phase. As such, they have been used as a delivery vessel for a number of drugs. Thus, low-molecular-weight iron, manganese or gadolinium chelates have been encapsulated in liposomes [6–8]. However, these are known to disrupt quite easily or to be taken up by the reticulo-endothelial system. Surface modification of the liposomes, such as PEG grafting, may enhance their stability [9, 10]. Polymerization of the lipid bilayer may achieve the same result [11]. Monomeric or polymeric chelates may also be substituted by one or more lipophilic groups in order to take part in the formation of the lipid bilayer [2, 12].

Beside increased blood-pool specificity, these liposomal contrast agents are usually characterized by a high efficacy in enhancing the contrast of MRA

images. Their relaxivity is high because of their high molecular weight and/or because of the restricted free rotation of the low-molecular-weight species inside the cavity of the vesicle.

However, so far, none of these potential MRA contrast agents has found a medical application, probably due to the high cost of their preparation and to patient-safety reasons [1, 13].

2.2.2

Particulate and Polymeric Contrast Agents

These particles and macromolecules are both characterized by a large size, which increases their blood retention by avoiding glomerular filtration. They behave pharmacokinetically similarly to plasma proteins.

Particulate agents have been prepared, such as ultrasmall iron oxides (USPIOs). However, their affinity for the reticulo-endothelial system is quite high, resulting in a fast decrease of the blood-pool concentration. Coated particles have therefore been synthesized (dextran-coated iron oxide nanoparticles or PEG-stabilized hydroxyapatite substituted with manganese). Human clinical trials have confirmed their efficacy in delineating the vasculature [14, 15]. Other particulate agents have been examined as potential gastro-intestinal contrast agents, such as Gd(III) loaded zeolites [16, 17] (gadolite™ from Pharmacyclics), clays [18, 19] or even particulate ion-exchange resins containing a variety of paramagnetic metal ions [20]. Very recently, new gadolinium loaded nanoparticles have been described as another potential gastro-intestinal agent [21]. The core of these particles consists in a methacrylic acid-ethyl acrylate copolymer able to bind Gd(III). This complex is encapsulated in a polymeric shell ensuring sequestration of the metal ion but enabling water exchange.

Many polymeric MRI contrast agents, the majority of which being Gd(III) complexes, have been obtained by using several synthetic methodologies.

Low molecular weight gadolinium chelating agents have been coupled to high molecular weight polymers whether natural [22] (proteins such as HSA) or artificial [23] (polyaminoacids like polylysine, oligosaccharides such as dextrans, dendrimers).

Cavagna et al. [24] have used polyaspartate as a model for polymeric chelating agents. The Gd(III) complex of this homopeptide (40 Gd ions for 220 aspartic acid units) has been characterized and shows a relaxivity per Gd(III) ion about eight times as high as $[\text{Gd}(\text{DOTA})]^-$. Linear and branched copolymeric ligands have therefore been prepared that incorporate DTPA bisamide [25] or DOTA monoamide units [26]. All these new compounds show some degree of enhanced relaxivity compared to their low molecular weight parent compound.

The addition of biocompatible PEG or MPEG chains further enhances residence time of the compounds in the circulation. These hydrophilic polymers also provide some protection from interactions with blood cells and plasma proteins while, at the same time, increasing the molecular weight.

2.2.3

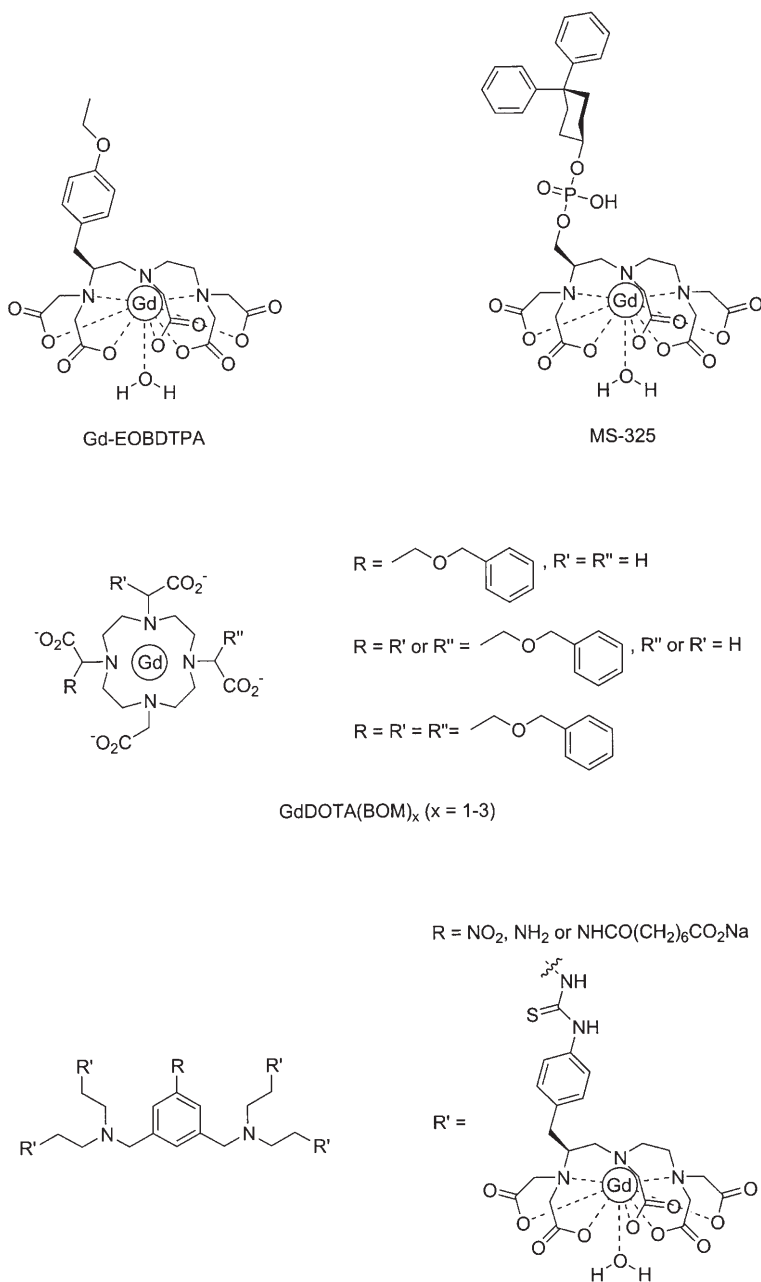
Non-Covalent Binding to Plasma Proteins

Fig. 3. Some amphiphilic ligands able to bind plasma proteins (Gd-EOBDTPA [27, 28]; MS-325 [3, 39]; GdDOTA(BOM)_x [30]; “molecular amplifier” [4])

The preceding classes of MRI contrast agents suffer from some drawbacks. Macromolecular agents may be incompletely excreted resulting in a higher toxicity. An immune response can also be observed following their injection. Furthermore, safety reasons have so far limited the use of liposomal agents to pre-clinical studies. Such concerns may soon find an answer but, in the mean time, research has progressed along another path, that of exploiting non-covalent binding to plasma proteins. Indeed, non-covalent binding being reversible, unbound chelates will be completely excreted through the kidneys or via the hepatobiliary route while bound chelates will remain in the blood stream longer. Amphiphilic ligands have therefore been synthesized by attaching one or more hydrophobic substituents to the chelating moiety (Fig. 3). MS-325, a dicyclohexyl substituted DTPA, has been developed along these lines and is currently undergoing phase III clinical trials [3, 31].

2.3

Remarks and New Approaches

Liposomes, particles and polymers and non-covalent binding to plasma proteins are three approaches towards a common goal: obtaining efficient blood-pool contrast agents. The efficacy of gadolinium based blood-pool agents can be estimated by their longitudinal relaxivity per metal ion, usually measured at 20 MHz. Figure 4 shows that there is a relatively good linear relationship between the 20 MHz relaxivity of several MRI contrast agents and their molecular weight. However, it appears that the relaxivity tends to level out when the molecular weight is higher than 10,000 [32, 33] (higher generation dendrimers, high molecular weight polymers). It should be noted that free rotation at the metal center may be responsible for a shortening of the local rotational correlation time [34] despite the slow rotation of the associated macromolecule.

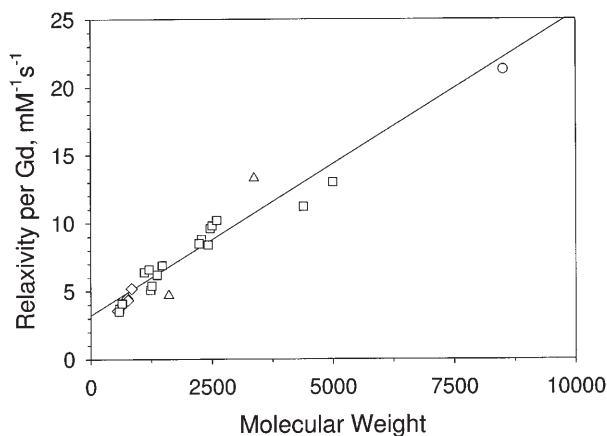


Fig. 4. Plot of relaxivity versus molecular weight for a series of gadolinium based MRI contrast agents (circles: Wiener et al. [32]; diamonds: Aime et al. [35]; triangles: Martin et al. [4]; squares: Ranganathan et al. [36])

It thus seems really important to design sterically hindered compounds where free rotation at the metal center is blocked. In this respect, interesting results have been obtained with the bifunctional chelating agent PhenHDO3A that will be presented later as it was not designed as a blood-pool agent but rather as a smart contrast agent.

Another approach has been tackled with by Sessler et al. [37, 38] who described gadolinium(III) complexes with texaphyrins as potential MRI contrast agents. When the expanded porphyrin ring is substituted by water solubilizing groups (Fig. 5), the chelate is sufficiently water soluble to be injected. It is

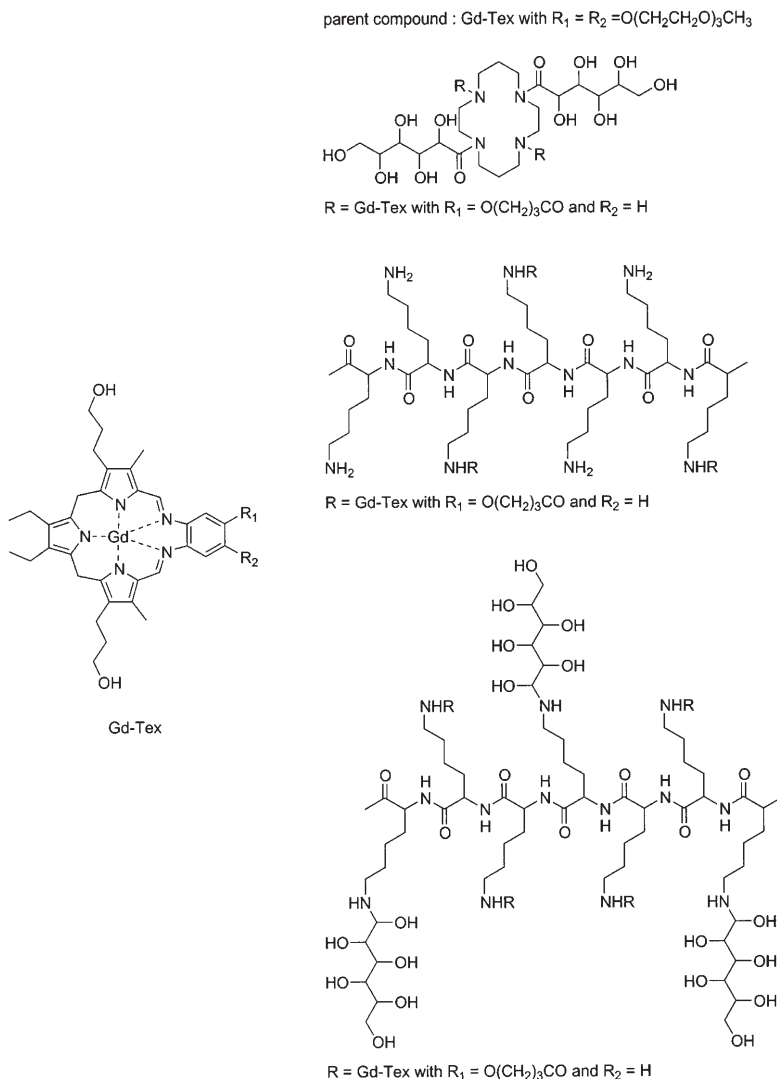


Fig. 5. Gd-texaphyrin derivatives [37, 38]

also physiologically well tolerated and is characterized by a relaxivity of $16.5 \text{ mM}^{-1} \text{ s}^{-1}$ at 50 MHz as can be expected from the high hydration of this planar compound. At 500 MHz, the relaxivity drops to $8 \text{ mM}^{-1} \text{ s}^{-1}$. On the other hand, a Gd-texaphyrin dimer (Fig. 5) exhibits a per gadolinium(III) relaxivity of $40 \text{ mM}^{-1} \text{ s}^{-1}$ at 500 MHz. Polymeric structures have been prepared. They are based on a polylysine backbone substituted with Gd-texaphyrins. δ -Gluconolactone has been added to the latter in order to increase its water solubility. Both compounds display enhanced relaxivities of respectively 90 and $315 \text{ mM}^{-1} \text{ s}^{-1}$ at 500 MHz.

Increasing the molecular weight of a gadolinium chelate does indeed provide a contrast agent with enhanced relaxivity, provided that free rotation at the metal ion is sufficiently hindered. It is not however the only way to improve the efficacy of a contrast agent as described later (see smart contrast agents).

3 Targeting MRI Agents

3.1 Scope and Limitations

Blood-pool agents behave quite similarly to the already approved MRI contrast agents. These molecules are extracellular agents that show a preferential distribution in the body only because of their size. Specificity in contrast enhancement is nonetheless highly desirable. Efficient tumor contrast enhancement could be achieved by targeting receptors on the cell surface. Due to the intrinsically higher resolution of MRI, this would ultimately result in a better three-dimensional delineation of tumors, thus enabling more precise surgical ablation or treatment. Gene therapy could also benefit from targeted MR imaging. Indeed, carefully chosen MRI contrast agents could help monitor gene delivery and expression. Further insight in the process of gene expression at the cellular level would also be gained by developmental biologists. "Smart" contrast agents play an important role for these last applications and will be developed later in this chapter.

This targeting approach does however present some difficulties. Specific organ or tissue delivery may be a problem and sometimes requires direct injection of the contrast agent at the delivery site. While this technique is not suitable for medical application, it is nonetheless quite important for fundamental studies [39]. Extracellular contrast agents, on the other hand, do not require such drastic procedures; intravenous injection is usually performed. Gastrointestinal agents and potential lung MRI contrast media have been administered orally and by inhalation of a spray respectively. Delivery of the diagnostic agent can thus eventually be tackled with. However, as Nunn et al. [6] recently pointed out, biological constraints limit the amount of targeting agent that can bind a targeted receptor. Indeed, targeted receptors are usually present in very low concentration (10^{-9} – 10^{-13} mol/g of tissue). Furthermore, if biological processes are being investigated, saturation of the receptor sites would obviously increase the contrast but it could disrupt the metabolic equilibrium of

Table 1. Minimal detectable concentrations of several contrast agents

Agent ^a	Lowest calculated concentration	References
[GdHPDO3A] ($R_1 = 3.7$)	$5 \cdot 10^{-7}$ mol/g ^c or 100 μ M	[5]
[GdHPDO3A] ($R_1 = 4.1$)	50 μ M ^d	[40]
[GdDTPA] ²⁻ ($R_1 = 4.3$)	100 μ M ^e	[39]
Bound max. relaxivity contrast agent ($R_1 = 200$)	$8.5 \cdot 10^{-10}$ mol/g	[5]
6-dendrimer-GdDTPA ^b ($R_1 = 5800$ per dendrimer)	$1.9 \cdot 10^{-10}$ mol/g	[5, 32]
Superparamagnetic iron oxide ($R_2 = 72000$ per particle)	$1.6 \cdot 10^{-11}$ mol/g	[5]

^a Relaxivity R_1 or R_2 in $\text{mM}^{-1}\text{s}^{-1}$.

^b 6th generation dendrimer substituted with 170 GdDTPA chelates.

^c At about 90 MHz.

^d At 500 MHz.

^e At about 20 MHz.

these same processes and ultimately lead to death. Thus, the main difficulty arises from the relatively low sensitivity of the MRI technique as compared to the target concentration.

Table I presents calculated minimal concentrations of contrast agents that would give visible enhancements in MR images. These concentrations are to be compared with typical receptor concentrations of about 10^{-9} – 10^{-13} mol/g of tissue [5]. Several MRI contrast agents reported in table I are characterized by minimum detectable concentrations that are included in this range. Some have indeed been shown to allow receptor detection in MR contrast enhanced images.

Receptor imaging is still in its infancy and only a few papers dealing with this issue have been published in the recent literature. Several approaches have been proposed and are presented below.

3.2

Cell Surface Targeting

Limitations imposed to the development of receptor targeted MRI contrast agents prompted Aime et al. [41] to propose another approach for tumor cell visualization. Non-covalent binding of negatively charged contrast agents to a positively charged oligomer of amino acids such as polyornithine or polyarginine could lead to accumulation of the contrast agent at the tumor site. Some tumors, such as brain tumors, lung carcinoma and some metastases, are indeed characterized by a larger negative charge on the cell surface than normal cells [42–44]. Three new ligands based on 1,4,7,10-tetraazacyclododecane have been synthesized (Fig. 6). They complex gadolinium in an octadentate fashion (four nitrogens on the macrocyclic ring, three acetate oxygens and one amide oxygen)

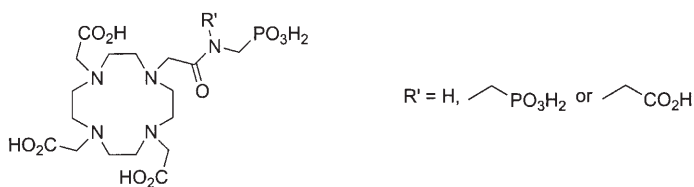


Fig. 6. Three new gadolinium-complexing ionisable ligands [41]

thus ensuring a very stable chelate. One or two ionisable groups (carboxylate or phosphonate) have been introduced on a pendant arm to form ion pairs with the polyaminoacids.

The electrostatic interaction between the small complex and the polyaminoacid depends on the pH and reaches a maximum at about neutral pH. Binding to the polycation results in the formation of a high molecular weight species and thus in an increased relaxivity because the rotational correlation time τ_r increases. The best results were obtained for the complex with two phosphonate groups on the pendant arm bound to a polyornithine containing 140 amino acid residues. As expected, binding decreases in saline and in human serum because of competition by other anions for the binding sites and due to some affinity of the chelates for plasma proteins. Nonetheless, when the diphosphonate substituted complex is dissolved in plasma at about 0.1 mmol/kg, 85% are bound to polyornithine despite the presence of other anions and of plasma proteins. This adduct appears as a good candidate for the proposed application.

This approach is argued by the authors as a promising alternative to other targeting methods. Indeed, the injected paramagnetic species is a small chelate that can be easily eliminated by the kidneys thus reducing the risks of toxic metal ion release. Furthermore, a pretargeting approach may be applied: first, the polyaminoacid is administered and allowed to localize and second, after blood clearance of the excess, the low molecular weight paramagnetic chelate is injected. This pretargeting approach would alleviate the problems associated with delivery of large molecules such as antibodies or even polyaminoacids to tumor cells.

3.3

Receptor Targeting

Efficient receptor targeting remains a major goal in the design of MRI contrast agents. Many systems have already been described notwithstanding the difficulties we addressed above.

3.3.3

Labeled Antibodies

Monoclonal antibodies can be grown against a variety of receptor sites. They thus represent an important category of targeting vectors. Their polypeptide chain may be labeled with many different signaling substituents such as

radionuclides, fluorescent moieties or even MRI contrast agents. Care must be taken to maintain the affinity of the antibody for its antigen, which in turn limits the number of groups that can be attached. The overall change in the net electrical charge of the substituted antibody should also be taken into account because it could alter its biodistribution.

It was realized very early on that attaching gadolinium(III) chelates to an antibody could lead to poor contrast agents. Unger et al. [45] substituted an IgG and an anticarcinoembryonic antigen (anti-CEA) monoclonal antibody with 4 and 1.5 GdDTPA chelates respectively. No measurable loss of antigen binding ability was reported. The authors were able to demonstrate that a minimal concentration of 10^{-1} mM in modified IgG was required for in vitro contrast enhancement at 0.35 T. Injecting the anti-CEA mAb to tumor-bearing hamsters resulted in a 10^{-4} mM concentration of antibody at the tumor site and thus in no contrast enhancement of the MR images. Very similar results were obtained by Anderson-Berg et al. [46] who could not see any contrast enhancement of a tumor in vivo even though a small T_1 difference was observed in excised tumors.

However, these early findings did not detract from the search for effective MRI contrast agents based on substituted antibodies. Several groups were indeed able to get some promising results with different approaches to alleviate the sensitivity problem. By using manganese instead of gadolinium, Khaw et al. [47] could actually prepare a conjugate between an antibody to cardiac myosin and a MnDTPA chelate that enhances the contrast of MR images of infarct-damaged cardiac tissue as the labeled antibody strongly binds to infarcted regions. Moreover, Curtet et al. [48–50] demonstrated the possibility of extensive substitution of some antibodies with minimal loss of immunoreactivity. Indeed, the authors modified two human colon adenocarcinoma monoclonal antibodies, namely 19–9 and 73–3, with as much as 25 GdDTPA without any noticeable decrease in antigen binding ability. The longitudinal relaxation time of targeted tumors was measured in vitro and showed a measurable 20% decrease. In vivo imaging was performed and good contrast was observed 24 hours after injection.

Polymeric protein mixtures were prepared by Kornguth et al. [51] by cross-linking anti-human T cell antibodies, gelatin and bovine serum albumin with DTPA dianhydride. The Gd(III) chelates were prepared and the protein mixture was used to effectively image human T cell implants, 48 to 72 hours after injection, in the presence of bovine T cells that were not contrast enhanced.

Dendrimeric and polymeric chelates can also be attached to mAbs in order to increase the number of relaxation agents per antibody without losing immunoreactivity. Thus, Shreve and Aisen [52] covalently linked polymeric paramagnetic ion chelates to mAbs. The antigen binding capacity of the substituted mAb was maintained in vitro. With about 50 chelates per mAb, a significant reduction of the proton longitudinal relaxation time was observed when the concentration of bound antibodies was less than $2\text{ }\mu\text{M}$. Similarly, a GdDTPA-substituted polylysine was coupled by reductive amination to a monoclonal antibody (RA96) after periodate oxidation [53]. This high molecular weight conjugate was still immunoreactive albeit less than the unreacted mAb (30%

decrease) and localized quite specifically at the tumor site (8.72% of the applied dose per gram). This specific binding was deemed sufficient to give specific contrast enhancement of the tumor site in MR images. By coupling GdDTPA and GdDOTA substituted polylysines to anti-CEA F(ab')₂ antibody fragments, Curtet et al. [54] managed to conjugate 24 to 28 paramagnetic metal ions per antibody while keeping the immunoreactivity of the labeled antibody to 80–85%. Relaxivity data showed that, as a result of their slower reorientation rate, both conjugated polychelates are more efficient than the unconjugated species and their low molecular weight counterparts, GdDTPA and GdDOTA, and that the GdDOTA derivative gives the highest enhancement. Conjugates localize slowly at the tumor site (10 to 15% of the injected dose). Tumor enhancement in the MR images was observed in 50% of the tested mice.

In order to ensure high contrast enhancement, mAbs can also be attached to large MRI contrast agents particles such as liposomes and nanoparticles. This method has been applied by Sipkins et al. [55] and Anderson et al. [56] for assessing tumor angiogenesis *in vivo*. *In vivo* monitoring of angiogenesis appears as an interesting indirect method for the detection of tumor growth and for assessing the efficacy of therapies. Blood vessels that grow during tumor angiogenesis are tortuous and very permeable, sometimes even to large proteins [57]. Moreover, they have been shown to express specific molecules such as integrin $\alpha_v\beta_3$ [58, 59]. By targeting the $\alpha_v\beta_3$ integrin, contrast enhanced MRI could provide a non-invasive method for monitoring tumor growth. MRI contrast agents were developed along these lines. Gadolinium loaded polymerized liposomes were prepared and $\alpha_v\beta_3$ integrin targeting was provided by conjugation of biotinylated mAbs to the liposomes via avidin linkers. The contrast agent was injected and allowed to accumulate at the tumor site for 24 hours. Clear delineation of the heterogeneous tumor vasculature was observed as opposed to the homogeneous enhancement observed when unconjugated liposomes were injected.

A similar approach was proposed by Anderson et al. [56] (Fig. 7). A lipophilic GdDTPA derivative was incorporated into a perfluorocarbon nanoparticle emulsion and a biotinylated lipid was added to the emulsion. Targeted Gd(III)-loaded nanoparticles were obtained by adding first avidin then the biotinylated mAb DM101, which is specific for the $\alpha_v\beta_3$ integrin. Several experiments were performed and the validity of this original approach was demonstrated. Indeed, only rabbits that were injected with the targeted agent showed a significant contrast enhancement (25%, 90 minutes after injection). Furthermore, if the receptor sites were saturated by injection of the free DM101 mAb prior to the injection of the targeted MRI contrast media, no enhancement could be detected. An efficient blood clot specific contrast agent was obtained by replacing the DM101 antibody by a biotinylated antifibrin antibody [60]. The biotin-avidin coupling technique had been applied earlier by Bulte et al. [61] who labeled human lymphocytes with specific biotinylated mAbs. Streptavidin was then added followed by biotinylated dextran coated iron oxide particles. Good negative contrast enhancement was observed in T₂-weighted images of lymphocyte suspensions but also, with the appropriate mAb, for the *in vivo* detection of small cell lung carcinoma implanted in mice brains [62].

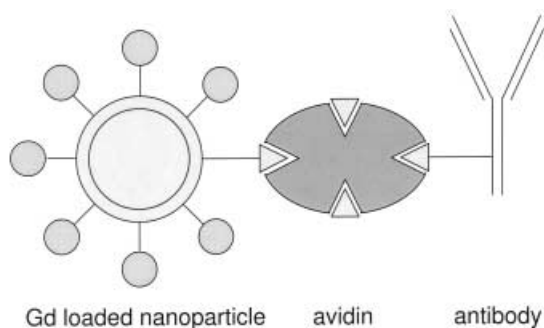


Fig. 7. Schematic representation of a Gd-loaded nanoparticle targeted to an antigen by using a biotin-avidin linkage to a mAb (gray circles represent Gd(III) chelates and white triangles stand for biotin), adapted from Anderson et al. [56], see text)

Despite many difficulties, efficient targeted MRI contrast agents have been developed based on antibodies. Low concentration of receptor sites has been tackled with and elegant solutions have been proposed. Antibody labeling may therefore find a place in the arsenal of target specific MRI contrast agents.

3.3.2

Low Molecular Weight Targeting Species

One of the biggest drawbacks of labeled antibodies is certainly their very slow accumulation at the target site. Being high molecular weight species, antibodies have a very slow diffusion rate towards tumor antigens that are usually buried deep inside the tumor mass where blood flows slowly. Localization of the antibody may therefore take days or even weeks, which is not very practical and can increase toxicity (cell internalization and metal ion release). Low molecular weight species, on the other hand, diffuse more easily and can be eliminated rapidly by glomerular filtration through the kidneys. It would thus be highly desirable to combine low molecular weight species and receptor targeting. This idea has been considered by several research groups who proposed some interesting approaches.

Early examples dealt with the targeting by MRI contrast agents of the asialoglycoprotein receptor that is expressed on the surface of hepatocytes. Labeled iron oxide particles [63, 64] and polylysine substituted with Gd-DTPA chelates [65] were used and good results were obtained due to the rapid turnover of the targeted receptor. Targeting of the adrenal gland was also achieved by using a cholesterol substituted Gd(III) chelate [66] represented in Fig. 8. Cholesterol accumulation at the target site resulted in a 162% increase of the MRI signal of the adrenal gland.

The pre-targeting paradigm has been described by Paganelli et al. [67]. Owing to the slow accumulation of an antibody at its target, the authors proposed to first inject a biotinylated mAb and to let it localize at the targeted site before adding avidin or streptavidin that can bind strongly to the biotin attached to the

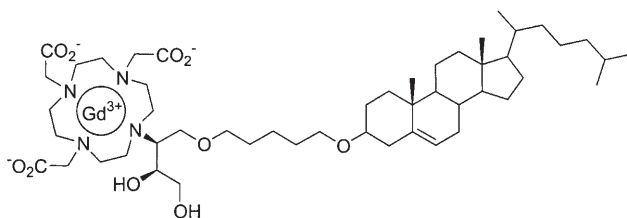


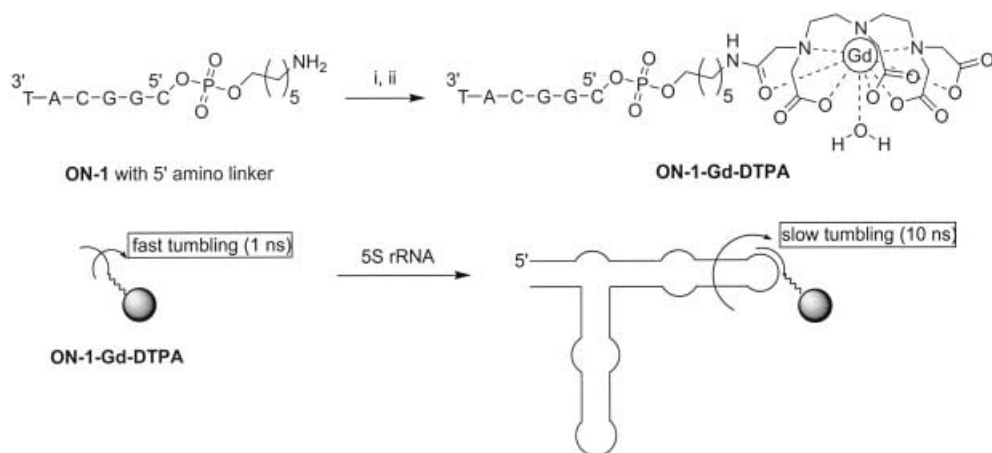
Fig. 8. Cholesterol-substituted Gd-DO3A complex targeted to the adrenal gland [66]

mAb. Biotinylated albumin can then be injected to remove excess avidin not bound to the targeted site. Finally, a biotinylated therapeutic or diagnostic agent is injected, that will bind the antibody-avidin complex while the excess is excreted through the kidneys. The pre-targeting concept is particularly well suited to specific delivery of radionuclides [68, 69] and cytotoxic agents to a tumor site. Damage to healthy tissue is indeed prevented as antibodies, that can be non-specifically internalized, have not been labeled with any toxic group. It does however suffer from the same limitations as MRI contrast agents based on antibodies: the number of receptor sites on the cell surface may not be sufficient to ensure contrast enhancement of the targeted region. New protocols are nevertheless being developed for increasing the amount of radioactivity delivered to a tumor site by the pretargeting approach. For example, biotinylated dendrimers have recently been evaluated for their ability to cross-link streptavidin. Generation 2, 3 and 4 dendrimers can indeed bind about 4 equivalents of radioiodinated streptavidin. Owing to their demonstrated rapid blood clearance, further investigation of their efficacy in enhancing radionuclide delivery was deemed necessary [70]. This extension of the pretargeting approach could clearly benefit the development of MRI pretargeting contrast media.

The Bertozzi group at Berkeley has explored another route [71] based on the abnormal glycosylation of tumor cell surfaces. The monosaccharide sialic acid is indeed overexpressed on many tumor cell oligosaccharide antigens. While sialic acid residues play many important roles [72], their abnormal expression on certain tumor cells has been related to the proliferation and metastatic state of certain types of cancers. Thus, overexpression of the glycosphingolipid disialosylgalactosylgloboside (Fig. 9) by renal cell carcinoma has been linked to the potential ability of these cells for forming lung metastases [73].

The very high difference between the density of sialic acid residues on cancer cell surfaces (up to 10^9 per cell) and on normal cells (only $20 \cdot 10^6$ for a normal human erythrocyte) has been exploited to develop a new MRI contrast agent that would specifically target the cancerous cell surface. Peracetylated *N*-levulinoylmannosamine was used as a substrate for introducing ketone-substituted sialic acids on tumor cell surfaces by taking advantage of the enzymes in the biosynthetic pathway of sialosides (Scheme 1). The ketone group thus attached to the cell surface does not prevent normal cell function. This reactive moiety does however provide a selective anchor for covalent binding of hydroxylamines or hydrazines [74, 75]. As shown in scheme 1, the addition of an aminoxy-sub-

One further advantage of low molecular weight species over labeled antibodies is the potential increase in relaxivity upon binding. As we reminded in the introduction, the rotational correlation time τ_r strongly affects the relaxivity of the contrast agent. All other parameters equal, slow tumbling molecules enhance solvent relaxation more effectively than rapidly reorienting ones. As pointed out by Hines et al. [76], this could favorably impact the development of targeted MRI contrast agents of higher efficacy. The authors applied this concept to design a new class of potential MRI contrast agents, namely paramagnetic oligonucleotides. By covalently binding a gadolinium(III) chelate to relatively short oligonucleotides – 6 bases –, they obtained paramagnetic probes that can act either as antisense targeting agents, thus recognizing a complementary sequence, or as aptamers, i. e. ligands able to bind antigenic sites on a cell surface [77] (Scheme 2). In any case, binding to the target should result in an increase of the rotational correlation time and therefore in a higher relaxivity. This was indeed observed by antisense binding of a paramagnetic oligonucleotide, ON-1-Gd-DTPA, to the ribosomal 5S rRNA of *E. Coli*. A fair 16% increase in relaxivity was observed upon binding. Additional experiments established the correlation between the observed enhancement and binding to the 5S rRNA. This early result shows the promise of this approach. Optimization of the targeted agent is obviously necessary but could lead to interesting new compounds.



Scheme 2. Top, synthesis of a paramagnetic oligonucleotide. (i) DTPA dianhydride in DMSO; (ii) GdCl₃; bottom: binding of the antisense probe to *E. Coli* 5S rRNA [77]

3.4

Internalization: Fluid Phase and Receptor Mediated Endocytosis

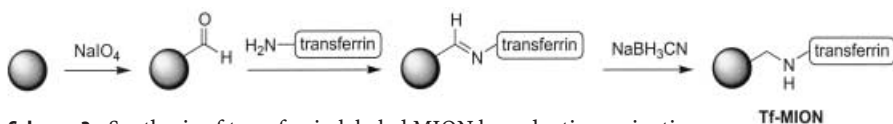
Apart from attaching MRI contrast agents to the cell surface, cell labeling may also be achieved by using cell uptake processes. Endocytosis, whether receptor mediated or not, and phagocytosis are mechanisms that may be considered and that could lead to accumulation of a magnetic label inside the cell. Provided the

internalization mechanism is efficient enough, the concentration of MRI contrast agent inside the cell will clearly exceed that which can be expected by binding on the surface of the same cell. This approach could therefore alleviate the main problem traditionally associated with cell surface targeting contrast agents, i.e. concentration. Several procedures have been devised to take advantage of the endocytosis processes for intracellular magnetic labeling.

Fluid phase endocytosis was the first mechanism to be considered for internalization of magnetic labels, as it does not rely on the presence of receptors on the surface of the cell. It can be a very efficient mechanism especially for undifferentiated and dividing cells. For example, gadolinium(III) texaphyrin, Gd-Tex (Fig. 5) has been shown to accumulate selectively and effectively at tumor sites [78]. Fluid phase endocytosis of dextran coated monocrystalline iron oxide nanoparticles (MION) has also been studied and gave interesting results [79–82], cell functions being maintained after endocytosis. Unfortunately, this mechanism is generally not very efficient, particularly in non-dividing cells [83].

Receptor mediated endocytosis, on the other hand, requires recognition by the receptor before internalization of the molecule. So far, two receptor mediated endocytosis protocols have mainly been studied for potential applications in MRI contrast enhancement, namely the transferrin and folic acid receptor systems.

Weissleder et al. [84] first showed that the human transferrin receptor (hTfR) can be used to internalize MRI contrast agents. The hTfR regulates cellular uptake of iron from transferrin, a plasmatic iron transport protein [85], via a receptor mediated endocytosis mechanism. Thus, MION particles (dextran coated iron oxide) were oxidized with sodium periodate. Holotransferrin was added and the resulting Schiff base adduct was reduced with sodium cyanoborohydride to give transferrin labeled MIONs, Tf-MION (Scheme 3).



Scheme 3. Synthesis of transferrin labeled MION by reductive amination

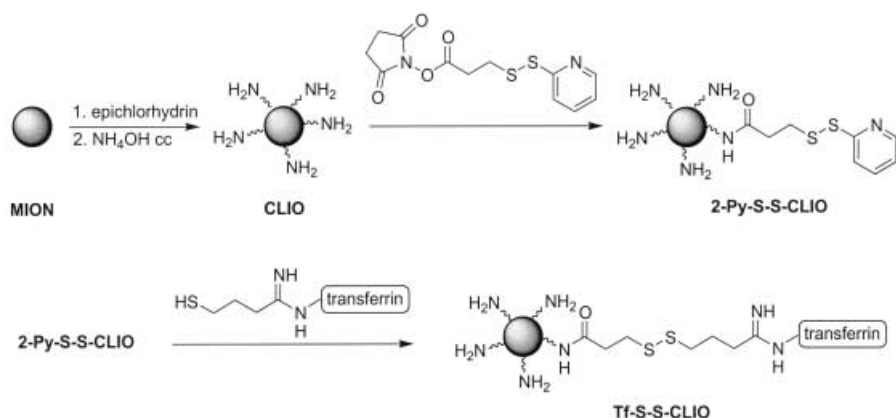
Cellular uptake of the targeted nanoparticles was measured and competition experiments with transferrin allowed to demonstrate that the magnetic nanoparticles were internalized mostly via the hTfR, although some non specific fluid phase endocytosis was also taking place. Finally both T_1 - and T_2 -weighted MR images of cell pellets in agar displayed enhanced contrast when transferrin labeled MIONs were internalized. This process is more efficient than transferrin endocytosis as it results in a significantly higher concentration of iron per cell ($1.68 \cdot 10^{10}$ instead of $8.7 \cdot 10^6$ in a specific example) because there is no downregulation of the targeted-MION uptake. Bulte et al. [86] labeled oligodendrocyte progenitor cells by using the same approach and successfully followed their migration with three-dimensional MR microscopy, thus demonstrating the viability of MRI tracking of cell migration, an essential step in the study of neur-

al cell transplantation. In a subsequent paper [87], this approach was applied *in vivo* in mice for imaging gene expression. Sarcoma cells were transfected with a gene encoding for an engineered transferrin receptor lacking iron downregulation elements. These cells were thus constantly overexpressing the engineered TfR. Transfected and control tumors were then injected into mice. Experiments demonstrated a strong correlation between overexpression of engineered TfR and uptake of transferrin-labeled MION, as about 500 % more labeled iron oxide nanoparticles were taken up by transfected cells than by control cells. MR images showed no contrast enhancement of the transfected tumor due to endogenous sources of iron only, but 24 hours after injection of labeled iron oxide nanoparticles, a clear difference between transfected and control tumor could be seen in T_2 -weighted images.

This first demonstration of MRI detection of gene expression holds promises for future applications. Imaging gene expression is indeed a crucial step both on a fundamental point of view, particularly in embryology, and on a practical point of view, especially in gene therapy. Imaging could play an important role in the rapid development of gene therapy as it could be used to demonstrate and quantify gene delivery by minimally invasive techniques and to monitor expression of delivered gene [88]. Nuclear imaging has already been applied but it suffers from a lack of resolution. Optical techniques may also be used but are of limited applicability for imaging in deep tissues. MR imaging, on the other hand, potentially offers very high resolution. Its applicability may however be hampered by its intrinsically low sensitivity although new developments in contrast agent design try to remedy this situation.

One example of a superior design has been reported by Högemann et al. [89] who reported on the preparation of improved transferrin-labeled MIONs. Indeed, coupling of transferrin to MION via periodate oxidation and Schiff base reduction causes a decrease of the protein affinity to its receptor. A dextran-coated monodispersed iron oxide colloid (MION) was thus cross-linked with epichlorohydrine. Amino groups were generated by heating in ammonia. The amino-substituted cross-linked iron oxide (CLIO) was then reacted with a bifunctional linker. The 2-pyridyl disulfide moiety was finally used to link CLIO to a transferrin modified by reaction with 2-iminothiolane (Scheme 4). This new reaction scheme allowed binding of about 4 times more transferrin per nanoparticle. Uptake was also substantially improved, which resulted in a 16-fold increase in *in vitro* efficacy of the contrast agent.

Not only gene expression, as in the preceding example, but also gene delivery may be followed by MR imaging. An original procedure was indeed proposed by Meade and coworkers [90] several years ago. Using electrostatic interactions, they were able to build a complex framework comprising negatively charged DNA and positively charged polylysine chains. By carefully choosing the substitution of the polyamino acids, DNA delivery and contrast enhancement could be achieved at the same time. Thus, poly-L-lysine was conjugated with transferrin in order to take advantage of the transferrin receptor endocytosis pathway. Similarly, poly-D-lysine was reacted with DTPA dianhydride and the polychelate was metallated with Gd(III). Enough side chains were left free to ensure electrostatic binding to DNA (Scheme 5). Cells were transfected *in vitro* with the



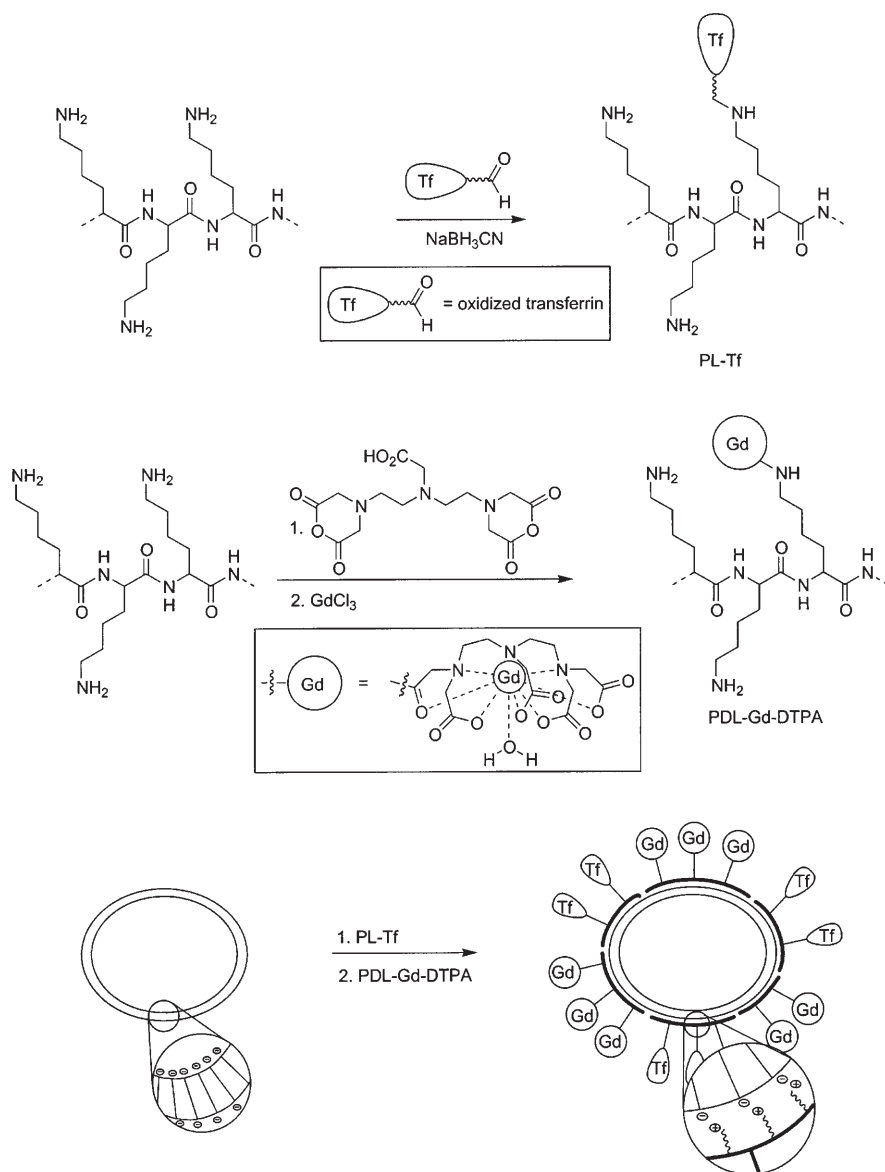
Scheme 4. Synthesis of transferrin labeled CLIO (Tf-S-S-CLIO) as proposed by Högemann et al. [89]

ternary complex formed between the luciferase plasmid and the substituted polylysines. Gene delivery and expression was established easily as it could be determined from the measurement of the fluorescence of the expressed luciferase. A two-fold increase of the intensity of T_1 -weighted MR images of capillary tubes containing transfected cells demonstrated the effective co-delivery of the MRI contrast agent. About 1200 Gd(III) ions were taken up in each cell which exceeds by far the number of chelates that can be attached to a monoclonal antibody.

Recently, interesting results were obtained with a folate receptor targeted MRI contrast agent [91]. Indeed, the folate receptor binds highly specifically to folic acid and is overexpressed in a variety of tumors, such as ovarian carcinoma [92]. Furthermore, the conjugation of high molecular weight species to the γ -carboxylic group of folic acid does not affect its ability to bind to its receptor [93, 94]. A dendrimer-core MRI contrast agent was thus synthesized (Scheme 6). A 4th generation PAMAMTM dendrimer was reacted with folic acid in the presence of carbodiimide. The remaining amine functionalities were then substituted with DTPA-like ligands by reaction with a DTPA substituted with an isothiocyanate moiety. Complexation of Gd(III) was performed as the last step [95].

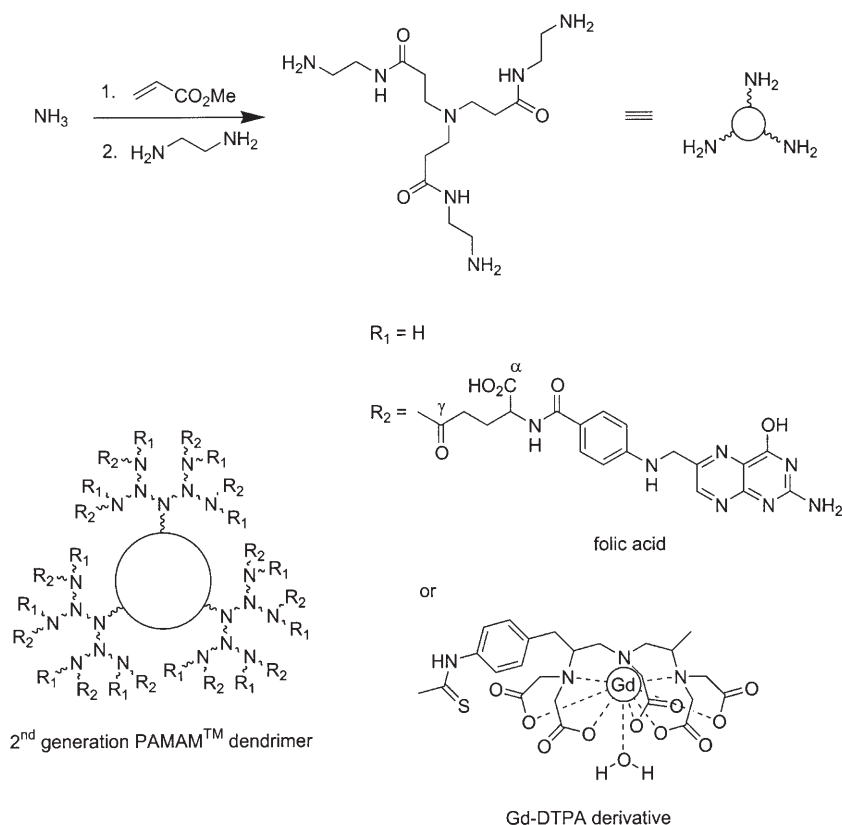
Compared with the extracellular agent Gd-HPDO3A, the targeted dendrimeric contrast agent gave a much higher contrast enhancement of human ovarian tumors that had been implanted in mice (-33% signal intensity compared to $+8\%$ in T_2 -weighted images recorded 24 hours after injection). These results confirmed earlier *in vitro* work [95]. Unfortunately, the mechanism responsible for tumor accumulation is still unknown.

Many cells, such as lymphocytes, do however lack efficient internalizing receptor systems. The development of a new and effective internalizing pathway thus appears as a very important goal. Weissleder et al. [83, 96] have tried to develop such a system by attaching a superparamagnetic iron oxide to a membrane translocating signal (MTS) peptide. Several MTSs have been described

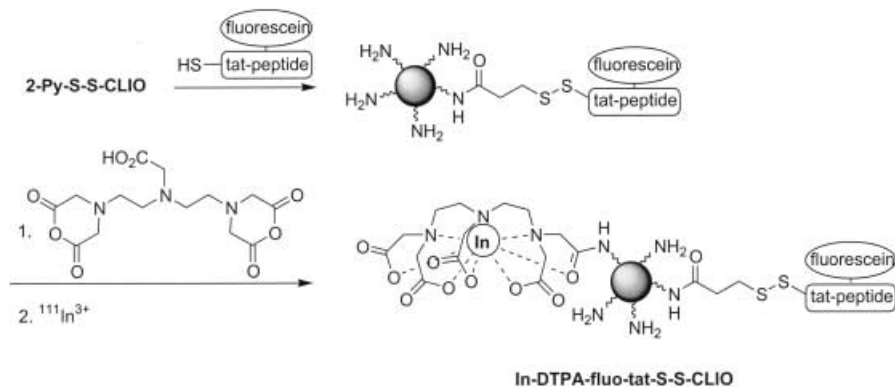


Scheme 5. Co-delivery of DNA and an MRI contrast agent according to Meade et al. [90]

but Weissleder chose to bind a short sequence of 10 amino acid residues from the HIV-1 tat protein that has been demonstrated to promote translocation of various molecules [97]. The 2-pyridyl-disulfide activated CLIO was conjugated to a fluorescein labeled tat-peptide (terminated by a Cys-Gly-Gly sequence) to get a MTS labeled superparamagnetic iron oxide (Scheme 7).



Scheme 6. Folate-targeted dendrimeric contrast agent (a 2nd generation species is presented); on a 4th generation dendrimer, 3 to 5 peripheral amine groups are randomly substituted by folic acid, the rest being conjugated to Gd-DTPA chelates



Scheme 7. Preparation of tat-peptide labeled superparamagnetic iron oxide particles (In-DTPA-fluo-tat-S-S-CLIO) according to Weissleder et al. [96]

Cellular uptake of tat-labeled iron oxide nanoparticles by three different cell lines was shown to be about 100-fold higher than that of unlabeled MION. This very effective internalization process resulted in as high as $12.7 \cdot 10^6$ particles per cell. It was therefore possible to record highly contrasted T_2 -weighted MR images of cell cultures. This method has since been applied for in vivo tracking of neural and hematopoietic progenitor cells [83]. The tat-labeled CLIO nanoparticles were further derivatized with DTPA dianhydride, so that ^{111}In could be chelated for simultaneous nuclear imaging (Scheme 7). Cells were then loaded with these nanoparticles. Their viability and in vivo distribution was demonstrated to be unaffected by the iron-load. Single cells could be visualized in vitro by magnetic resonance imaging at high field (14.1 T). In vivo experiments at lower field proved that between 1 and 10 labeled cells per voxel in the liver are enough to get a 32% contrast enhancement (organ intensity is reduced due to magnetic susceptibility effects of the iron oxide nanoparticles). Gd(III) and Dy(III) DOTA-like chelates were conjugated to a similar tat membrane translocation peptide [98] (Fig. 10). Cellular uptake could be established by using the ^{111}In analog of the labeled lanthanide chelate, while negligible internalization of the unlabeled ^{111}In -DOTA complex was observed. Depending on the nature of the lanthanide ion, MRI of labeled cells showed a positive or negative contrast enhancement of labeled cells. Intracellular concentration of the complex is therefore sufficient for imaging purpose even if the tat-DOTA Gd(III) complex is characterized by a lower relaxivity when inside the cell ($2.2 \text{ mM}^{-1} \text{ s}^{-1}$ at 1.5 T and 20°C) than in aqueous solution ($4.1 \text{ mM}^{-1} \text{ s}^{-1}$ at 1.5 T and 20°C), as could be expected because of the slower intracellular water diffusion rate.

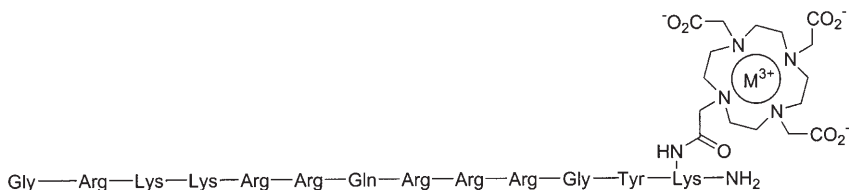


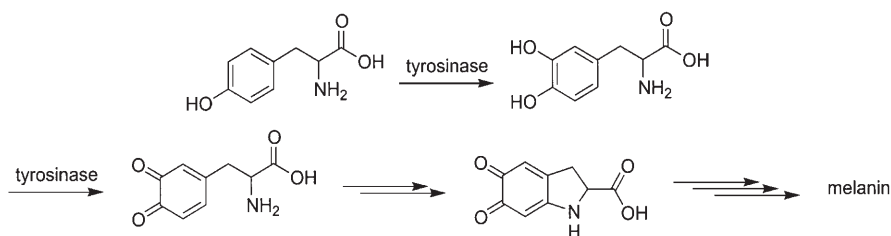
Fig. 10. Structure of a tat-peptide labeled DOTA chelate [98] ($M^{3+} = \text{Dy}^{3+}, \text{Gd}^{3+}$ or $^{111}\text{In}^{3+}$)

3.5

Direct Imaging of Gene Expression

In vivo monitoring of gene expression represents one of the challenges facing gene therapy. As we mentioned earlier, solving this problem would also greatly benefit developmental biology by allowing scientists to map gene expression and to follow cell migration. We have described several such examples that use targeted MRI contrast agents in preceding pages. Another possibility has been explored by Weissleder et al. [99, 100]. The authors hypothesized that expression of the tyrosinase gene could be imaged by following the product of this expression, i.e. melanin. Melanin production does indeed depend on tyrosinase as this enzyme catalyzes the first two steps of its synthesis, namely the hydroxylation of

tyrosine in dioxyphenylalanine (DOPA) and the oxidation of DOPA in DOPAquinone. DOPAquinone then goes through several synthetic intermediates to ultimately form melanin (Scheme 8). Furthermore, melanin is known for its high affinity for metal ions, particularly iron.



Scheme 8. Synthesis of melanin from tyrosine

Non melanotic cells were thus transfected with a tyrosinase-encoding gene and monitored for gene expression. Binding of ^{111}In by melanin was demonstrated by scintigraphy of control and transfected cell cultures. Similarly, T_1 -weighted MR images of cells grown in an iron-supplemented medium validated the hypothesis as only those cells that were transfected showed a higher signal intensity. The tyrosinase gene could thus act as a reporter gene, i.e. a marker of gene delivery.

Nevertheless, some issues have to be addressed before this approach can be applied. Firstly, the tyrosinase gene is quite large and would be difficult to add to a delivery vector. Secondly, melanin production may be too low in vivo for effective MR detection of its metal complex [100]. Finally, potentially high toxicity of melanin and its precursors could restrict the applicability of this reporter gene [99].

4 Smart Contrast Agents

4.1 Definition

As opposed to extracellular agents, the so-called smart MRI contrast agents generate a signal that depends on some variable in their immediate environment (Fig. 11). Various stimuli, ranging from pH to enzymes, have been exploited for generating intelligent agents. Several examples are outlined below. It should be remembered here that the percent change in relaxivity, and not its absolute value, is probably the most important factor for obtaining an efficient smart contrast agent. As could be expected, smart contrast agents have been built on Gd(III) systems because their relaxivity can be dictated by their environment. The number of water molecules in the first coordination sphere, the water exchange rate and the rotational correlation time have a strong effect on the relaxivity of the compounds and, as exemplified below, can be influenced by many factors.

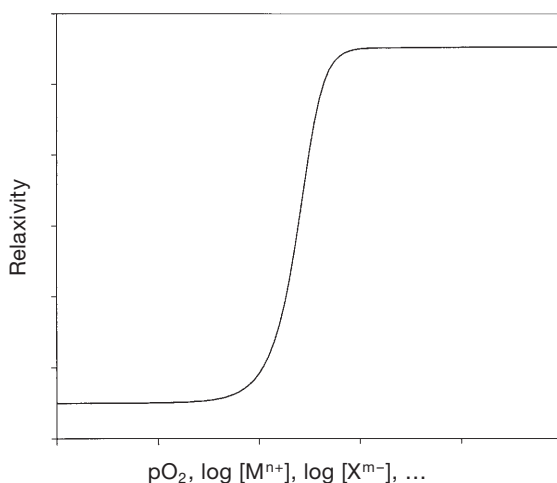


Fig. 11. Ideal relaxivity behavior of a smart contrast agent in response to a stimulus

4.2

Several Examples

4.2.1

Temperature Sensitive

Hyperthermia is an important therapeutic tool in the treatment of tumors. Its application does however require a tight control of the temperature, hence the need for contrast agents that would allow its constant monitoring during the entire therapy. Magnetic resonance spectroscopy has already been proposed for measuring the temperature of a sample. Indeed, Aime et al. [101] measured the temperature dependence of the ¹H chemical shift of a methyl group of an Yb(III) chelate. A linear correlation was found for the lanthanide-induced shift in the explored temperature domain. It was however later recognized that the observed shift depends on the nature of the tissue in which the MRI spectroscopic probe is placed, thus limiting the applicability of this technique to relative measurements at best [102]. The problem of temperature monitoring was attacked from another angle by Fossheim et al. [103], who synthesized a temperature sensitive liposomal MRI contrast agent (Fig. 12). Liposomal composition was chosen such that the membrane phase transition, from gel to liquid crystal, was taking place at the right temperature. This phase transition is indeed accompanied by a change in the membrane permeability to water molecules. At a temperature below the transition, the water exchange rate is fairly slow and the relaxivity of the encapsulated contrast agent remains low while, above the transition temperature, water exchanges rapidly through a more permeable membrane and the efficacy of the contrast agent increases dramatically. By adjusting the composition of the lipid membrane of the liposome, the transition temperature can be fine-tuned in order to suit the needs.

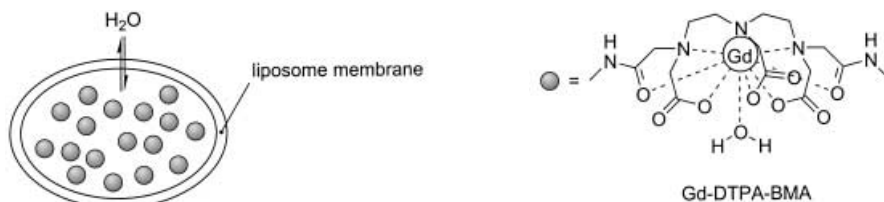


Fig. 12. Thermosensitive liposomal MRI contrast agent as described by Fossheim et al. [103]

4.2.2

pH Sensitive

The reversal of the pH gradient at tumor cells has been known for quite some time. While, in normal tissue, the extracellular medium is slightly basic, the opposite situation is observed in tumor tissues [104]. The intracellular pH, on the other hand, is almost the same for both kinds of cells due to homeostatic mechanisms. Therefore triggering MRI contrast agents by pH variation seems like a promising method for highlighting tumors. Several pH sensitive MRI contrast agents have already been developed.

The gadolinium(III) complex of a DOTA tetraamide derivative (Fig. 13) has been prepared by Zhang et al. [105] who observed the interesting behavior of its relaxivity versus pH. Indeed, starting from pH 4, the relaxivity first increases until pH 6. It then decreases until reaching a minimum at pH 8.5; it remains at this minimum between pH 8.5 and 10.5 then increases again. A complete analysis of the system was performed, including the recording of ^{31}P and ^{17}O NMR spectra and fluorescence measurements on isostructural lanthanide complexes. The unusual pH dependence of the relaxivity could be accounted for by the presence on the ligand molecule of uncoordinated phosphonate groups. The protonation of these ionisable groups between pH 9 and 6 can catalyze the exchange of protons between the bound water molecule and the bulk by providing an efficient hydrogen bond network. This network could be disrupted at lower pHs by further protonation, leading to a decreased relaxivity. The relaxivity increase observed at higher pH can be ascribed to a facile exchange of bound water protons catalyzed by hydroxyl ions. Careful modification of a simple Gd(III) complex can thus provide a pH sensitive contrast agent.

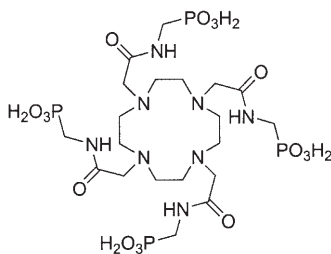


Fig. 13. DOTA tetraamide derivative, the Gd(III) complex of which is a pH sensitive MRI contrast agent

Advantage has also been taken from the formation of a ternary complex between a Gd(III) chelate and carbonate ions [106]. The coordination sphere of a Gd(III) complexed by a heptadentate ligand shown in Fig. 14 is incomplete. The relaxivity of this complex can therefore be affected by the saturation of its coordination sphere either by two water molecules or a bidentate ligand such as hydrogenocarbonate (Fig. 14). This was readily observed by measuring the relaxivity of the complex as a function of pH in a saturated aqueous solution of sodium hydrogenocarbonate. The relaxivity of the complex changes from about $7.5 \text{ mM}^{-1}\text{s}^{-1}$ at low pH to $1.9 \text{ mM}^{-1}\text{s}^{-1}$ at high pH, reflecting the replacement of two water molecules in the first coordination sphere by a carbonate ion.

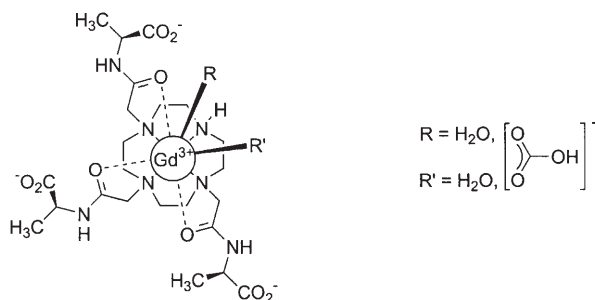


Fig. 14. Hydrogenocarbonate and pH-sensitive MRI contrast agent [106]

The degree of hydration of Gd(III) ions also plays the important role in the pH dependence of a polyionic MRI contrast agent described by Mikawa et al. [107, 108]. A poly-Gd-DTPA chelate was prepared by reaction of DTPA dianhydride with 1,3-propanediamine followed by Gd(III) chelation. In the right pH range, the excess negative charge of the poly-Gd-DTPA complex can then be neutralized with poly(2-(diethylamino)ethyl methacrylate) (Fig. 15). The pH behavior of the relaxivity of a stoichiometrically neutral mixture of the polycation and the negatively charged polychelate is interesting. The relaxivity first decreases from pH 5 to about 7, as can be expected from an increased electrostatic interaction, the polyamine being positively charged and the carboxylic groups on the poly-Gd-DTPA being progressively deprotonated. This enhanced interaction being accompanied by a release of water molecules, the relaxivity of the polyion is reduced. When the pH reaches 8, the relaxivity increases because the amino groups of the polymethacrylate are neutralized. As the charge neutrality is not respected anymore, the two polymers separate and water molecules are able to access the first coordination sphere of the Gd(III) ion.

Unbalanced polymer mixtures are not as efficient as the charge balanced mixture. Early in vivo trials in mice are encouraging, the MRI signal being more intense at sites where the pH is lower, i.e. at tumor sites.

A structural change in a gadolinium complex may result in a relaxivity change when it goes together with a change in the hydration state of the metal

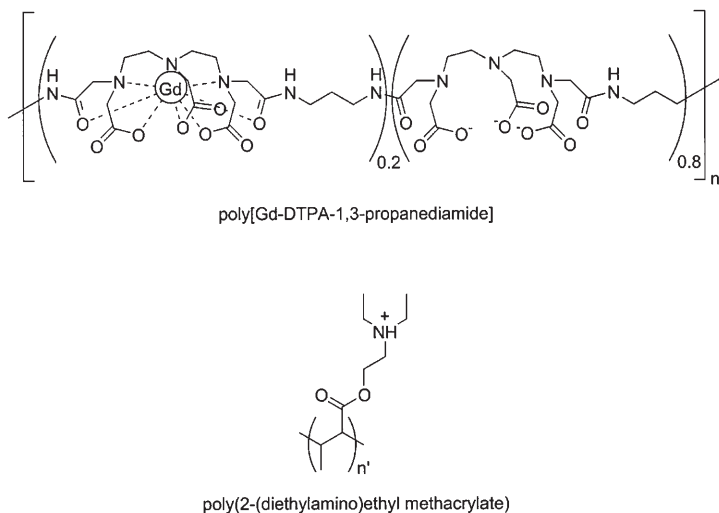


Fig. 15. Polyionic Gd(III) chelate as proposed by Mikawa et al. [107, 108]

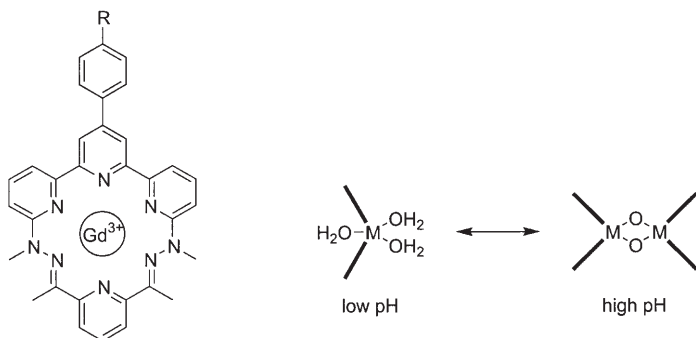


Fig. 16. Left, gadolinium-hexaazacomplex and, right, its proposed pH behavior [109] (the bold line represents a side-view of the ligand)

ion. This was observed for a planar gadolinium complex akin to Gd-texaphyrins (Fig. 16), the relaxivity of which decreases steadily and reversibly from pH 6 to 11 [109].

Based on the interpretation of luminescence measurements and pH titration results, the formation of a μ -dioxo dimer (see Fig. 16) at high pH has been proposed to account for this original pH behavior as this dimer does not possess any coordinated water molecule or hydroxyl ion.

The four examples given above illustrate the effect of water exchange or more exactly proton exchange rate and of the number of water molecules in the first coordination sphere of the paramagnetic metal ion on the water proton relaxation rate. Nonetheless, the relaxivity of a contrast agent can also be strongly

affected by its tumbling rate, hence the development of potential MRI contrast agents, the structure of which depends on pH. Noting the propensity of basic polyaminoacids, such as polylysine and polyornithine, to change their structure according to the pH of the solution, Aime et al. [110, 111] prepared new macromolecular systems by reacting polyornithine with a DO3A derivative substituted by a squaric ester moiety (Fig. 17). At low pH (<4), the Gd(III) complex is characterized by a relaxivity of about $23 \text{ mM}^{-1}\text{s}^{-1}$. The amino acid side chains are indeed protonated and highly hydrated at acidic pHs. Therefore they tend to stay as far apart as possible, which means highly mobile Gd(III) chelates. On the other hand, as soon as the pH is raised, side chains are deprotonated and intramolecular hydrogen bonds lead to the formation of a highly rigid and sterically hindered structure. The relaxivity of the gadolinium complex increases accordingly and reaches a maximum value of $32 \text{ mM}^{-1}\text{s}^{-1}$ at pH 8. In order to achieve this variation of the relaxivity with pH, it is essential to keep a limited degree of substitution of the amino acid side chains, as free amine moieties are responsible for the observed structural modifications.

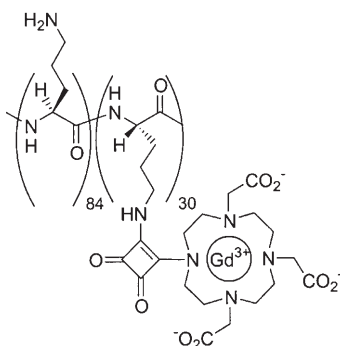


Fig. 17. Structure of a macromolecular polyornithine Gd-DO3A complex, note that the 84 unsubstituted and the 30 substituted residues are randomly distributed on the polypeptide chain

4.2.3

Oxygen Pressure Responsive

Oxygen is an important parameter in living systems. Variations in partial blood oxygen pressure have been linked to several pathologies such as stroke. Measuring blood oxygenation thus appears as an interesting goal for new smart contrast agents. Two such systems have been developed by the group of Aime in Turin, Italy [112, 113].

The Gd-DOTP chelate (Fig. 18) has been examined as a potential allosteric effector of hemoglobin [113]. Human hemoglobin is a tetrameric protein whose quaternary structure is affected by an allosteric effector. Binding of this low molecular weight species stabilizes the so-called T-form of hemoglobin, which is characterized by a low oxygen affinity, as opposed to the R-form, a very efficient

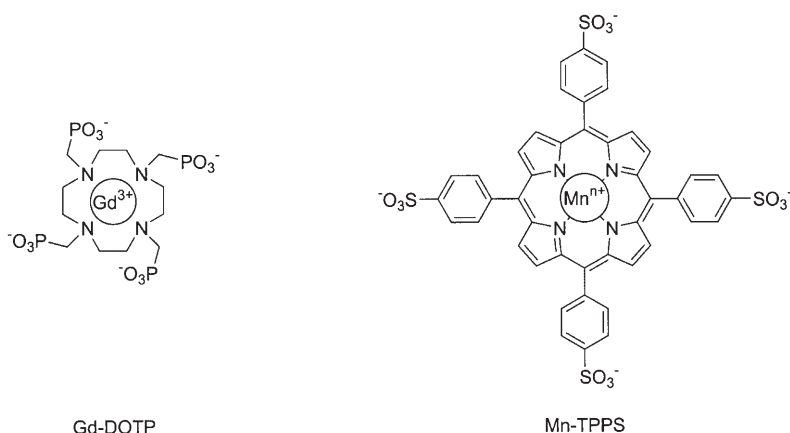


Fig. 18. Two MRI contrast agents proposed by Aime et al. [112, 113]

oxygen binder. The natural effector being 2,3-diphosphoglycerate and acting via electrostatic interactions, Aime and his colleagues theorized that the tetraphosphonate Gd(III) complex Gd-DOTP could function in a similar manner. They were able to show that the complex does indeed bind T-form hemoglobin more effectively than it does recognize the R-form, the strong interaction being accompanied by an increase of the relaxivity by a factor of 5. This enhanced relaxivity can obviously be attributed to the slow tumbling rate of the macro-molecular adduct when compared to the fast reorientation of the small Gd-DOTP chelate.

Hemoglobin being confined in red blood cells, the applicability of the preceding protocol appears scarce. Therefore, the same group studied another compound, namely the manganese complex of 5,10,15,20-tetrakis(*p*-sulfonatophenyl)-porphyrin or TPPS [112] (Fig. 18). This complex may exist in two different redox states, the Mn(II) complex being oxidized to the Mn(III) derivative by oxygen. Careful analysis of the relaxation behavior of the two redox states showed that both have the same relaxivity at MRI relevant frequencies (about 20 MHz). Fortunately, the relaxivity of the Mn(II)-TPPS complex depends on the reorientation time while that of Mn(III)-TPPS is essentially function of the electronic relaxation time of the metal ion. Therefore, the formation of a high molecular weight adduct decreases the tumbling rate of both species but only affect the relaxivity of the Mn(II) complex. Interaction with poly- β -cyclodextrin was tested. Formation of the high molecular weight species did indeed increase the relaxivity of the Mn(II) species by a factor of 4 while that of the Mn(III) complex stayed essentially unchanged. The system sensitivity to oxygen pressure was then demonstrated by measuring the decrease of the relaxivity in the presence of increasing amounts of oxygen. Other paramagnetic redox switches may be of interest. One such redox couple is the Eu(II)/Eu(III) system, in which the former has the same electronic structure as Gd(III) and could therefore lead to the development of very effective contrast agents [114].

4.2.4

Enzyme Responsive

The elaboration of enzyme responsive MRI contrast agents could provide a means of measuring enzyme activity and enzyme localization. Imaging at a molecular level is indeed one of the major challenges for the future of the technique as it would provide great insight into physiological and pathological processes at a fundamental level, either molecular or cellular [115]. The sensitivity of MRI contrast agents to specific enzymes depends on the mechanism of their interaction as illustrated below.

Provided the interactions between a contrast agent and an enzyme are sufficiently strong, a large increase in relaxivity will be observed due to the increased rotational correlation time of the adduct. This behavior was observed for a Gd-DTPA derivative substituted by an arylsulfonamide pendant arm [116].

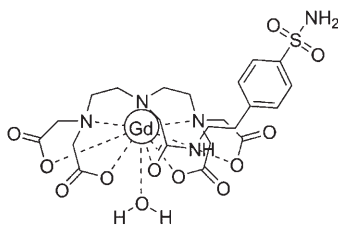
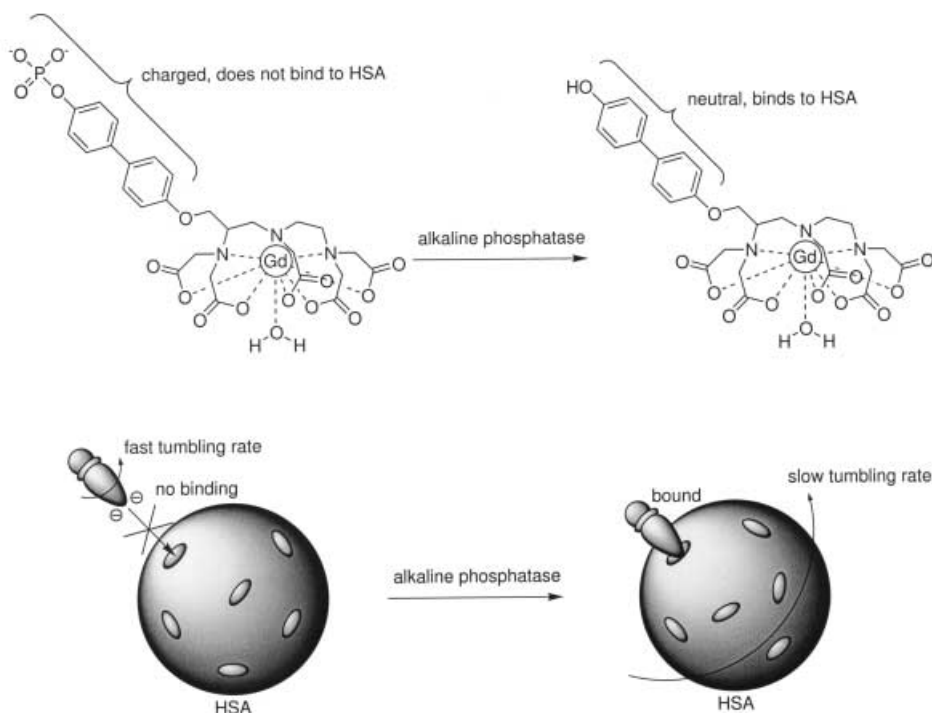


Fig. 19. Sulfonamide-substituted Gd-DTPA complex that can act as an inhibitor of carbonic anhydrase

This compound, represented in figure 19, like many primary sulfonamides [117, 118], does indeed act as an inhibitor of carbonic anhydrase, an ubiquitous zinc enzyme that catalyzes CO_2 fixation. A relaxometric titration of the substituted Gd(III) chelate by carbonic anhydrase confirmed the formation of an addition product with a stability constant of about $15000 \pm 5000 \text{ M}^{-1}$. The stability of the adduct is large enough to ensure a long circulation time of the contrast agent while simultaneously limiting toxicity problems that might arise if the association constant was higher [3]. As expected, the relaxivity of the adduct is much higher than that of the free low molecular weight complex (from 5 to about $27 \text{ mM}^{-1}\text{s}^{-1}$ at 20 MHz). However using this contrast agent as a blood-pool agent was deemed impossible. Experiments on whole blood samples failed to show enough binding to the small quantity of carbonic anhydrase displayed on the surface of red blood cells. This new enzyme specific MRI contrast agent could nonetheless be useful for imaging certain tissues.

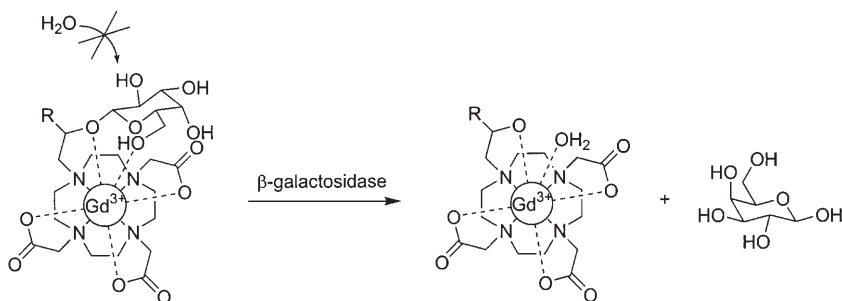
MRI contrast agents may also act as enzyme substrates, the enzyme-catalyzed reaction resulting in an enhancement of the relaxivity of the contrast agent. Proof of principle has been given by Lauffer et al. [119] who synthesized a Gd-DTPA chelate with a hydrophobic sidearm terminated by a phosphate group. This ionic moiety prevents the binding of the MRI agent in the lipophilic pockets of human serum albumin (HSA). Cleavage of the phosphate by alkaline phosphatase transforms the prodrug in an active agent that is able to bind to the

protein because of an increased hydrophobicity (Scheme 9). The formation of the complex between HSA and the hydrophobic MRI contrast agent increases its relaxivity by about 70% because of the slower tumbling rate of the macromolecular adduct.



Scheme 9. Activation of a Gd-DTPA derivative by alkaline phosphatase

The relaxivity of a gadolinium(III) based contrast agent depends not only on the rotational correlation time of the compound but also on the number of water molecules in the first coordination sphere of the metal ion. Advantage has been taken from this dependence to generate an enzyme-sensitive MRI contrast agent, the relaxivity of which increases upon activation by the enzyme thanks to the liberation of free coordination sites for water molecules. Moats et al. [120] have designed an analog of DOTA, i.e. a galactopyranosyl substituted 1-hydroxyethyl-1,4,7,10-tetraazacyclododecane-4,7,10-triacetic acid (Scheme 10, R = H). When this ligand binds Gd(III), all nine coordination sites of the metal ion are occupied and there is no water molecule in the first coordination sphere. When β -galactosidase cleaves the galactopyranosyl moiety enzymatically, a free coordination site appears, that is quickly occupied by a water molecule, hence the 20% increase in relaxivity observed in the presence of the enzyme. If the inactive complex is rigidified by adding a methyl group on the galactopyranosyl linker [121] (Scheme 10, R = Me), free rotation of the sugar moiety is further hindered and water access to the first coordination sphere of the Gd(III) ion is



Scheme 10. Activation of a Gd(III) based MRI contrast agent by the enzyme β -galactosidase (R = H or Me)

further decreased. Consequently, cleavage of the sugar pendant arm irreversibly increases the relaxivity by a factor of three (from 0.903 to $2.72 \text{ mM}^{-1}\text{s}^{-1}$).

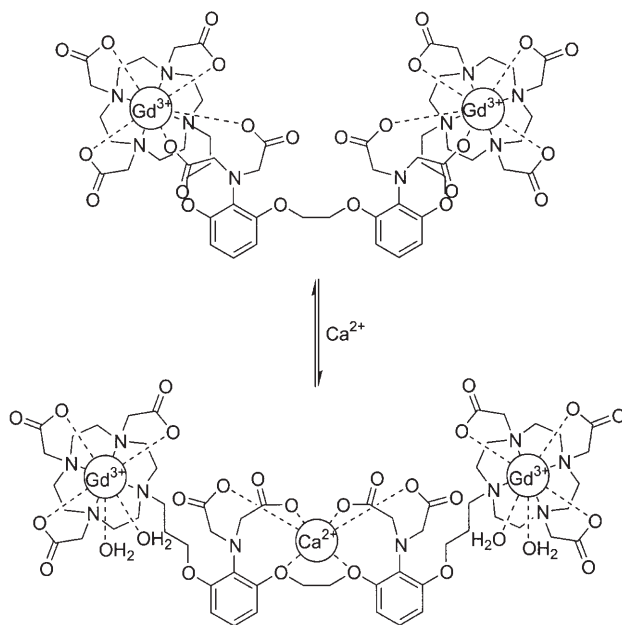
The enzyme β -galactosidase has been used as a marker of gene delivery and expression in gene therapy and developmental biology as it is not expressed naturally in human cells. Detection has usually been performed on excised tissue by colorimetric assay. On the contrary, this MRI contrast agent has been used to monitor gene expression in vivo in a developing embryo of *Xenopus Laevis* [121]. The paramagnetic probe was injected into both cells of the embryo at the two-cell stage while the mRNA encoding for β -galactosidase was delivered in only one cell. MR images of the developed embryo display a clear difference between both sides of the animal. This was expected because the first mitosis in an embryo is known to define the left and right sides of the future animal. MRI has also the advantage of allowing in vivo imaging of deep tissues, something not possible with classical optical techniques. Furthermore, the authors were able to demonstrate gene translation and expression by injecting a DNA construct containing the *lacZ* gene encoding for β -galactosidase. Only those cells expressing the enzyme were detected by MRI, thus showing that this contrast agent is not just a cell tracer but is sensitive to gene expression. This method holds great promise for mapping gene expression in vivo in developmental biology and gene therapy. Improvements are obviously needed, as microinjection is not applicable to patients.

4.2.5

Metal Ion Concentration Dependent

Several metal ions are essential or beneficial to life while others, such as lead, cadmium or mercury, are highly detrimental. Many diseases have been associated in a way or another to altered metal ion concentrations in the body. Deficiencies can be as damaging as overloads. Copper deficiency has been associated to anemia while excess copper can lead to Wilson's disease (liver cirrhosis). Anemia may also be caused by a lack of iron and overload of this same metal ion is connected to thalassemia and siderosis [122]. In vivo determination of metal ion distribution is thus highly desirable and progresses have been made towards the design of MRI contrast agents sensitive to the concentration of metal ions.

Calcium (Ca^{2+}) is probably one of the most important metal ions for life. Its roles are numerous both in healthy and damaged tissues. It controls muscular contraction, neural cell communication, hormonal secretion, ... Its signaling ability is unrivaled but its concentration should not exceed a critical level, above which cell death may occur [123]. The development of selective fluorescent probes has helped in the understanding of calcium multiple roles [124], but their use is restricted to transparent samples of a limited thickness because of light absorption and scattering. In order to improve calcium detection in vivo, contrast-enhanced MRI presents the advantage of being insensitive to sample depth. Li et al. [125] have therefore proposed a new MRI contrast agent, Gd-DOPTA, the relaxivity of which depends on calcium concentration (Scheme 11). Gd-DOPTA consists of two different subunits: a derivative of 1,2-bis(o-aminophenoxy)ethane- N,N,N',N' -tetraacetic acid (BAPTA) known for its high selectivity towards calcium [126, 127] linked to a 1,4,7-tris(carboxymethyl)-1,4,7,10-tetraazacyclododecane (DO3A) that can chelate lanthanide ions. When calcium is added to a solution of the Gd(III) complex, the relaxivity per gadolinium ion increases by about 80 % (from 3.26 to 5.76 $\text{mM}^{-1}\text{s}^{-1}$). The mechanism that has been proposed to account for this observation is presented in scheme 11. The first coordination sphere of Gd(III) is completed either by two carboxylates from the closest iminodiacetate moiety of the calcium binding subunit or by two water molecules when calcium is bound to the BAPTA ligand. Thus, Gd-DOPTA is a calcium sensitive MRI contrast agent that may help to assess calcium activity in cells not accessible by optical techniques.



Scheme 11. Activation of a calcium-sensitive MRI contrast agent according to Li et al. [125] (see text)

As important as calcium is probably iron [122]. Iron is the metal center of many essential proteins and enzymes, such as hemoglobin, an oxygen carrier, or peroxidase, that oxidizes hydrogen peroxide, or even the large family of cytochromes, which act as electron transfer proteins in many important biochemical processes [85]. New families of MRI contrast agents have been designed such that their relaxivity is iron concentration dependent [128–130]. The two latest are based on Gd(III) chelates (Fig. 20) but differ by the mechanism responsible for their iron sensitivity and will be described further.

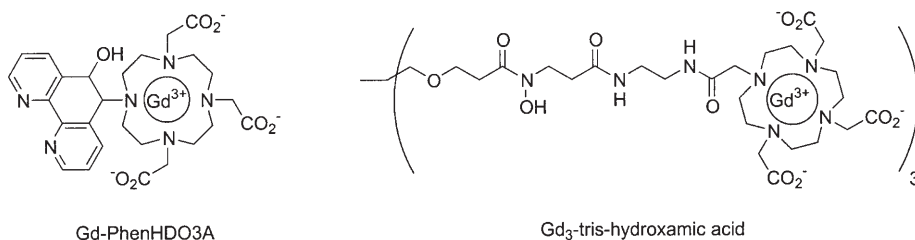
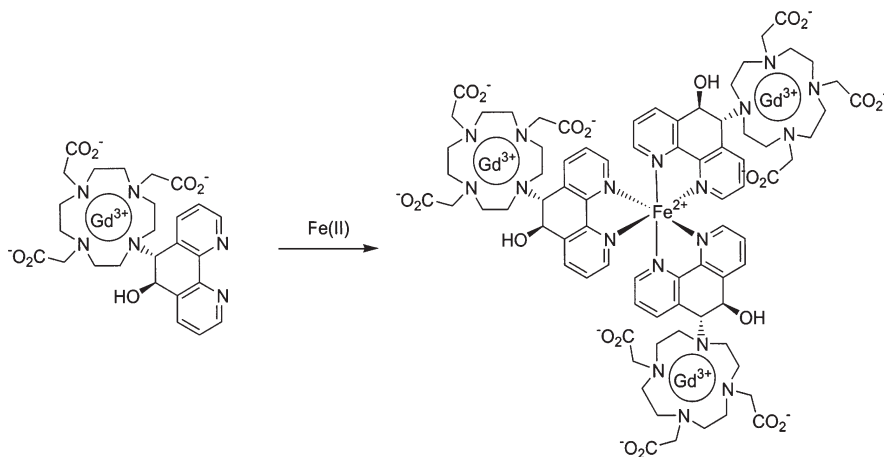


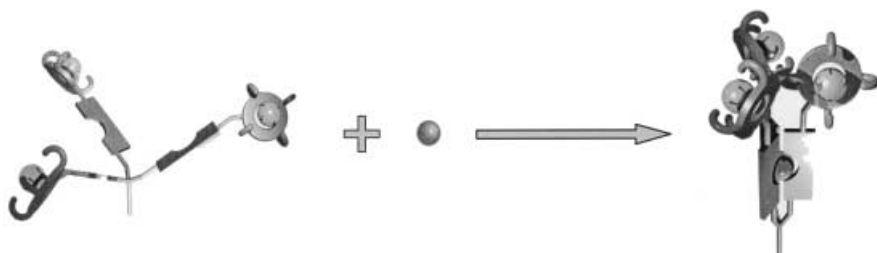
Fig. 20. Two recent examples of iron-sensitive MRI contrast agents [129, 130]

The first family, whose prototypical member is Gd-PhenHDO3A (Fig. 20), relies on the formation of a supramolecular entity by self-assembly around iron to get an increase of relaxivity of about 145% (from 5.1 to 12.5 mM⁻¹s⁻¹). Indeed the increase of the molecular weight accompanying self-assembly results in a slowdown of the tumbling rate, hence a higher relaxivity (Scheme 12). In this case, the 5,6-dihydrophenanthroline subunit acts as a bidentate ligand for both Fe(II) and Gd(III). This chelating mode forces the rotational correlation time at the paramagnetic Gd(III) ion to be equal to that of the entire self-assembled species.



Scheme 12. Self-assembly of Gd-PhenHDO3A around Fe(II) resulting in an increased relaxivity

A second group of iron sensitive MRI contrast agents uses iron chelation by a tris-hydroxamate ligand in order to restrict free rotation at the gadolinium centers (Scheme 13), thereby increasing the relaxivity of the contrast agent without changing its molecular weight. This new approach gave interesting results with a 57 % relaxivity increase upon iron binding (from 5.4 to 8.5 mM⁻¹s⁻¹ at 20 MHz) in the case of the molecule shown in Fig. 20.



Scheme 13. Wrapping of a tris-Gd-chelate tris-hydroxamate around Fe(III), responsible for an enhanced relaxivity of the contrast agent

5 Concluding Remarks

MRI contrast agents that are currently used clinically are all non specific extra-cellular agents. Their ability to enhance the contrast of MRI images stems essentially from their preferential blood distribution and their small size. Furthermore, the relatively low sensitivity of the magnetic resonance technique requires the injection of large amounts of contrast agent.

Two main goals are currently pursued by many laboratories around the world: increased efficacy and enhanced specificity. We have reported in this contribution several examples that point in these two directions. We have also tried to point the reader to important factors that may affect the development of new, more efficient and more specific MRI contrast agents. Much work however remains to be done in order to put these new and exciting results to practical use.

Acknowledgement. The Fond National de la Recherche Scientifique, F.N.R.S. Belgium, and the Institut Interuniversitaire des Sciences Nucléaires, I.I.S.N. Belgium, are gratefully acknowledged for their financial support. V.J. is Chercheur Qualifié of the F.N.R.S.

6 References

1. Bogdanov Jr A, Lewin M and Weissleder R (1999) *Adv Drug Delivery Rev* 37:279
2. Weissig V, Babich J and Torchilin V (2000) *Colloids Surf, B* 18:293
3. Caravan P, Ellison JJ, McMurry TJ and Lauffer RB (1999) *Chem Rev* (Washington, DC) 99:2293
4. Martin VV, Ralston WH, Hynes MR and Keana JF (1995) *Bioconjugate Chem* 6:616
5. Nunn AD, Liner KE and Tweedle MF (1997) *Q J Nucl Med* 41:155

6. Unger EC, Fritz T, Wu G et al. (1994) *J Liposome Res* 4:811
7. Paeuser S, Reszka R, Wagner S, Wolf KJ, Buhr HJ and Berger G (1997) *Anti-Cancer Drug Des* 12:125
8. Fossheim SL, Collet JM, Mansson S, Fahlvik AK, Muller RN and Klaveness J (1998) *Invest Radiol* 33:810
9. Woodle MC, Newman MS and Cohen JA (1994) *J Drug Targeting* 2:397
10. Basanez G, Goni FM and Alonso A (1997) *FEBS Lett* 411:281
11. Storrs RW, Troper FD, Li HY, Song CK, Sipkins DA, Kuniyoshi JK, Bednarski MD, Strauss HW, and Li KCP (1995) *J Magn Reson Imaging* 5:719
12. Kim SK, Pohost GM and Elgavish GA (1992) *Bioconjugate Chem* 3:20
13. Naevestad A, Fossheim SL and Fahlvik AK (1999) Preparation and structure-activity relationships of particulate magnetic agents. In: Thomsen HS, Muller RN and Mattrey RF (eds) *Trends in contrast media*. Springer-Verlag, Heidelberg, chap 16
14. McLachlan SJ, Morris MR, Lucas MA, Fisco RA, Eakins MN, Fowler DR, Scheetz RB and Olukotun AY (1994) *J Magn Reson Imaging* 4:301
15. Anzai Y, Prince MR, Chenevert TL, Maki JH, Londy F, London M, and McLachlan SJ (1997) *J Magn Reson Imaging* 7:209
16. Young SW, Balkus Jr KJ and Sherry AD (1995) US Patent 5429813
17. Young SW, Qing F, Rubin D, Balkus Jr KJ, Engel JS, Lang J, Dow WC, Mutch JD and Miller RA (1995) *J Magn Reson Imaging* 5:1
18. Balkus Jr KJ and Shi J (1996) *Langmuir* 12:6277
19. Balkus Jr KJ and Shi J (1996) *J Phys Chem* 100:16429
20. Braybrook JH and Hall LD (1991) *Polym Int* 26:251
21. Reynolds CH, Annan N, Beshah K, Huber JH, Shaber SH, Lenkinski RE and Wortman JA (2000) *J Am Chem Soc* 122:8940
22. Niemi P, Reisto T, Hemmilä I and Kormanen M (1991) *Invest Radiol* 26:820
23. Rebizak R, Schaefer M and Dellacherie E (1998) *Bioconjugate Chem* 9:94
24. Cavagna F, Luchinat C, Scozzfava A and Xia Z (1994) *Magn Reson Med* 31:58
25. Toth E, Helm L, Kellar KE and Merbach AE (1999) *Chem Eur J* 5:1202
26. Ladd DL, Hollister R, Peng X, Wei D, Wu G, Delecki D, Snow RA, Toner JL, Kellar K, Vinay JE, Desay C, Raymond G, Kinter LB, Dessler TS and Rubi DL (1999) *Bioconjugate Chem* 10:361
27. Vander Elst P, Maton F, Laurent S, Seghi F, Chapelle F and Muller RN (1997) *Magn Reson Med* 38:604
28. Weinmann H-J, Schuhmann-Giampieri G, Schmitt-Willich H, Vogler H, Frenzel T and Gries H (1991) *Magn Reson Med* 22:233
29. Muller RN, Radüchel B, Laurent S, Platzek J, Piérart C, Mareski P and Vander Elst P (1999) *Eur J Inorg Chem* 1949
30. Aime S, Botta M, Fasano M, Crich SG and Terreno E (1996) *J Biol Inorg Chem* 1:312
31. Parmelee DJ, Walovitch RC, Ouellet-Hillori S and Lauffer RB (1997) *Invest Radiol* 32:741
32. Wiener EC, Brechbiel MW, Brothers H, Magin RL, Gansow OA, Tomalia DA and Lauterbur PC (1994) *Magn Reson Med* 31:1
33. Wiener EC, Auteri FP, Chen JW, Brechbiel MW, Gansow OA, Schneider DS, Belford RL, Clarkson RB and Lauterbur PC (1996) *J Am Chem Soc* 118:7774
34. André JP, Toth E, Fischer H, Seelig A, Mäcke HR and Merbach AE (1999) *Chem Eur J* 5:2977
35. Aime S, Anelli PL, Botta M, Fedeli F, Grandi M, Paoli P and Uggeri F (1992) *Inorg Chem* 31:2422
36. Ranganathan RS, Fernandez ME, Kang SI, Nunn AD, Ratsep PC, Pillai KMR, Zhang X and Tweedle MF (1998) *Invest Radiol* 33:779
37. Sessler JL, Mody TD, Hemmi GW, Lynch V, Young SW and Miller RA (1993) *J Am Chem Soc* 115:10368
38. Sessler JL, Kral V, Hoehner MC, Chin KOA and Divila RM (1996) *Pure Appl Chem* 68:1291
39. Okuhata Y (1999) *Adv Drug Delivery Rev* 37:121
40. Ahrens ET, Rothbacher U, Jacobs RE and Fraser SE (1998) *Proc Natl Acad Sci USA* 95:8443

41. Aime S, Botta M, Garino E, Geninatti Crich S, Giovenzana G, Pagliarin R, Palmisano G and Sisti M (2000) *Chem Eur J* 6:2609
42. Anghileri MJ, Heidebreder M and Mathes R (1976) *J Nucl Biol Med* 20:79
43. Mehrishi JN (1969) *Eur J Cancer* 5:427
44. Yasui, K and Nakamura, Y (2000) *Biol Pharm Bull* 23:318
45. Unger EC, Totty WG, Neufeld DM, Otsuka FL, Murphy WA, Welsh MS, Connett JM and Philpott GW (1985) *Invest Radiol* 20:693
46. Anderson-Berg WT, Strand M, Lempert TE, Rosenbaum AE and Joseph PM (1986) *J Nucl Med* 27:829
47. Khaw BA, Gold HK and Goldman M (1989) US Patent 4859450
48. Curtet C, Bourgoïn C, Bohy J, Saccavini JC, Thedrez P, Akoka S, Tellier C and Chatal JF (1988) *Int J Cancer Suppl* 2:2126
49. Curtet C, Tellier C, Bohy J, Conti ML, Saccavini JC, Thedrez P, Douillard JY, Chatal JF and Koprowski H (1986) *Proc Natl Acad Sci USA* 83:4277
50. Curtet C, Bourgoïn C, Bohy J, Saccavini JC, Thedrez P, Akoka S, Tellier C and Chatal JF (1988) *Int J Cancer Suppl* 2:126
51. Kornguth SE, Turski PA, Perman WH, Schultz R, Kalinke T, Reale R and Raybaud F (1987) *J Neurosurg* 66:898
52. Shreve P and Aisen AM (1986) *Magn Reson Med* 3:336
53. Gohr-Rosenthal S, Schmitt-Willich H, Ebert W and Conrad J (1993) *Invest Radiol* 28:789
54. Curtet C, Maton F, Havet T, Slinkin M, Mishra A, Chatal JF and Muller RN (1998) *Invest Radiol* 33:752
55. Sipkins DA, Cheresch DA, Kazemi MR, Nevin LM, Bednarski MD and Li KCP (1998) *Nat Med (NY)* 4:623
56. Anderson SA, Rader RK, Westlin WF, Null C, Jackson D, Lanza GM, Wickline SA and Kotyk JJ (2000) *Magn Reson Med* 44:433
57. Brasch R, Pham C, Shames D, Roberts T, van Dijke K, van Bruggen N, Mann J, Ostrowitzki S and Melnyk O (1997) *J Magn Reson Imaging* 7:68
58. Brooks PC, Clark RAF and Cheresch DA (1994) *Science (Washington, DC)* 264:569
59. Neeman M (2000) *Cancer Metastasis Rev* 19:39
60. Lanza GM, Wallace KD, Scott MJ, Cacheris WP, Abdenschein DR, Christy DH, Sharkey AM, Miller JG, Gaffney PJ and Wickline SA (1996) *Circulation* 95:3334
61. Bulte JWM, Hoekstra Y, Kamman RL, Magin RL, Webb AG, Briggs RW, Go KG, Hulstaert CE, Miltenyi S, The TH (1992) *Magn Reson Med* 25:148
62. Go KG, Bulte JWM, de Ley L, The TH, Kamman RL, Hulstaert CE, Blaauw EH and Ma LD (1993) *Eur J Radiol* 16:171
63. Reimer P, Weissleder R, Lee AS, Wittenberg J and Brady TJ (1990) *Radiology (Oak Brook, Ill)* 177:729
64. Weissleder R, Reimer P, Lee AS, Wittenberg J and Brady TJ (1990) *Am J Roentgenol* 155:1161
65. Vera DR, Buonocore MH, Wisner ER, Katzberg RW and Stadalnik RC (1995) *Acad Radiol* 2:497
66. Muhler A (1995) *J Magn Reson Imaging* 5:7
67. Paganelli G, Siccardi A, Malcovati M, Scassellati G and Fazio F (1992) EP Patent 496074
68. Paganelli G, Orecchia R, Jereczek-Fossa B, Grana C, Cremonesi M, De Braude F, Tradati N and Chinol M (1998) *Eur J Nucl Med* 25:1336
69. Paganelli G, Grana C, Chinol M (1997) *Eur J Nucl Med* 24:908
70. Scott WD, Pathare PM, Hamlin DK, Buhler KR and Vessella RL (1998) *Bioconjugate Chem* 9:813
71. Lemieux GA, Yarema KJ, Jacobs CL and Bertozzi CR (1999) *J Am Chem Soc* 121:4278
72. Schauer R (1985) *Trends Biotechnol* 3:57
73. Hakomori S and Zhang Y (1997) *Chem Biol* 4:97
74. Mahal LK and Bertozzi CR (1997) *Chem Biol* 4:415
75. Yarema KJ, Mahal LK, Bruehl RE, Rodriguez EC and Bertozzi CR (1998) *J Biol Chem* 273:31168

76. Hines JV, Ammar GM, Buss J and Schmallbrock P (1999) *Bioconjugate Chem* 10:155
77. Charlton J, Sennello J and Smith D (1997) *Chem Biol* 4:809
78. Young SW, Sidhu MK, Qing F, Muller HH, Neuder M, Zanassi G, Mody TD, Hemmi GW, Sessler JL, and Miller RA (1994) *Invest Radiol* 29:330
79. Yeh TC, Zhang W, Ildstad SC and Ho C (1993) *Magn Reson Med* 30:617
80. Yeh TC, Zhang W, Ildstad SC and Ho C (1995) *Magn Reson Med* 33:200
81. Schoepf U, Marecos EM, Melder RJ, Jain RK and Weissleder R (1998) *BioTechniques* 24:642
82. Dodd SJ, Williams M, Suhan JP, Williams DS, Koretsky AP and Ho C (1999) *Biophys J* 76:103
83. Lewin M, Carlesso N, Tung CH, Tang XW, Cory D, Scadden DT and Weissleder R (2000) *Nat Biotechnol* 18:410
84. Moore A, Basilion JP, Chiocca EA and Weissleder R (1998) *Biochim Biophys Acta* 1402:239
85. Crichton RR (1991) *Inorganic biochemistry of iron metabolism*. Ellis Horwood, New York
86. Bulte JWM, Zhang SC, van Gelderen P, Herynek V, Jordan EK, Duncan ID and Frank JA (1999) *Proc Natl Acad Sci USA* 96:15256
87. Weissleder R, Moore A, Mahmood U, Bhorade R, Benveniste H, Chiocca EA and Basilion JP (2000) *Nat Med (NY)* 6:351
88. Wunderbaldinger P, Bogdanov Jr A and Weissleder R (2000) *Eur J Radiol* 34:156
89. Högemann D, Josephson L, Weissleder R and Basilion JP (2000) *Bioconjugate Chem* 11:941
90. Kayyem JF, Kumar RM, Fraser SE and Meade TJ (1995) *Chem Biol* 2:615
91. Konda SD, Aref M, Brechbiel MW and Wiener EC (2000) *Invest Radiol* 35:50
92. Moghimi SM and Rajabi-Siahboomi AR (2000) *Adv Drug Delivery Rev* 41:129
93. Lee RJ and Huang L (1996) *J Biol Chem* 271:8481
94. Sudimack J and Lee RJ (2000) *Adv Drug Delivery Rev* 41:147
95. Wiener EC, Konda SD, Shadron A (1997) *Invest Radiol* 32:748
96. Josephson L, Tung CH, Moore A and Weissleder R (1999) *Bioconjugate Chem* 10:186
97. Vivès E, Brodin P and Lebleu B (1997) *J Biol Chem* 272:16010
98. Bhorade R, Weissleder R, Nakakoshi T, Moore A and Tung C-H (2000) *Bioconjugate Chem* 11:301
99. Bogdanov Jr A and Weissleder R (1998) *Trends Biotechnol* 16:5
100. Weissleder R, Simonova M, Bogdanova A, Bredow S, Enochs WS and Bogdanov Jr A (1997) *Radiology (Oak Brook, Ill)* 204:425
101. Aime S, Botta M, Fasano M, Terreno E, Kinches P, Calabi L and Paleari L (1996) *Magn Reson Med* 35:648
102. Peters RD and Henkelman RM (2000) *Magn Reson Med* 43:62
103. Fossheim SL, Il'yasov KA, Hennig J and Bjornerud A (2000) *Acad Radiol* 7:1107
104. Gerweck LE and Seetharaman K (1996) *Cancer Res* 56:1194
105. Zhang S, Wu K and Sherry AD (1999) *Angew Chem Int Ed* 38:3192
106. Aime S, Barge A, Botta M, Howard JAK, Katakly R, Lowe MP, Moloney JM, Parker D and de Sousa AS (1999) *Chem Commun (Cambridge)* 1047
107. Mikawa M, Miwa N, Bräutigam M, Akaike T and Maruyama A (1998) *Chem Lett* 693
108. Mikawa M, Miwa N, Bräutigam M, Akaike T and Maruyama A (2000) *J Biomed Mater Res* 49:390
109. Hall J, Häner R, Aime S, Botta M, Faulkner S, Parker D and de Sousa AS (1998) *New J Chem* 627
110. Aime S, Botta M, Geninatti Crich S, Giovenzana G, Palmisano G and Sisti M (1999) *Bioconjugate Chem* 10:192
111. Aime S, Botta M, Geninatti Crich S, Giovenzana G, Palmisano G and Sisti M (1999) *Chem Commun (Cambridge)* 1577
112. Aime S, Botta M, Gianolio E and Terreno E (2000) *Angew Chem Int Ed* 39:747
113. Aime S, Ascenzi P, Comoglio E, Fasano M and Paoletti S (1995) *J Am Chem Soc* 117:9365
114. Burai L, Tóth E, Seibig S, Scopelliti R and Merbach A (2000) *Chem Eur J* 6:3761

115. Rudin M (2000) *Nat Biotechnol* 18:383
116. Anelli PL, Bertini I, Fragai M, Lattuada L, Luchinat C and Parigi G (2000) *Eur J Inorg Chem* 625
117. Ilies M, Supuran CT, Scozzafava A, Casini A, Mincione F, Menabuoni L, Caproiu MT, Maganu M and Banciu MD (2000) *Bioorg Med Chem* 8:2145
118. Maren TH (1967) *Physiol Rev* 47:595
119. Lauffer RB, McMurry TJ, Dunham SO, Scott DM, Parmelee DJ and Dumas S (1997) WO Patent 9736619
120. Moats RA, Fraser SE and Meade TJ (1997) *Angew Chem Int Ed* 36:726
121. Louie AY, Hüber MM, Ahrens ET, Rothbächer U, Moats R, Jacobs RE, Fraser SE and Meade TJ (2000) *Nat Biotechnol* 18:321
122. Taylor DM and Williams DR (1995) Trace elements medicine and chelation therapy. Royal Society of Chemistry, Cambridge, UK
123. Berridge MJ, Lipp P and Bootman MD (2000) *Nat Rev Mol Cell Biol* 1:11
124. Tsien RY (1994) *Chem Eng News* 72:34
125. Li W, Fraser SE and Meade TJ (1999) *J Am Chem Soc* 121:1413
126. Gryniewicz G, Poenie M and Tsien RY (1985) *J Biol Chem* 260:3440
127. Tsien RY (1980) *Biochemistry* 19:2396
128. Aime S, Botta M, Fasano M and Terreno E (1993) *Spectrochim Acta, Part A* 49 A:1315
129. Comblin V, Gilsoul D, Hermann M, Humblet V, Jacques V, Mesbahi M, Sauvage C and Desreux JF (1999) *Coord Chem Rev* 185–186:451
130. Desreux JF, Jacques V, Humblet V, Hermann M, Comblin V and Tweedle MF (2000) US Patent 6056939

Non-Gadolinium-Based MRI Contrast Agents

Daniel D. Schwert¹, Julian A. Davies¹, Nicholas Richardson²

¹ Department of Chemistry, University of Toledo, Toledo, OH 43606, USA
E-mail: dschwer@uoft02.utoledo.edu, E-mail: jdavies@uoft02.utoledo.edu

² Department of Chemistry & Physics, Wagner College, Staten Island, NY 10301, USA
E-mail: nrichard@wagner.edu

Contrast agents for magnetic resonance imaging based on metal ions other than gadolinium(III) including manganese(II), manganese(III), iron(III) and copper(II), have been investigated over the past decade. Although the intrinsic properties of these metal ions tend to make these agents less attractive than gadolinium(III)-based agents, the large volume of literature on the biochemistry of these metal ions has allowed for the development of viable contrast agents. Agents specific for tissues such as the liver, pancreas, adrenals, cancerous tumors, and even the insides of cells and neuronal tracts as well as non-specific agents have been developed and tested in animal models. Two manganese(II)-based agents, the liver-specific agent manganese(II)-dipyridoxal diphosphate (Teslascan®) and an oral agent containing manganese(II) chloride (LumenHance®), and one ferric ammonium citrate-containing oral agent (FerriSeltz®) are available clinically for human use. Information on the toxicity, relaxivity, image enhancement, and tissue specificity of agents is discussed here. In addition to agents designed for use in living systems, contrast agents that measure pH and redox reactions in non-living systems have also been investigated and will be discussed.

Keywords: MRI Contrast Agents, Manganese, Iron, Copper

1	Introduction	167
2	Manganese Agents	169
2.1	Manganese(II) Agents	169
2.1.1	MnCl ₂	169
2.1.2	Mn-DPDP	170
2.1.3	Manganese(II)-Containing Liposomes	172
2.1.4	Other Manganese(II) Agents	173
2.2	Manganese(III) Porphyrins	175
2.2.1	Mn-TPPS _n	175
2.2.2	Mn-Mesoporphyrin	176
2.2.3	Mn-Hematoporphyrin	177
2.2.4	Mn-TPP	178
2.2.5	ATN-10	179
2.2.6	Mn-BOPP	180
2.2.7	Other Manganese(III) Porphyrins	180
3	Iron Agents	182
3.1	Fe-EHPG and Derivatives	183
3.2	Fe-HBED	185

3.3	Desferrioxamine B Derivatives	185
3.4	Ferric Ammonium Citrate	187
3.5	Other Iron(III) Agents	188
4	Copper Agents	190
4.1	Copper(II) Ions	191
4.2	Copper(II) Tetramic Acid Derivatives	192
4.3	Other Copper(II) Agents	192
5	Conclusions	193
6	References	193

List of Abbreviations

BOPP	boronated protoporphyrin
CNR	contrast-to-noise ratio
DF	desferrioxamine B
DOTA	1,4,7,10-tetrakis(carboxymethyl)-1,4,7,10-tetraazacyclododecanate
DPDP	dipyridoxal diphosphate
DPP	dihydroxypropyldecylamine
DTPA	diethylenetriaminepentaacetic acid
EDTA	ethylenediaminetetraacetic acid
EHPG	<i>N,N'</i> -ethylenebis-[2-(<i>o</i> -hydroxyphenyl)glycine]
FAC	ferric ammonium citrate
GDF	<i>N</i> -(glutaryl)desferrioxamine B
GRE	gradient recalled echo
HBED	<i>N,N'</i> -bis(2-hydroxybenzyl)ethylenediamine- <i>N,N'</i> -diacetate
HP	hematoporphyrin
HP-DO3A	10-(2-hydroxypropyl)-1,4,7,10-tetraazacyclododecane-1,4,7-triacetate
HSA	human serum albumin
i.p.	intraperitoneal
i.v.	intravenous
LD ₅₀	lethal dose for fifty percent of animals
MnHA	manganese-substituted hydroxylapatite
MP	mesoporphyrin
MRCP	magnetic resonance cholangiopancreatography
MRI	magnetic resonance imaging
MRU	magnetic resonance urography
PAS	<i>p</i> -aminosalicylic acid
PcS ₄	tetrasulfonated phthalocyanine
PEG	polyethylene-glycol
pen	penicillamine
PGDF	<i>N</i> -(3-phenylglutaryl)desferrioxamine B

PSDF	<i>N</i> -(2(3)-phenylsuccinyl)desferrioxamine B
R_1	spin-lattice relaxivity
R_2	spin-spin relaxivity
SA	stearic acid
SDF	<i>N</i> -(succinyl)desferrioxamine B
T_1	spin-lattice or longitudinal relaxation time
T_2	spin-spin or transverse relaxation time
TA	tetramic acid
THF-ASP	2,4-bis(1-tetrahydro-fulfuroxyethyl)-deuteroporphynyl(IX)-6,7-bisaspartic acid
TMPyP	<i>meso</i> -tetrakis(4- <i>N</i> -methyl-pyridiniumyl)porphyrin
TPP	tetraphenylporphyrin
TPPS ₄	tetra-(4-sulfonatophenyl) porphyrin
TTHA	triethylenetetraaminehexaacetic acid
UROP-I	uroporphyrin I

1

Introduction

Contrast agents for magnetic resonance imaging (MRI) are useful for the determination of several conditions within the body. Blood flow, organ status and location of disease states can all be monitored using MRI contrast agents. These agents act by raising or lowering the signal intensity of a given region on a MR image. Paramagnetic metal ions affect both the spin-lattice (longitudinal, T_1) and spin-spin (transverse, T_2) relaxation times of protons. Pulse sequences designed to highlight these changes are employed to visualize the location of the contrast agent molecules.

Gadolinium(III) complexes have received the most attention as contrast agents for MRI [1]. With seven unpaired electrons, a large magnetic moment, and a suitably long electronic relaxation time, gadolinium(III) is the ideal paramagnetic metal ion for use in a MRI contrast agent. Unfortunately there is no natural human biochemistry for gadolinium(III) that can be exploited when designing contrast agents. Concerns about the increasing amounts of gadolinium in ground water as a result of the use of these agents have been raised [2, 3]. Agents based on manganese(II), manganese(III), iron(III), and copper(II) ions are attractive alternatives because these metals occur in large amounts in the environment and a large body of information on the human biochemistry of these elements is available. These agents are not as attractive as gadolinium(III), however, because each have fewer unpaired electrons, lower magnetic moments and shorter electronic relaxation times. Knowledge of the biological fates of these metals can be utilized in order to maximize the utility of these agents despite their shortcomings as compared to gadolinium(III)-based agents.

Several considerations must be taken into account when designing and evaluating potential MRI contrast agents. The relaxivities (R_1 and R_2) of a contrast

agent are measures of the efficacy of the agent in reducing the T_1 and T_2 values of water protons in the immediate vicinity of the agent as a function of concentration. The relaxivities of contrast agents are dependent on the magnetic field strength and temperature employed in the measurement and these values should be reported whenever possible.

The measurement of the relaxivity of a contrast agent may not provide a direct correlation to the *in vivo* relaxivity, however. One of the factors influencing the relaxivity of a contrast agent is the rate at which the agent tumbles in solutions [4]. Changes in the viscosity of a solution slow this tumbling and increase the relaxivity. Another way to alter the tumbling rate of a molecule is to attach it to a macromolecule, such as a protein. There are two common ways to approach this: covalent bonding of the agent to a macromolecule before administration of the agent and administration of a small-molecule agent that non-covalently binds to a macromolecule *in vivo*.

Another critical consideration for contrast agents is the toxicity. Acute toxicity is usually more important than chronic toxicity as the administration of the agents on a regular basis (i.e. daily) is rarely necessary. The easiest measure of acute toxicity is the lethal dose for fifty percent of animals exposed to the agent (LD_{50}). While this value measures only the most extreme effect of toxicity (death), it is nonetheless useful for comparison purposes. Toxicity data are often dependent upon the species of animal as well as the route of administration, including intravenous (i.v.) and intraperitoneal (i.p.) injections. Information on subacute toxicity in humans, including nausea and dizziness, is also of interest. The toxicity of an agent is dependent on several factors including the thermodynamic and kinetic stability of the agent, osmolality of the injection solution, and the rate of clearance.

The biological distribution of agents is also important. Preferably contrast agents localize in one tissue type in preference to other tissues in order to highlight the pathology of the target tissue. Contrast agent specific for the liver, pancreas, adrenal glands, myocardium, lymph nodes and cancerous tumors have all been investigated [5]. Protein-bound contrast agents are useful as potential blood-pool agents as they are typically cleared at a slower rate from the body than small-molecule agents which do not bind to proteins [6].

This review focuses on the development since 1990 of contrast agents based on manganese(II), manganese(III), iron(III) and copper(II). Information on contrast agent development before this time can be found in any one of several reviews [7–10]. Superparamagnetic iron oxides, more exotic contrast agents such as nitroxide spin labels and hyperpolarized xenon, and proton density agents, including barium, clays, perfluorocarbons, and oil emulsions are beyond the scope of this review (for examples of these agents the reader is referred to [11–14]). The structures shown represent the ligands in their fully-protonated states with the exception of the structure in Fig. 21, which represents metal complexes with mixed ligands. When complexed to metal ions and at physiological pH the protonation states will vary accordingly.

2 Manganese Agents

One of the earliest contrast agents to be used was a solution of manganese(II) chloride [15]. The measured R_1 value for aquo manganese(II) at 20 MHz and 37 °C is $8.0 \pm 0.1 \text{ mM}^{-1} \text{ s}^{-1}$ [16] and at 40 MHz and 40 °C it is $6.0 \text{ mM}^{-1} \text{ s}^{-1}$ [17]. The R_2 value at 40 MHz and 40 °C is $57.2 \text{ mM}^{-1} \text{ s}^{-1}$ [17]. It was quickly determined, though, that i. p. and i. v. manganese(II) were too toxic to be used in clinical practice. The LD_{50} in mice for MnCl_2 is 0.3 mmol kg^{-1} injected i. v. [18] and 1.0 mmol kg^{-1} injected i. p. [19], but if the compound is administered orally, the LD_{50} increases to $13.6 \text{ mmol kg}^{-1}$ [19]. Similar results were seen in rats, with an i. p. LD_{50} of 0.7 mmol kg^{-1} and an oral LD_{50} of 7.5 mmol kg^{-1} [20]. A more complete review of the toxicity of manganese(II) as it pertains to MR contrast agents has been published [21]. No corresponding toxicity and relaxivity data are available for aquo manganese(III) because the free ion is not stable above pH 0 and is reduced to manganese(II) [22].

Manganism, the result of overexposure to manganese, primarily affects the brain [23]. Severe psychiatric symptoms including hyperirritability, violent acts, and hallucinations are characteristic of manganism. These symptoms manifest themselves due to the ability of manganese(II) to cross the blood-brain barrier [24]. Manganese(II) ions also interfere with the calcium channels of cardiac cells, which leads to decreased ability of the heart muscle to contract [25]. This results in a decrease in heart rate, an increase in aortic pressure and ventricular fibrillation [25, 26]. Manganese has been found to interfere with DNA replication and has been shown to increase the occurrence of cancer [27].

2.1 Manganese(II) Agents

2.1.1 MnCl_2

The toxicity of orally-administered MnCl_2 is lower than the i. v. toxicity due to two factors: low rate of absorption and presystemic elimination. Between 1–9 % of ingested manganese(II) is absorbed, depending on the formulation and amount ingested [28–30]. Manganese(II) that is ingested is carried through the portal vein to the liver before entering systemic circulation. Approximately 30–35 % of the manganese in the portal vein is absorbed by the liver resulting in smaller amounts of metal in the bloodstream as compared to i. v. injection [31]. This absorption by the liver increases the signal-to-noise ratio on T_1 -weighted images by 88 % two hours after ingestion of 0.2 mmol kg^{-1} MnCl_2 by rats [17]. In the same animals, implanted Walker 256 mammary carcinosarcoma enhanced only 6 % and the liver-to-tumor contrast-to-noise ratio (CNR) increased by 375 %.

Manganese(II) chloride has also been investigated as an oral contrast agent for the gastrointestinal system. LumenHance® is a mixture of MnCl_2 , polygalacturonic acid, xanthan gum, sucrose, sodium acetate, glycine, sodium bicarbonate, sodium benzoate, and artificial strawberry flavoring [32]. The R_1 value of the

solution at 10 MHz and 37 °C is $20.9 \text{ mM}^{-1} \text{ s}^{-1}$ and the R_2 value is $35.0 \text{ mM}^{-1} \text{ s}^{-1}$ under the same conditions, values substantially different from those for MnCl_2 in water [33]. The agent is administered in three doses of 300 ml each in a 45-minute period leading up to imaging. Owing to the high R_1 and R_2 values, LumenHance® acts as both a T_1 agent, increasing the signal intensity on T_1 -weighted images, and as a T_2 agent, reducing the signal intensity on T_2 -weighted images [33]. Variation in readers was seen in the clinical trials, but between 8–26% of the patients investigated demonstrated significant additional information impacting diagnostic and management decisions [32, 34]. The agent was found to be relatively safe, with the amount of adverse events reported with LumenHance® (24%) similar to the amount reported with a placebo (22%) [32]. The only potential complication with LumenHance® is the large volume of liquid that is required to be consumed, as 14% of the patients were unable to consume at least 800 ml of the solution [32].

Approaching the problem from a different direction, a MnCl_2 -based enema has been developed [35]. The signal intensity reached with the enema using a T_1 -weighted pulse sequence was only 41% of the value obtained with a gadopentetate solution at a concentration of 10 mM. This value was considered too low for routine use.

Topical application of MnCl_2 has also been investigated [36]. Application of MnCl_2 to the naris of mice allowed for visualization of the olfactory pathway as the Mn^{2+} ions were transported up the neuronal tract. Administration of this agent did not affect the ability of the mice to detect odors and the amount of manganese(II) accumulated in tissue was below the intracellular toxicity levels. Injection of MnCl_2 into the aqueous humor of the eyes of mice demonstrated enhancement of the vitreal humor and the optic tract.

The visualization of the optic and olfactory nerves was possible due to the ability of manganese(II) to be taken up by the calcium(II) channels in neurons [37]. Another example of the utility of MnCl_2 in the imaging of neurons is demonstrated by the infusion of $3.6 \mu\text{mol min}^{-1}$ of MnCl_2 into anesthetized rats [38]. In T_1 -weighted images the signal intensity in the brain ventricles increased by approximately 50%. Injection of glutamate, which is known to increase calcium influx, with inositol, which ruptures the blood-brain barrier and allows the glutamate to reach brain neurons, increases the signal intensity of the brain by $238 \pm 23\%$ during MnCl_2 administration.

2.1.2

Mn-DPDP

The only injectable manganese(II) agent to be approved for clinical use in the U.S. is Teslascan®, a solution of the manganese(II) complex of dipyradoxal diphosphate (DPDP, Fig. 1). This agent is taken up preferentially by normal hepatocytes, leading to determination of organ function and identification of cancerous tumors. In aqueous solution, the R_1 of Mn-DPDP is $2.8 \text{ mM}^{-1} \text{ s}^{-1}$ and the R_2 is $3.7 \text{ mM}^{-1} \text{ s}^{-1}$ at 20 MHz and 40 °C [18] and $1.88 \text{ mM}^{-1} \text{ s}^{-1}$ and $2.18 \text{ mM}^{-1} \text{ s}^{-1}$, respectively, at 20 MHz and 37 °C [39]. In liver tissue, these values increase to $21.7 \text{ mM}^{-1} \text{ s}^{-1}$ and $62.7 \text{ mM}^{-1} \text{ s}^{-1}$, respectively, at 20 MHz and 40 °C [18].

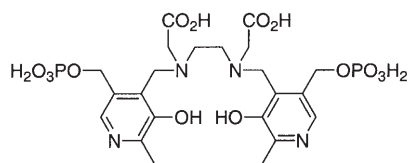


Fig. 1. Dipyridoxal diphosphate (DPDP)

The DPDP ligand was synthesized in order to lower the toxicity of the manganese(II) ion and to provide selective tissue uptake [40]. The LD_{50} of an i.v. dose of Mn-DPDP is between $1.9\text{--}5.4\text{ mmol kg}^{-1}$ in mice [18, 41]. No mortalities occurred in dogs injected i.v. with 1.8 mmol kg^{-1} [41]. With the recommended clinical dose of $0.005\text{ mmol kg}^{-1}$, the safety factor for Mn-DPDP is at least 360 [41]. In the European phase III clinical trials adverse events were reported for 46 of 624 patients (7%) [42]. In comparison, 123 of 546 patients (23%) in the U.S. clinical trials reported at least one adverse event [43]. In both trials the most common complaints were headache, vomiting and nausea. In addition, 377 of 546 patients (69%) in the U.S. trials and 26 of 624 patients (4%) in the European trials reported discomfort at the site of injection. The difference between the two trials is likely due to the method of administration and formulation of the Mn-DPDP solution. In the European trials, a 0.010 mM solution of the agent was slowly infused while in the U.S. trials Mn-DPDP was administered as a bolus injection of a 0.050 mM solution. Experiments have demonstrated a lower incidence of adverse events with infusion of the agent [44].

The mechanism of uptake of Mn-DPDP was originally thought to be due to the recognition of the DPDP ligand by pyridoxine transporters on hepatocytes. Competition studies between Mn-DPDP and pyridoxine demonstrated that the uptake of the two compounds was by different mechanisms [45]. It was found that the uptake mechanism of Mn-DPDP involved the release of manganese from the complex [46]. This release occurs *in vivo* as a result of transmetallation of the complex with zinc(II) [47]. The stability constant for Mn-DPDP is $10^{15.1}$, considerably less than the $10^{18.95}$ stability constant for Zn-DPDP [40]. The rate of manganese(II) release from Mn-DPDP is slowed by the limited amount of zinc(II) available in blood, but approximately 80% of the administered manganese is released from the complex [47]. This slowed release accounts for the lower toxicity of Mn-DPDP as compared to $MnCl_2$. The release of manganese(II) may also account for the flushing and sensation of warmth felt at the site of injection of the agent in clinical trials [42, 44, 48]. Free manganese(II) is a known vasodilator and in experiments with bovine mesenteric arteries, Mn-DPDP produced effects similar to $MnCl_2$ [49].

The slow release of manganese(II) from Mn-DPDP alters the tissue distribution of the metal ion. Free manganese ion is not cleared by the kidneys, but 43% of an injected dose of Mn-DPDP in rats was excreted renally as either Mn-DPDP or other metabolites [18]. In addition, less cardiac accumulation of manganese(II) was seen with Mn-DPDP than $MnCl_2$, leading to reduced cardiotoxicity for the complex [25, 26, 50, 51]. The bulk of the remaining manganese(II)

from Mn-DPDP is absorbed by the pancreas and healthy hepatocytes in the liver [50, 52].

Initial experiments on humans demonstrated the effectiveness of Mn-DPDP as a hepatobiliary agent. Ten minutes after injection of $0.010 \text{ mmol kg}^{-1}$ of Mn-DPDP, liver signal enhancement was 75–100% of the baseline levels in healthy subjects [53]. In one study of patients with hepatocellular carcinoma, all forty-one hepatocellular tumors evaluated showed positive enhancement while only 13 of 162 nonhepatocellular tumors (13%) showed positive enhancement [54]. The remaining nonhepatocellular tumors showed no perceivable enhancement, allowing them to be distinguished from enhanced healthy liver tissue. In the European phase III trials, investigators determined that of the 621 patient images examined, 45% of the enhanced images contained information not found in the unenhanced images [42]. Similar results were found in an independent evaluation of the results of the study [55] and in the U.S. phase III trials [48].

In addition to use as a hepatocellular contrast agent, Mn-DPDP has been investigated as an agent for pancreatic and adrenal imaging. The normal pancreatic signal-to-noise ratio increased $92 \pm 28\%$ in enhanced gradient-echo images while pancreatic tumors demonstrated no significant increase in the signal-to-noise ratio [56]. Another study found that MRI with Mn-DPDP was slightly more accurate than contrast-enhanced computed tomography in the detection and staging of pancreatic tumors, but not significantly so [57]. In a study investigating the enhancement of adrenal glands after injection of Mn-DPDP, all of the adrenal glands demonstrated enhancement (mean 38%) [58]. Three adrenal adenomas also enhanced, but two metastases did not enhance, leading to speculation that Mn-DPDP could be used to detect metastatic cancer in the adrenals.

2.1.3

Manganese(II)-Containing Liposomes

Encapsulation of contrast agents in liposomes decreases the toxicity of the agents and increases their hepatobiliary uptake [59]. Manganese(II) chloride encapsulated in liposomes has an LD_{50} value in mice at least seven times higher than that of free MnCl_2 [60]. The R_1 value of one preparation of liposome-encapsulated MnCl_2 was $35.34 \text{ mM}^{-1} \text{ s}^{-1}$ at 20 MHz [61]. In rats with mammary carcinoma (R3230AC) implanted in the liver, detection of the tumors was improved as the liver was enhanced up to 90 minutes post-injection of the contrast agent encapsulated in liposomes [60]. Intraarticular injection of MnCl_2 -containing liposomes allows for the visualization of both mechanical and enzymatic cartilage lesions in temporomandibular joints of neonatal and 4-week-old pigs [62]. The enhancement lasted for at least 300 minutes.

The alternative to encapsulation of free manganese (called “ensomes”) is to complex the manganese(II) with a ligand embedded in the lipid bilayer (“memsomes”). Ethylenediaminetetraacetic acid (EDTA)-dihydroxypropyldecylamine (EDTA-DDP, Fig. 2) was ligated to manganese(II) and inserted into the bilayer of liposomes [61]. The 30-nm diameter liposomes formed had an R_1 value at 20 MHz of $37.4 \text{ mM}^{-1} \text{ s}^{-1}$. When injected into rats with implanted C5 epitheloid

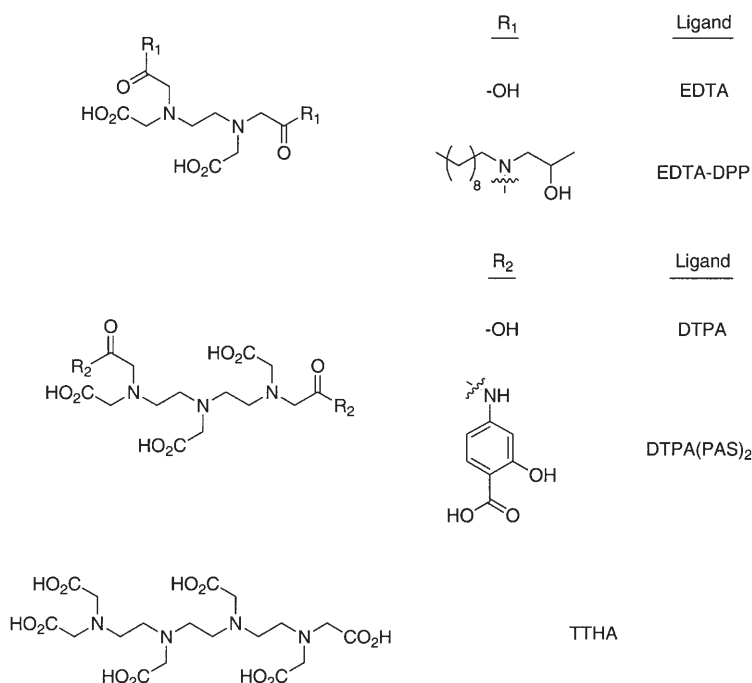


Fig. 2. Derivatives of polycarboxylic acid ligands

carcinoma, the Mn-EDTA-DDP memsomes increased the liver-to-tumor CNR to 105.90 ± 11.54 six minutes post-injection of $15.0 \mu\text{mol Mn kg}^{-1}$. In comparison, MnCl_2 ensomes increased the CNR to 50 ± 8.51 when injected at the same concentration. The memsome agents were tolerated better than the ensomes and free MnCl_2 .

Another liposome-entrapped lipophilic chelate of manganese(II), described as diethylenetriaminepentaacetic acid (DTPA)-stearate (DTPA-SA), demonstrated greater relaxivity in rat livers when compared with gadolinium vesicles [63]. This increase in relaxivity led to high enhancement of dog livers which persisted for at least 45 minutes after injection. The ligand DTPA-SA was reportedly synthesized by a literature route [64] but this reference does not describe a specific synthesis of DTPA-SA and several structures are possible for a compound described by such a name. Unfortunately this increase in relaxivity and signal intensity was attributed to the slow release of manganese(II) from the liposomes, making them unsuitable for clinical use.

2.1.4

Other Manganese(II) Agents

Different particulate manganese(II) mixtures for MR imaging have been prepared. Manganese(II) carbonate particles have a R_1 value of $0.06 \text{ mM}^{-1} \text{ s}^{-1}$ in water at 20 MHz and 40 °C and the R_2 values varied depending on the echo time

used to make the measurement [65]. In liver homogenate, the R_1 value increases to $25.04 \text{ mM}^{-1} \text{ s}^{-1}$ after 114 minutes of incubation time. The authors speculate that this is due to the dissolution of the particles to form free Mn^{2+} . This results in $34 \pm 7.2\%$ enhancement of the liver image 125 minutes after injection of $0.01 \text{ mmol Mn kg}^{-1}$ into rats and this enhancement remains fairly constant past 300 minutes post-injection. The stability of polyethyleneglycol-stabilized manganese-substituted hydroxylapatite (MnHA) was investigated with the expectation of using these agents as reticuloendothelial-specific agents [66]. The MnHA particles have R_1 values of $21 \text{ mM}^{-1} \text{ s}^{-1}$ and $11 \text{ mM}^{-1} \text{ s}^{-1}$ at 20 MHz and 40°C for 10-nm and 100-nm particles, respectively. The larger particles were found to break down in vivo into smaller particles that are stable in plasma and blood.

An alternative to manufacturing solutions of manganese(II) is the use of foodstuffs rich in the ion. Blueberry juice is known to be rich in manganese(II), and also contains paramagnetic iron(III) [67, 68]. Initial experiments demonstrated that blueberry juice with concentrations of manganese greater than 0.3 mg L^{-1} acted as a positive contrast agent in T_1 -weighted imaging scans and as a negative contrast agent in T_2 -weighted imaging scans [69]. In subsequent experiments on 21 healthy volunteers using T_1 -weighted imaging scans, blueberry juice significantly increased the signal intensity of the stomach in all subjects, significantly increased the signal intensity of duodenum in thirteen subjects and moderately increased the signal intensity in the other eight, and the increase in signal intensity of the proximal intestine was significant in seven subjects, moderate in five subjects, and minor in nine subjects [68]. Blueberry juice also lowered the amount of ghost artifacts seen due to bowel motion [67].

The water extract from *Theae folium* (green tea) contains manganese complexed by a pectin-like polysaccharide [70]. Administration of a preparation of this extract resulted in an increased signal of the stomach contents in T_1 -weighted imaging [70]. Manganese(II) pectin also showed contrast-enhancing activity in phantoms [71].

A series of manganese(II) chelates attached to polysaccharide molecules were synthesized and the R_1 values were measured [72]. Ethylenediaminetetraacetic acid (Fig. 2) chelated to manganese(II) and attached to sucrose-epichlorohydrin copolymer and aminoethyl dextran yielded R_1 values of $19.2 \text{ mM}^{-1} \text{ s}^{-1}$ and $12.8 \text{ mM}^{-1} \text{ s}^{-1}$, respectively, at 10 MHz and 37°C in a 1:2.13 glycerol-water mixture. Diethylenetriaminepentaacetic acid (Fig. 2) and triethylenetetraaminehexaacetic acid (TTHA, Fig. 2) were both conjugated to dextran molecules. Chelating of manganese(II) ions resulted in complexes with R_1 values at 10 MHz and 37°C of $7.7 \text{ mM}^{-1} \text{ s}^{-1}$ for Mn-DTPA-dextran and $5.5 \text{ mM}^{-1} \text{ s}^{-1}$ for Mn-TTHA-dextran in a 1:2.13 glycerol-water mixture. The glycerol-water mixture was used instead of pure water as the mixture has relaxation properties similar to those of bodily fluids.

Small volumes of MnSO_4 were used to visualize different tissue zones within the cartilage of chicken femoral condyles and pig temporomandibular joints [73]. The images, obtained at 9.4 T using MR microscopy techniques, demonstrate five different tissue types in the chicken samples that were soaked in MnSO_4 : surface layer, fibrous zone, articular cartilage, growth cartilage, and cancellous bone. Injection of MnSO_4 into the pig joint allowed for similar visualiza-

tion of structures. The authors speculate that the Mn^{2+} ions are interacting with the anionic proteoglycans in the cartilage allowing for differentiation of tissues.

2.2

Manganese(III) Porphyrins

Porphyrins are planar compounds composed of four pyrrole-like five-membered rings linked by methene bridges [74]. Four nitrogen atoms bearing two protons point inward in the center of the structure and allow for the coordination of metals. For manganese porphyrins, manganese(II) inserted into the porphyrin ring is quickly oxidized to manganese(III) [75]. The accumulation of porphyrins in cancerous tumors by an as-yet undetermined mechanism has led to the use of these agents as photosensitizers in photodynamic therapy for the treatment of cancers [76]. Irradiation of the porphyrins leads to the formation of reactive oxygen species that cause oxidative cell damage. Such damage indicates a potential problem with porphyrins; namely, that accumulation of the porphyrin molecules in the skin may lead to photosensitivity in the skin that could result in harm to the patient [76, 77].

2.2.1

Mn-TPPS_n

One of the earliest paramagnetic metalloporphyrin agents investigated was the manganese(III) complex of tetra-(4-sulfonatophenyl) porphyrin (TPPS₄, Fig. 3) [16]. The R_1 of this agent was found to be $10.36 \pm 0.09 \text{ mM}^{-1} \text{ s}^{-1}$ at 20 MHz and 37 °C [16], an unusually high value for a manganese(III) agent. This high relaxivity was attributed to both the anisotropy of the ground-state wave function of the metal ion and to the longer-than-expected paramagnetic relaxation time of the manganese(III) spins [78]. The R_1 value increased in human plasma [79], an effect that was later attributed to the binding of Mn-TPPS₄ to human serum albumin (HSA) [80]. The LD₅₀ of Mn-TPPS₄ has been reported to be approximately $0.50 \text{ mmol kg}^{-1}$ when injected i. v. into mice [81, 82] and toxic side effects have been reported with doses as low as $0.25 \text{ mmol kg}^{-1}$ [83, 84]. In addition to the high toxicity of this agent, the green-colored metalloporphyrin complex has been reported to change the color of the skin of mice and rats up to two days

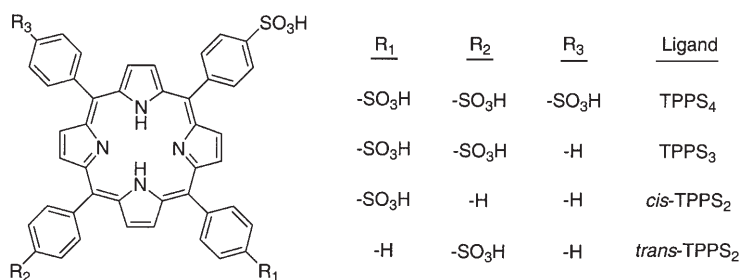


Fig. 3. Sulfonatoporphyrin derivatives

post-injection [84–88]. This color change appears to be only cosmetic, however, as no cutaneous photosensitivity has been reported in mice [77].

Investigations of Mn-TPPS₄ in animal tumor models show that the agent accumulates in several different tumor types. Up to four days post-injection of Mn-TPPS₄, rat brain gliomas (F98) were selectively enhanced as compared to peritumoral tissue [85]. Malignant Schwannoma (RN6) and E367 neuroblastoma were also enhanced with this contrast agent [89, 90]. In vivo relaxometry experiments on rats implanted with all three tumor models demonstrated a $30 \pm 7\%$ reduction in the T_1 values of the tumors after i. p. injection of $0.25 \text{ mmol kg}^{-1}$ Mn-TPPS₄ [91]. Enhancement of brain tumors had been proposed to be due to selective uptake of the metalloporphyrin by peripheral benzodiazepine receptors, but this assertion was later proved false [92, 93]. Subcutaneous human breast carcinoma (MCF-7) in nude mice demonstrated enhancement that was discernable 24 hours post-injection, when the background level of the surrounding tissues had decreased [83, 84]. This enhancement lasted up to eight days post-injection for both MCF-7 tumors and human colon carcinoma (LS-174 T) in nude mice [79]. Manganese(III)-TPPS₄ was not found to significantly enhance liver metastases of human mammary carcinoma (R3230 AC) in rats, as compared to normal liver tissue [94]. More recent experiments have evaluated Mn-TPPS₄ as an agent for the detection of malignant skin tumors, finding that the metalloporphyrin was useful but not advantageous over the readily-available Gd-DTPA [88].

Initially the image enhancement by Mn-TPPS₄ was thought to be due to the tumor-specificity for the agent. Further research has shown that Mn-TPPS₄ is not tumor-specific but necrosis-specific [87]. Both necrotic tumors and necrotic renal and hepatic tissue demonstrated at least 150% contrast ratio after injection of Mn-TPPS₄. Surprisingly, the manganese content of the necrotic renal and hepatic tissue was not significantly elevated, suggesting that there is not a large amount of the agent present and that the increased image enhancement is at least partly due to specific binding of the agent, which consequently increased the relaxivity.

Other manganese(III) sulfonatoporphyrins with progressively fewer sulfonate groups (TPPS₃, *cis*-TPPS₂, *trans*-TPPS₂, Fig. 3) have also been investigated as contrast agents for MRI [84, 95]. Twenty-four hours after injection of the agents into mice bearing subcutaneous mammary carcinoma (SMT-F), all four agents exhibited a decrease in the relaxation rate of the tumor cells with Mn-TPPS₃ demonstrating the greatest relaxivity [95]. Manganese(III)-TPPS₃ also demonstrated the highest tumor concentration and the greatest tumor-muscle ratio. This result was supported by later research with mice bearing MCF-7 human breast carcinoma [84].

2.2.2

Mn-Mesoporphyrin

The mesoporphyrin (MP, Fig. 4) complex of manganese(III) has been investigated as a hepatobiliary contrast agent. In water at 20 MHz and 40 °C, the R_1 value for Mn-MP is $1.9 \pm 0.1 \text{ mM}^{-1} \text{ s}^{-1}$ [96]. This value increases to $2.35 \text{ mM}^{-1} \text{ s}^{-1}$ in bovine plasma due to interactions with bovine serum albumin. While these in

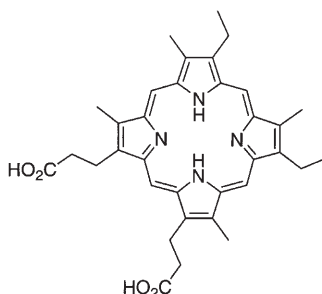


Fig. 4. Mesoporphyrin (MP)

vitro relaxivities are relatively low, the calculated relaxivity of Mn-MP in the liver ($R_1 = 15.7 \text{ mM}^{-1} \text{ s}^{-1}$) is comparable to those of the gadolinium(III) agents Gd-EOB-DTPA and Gd-BOPTA ($R_1 = 16.6 \text{ mM}^{-1} \text{ s}^{-1}$ and $14.6 \text{ mM}^{-1} \text{ s}^{-1}$, respectively) [97, 98]. Unlike Mn-TPPS₄, Mn-MP was not found to discolor the skin of rats [96].

Manganese(III)-MP was originally investigated to determine the ability of the agent to discriminate rat brain gliomas from normal brain tissue [99]. While the agent enhanced the tumors up to 48 hours post-injection, Mn-MP demonstrated greater potential as a hepatobiliary agent. Manganese(III)-MP enhances normal liver (peak enhancement 43%) without enhancing abscesses or mammary adenocarcinoma (R3230 AC) metastases in rats [94]. This enhancement lasted over a 60-minute observation period. Over a three-hour period, 65% of an intravenous injection of 0.1 mmol kg^{-1} Mn-MP was cleared into the bile [96]. Further evidence of the efficacy of Mn-MP as a hepatobiliary agent was demonstrated in rabbits implanted with VX-2 liver carcinoma [100]. The normal liver was enhanced ($99.7 \pm 14.7\%$) while the tumor tissue was not ($14.8 \pm 13.9\%$) when the agent was injected i.v. at $0.04 \text{ mmol kg}^{-1}$.

Intestinal absorption studies of Mn-MP were undertaken in an effort to assess the viability of the metalloporphyrin as an oral hepatobiliary agent [101, 102]. Mixed micelles of Mn-MP complexed with monoolein and taurocholate were administered to rats, resulting in liver image enhancement 68% above baseline levels six hours after administration [101]. In pigs, the mixed micelle preparation showed variable enhancement over 24 hours. Observation that Mn-MP interacts with oleic acid vesicles [103] led to investigations of the effect of oleic acid on the absorption rate of Mn-MP from the small bowel into the circulatory system [102, 104]. The increase in absorption of the complex was mediated by a decrease in the relaxivity of the metalloporphyrin resulting from the interaction with the lipid vesicles.

2.2.3

Mn-Hematoporphyrin

The biodistribution of hematoporphyrin (HP, Fig. 5) complexes of radioactive metals has been well-characterized, making such complexes logical choices for investigation as MRI contrast agents [105, 106]. Manganese(III)-HP increased the signal intensity of rat livers an average of $37 \pm 11\%$ 24 hours after two injec-

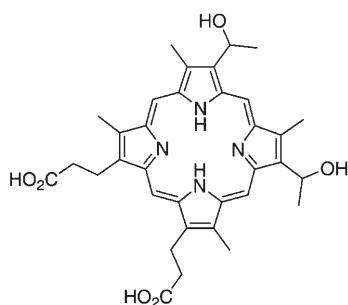


Fig. 5. Hematoporphyrin (HP)

tions of Mn-HP totaling $0.025 \text{ mmol kg}^{-1}$ [107]. No evidence of dissociation of manganese(III) from the porphyrin was noted [108], but the injection of $0.038 \text{ mmol kg}^{-1}$ of Mn-HP led to the death of five of fifteen rats [107].

2.2.4

Mn-TPP

The tetraphenylporphyrin (TPP, Fig. 6) complex of manganese(III) has one of the highest R_1 values reported for manganese-porphyrin agents, $13.0 \text{ mM}^{-1} \text{ s}^{-1}$ at 20 MHz [109]. Injection of this agent into rats led to a greenish color in the skin of the rats that faded over the course of 48 hours. After injection of $0.05 \text{ mmol kg}^{-1}$ Mn-TPP into rats with undifferentiated hepatocellular carcinomas, homogeneous enhancement of the tumors was seen almost immediately and decayed over time. Undifferentiated hepatomas, both implanted and primary, showed delayed enhancement that corresponded to histologically determined intratumoral necrosis and thrombosis.

The observation that the agent accumulated in necrotic tissue and not specifically or preferentially into viable tumors led to the investigation of the agent as a marker for necrosis [110]. Acute myocardial infarctions were induced in rats

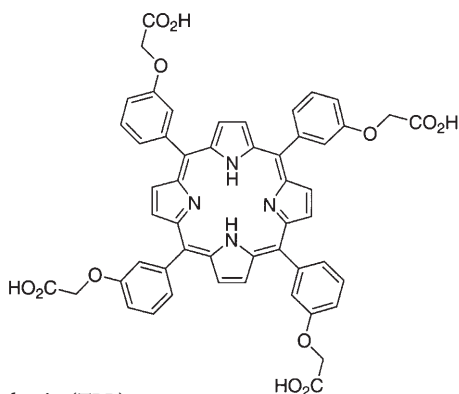


Fig. 6. Tetraphenylporphyrin (TPP)

and the animals were injected with varying concentrations of Mn-TPP. At concentrations greater than $0.05 \text{ mmol kg}^{-1}$, the contrast between normal myocardium and infarcts increased by up to 200%. Necrotic lesions as small as 1 mm in size were detected with no false positive or false negative results.

2.2.5

ATN-10

The manganese(III) complex of the DTPA-ester of 2-[1-(2-hydroxyethoxy)ethyl]-4-vinyl-deuteroporphyrin (IX) (Fig. 7) has been investigated as both a manganese(III)-based contrast agent (ATN-10) and as a heteronuclear contrast agent containing both manganese(III) and gadolinium(III) (Gd-ATN-10) [111–113]. The manganese-only complex was investigated in rat brain tumors (9L gliomas) and demonstrated the ability to distinguish between brain tumor, cold injury model and cytotoxic brain edema after injection of $0.02 \text{ mmol kg}^{-1}$ of ATN-10 [111]. Further research has shown a maximum tumor/normal tissue concentration ratio of ATN-10 of 18.0 was obtained 24 hours after administration of $0.04 \text{ mmol kg}^{-1}$ of the contrast agent [114]. The results of these experiments, however, have been called into question [115]. It has been pointed out that the tumor model used was of a malignant type and, owing to the lack of differentiation between viable and necrotic tissue, the accumulation of the ATN-10 in the tumor may be due to the localization of the porphyrin in necrotic tissue and not due to tumor-specificity.

Gadolinium(III) was complexed to the DTPA component of ATN-10 for possible use in neutron capture therapy [113]. An additional benefit of the incorporation of gadolinium(III) into ATN-10 is the increase in the relaxivity of the agent [113]. Injection of Gd-ATN-10 into rats with 9L gliosarcomas demonstrated an increase in the signal intensity of the tumor. The agent potentially has toxicity problems, though, as it was demonstrated that the metal ions may dissociate from the complex.

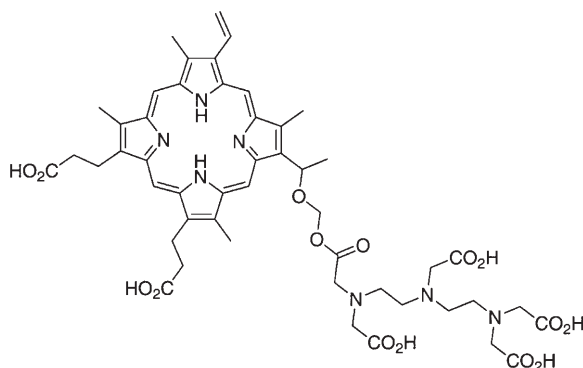


Fig. 7. The DTPA-ester of 2-[1-(2-hydroxyethoxy)ethyl]-4-vinyl-deuteroporphyrin (IX)

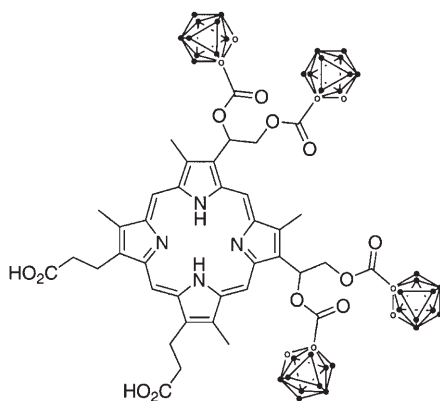


Fig. 8. Boronated protoporphyrin (BOPP). The closed circles represent B-H groups and the open circles represent CH or C groups

2.2.6

Mn-BOPP

Boronated protoporphyrin (2,4-(α,β -dihydroxyethyl)deuterioporphyrin IX, BOPP, Fig. 8), a neutron capture agent, localizes in cerebral gliomas with a ratio of 400:1 as compared with normal brain tissue [116]. The manganese(III) complex of BOPP was investigated as a MRI contrast agent in the expectation that it would behave similarly to the free base BOPP and would act in the dual role of tumor detector and radiation sensitizer [117]. The R_1 value for Mn-BOPP at 10.7 MHz and 37 °C is 4.43 mM⁻¹ s⁻¹. When 0.02 mmol kg⁻¹ Mn-BOPP was injected into rats with 9L cerebral gliomas the tumors had approximately 62% greater signal intensity as compared to normal brain tissue twenty-four hours post-injection. No discoloration of the animals was observed.

The toxicity of Mn-BOPP is approximately twice that of the unmetallated compound [118]. For this reason liposomal preparations of Mn-BOPP were investigated. The optimal liposome composition was determined and liposomal Mn-BOPP was better tolerated than the free drug in mice.

2.2.7

Other Manganese(III) Porphyrins

The manganese(III) complex of uroporphyrin I (UROP-I, Fig. 9) has a R_1 value of 4.75 mM⁻¹ s⁻¹ at 10 MHz in aqueous solution at pH 6.5 [119]. At 300 MHz in human plasma the R_1 value increases to 4.8 mM⁻¹ s⁻¹. Injection into rats with 9L cerebral gliomas demonstrated enhancement of the tumors in 16 of 18 rats studied. This enhancement continued for at least 24 hours post-injection. Unfortunately Mn-UROP-I is too toxic to be used in a clinical setting (LD₅₀ of approximately 0.18 mmol kg⁻¹ in rats).

The tetrasulfonated phthalocyanine (PcS₄, Fig. 10) complex of manganese (III) has a R_1 value of 10.10 mM⁻¹ s⁻¹ at 10.7 MHz and 37 °C and has a LD₅₀ in

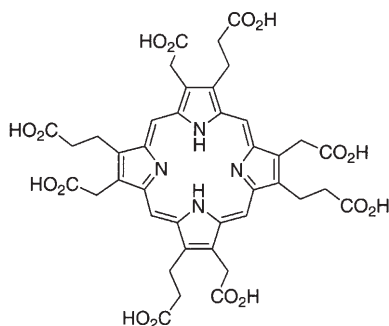


Fig. 9. Uroporphyrin I (UROP-I)

mice of 600 mg kg^{-1} [120]. The structure shown in Fig. 10 is taken directly from the reference but analytical data presented in the paper do not appear to support this structure. Injection (96 mg kg^{-1}) into mice bearing human breast carcinoma demonstrated a maximum increase in the tumor intensity of $131.8 \pm 32.8\%$ over twenty four hours. The animals were reported to turn blue for three-to-five days after injection.

2,4-Bis(1-tetrahydro-fulfuroxyethyl)-deuteroporphynyl(IX)-6,7-bisaspatic acid (THF-ASP, Fig. 11) is a derivative of hematoporphyrin. The manganese(III) complex of THF-ASP (ATN-4 T) has a LD_{50} of more than 2 g kg^{-1} in mice [121]. In mice implanted with PC-3 human prostate carcinoma tumors the average increase in tumor-to-muscle ratio was 32% 1 hour after injection. VX-2 squamous cell carcinoma implanted in rabbits also demonstrated increased tumor-to-muscle enhancement after injection of ATN-4 T [122]. No phototoxicity was demonstrated in the rabbits.

Similar to Gd-ATN-10 and Mn-BOPP, KADTF, a manganese(III) complex of 2-[1-(2-hydroxyethoxy)ethyl]-4-vinyl-deuteroporphyrin (IX) attached to the radiation sensitizer KU2280 (Fig. 12), was conceived as both a method of detecting cancerous tumors and of treating them [123]. The R_1 value for KADTF in water at 10.7 MHz and 37°C is $7.15 \text{ mM}^{-1} \text{ s}^{-1}$ and the LD_{50} in mice was reported to be

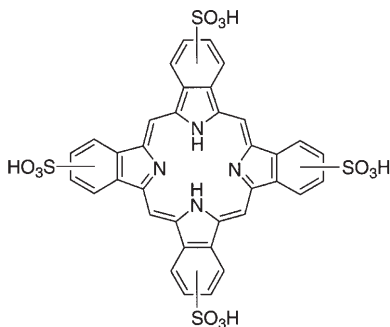


Fig. 10. Tetrasulfonated phthalocyanine (PcS_4)

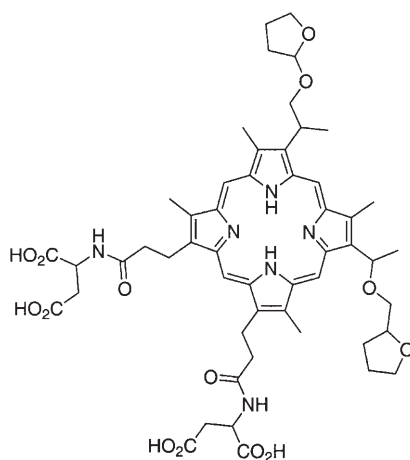


Fig. 11. 2,4-bis(1-tetrahydrofurfuroxyethyl)-deuterioporphynyl(IX)-6,7-bisaspartic acid (THF-ASP)

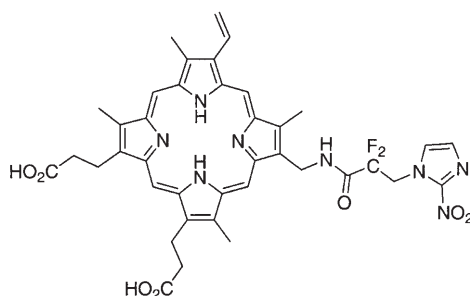


Fig. 12. 2-[1-(2-Hydroxyethoxy)ethyl]-4-vinyl-deuterioporphyrin (IX) attached to the radiation sensitizer KU2280

at least 0.8 mmol kg^{-1} or higher. Injection of KADTF into squamous cell carcinoma-bearing mice resulted in increase in tumor signal intensity of greater than 100 % without a decrease in the effectiveness of the agent as a radiosensitizer.

3 Iron Agents

High-spin d^5 iron(III) would seem to be an ideal candidate as a MRI contrast agent. It has five unpaired electrons and a large volume of literature on the biochemistry of iron is available. Naturally occurring low molecular weight iron-sequestering agents, siderophores, are available for use as ligands and for the development of model systems [124, 125]. The R_1 value for aquo iron(III) at 20 MHz and 37°C is $6.8 \pm 0.2 \text{ mM}^{-1} \text{ s}^{-1}$ [16]. Unfortunately iron(III) is toxic in its free form, with an LD_{50} in mice of $0.42 \text{ mmol kg}^{-1}$ when injected i. p., $0.88 \text{ mmol kg}^{-1}$ when injected i. v., and 7.9 mmol kg^{-1} when administered orally [19]. Acute

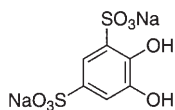


Fig. 13. Tiron®

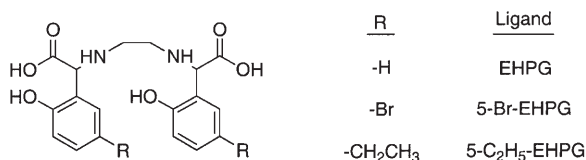
iron poisoning leads to increased respiration and pulse rates, as well as congestion of blood vessels [27]. Levels less than $500 \mu\text{g dL}^{-1}$ plasma are associated with the chance of shock and coma [126].

The greatest concern with iron(III) is the ability of the ion to participate in redox reactions and to catalyze the oxidation of organic substrates. Even benzene has been hydroxylated in the presence of iron(III)-catecholate complexes and hydrogen peroxide in one model system [127, 128]. Iron(III) complexes have also been known to behave as Lewis acid catalysts for hydrolysis of phosphates [129]. Complete coordination of iron(III) lessens the degree of toxicity by decreasing the amount of oxidative cell damage and eliminating open coordination sites to minimize the Lewis acid character. One such example of this approach is the treatment with the ligand Tiron® (Fig. 13) of Chinese hamster V79 cells [130]. The cells were protected against oxygen- and hydrogen peroxide-induced cytotoxicity from redox-active metals such as iron(III). Unfortunately, the complete coordination of iron(III) eliminates the possibility of inner-sphere coordination of water, leaving outer-sphere and second-sphere coordination as the only mechanisms for relaxation. This limitation decreases the efficacy of iron(III)-based contrast agents but has not stopped investigation into the viability of such agents.

3.1

Fe-EHPG and Derivatives

N,N'-Ethylenebis-[2-(*o*-hydroxyphenyl)glycine] (EHPG, Fig. 14) is found in nature as a transporter of iron(III) in plants [131]. The ligand occurs as two stereoisomers (*rac*-EHPG and *meso*-EHPG) which are in approximately 1:1 ratio in unseparated mixtures of EHPG [132]. The iron(III) complexes of the two diastereomers have different stability constants ($\log K = 33.28$ for *meso*-EHPG and $\log K = 35.54$ for *rac*-EHPG) [133]. Unless otherwise stated, the information given here is for a mixture of the stereoisomers. The R_1 value of this complex is $0.9 \text{ mM}^{-1} \text{ s}^{-1}$ and the R_2 value is $1.2 \text{ mM}^{-1} \text{ s}^{-1}$ at 10.7 MHz and 37°C [134]. The R_1 value increases to $1.313 \text{ mM}^{-1} \text{ s}^{-1}$ at 300 MHz and 37°C [135]. For the individual stereoisomers, the R_1 values at 20 MHz and 5°C are $1.37 \text{ mM}^{-1} \text{ s}^{-1}$ for *rac*-Fe-

Fig. 14. Derivatives of *N,N'*-ethylenebis-[2-(*o*-hydroxyphenyl)glycine] (EHPG)

EHPG and $1.41 \text{ mM}^{-1} \text{ s}^{-1}$ for *meso*-Fe-EHPG [136]. Binding experiments with HSA demonstrated a difference in the binding affinities of the two complexes [136]. The association constant for the dominant binding site of *rac*-Fe-EHPG to HSA is $1.3 \pm 0.3 \times 10^3 \text{ M}^{-1}$ and the relaxivity increases approximately four times because of this binding. The *meso*-Fe-EHPG demonstrated almost no observable binding to HSA ($K = 340 \pm 80 \text{ M}^{-1}$) and an increase in relaxivity of approximately two. The LD_{50} of the complex in mice is reported as between 3.4 mmol kg^{-1} [137] and 8.0 mmol kg^{-1} [135].

In addition to different affinities for HSA in vitro, the two stereoisomers of Fe-EHPG have different distributions in vivo [133]. The *meso*-Fe-EHPG complex is cleared from the blood more slowly than *rac*-Fe-EHPG. The rate of liver uptake was also different for the two diastereomers.

Animal experiments with Fe-EHPG demonstrate the effectiveness of this agent as a hepatobiliary contrast agent. Fifteen minutes after i.v. injection of $0.05 \text{ mmol kg}^{-1}$ Fe-EHPG into mice the liver images demonstrated $64 \pm 14\%$ enhancement and the gallbladder demonstrated enhancements of greater than 500% using a T_1 -weighted pulse sequence [134]. T_1 -weighted imaging of dogs revealed that the signal intensity of the liver parenchyma increased 30% after injection of $0.167 \text{ mmol kg}^{-1}$ Fe-EHPG [135].

The capability of Fe-EHPG as a contrast agent for the detection of tumors was also demonstrated. In separate experiments utilizing mice with either intrahepatic implants of reticulum cell sarcoma (M5076) tumors or chemically-induced undifferentiated colon (C-26) tumors, liver-tumor CNR was significantly higher on all post-injection T_1 -weighted images [138]. For small lesions ($< 3 \text{ mm}$), post-injection T_1 -weighted images revealed 99 lesions while pre-injection T_1 - and T_2 -weighted images showed 37 and 49 lesions, respectively. The difference was less for 3–5 mm lesions (153 for T_1 -weighted post-injection images, 104 and 114 for T_1 - and T_2 -weighted preinjection images) and all three image sets revealed lesions $> 5 \text{ mm}$ in size.

Several derivatives of Fe-EHPG have been synthesized and investigated to see if the substitution of functional groups influences the characteristics of the complex as a MRI contrast agent. Substitution of a bromine atom into the 5-position (5-Br-EHPG, Fig. 14) results in two iron complexes: *rac*-Fe-5-Br-EHPG and *meso*-Fe-5-Br-EHPG. As with the unbrominated complexes, *rac*-5-Br-EHPG and *meso*-Fe-5-Br-EHPG have different properties. The R_1 values at 20 MHz and 37°C are $0.84 \pm 0.02 \text{ mM}^{-1} \text{ s}^{-1}$ for *rac*-Fe-5-Br-EHPG and $1.03 \pm 0.02 \text{ mM}^{-1} \text{ s}^{-1}$ for *meso*-Fe-5-Br-EHPG [139]. The three binding constants measured for *rac*-Fe-5-Br-EHPG to HSA are 7.8, 1.4 and $0.2 \times 10^4 \text{ M}^{-1}$. The addition of bilirubin displaces *rac*-Fe-5-Br-EHPG from the primary binding site. *Meso*-Fe-5-Br-EHPG binds to two binding sites on HSA with binding constants of 2.6 and $1.1 \times 10^4 \text{ M}^{-1}$. Bilirubin displaces *rac*-5-Br-EHPG from its secondary binding site indicating that the two complexes bind to different sites with different affinities. The relaxivities of these complexes increase by 2–5 times as a result of these binding interactions. Upon i.v. injection into dogs, Fe-5-Br-EHPG demonstrated comparable liver image enhancement to that obtained with Fe-EHPG when administered at $0.167 \text{ mmol kg}^{-1}$ in T_1 -weighted images [135].

A derivative of EHPG with an ethyl group attached in the 5 position (5-C₂H₅-EHPG, Fig. 14) was also synthesized and evaluated [140]. At 20 MHz and 37 °C, the R_1 value of Fe-5-C₂H₅-EHPG was 0.94 mM⁻¹ s⁻¹ and the R_2 value was 0.96 mM⁻¹ s⁻¹. This derivative also binds to HSA. The LD₅₀ in mice is 3.49 mmol kg⁻¹. Up to one hour post-injection in T₁-weighted images, the signal intensity of rat livers was enhanced by 40%.

3.2

Fe-HBED

The structure of *N,N'*-bis(2-hydroxybenzyl)ethylenediamine-*N,N'*-diacetate (HBED, Fig. 15) is similar to that of EHPG, with the important difference being the lack of stereocenters in HBED. The Fe-HBED complex is more stable than the Fe-EHPG complexes, with a log K of 39.68 [141]. The R_1 values for Fe-HBED, 1.22 mM⁻¹ s⁻¹ at 20 MHz and 5 °C [136] and 1.1 mM⁻¹ s⁻¹ at 10.7 MHz and 37 °C [134], are lower than those for either Fe-EHPG diastereomer. The R_2 value for Fe-HBED is 1.2 mM⁻¹ s⁻¹ at 10.7 MHz and 5 °C [134]. The LD₅₀ of Fe-HBED in mice is 2 mmol kg⁻¹ [137]. As compared to Fe-EHPG, Fe-HBED demonstrates a stronger binding interaction with HSA, with an association constant of $1.7 \pm 0.45 \times 10^3$ M⁻¹ for the primary binding site [136]. The binding interactions between Fe-HBED and HSA account for an increase in the relaxivity of the complex of four times. Fifteen minutes after i.v. injection of 0.05 mmol kg⁻¹ of Fe-HBED into mice the liver enhancement was 54 ± 11 % [134].

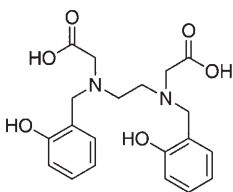


Fig. 15. *N,N'*-bis(2-hydroxybenzyl)ethylenediamine-*N,N'*-diacetate (HBED)

3.3

Desferrioxamine B Derivatives

The iron(III) complex of the microbial siderophore desferrioxamine B (DF, Fig. 16) was investigated as a MRI contrast agent [142], but the rapid injection of this agent may result in a precipitous drop in blood pressure [143]. For this reason, the primary amine on Fe-DF was conjugated with polyethylene-glycol to form Fe-PEG-DF (Fig. 16) [143, 144]. The new derivative has a R_1 value of 1.35 mM⁻¹ s⁻¹ and R_2 value of 1.67 mM⁻¹ s⁻¹ at 20 MHz and 37 °C, both values are similar to those of Fe-DF under the same conditions [143]. The LD₅₀ for Fe-PEG-DF in mice is 7.7 mmol kg⁻¹ and no blood pressure drops were observed after injection of Fe-PEG-DF. The enhancement of dog kidneys after injection of 0.2 mmol kg⁻¹ Fe-PEG-DF was similar to the enhancement profile caused by Gd-DTPA [143].

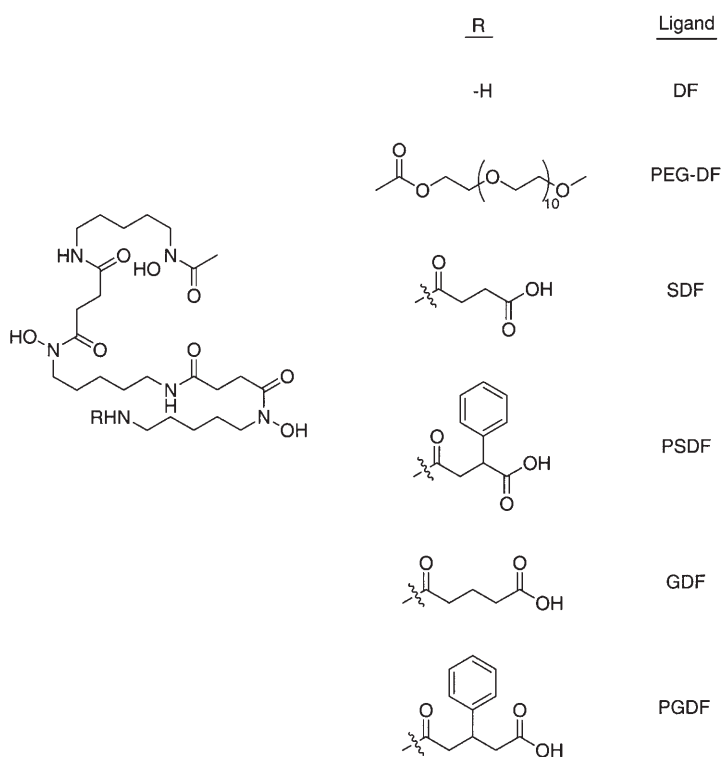


Fig. 16. Derivatives of desferrioxamine B (DF)

More lipophilic derivatives of DF were synthesized in an attempt to increase the liver uptake of the agent [145]. *N*-(Succinyl)desferrioxamine B (SDF), *N*-(2(3)-phenylsuccinyl)desferrioxamine B (PSDF), *N*-(glutaryl)desferrioxamine B (GDF) and *N*-(3-phenylglutaryl)desferrioxamine B (PGDF) were all prepared (Fig. 16) and the iron(III) complexes were tested. Racemic mixtures of Fe-PSDF and Fe-PGDF were formed in the syntheses and used without further separation. The R_1 values for the four derivatives at 10.7 MHz and 37 °C are 2.3 mM⁻¹ s⁻¹, 2.0 mM⁻¹ s⁻¹, 2.1 mM⁻¹ s⁻¹ and 2.0 mM⁻¹ s⁻¹, respectively, all close to the R_1 value of Fe-DF of 2.3 mM⁻¹ s⁻¹ under the same conditions [145]. None of the derivatives nor the parent compound showed substantial binding to HSA [145, 146]. After i. v. injection of 0.2 mmol kg⁻¹ into rats, the enhancement patterns of T₁-weighted images with Fe-DF, Fe-SDF and Fe-GDF were all similar [145]. Renal enhancement was seen with little or no enhancement of other organs. Both Fe-PSDF and Fe-PGDF gave markedly different enhancement patterns. The small intestine lumen was strongly enhanced (maximum of 150%) post-injection. Surprisingly, only 20% enhancement of the liver was seen, suggesting that Fe-PSDF and Fe-PGDF are both rapidly taken up by the liver and excreted into the bile. In vivo competition experiments demonstrate that bromosulfophthalein interferes with Fe-PGDF liver uptake, suggesting that the two anions make use of the same transporter mechanism [146, 147].

3.4

Ferric Ammonium Citrate

Ferric ammonium citrate (FAC) is the major ingredient in liquid Geritol® and was originally investigated as an oral contrast agent due to the approval of the agent as a foodstuff [148]. The R_1 value of FAC at 16 MHz is $1.60 \text{ mM}^{-1} \text{ s}^{-1}$ [149]. Diluted solutions of Geritol® in water were tolerated by patients but the agent was distributed inhomogeneously throughout the small bowel [150]. Unfortunately Geritol® is also 12% ethanol, precluding its use in large volumes as a contrast agent [148].

A mixture of FAC with sodium hydrogen carbonate, tartaric acid, aspartame and artificial grape flavoring was prepared [151]. This agent, alternately referred to as OMR (oral magnetic resonance) and FerriSeltz®, forms a carbonated grape drink when dissolved in water and, unlike Geritol®, contains no alcohol. In phase II and phase III trials in the U.S., forty-eight of 220 patients (22%) reported minor side effects, with diarrhea being the most common [152]. A similar amount of adverse events were reported in the European trials [153], while in the Japanese clinical trials only one patient of 167 reported an adverse event [154]. The difference between the studies may in part be due to the higher volume of solution and larger amount of FAC administered in the European and U.S. trials (600 ml solution containing 1200 and 2400 mg FAC) [152, 153] as compared to the Japanese trials (300 ml solution containing 600 mg and 1200 mg FAC) [154].

In the Japanese study, 600 mg and 1200 mg FAC were administered and both solutions were judged to provide clinically adequate T_1 -weighted imaging though the stomach and duodenum appeared brighter after administration of 1200 mg FAC [154]. In both the U.S. and European clinical trials 1200 mg and 2400 mg FAC were used [152, 153]. When the results of both dose groups in the U.S. trials were combined, administration of FAC contributed new or additional information that potentially changed diagnosis, management or surgical approach in 142 of 220 cases (64%) and in 22 of the 142 patients (15%). A retrospective analysis of the U.S. clinical trials confirmed the efficacy of FAC as a contrast agent for the upper abdomen [155]. In the European trials, T_1 -weighted gradient recalled echo (GRE) images provided diagnostic confidence equal to or greater than that in the precontrast images [153]. Use of GRE and T_1 and T_2 spin-echo imaging sequences provided more diagnostic information than precontrast images, regardless of the dose used. A separate study demonstrated the utility of FerriSeltz in imaging of the pharynx during swallowing [156].

The addition of other compounds to solutions of FAC has been investigated to determine the effect of these other agents on the performance of FAC as an oral contrast agent. FerriSeltz was added to a 1:5 mixture of water and milk in an attempt to improve contrast in the small intestine [157]. The agent was employed in MR cholangiopancreatography (MRCP, 20 patients) and urography (MRU, 20 volunteers) experiments using single-shot rapid acquisition with relaxation enhancement sequences. In MRCP, the signals from the gastrointestinal organs were better eliminated on all of the post-contrast images and the image quality was improved in all but one patient as compared to the precon-

trast images. In MRU, the signals from the gastrointestinal organs were better eliminated in all but one of the post-contrast images and the image quality improved in all but two (one equal, one inferior) of the post-contrast images as compared to the precontrast images. Optimized corn oil emulsions (20%) containing Geritol® (12%) and ice cream and milk (30% and 38%, respectively, to improve palatability) provided “excellent” enhancement of at least 80% of the bowel in five volunteers using three different pulse combinations [158]. Generic FAC in corn oil emulsification also provided similar results in one subject, but the taste of the preparation was not rated as highly as the ice cream-containing agents. A solution of FAC doped with 6% barium sulfate was prepared, allowing the filling of the bowel to be monitored by fluoroscopic techniques [149]. The addition of the barium lowered the R_1 value to $0.5 \text{ mM}^{-1} \text{ s}^{-1}$ at 16 MHz. Very little difference was found between doped and undoped sample of FAC using a series of spin-echo sequences. Another FAC/barium sulfate solution, this one containing 1% w/v FAC and 2% w/w barium sulfate, offered no advantage over baseline examination of the small bowel [159]. A highly viscous ($\sim 14,000 \text{ cp}$ at 25°C) mixture of FAC and carboxymethylcellulose sodium paste was investigated for opacification of the esophagus using T_1 -weighted SE imaging [160]. In twenty patients with esophageal disorders, the esophageal lumen at the site of the lesion was identified in sixteen cases. Thirty-two of thirty-eight (84.2%) sagittal images of patients with abnormal esophagus were judged to be of “excellent” quality.

3.5

Other Iron(III) Agents

The use of blueberry juice, which contains iron(III), as an oral contrast agent was discussed above [67–69]. Other food stuffs were added to iron(III) chloride and investigated as oral contrast agents [161]. Compounds added to iron(III) include phytic acid (Fig. 17), tannins, inositol, cellulose, polyethylene glycol and polyvinylpyrrolidone. The pH of the solutions and the identity of the compounds produced in solution were not reported although it was speculated that the iron-phytate solution formed an oligomer. The R_1 values at 20 MHz for the solutions were: iron and phytate, $3.04 \text{ mM}^{-1} \text{ s}^{-1}$; iron and phytate in a 1% solution of cellulose, $1.60 \text{ mM}^{-1} \text{ s}^{-1}$; iron and tannic acid, $1.046 \text{ mM}^{-1} \text{ s}^{-1}$; and iron and oxalic acid, $1.72 \text{ mM}^{-1} \text{ s}^{-1}$. As the mixture of iron(III) and phytate possessed the highest R_1 value, the optimal ratio of iron(III) and phytate was determined and used in further studies. A 1:1.5 ratio of iron(III):phytate was mixed with xanthan gum (to increase viscosity to 10 cp), propylene glycol (to increase osmolality to 270 mosM), acetic acid (to buffer the solution) and saccharin and vanillin (to improve taste) to produce an oral contrast agent solution. Five human volunteers ingested 900 ml of solution containing 50 to 250 mg L^{-1} iron in 50-mg increments and were imaged. A solution containing 200 mg L^{-1} iron was found to be the most effective for enhancing the bowel. Ingestion of this solution by five volunteers demonstrated that the contrast agent significantly improved the delineation of anatomic features and decreased the amount of artifacts. No side effects were noted and no changes in the serum levels of iron were found.

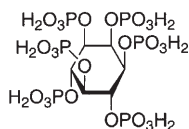


Fig. 17. Phytic acid

An iron(III) glycerophosphate solution was prepared and evaluated as a potential agent for MR colonography [35]. The effect of this solution on the T_1 -value of water was greater than that seen with gadopentetate dimeglumine enema solutions. When the 45 mmol L⁻¹ solution of iron glycerophosphate was injected into pigs, the mean CNR of the colonic lumen was 48 ± 5 relative to surrounding tissues on T_1 -weighted images. The colonic wall CNR was 21 ± 3 and 10 ± 4 relative to the colonic lumen and surrounding structures, respectively. No evidence of iron uptake into colonic mucosal cells was found.

Iron(III) complexed to polymeric backbones yielded high-molecular weight agents [72]. An iron(III)-DTPA-dextran conjugate has an R_1 value of 5.0 mM⁻¹ s⁻¹ at 10 MHz and 37 °C in a 1:2.13 solution of glycerol and water. For comparison purposes, the iron(II) analog of the conjugate had an R_1 value of 2.0 mM⁻¹ s⁻¹. The effect of the conjugation of iron(III)-DTPA to dextran is demonstrated by the huge increase in relaxivity as compared to iron(III)-DTPA (0.72 mM⁻¹ s⁻¹). Under the same conditions, iron(III)-EDTA-sucrose-epichlorohydrin copolymer conjugate had an R_1 value of 0.5 mM⁻¹ s⁻¹ and iron(III)-carboxymethyl-dextran compound had an R_1 value of only 0.07 mM⁻¹ s⁻¹. The glycerol-water solution was used instead of water since this solution has relaxation properties similar to those of body fluids.

A heterobimetallic MR contrast agent containing both iron(III) and gadolinium(III) was prepared using a DTPA-based ligand [162]. Bis(salicylamide)-DTPA (DTPA(PAS)₂, Fig. 2) was synthesized and complexed with gadolinium(III) yielding a complex with an R_1 value of 4.6 mM⁻¹ s⁻¹ at 20 MHz and 25 °C, similar to the value of Gd-DTPA. Addition of iron(III) to the solution produced two different complexes with higher relaxivities, [(H₂O)-Gd-DTPA(PAS)₂]₂-Fe(H₂O)₂ and [(H₂O)-Gd-DTPA(PAS)₂]₃-Fe, depending on the pH of the solution.

The iron(III) tris-complex of Tiron® (Fig. 13) has an R_1 value of 3.15 mM⁻¹ s⁻¹ at 60 MHz and 25 °C [163]. This value is higher than that reported for any other low-molecular weight iron(III) complex [10]. Injection of 0.15 mmol kg⁻¹ into rats demonstrated maximum increases in the kidney and liver image signals of 137% and 73%, respectively. No toxic effects were seen at this concentration, but all animals injected with 0.3 mmol kg⁻¹ of contrast agent died.

Both 1,4,7,10-tetrakis(carboxymethyl)-1,4,7,10-tetraazacyclododecanate (DOTA) and 10-(2-hydroxypropyl)-1,4,7,10-tetraazacyclododecane-1,4,7-triacetate (HP-DO3A) (Fig. 18) have been used as ligands for gadolinium(III) in commercially available MR contrast agent solutions [164, 165]. The analogous iron(III) structures have R_1 values at 20 MHz and 40 °C of 0.4 mM⁻¹ s⁻¹ and 0.5 mM⁻¹ s⁻¹ for Fe-DOTA and Fe-HP-DO3A, respectively [166]. The iron(III) complex with the natural chelator mugineic acid (Fig. 19), demonstrated similar contrast-enhancement behavior to both Fe-DF and Gd-DTPA [71]. The iron(III) complexes with the porphyrins TPPS₄ (Fig. 3) and *meso*-tetrakis(4-*N*-methyl-

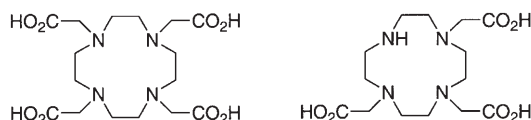


Fig. 18. 1,4,7,10-tetrakis(carboxymethyl)-1,4,7,10-tetraazacyclododecanate (DOTA, *left*) and 10-(2-hydroxypropyl)-1,4,7,10-tetraazacyclododecane-1,4,7-triacetate (HP-DO3A, *right*)

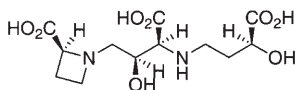


Fig. 19. Mugeniec acid (MA)

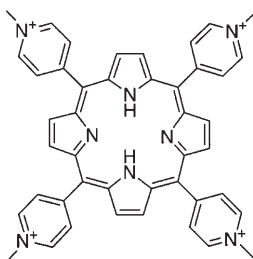


Fig. 20. *Meso*-tetrakis(4-*N*-methyl-pyridiniumyl)porphyrin (TMPyP)

pyridiniumyl)porphyrin (TMPyP, Fig. 20) were found to be unsuitable for use as MRI contrast agents due to a large drop-off in relaxivity above pH 6 [80, 167]. This drop-off is attributable to the formation of dimers and the generation of low-spin adducts upon binding to biomolecules. Synthesis of iron-DTPA-SA liposomes (Fig. 2) yielded liposomes that were too unstable to investigate further [63].

The utility of iron as a MRI contrast agent in non-living systems has also been explored [168]. Due to the different numbers of unpaired electrons, iron(II) and iron(III) have different relaxivities (at 20 MHz and 37 °C the R_1 values are $0.43 \text{ mM}^{-1} \text{ s}^{-1}$ and $8.37 \text{ mM}^{-1} \text{ s}^{-1}$, respectively) [169]. Using appropriate T_1 -weighted imaging techniques the oxidation of iron(II) to iron(III) and the reduction of iron(III) to iron(II) can be observed by the change in the effect of the metal ions on water molecules [168]. This was demonstrated by the migration of sodium bromate, an oxidizing agent, and ascorbic acid, a reducing agent, through polyacrylamide gels doped with iron(II) and iron(III), respectively.

4

Copper Agents

Understandably, complexes of copper have received little attention as contrast agents for MRI. Copper(II) ions have only one unpaired electron and thus have a significantly lower relaxivity than manganese(II), manganese(III) or iron(III).

The R_1 value of copper(II) chloride at 20 MHz and 37 °C has been reported as $0.836 \pm 0.004 \text{ mM}^{-1} \text{ s}^{-1}$ and as $1.0 \text{ mM}^{-1} \text{ s}^{-1}$ [16, 170]. On the other hand, free copper(II) is relatively non-toxic (i. p. LD_{50} in mice is 55 mmol kg^{-1}) as compared to manganese and iron ions [19]. This allows for the injection of greater amounts of copper(II), somewhat lessening the handicap of a lower R_1 . Symptoms of acute copper toxicity include tension, hemolytic anemia with intravascular hemolysis, uremia, and cardiovascular collapse [27]. Copper(II) ions oxidize unhindered sulfhydryl groups on proteins, forming disulfide linkages, while themselves being reduced to copper(I) [22].

4.1

Copper(II) Ions

Copper(II) chloride has been investigated as a potential contrast agent for MR microscopy of cartilage [171, 172]. Copper(II) ions migrate through the cartilage, interacting with the anionic proteoglycan molecules. This interaction slows the relative rate of diffusion as compared to Cu-EDTA (Fig. 2) which cannot interact with the proteoglycans [171]. The binding of the copper(II) ions leads to an increase in the relaxivity of the ions. Evidence of the involvement of the proteoglycans was found by neutralization of the anionic groups on the proteoglycans by either acid or enzymatic digestion [172]. Changing the proteoglycans led to a decrease in the effect of the ions on the relaxation of local protons.

The diffusion of copper(II) ions in non-living systems has also been investigated using MRI techniques [173]. As the paramagnetic ions diffuse through aqueous systems the relaxation rates of the water protons change, allowing for visualization of concentration gradients of copper(II). Using null-point imaging, the rate of diffusion of a copper(II) sulfate solution through polyacrylamide gels and samples of Richemont limestone was monitored [174]. The natural heterogeneity of the rock samples was easily seen in the irregular advance of the copper(II) solution. The rate of diffusion of copper(II) ions through a variety of gel systems was determined using similar techniques [168]. The rate of diffusion of sulfuric acid through a polyacrylamide gel was monitored using similar principles [175]. The R_1 value of aquo copper(II) ions ($1.0 \text{ mM}^{-1} \text{ s}^{-1}$ at 10 MHz and 37 °C) is higher than that of Cu-EDTA ($0.3 \text{ mM}^{-1} \text{ s}^{-1}$ at 10 MHz and 37 °C) due to the reduction in the number of inner-sphere water molecules in the EDTA complex [170]. As the pH of a solution of Cu-EDTA is lowered, the carboxylate groups on the ligand are protonated and no longer interact with the metal center. This frees more coordination sites for inner-sphere water molecules and results in an increase in the relaxivity of the copper complex. Copper(II)-EDTA-doped polyacrylamide gels were spotted with sulfuric acid and the change in the relaxivity of the copper(II) solution was visualized as the acid diffused throughout the gel [175].

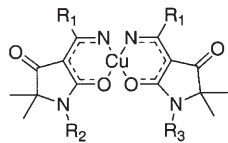
	<u>R₁</u>	<u>R₂</u>	<u>R₃</u>	<u>Isomer</u>	<u>Complex</u>
	-CH ₃	-CH ₃	-CH ₃	Z/Z	Cu-aTA
	-CH ₃	-CH ₂ CH ₃	-CH ₂ CH ₃	E/E	Cu-bTA
	-CH ₃	-CH ₃	-CH ₂ CH ₃	n.d.	Cu-cTA
	-H	-CH ₃	-CH ₃	E/E	Cu-dTA
	-CH ₂ CH ₃	-CH ₃	-CH ₃	Z/E	Cu-eTA
	-CH ₃	-H	-H	n.d.	Cu-fTA

Fig. 21. Derivatives of tetramic acid (TA)

4.2

Copper(II) Tetramic Acid Derivatives

A series of derivatives of tetramic acid were synthesized and complexed to copper(II) (Cu-TA, Fig. 21) [176, 177]. At 300 MHz, the R_1 value of Cu-aTA is $0.073 \pm 0.004 \text{ mM}^{-1} \text{ s}^{-1}$ and the R_2 value is $0.091 \pm 0.006 \text{ mM}^{-1} \text{ s}^{-1}$ [176]. The ability of the Cu-TA derivatives to cross membranes was measured using defolliculated *Xenopus laevis* oocytes as model cells. Using MR microscopy techniques, Cu-aTA, Cu-bTA, Cu-cTA and Cu-eTA were all found to cross into the cytoplasm of the cells [177]. Additionally, atomic absorption spectroscopy revealed the presence of Cu-dTA and Cu-fTA, suggesting that while the complexes failed to cross the cell membrane that they were stored in the membrane-bilayer. Liquid chromatography experiments demonstrated that Cu-aTA crosses membranes intact [176].

4.3

Other Copper(II) Agents

Mixture of D-penicillamine (pen, Fig. 22) and copper(II) chloride forms a complex of the formula $[\text{Cu(I)}_8\text{Cu(II)}_6\text{pen}_{12}]^{5-}$. The R_1 value of this complex at 300 MHz and 23°C is $0.586 \text{ mM}^{-1} \text{ s}^{-1}$ [178]. The carboxylate groups on the cluster have been shown to react with aziridines such as XAMA-7 (Fig. 23) which in turn can be reacted with biotin [179]. The copper clusters can then be attached to antibodies or other biotinylated proteins via an avidin linker molecule.

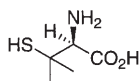


Fig. 22. D-Penicillamine (pen)

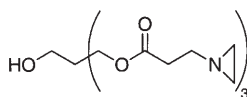


Fig. 23. XAMA-7

Organic polymers with copper(II) complexes attached result in high-molecular weight agents [72]. A copper(II)-DTPA-dextran conjugate has an R_1 value of $0.6 \text{ mM}^{-1} \text{ s}^{-1}$ at 10 MHz and 37°C in a 1:2.13 solution of glycerol and water. A copper(II)-mercaptosuccinic acid-dextran conjugate has the same R_1 value under the same conditions. A copper(II)-carboxymethylcellulose complex had a higher R_1 value of $2.0 \text{ mM}^{-1} \text{ s}^{-1}$ under the same conditions. The glycerol-water solution was used instead of water since this solution has relaxation properties similar to those of bodily fluids.

5 Conclusions

Research has demonstrated that non-gadolinium-based contrast agents for MRI are viable alternatives to gadolinium-based agents. One intravenous and two oral contrast agents utilizing manganese and iron as paramagnets have already been approved for clinical use in many countries. The natural biochemistry of these metals makes a greater knowledge base on the distribution of the ions and their complexes in the body available for researchers to exploit and extend upon, allowing for development of targeted agents. The inherently low relaxivity of the non-gadolinium-based contrast agents may be enhanced by designing complexes that interact with serum proteins and other macromolecules. While it is doubtful that the relaxivities of non-gadolinium-based agents will ever surpass the highest of those of gadolinium-based agents, the opportunity for targeted, high-relaxivity agents is there.

6 References

1. Caravan P, Ellison JJ, McMurry TJ, Lauffer RB (1999) *Chem Rev* 99:2293–2352
2. Bau M, Dulski P (1996) *Earth Planet Sci Lett* 143:245–255
3. Kümmerer K, Helmers E (2000) *Environ Sci Technol* 34:573–577
4. Lester CC, Bryant RG (1992) *Magn Reson Med* 24:236–242
5. Rinck PA (1993) *Magnetic Resonance in Medicine*. Blackwell Scientific, Oxford
6. Bogdanov AA, Lewin M, Weissleder R (1999) *Adv Drug Delivery Rev* 37:279–293
7. Lauffer RB (1987) *Chem Rev* 87:901–927
8. Lauffer RB (1990) *Magnetic Resonance Quarterly* 6:65–84
9. White DL (1991) *Magn Reson Med* 22:309–312
10. Richardson N, Davies JA, Radüchel B (1999) *Polyhedron* 18:2457–2482
11. Bonnemain B (1998) *J Drug Targeting* 6:167–174
12. Kuppusamy P, Wang P, Shankar RA, Ma L, Trimble CE, Hsia CJC, Zweier JL (1998) *Magn Reson Med* 40:806–811
13. Albert MS, Cates GD, Driehuys B, Happer W, Saam B, Springer CS, Jr, Wishnia A (1994) *Nature* 370:199–201
14. Brown JJ (1996) *Magnetic Resonance Imaging Clinics of North America* 4:25–35
15. Lauterbur PC, Mendonça-Dias HM, Rudin AM (1978) Augmentation of tissue water proton spin-lattice relaxation by in vivo addition of paramagnetic ions. In: Dutton PL, Leigh JS, Scarpa A (eds) *Frontiers of Biological Energetics*, vol 1. Academic, New York, pp 752–759
16. Chen C-W, Cohen JS, Myers CE, Sohn M (1984) *FEBS Lett* 168:70–74
17. Kreft BP, Baba Y, Tanimoto A, Finn JP, Stark DD (1993) *Radiology* 186:543–548

18. Elizondo G, Fretz CJ, Stark DD, Rocklage SM, Quay SC, Worah D, Tsang Y-M, Chen MC-M, Ferrucci JT (1991) *Radiology* 178:73–78
19. Calculated from NIOSH (1982) Registry of the Toxic Effects of Chemical Substances. U. S. Government Printing Office, Washington, D.C.
20. Holbrook DJ, Washington ME, Leake HB, Brubaker PE (1975) *Environ Health Perspect* 10:95–101
21. Misselwitz B, Mühler A, Weinmann H-J (1995) *Invest Radiol* 30:611–620
22. Martin RB (1986) Bioinorganic chemistry of metal ion toxicity. In: Sigel H (ed) *Concepts on Metal Ion Toxicity (Metal Ions in Biological Systems)*, vol 20. Marcel Dekker, New York p 21–65
23. Keen CL, Lönnerdal B, Hurley LS (1984) Manganese. In: Frieden E (ed) *Biochemistry of the Essential Ultratrace Elements*. Plenum, New York p 89–132
24. Aschner M, Aschner JL (1991) *Neurosci Biobehav Rev* 15:333–340
25. Brurok H, Schjøtt J, Berg K, Karlsson JOG, Jynge P (1995) *Invest Radiol* 30:159–167
26. Brurok H, Schjøtt J, Berg K, Karlsson JOG, Jynge P (1997) *Invest Radiol* 32:205–211
27. Luckey TD, Venugopal B (1977) *Metal Toxicity in Mammals*. Plenum, New York
28. Greenberg DM, Copp DH, Cuthbertson EM (1943) *J Biol Chem* 147:749–756
29. Kojima S, Hirai M, Kiyozumi M, Sasawa Y, Nakagawa M, Shin-o T (1983) *Chem Pharm Bull* 31:2459–2465
30. Sandström B, Davidsson L, Cederblad Å, Eriksson R, Lönnerdal B (1986) *Acta Pharmacol Toxicol* 59:60–62
31. Thompson TN, Klaassen CD (1982) *Toxicol Appl Pharmacol* 64:236–243
32. Small WC, DeSimone-Macchi D, Parker JR, Sukerkar A, Hahn PF, Rubin DL, Zelch JV, Kuhlman JE, Outwater EK, Weinreb JC, Brown JJ, de Lange EE, Woodward PJ, Arildsen R, Foster GS, Runge VM, Aisen AM, Muroff LR, Thoeni RF, Parisky YR, Tanenbaum LN, Totterman S, Herfkens RJ, Knudsen J, Laster RE, Duerinckx A, Stillman AE, Spritzer CE, Saini S, Rofsky NM, Bernardino ME (1999) *Journal of Magnetic Resonance Imaging* 10:15–24
33. Bernardino ME, Weinreb JC, Mitchell DG, Small WC, Morris M (1994) *Journal of Magnetic Resonance Imaging* 4:872–876
34. Small WC, Macchi DD, Parker JR, Bernardino ME (1998) *Academic Radiology* 5:S147–S150
35. Luboldt W, Frohlich JM, Schneider N, Weishaupt D, Landolt F, Debatin JF (1999) *Radiology* 212:265–269
36. Pautler RG, Silva AC, Koretsky AP (1998) *Magn Reson Med* 40:740–748
37. Narita K, Kawasaki F, Kita H (1990) *Brain Res* 510:289–295
38. Lin Y-J, Koretsky AP (1997) *Mag Reson Med* 38:378–388
39. Tirkkonen B, Aukrust A, Couture E, Grace D, Haile Y, Holm KM, Hope H, Larsen Å, Sivertsen Lunde H, Sjøgren CE (1997) *Acta Radiol* 38:780–789
40. Rocklage SM, Cacheris WP, Quay SC, Hahn FE, Raymond KN (1989) *Inorg Chem* 28:477–485
41. Larsen LE, Grant D (1997) *Acta Radiol* 38:770–779
42. Torres CG, Lundby B, Tufte Sterud A, McGill S, Gordon PB, Strand Bjerknes H (1997) *Acta Radiol* 38:631–637
43. Federle MP, Chezmar JL, Rubin DL, Weinreb JC, Freeny PC, Semelka RC, Brown JJ, Borrello JA, Lee JKT, Mattrey R, Dachman AH, Saini S, Harmon B, Fenstermacher M, Pelsang RE, Harms SE, Mitchell DG, Halford HH, Anderson MW, Johnson CD, Francis IR, Bova JG, Kenney PJ, Klippenstein DL, Foster GS, Turner DA, Stillman AE, Nelson RC, Young SW, Patt RH, Rifkin M, Seltzer SE, Gay SB, Robison RO, Sherwin PF, Ballerini R (2000) *Journal of Magnetic Resonance Imaging* 12:186–197
44. Rummeny E, Ehrenheim C, Gehl HB, Hamm B, Laniado M, Lodemann KP, Schmiedel E, Steudel A, Vogl TG (1991) *Invest Radiol* 26:S142–S145
45. Gallez B, Baudelet C, Adline J, Charbon V, Lambert DM (1996) *Magn Reson Imaging* 14:1191–1195
46. Gallez B, Bacic G, Swartz HM (1996) *Magn Reson Med* 35:14–19

47. Toft KG, Hustvedt SO, Grant D, Martinsen I, Gordon PB, Friisk GA, Korsmo ÅJ, Skotland T (1997) *Acta Radiol* 38:677–689
48. Federle M, Chezmar J, Rubin DL, Weinreb J, Freeny P, Schmiedl UP, Brown JJ, Borrello JA, Lee JKT, Semelka RC, Mattrey R, Dachman AH, Saini S, Harms SE, Mitchell DG, Anderson MW, Halford HH, Bennett WF, Young SW, Rifkin M, Gay SB, Ballerini R, Sherwin PF, Robison RO (2000) *Journal of Magnetic Resonance Imaging* 12:689–701
49. Asplund A, Grant D, Karlsson JOG (1994) *J Pharmacol Exp Ther* 271:609–614
50. Ni Y, Petr  C, Bosmans H, Miao Y, Grant D, Baert AL, Marchal G (1997) *Acta Radiol* 38:700–707
51. Br rok H, Berg K, Sneen L, Grant D, Karlsson JOG, Jynge P (1999) *Invest Radiol* 34:470–476
52. Southon TE, Grant D, Bj rnerud A, Moen OM, Spilling B, Martinsen I, Refsum H (1997) *Acta Radiol* 38:708–716
53. Lim KO, Stark DD, Leese PT, Pfefferbaum A, Rocklage SM, Quay SC (1991) *Radiology* 178:79–82
54. Rofsky NM, Weinreb JC, Benardino ME, Young SW, Lee JKT, Noz ME (1993) *Radiology* 188:53–59
55. Rummeny EJ, Torres CG, Kurdziel JC, Nilsen G, Op de Beeck B, Lundby B (1997) *Acta Radiol* 38:638–642
56. Gehl H-B, Urhahn R, Bohndorf K, Klever P, Hauptmann S, Lodemann K-P, Matern S, Schumpelick V, G nther RW (1993) *Radiology* 186:795–798
57. Romijn MG, Stoker J, van Eijck CHJ, van Muiswinkel JM, Torres CG, Lam ris JS (2000) *Journal of Magnetic Resonance Imaging* 12:261–268
58. Mitchell DG, Outwater EK, Matteucci T, Rubin DL, Chezmar JL, Saini S (1995) *Radiology* 194:783–787
59. Tilcock C (1993) Lipsomal paramagnetic magnetic resonance contrast agents. In: Gregoriadis G (ed) *Liposome Technology Entrapment of Drugs and Other Materials*, vol II. CRC
60. Niesman MR, Bacic GG, Wright SM, Swartz HM, Magin RL (1990) *Invest Radiol* 25:545–551
61. Unger E, Fritz T, Shen DK, Wu G (1993) *Invest Radiol* 28:933–938
62. Gr nder W, Biesold M, Wagner M, Werner A (1998) *Invest Radiol* 33:193–202
63. Schwendener RA, W thrich R, D ewell S, Wehrli E, von Schulthess GK (1990) *Invest Radiol* 25:922–932
64. Eckelman WC, Karesh SM, Reba RC (1975) *J Pharm Sci* 64:704–706
65. Wisner ER, Merisko-Liversidge E, Kellar K, Katzberg RW, Karpinski PH, Amparo EG, Drake C, Griffey SM, Brock JM (1995) *Academic Radiology* 2:140–147
66. Fallis S, Beaty-Nosco J, Dorshow RB, Adzamli K (1998) *Invest Radiol* 33:847–852
67. Papanikolaou N, Karantanas A, Maris T, Gourtsoyiannis N (2000) *Journal of Computer Assisted Tomography* 24:229–234
68. Karantanas AH, Papanikolaou N, Kalef-Ezra J, Challa A, Gourtsoyiannis N (2000) *European Radiology* 10:909–913
69. Hiraishi K, Narabayashi I, Fujita O, Yamamoto K, Sagami A, Hisada Y, Saika Y, Adachi I, Hasegawa H (1995) *Radiology* 194:119–123
70. Mino Y, Yamada K, Takeda T, Nagasawa O (1996) *Chem Pharm Bull* 44:2305–2308
71. Mino Y, Kitagaki H, Sasaki M, Ishii K, Mori T, Yamada K, Nagasawa O (1998) *Biol Pharm Bull* 21:1385–1388
72. Rongved P, Klaveness J (1991) *Carbohydr Res* 214:315–323
73. Kusaka Y, Gr nder W, Rumpel H, Dannhauer K-H, Gersonde K (1992) *Magn Reson Med* 24:137–148
74. Eales L (1979) Clinical chemistry of the porphyrins. In: Dolphin D (ed) *The Porphyrins*, vol IVA. Academic, New York p 663–804
75. Buchler JW (1979) Synthesis and properties of metalloporphyrins. In: Dolphin D (ed) *The Porphyrins*, vol I A. Academic, New York p 389–483
76. Dougherty TJ, Gomer CJ, Henderson BW, Jori G, Kessel D, Korbek M, Moan J, Peng Q (1998) *J Natl Cancer Inst* 90:889–905

77. Musser DA, Fiel RJ (1991) *Photochem Photobiol* 53:119–123
78. Koenig SH, Brown RD, Spiller M (1987) *Magn Reson Med* 4:252–260
79. van Zijl PCM, Place DA, Cohen JS, Faustino PJ, Lyon RC, Patronas NJ (1990) *Acta Radiol Suppl* 374:75–79
80. Yushmanov VE, Tominaga TT, Borissevitch IE, Imasato H, Tabak M (1996) *Magn Reson Imaging* 14:255–261
81. Fiel RJ, Button TM, Gilani S, Mark EH, Musser DA, Henkelman RM, Bronskill MJ, van Heteren JG (1987) *Magn Reson Imaging* 5:149–156
82. Lyon RC, Faustino PJ, Cohen JS, Katz A, Mornex F, Colcher D, Baglin C, Koenig SH, Hambright P (1987) *Magn Reson Med* 4:24–33
83. Place DA, Faustino PJ, van Zijl PCM, Chesnick A, Cohen JS (1990) *Invest Radiol* 25:S69–S70
84. Place DA, Faustino PJ, Berghmans KK, van Zijl PCM, Chesnick AS, Cohen JS (1992) *Magn Reson Imaging* 10:919–928
85. Bockhorst K, Höhn-Berlage M, Kocher M, Hossmann K-A (1990) *Magn Reson Imaging* 8:499–504
86. Bockhorst K, Höhn-Berlage M, Ernestus R-I, Tolxdorff T, Hossmann K-A (1993) *Magn Reson Imaging* 11:655–663
87. Ni Y, Petré C, Miao Y, Yu J, Cresens E, Adriaens P, Bosmans H, Semmler W, Baert AL, Marchal G (1997) *Invest Radiol* 32:770–779
88. Mäurer J, Strauss A, Ebert W, Bauer H, Felix R (2000) *Melanoma Res* 10:40–46
89. Ernestus R-I, Wilmes LJ, Hoehn-Berlage M (1992) *Clin Exp Metastasis* 10:345–350
90. Wilmes LJ, Hoehn-Berlage M, Els T, Bockhorst K, Eis M, Bonnekoh P, Hossmann K-A (1993) *Journal of Magnetic Resonance Imaging* 3:5–12
91. Hoehn-Berlage M, Bockhorst K (1994) *Technology and Health Care* 2:247–254
92. Ikezaki K, Nomura T, Takahashi M, Zieroth BF, Fukui M (1994) *Acta Neurochir Suppl* 60:353–355
93. Ikezaki K, Nomura T, Takahashi M, Fritz-Zieroth B, Inamura T, Fukui M (1994) *Neurol Res* 16:393–397
94. Schmiedl UP, Nelson JA, Starr FL, Schmidt R (1992) *Invest Radiol* 27:536–542
95. Fiel RJ, Musser DA, Mark EH, Mazurchuk R, Alletto JJ (1990) *Magn Reson Imaging* 8:255–259
96. Schmiedl UP, Nelson JA, Robinson DH, Michalson A, Starr F, Frenzel T, Ebert W, Schuhmann-Giampieri G (1993) *Invest Radiol* 28:925–932
97. Schuhmann-Giampieri G, Schmitt-Willich H, Press W-R, Negishi C, Weinmann H-J, Speck U (1992) *Radiology* 183:59–64
98. Vittadini G, Felder E, Tirone P, Lorusso V (1988) *Invest Radiol* 23:S246–S248
99. Nelson JA, Schmiedl U, Shankland EG (1990) *Invest Radiol* 25:S71–S73
100. Robinson DH, Schmiedl UP, Starr FL, Nelson JA, Malek R (1995) *Academic Radiology* 2:43–49
101. Schmiedl UP, Nelson JA, Teng L, Starr F, Malek R, Ho RJY (1995) *Academic Radiology* 2:994–1001
102. von Ingersleben G, Schmiedl UP, Dong P, Nelson JA, Starr F, Ho RJY (1997) *Academic Radiology* 4:355–360
103. Dong P, Choi P, Schmiedl UP, Nelson JA, Starr FL, Ho RJY (1995) *Biochemistry* 34:3416–3422
104. Liu T, Bui T, Schmiedl UP, Ho RJY (1999) *Invest Radiol* 34:615–620
105. Fawwaz RA, Winchell HS, Frye F, Hemphill W, Lawrence JH (1969) *J Nucl Med* 10:581–585
106. Fawwaz RA, Hemphill W, Winchell HS (1971) *J Nucl Med* 12:231–236
107. Bohdiewicz PJ, Lavalley DK, Fawwaz RA, Newhouse JH, Oluwole SF, Alderson PO (1990) *Invest Radiol* 25:765–770
108. Fawwaz R, Bohdiewicz P, Lavalley D, Wang T, Oluwole S, Newhouse J, Alderson P (1990) *Int J Radiat Appl Instrum Part B* 17:65–72
109. Ni Y, Marchal G, Yu J, Lukito G, Petré C, Wevers M, Baert AL, Ebert W, Hilger C-S, Maier F-K, Semmler W (1995) *Academic Radiology* 2:687–699

110. Marchal G, Ni Y, Herijgers P, Flameng W, Petré C, Bosmans H, Yu J, Ebert W, Hilger C-S, Pfeifferer D, Semmler W, Baert AL (1996) *European Radiology* 6:2–8
111. Fujimori H, Matsumura A, Yamamoto T, Shibata Y, Yoshizawa T, Nakagawa K, Yoshii Y, Nose T, Sakata I, Nakajima S (1997) *Acta Neurochir* 70:167–169
112. Yamamoto T (1999) *Neurosurgery* 44:1149–1150
113. Matsumura A, Shibata Y, Yamamoto T, Nakagawa K, Yasuda S, Nakajima S, Sakata I, Yoshizawa T, Nose T (1997) *Neurologia Medico-Chirurgica* 37:327–331
114. Yamamoto T, Matsumura A, Shibata Y, Fujimori H, Nakai K, Yoshida F, Nose T, Sakata I, Nakajima S, Miwa N (1998) *Neurosurgery* 42:1332–1338
115. Ni Y, Miao Y, Semmler W, Marchal G (1999) *Neurosurgery* 44:1146–1149
116. Hill JS, Kahl SB, Kaye AH, Styli SS, Koo M-S, Gonzales MF, Vardaxis NJ, Johnson CI (1992) *Proc Natl Acad Sci USA* 89:1785–1789
117. Huang LR, Straubinger RM, Kahl SB, Koo M-S, Alletto JJ, Mazurchuk R, Chau RI, Thamer SL, Fiel RJ (1993) *Journal of Magnetic Resonance Imaging* 3:351–356
118. Zhou R, Balasubramanian SV, Kahl SB, Straubinger RM (1999) *J Pharm Sci* 88:912–917
119. McMillan JH, Cox GC, Kimler BF, Spicer JS, Batnitzky S (1991) *Magn Reson Imaging* 9:553–558
120. Saini SK, Jena A, Dey J, Sharma AK, Singh R (1995) *Magn Reson Imaging* 13:985–990
121. Suzuki T, Nakano K, Tomiyoshi K, Sakata I, Endo K, Yamanaka H (1996) *J Urol* 156:1850–1852
122. Kobayashi M, Tajiri H, Hayashi T, Kuroki M, Sakata I (1999) *Cancer Lett* 137:83–89
123. Nakajima S, Shigemi N, Murakami N, Aburano T, Sakata I, Maruyama I, Inoue M, Take-mura T (1997) *Anti-Cancer Drugs* 8:386–390
124. Neiland JB (1981) Microbial iron transport compounds (siderophores) as chelating agents. In: Martell AE, Anderson WF, Badman DG (eds) *Development of Iron Chelators for Clinical Use*. Elsevier/North Holland, New York p 13–31
125. Cotton FA, Wilkinson G, Murillo CA, Bochmann M (1999) *Advanced Inorganic Chemistry*. John Wiley and Sons, New York
126. Braunwald E, Isselbacher KJ, Petersdorf RG, Wilson JD, Martin JB, Fauci AS (1987). McGraw-Hill Books, New York
127. Hotta K, Tamagaki S, Suzuki Y, Tagaki W (1981) *Chem Lett* 6:789–790
128. Tamagaki S, Suzuki K, Tagaki W (1989) *Bull Chem Soc Jpn* 62:148–152
129. Sadler NP, Chuang C-C, Milburn RM (1995) *Inorg Chem* 34:402–404
130. Krishna CM, Liebmman JE, Kaufman D, DeGraff W, Hahn SM, McMurphy T, Mitchell JB, Russo A (1992) *Arch Biochem Biophys* 294:98–106
131. Frost AE, Freedman HH, Westerback SJ, Martell AE (1958) *J Am Chem Soc* 80:530–536
132. Patch MG, Simolo KP, Carrano CJ (1982) *Inorg Chem* 21:2972–2977
133. Madsen SL, Bannochie CJ, Martell AE, Mathias CJ, Welch MJ (1990) *J Nucl Med* 31:1662–1668
134. Hoener B-A, Engelstad BL, Ramos EC, Macapinlac HA, Price DC, Johnson TR, White DL (1991) *Journal of Magnetic Resonance Imaging* 1:357–362
135. Liu G-C, Wang Y-M, Jaw T-S, Chen H-M, Sheu R-S (1993) *J Formosan Med Assoc* 92:359–366
136. Larsen SK, Jenkins BG, Memon NG, Lauffer RB (1990) *Inorg Chem* 29:1147–1152
137. Stark DD, Elizondo G, Fretz CJ (1990) *Invest Radiol* 25:S58
138. Shtern F, Garrido L, Compton C, Swiniarski JK, Lauffer RB, Brady TJ (1991) *Radiology* 178:83–89
139. Jenkins BG, Armstrong E, Lauffer RB (1991) *Magn Reson Med* 17:164–178
140. Sheu R-S, Liu G-C, Wang Y-M, Jaw T-S, Chen H-M, Kuo Y-T (1997) *Kaohsiung J Med Sci* 13:75–85
141. Martell AE (1981) The design and synthesis of chelating agents. In: Martell AE, Anderson WF, Badman DG (eds) *Development of Iron Chelators for Clinical Use*. Elsevier/North-Holland, New York p 67–104
142. Worah D, Berger AE, Burnett KR, Cockrill HH, Kanal E, Kendall C, Leese PT, Lyons KP, Ross E, Wolf GL, Quay SC (1988) *Invest Radiol* 23:S281–S285

143. Duewell S, Wüthrich R, von Schulthess GK, Jenny HB, Muller RN, Moerker T, Fuchs WA (1991) *Invest Radiol* 26:50–57
144. von Schulthess GK, Duewell S, Jenny H-B, Wüthrich R, Peter HH (1990) *Invest Radiol* 25:S48
145. Muetterties KA, Hoener B-A, Engelstad BL, Tongol JM, Wikstrom MG, Wang S-C, Eason RG, Moseley ME, White DL (1991) *Magn Reson Med* 22:88–100
146. White DL, Eason RG, Alkire AL, Price DC, Hoener BA, Milco LA, Keen RE, Barnhart JL (1991) *Invest Radiol* 26:S146–S147
147. Hoener B-A, Tzika AA, Englestad BL, White DL (1991) *Magn Reson Med* 17:509–515
148. Wesbey GE, Brasch RC, Engelstad BL, Moss AA, Crooks LE, Brito AC (1983) *Radiology* 149:175–180
149. Rubin DL, Muller HH, Young SW (1992) *Magn Reson Med* 23:154–165
150. Tart RP, Li KCP, Storm BL, Rolfes RJ, Ang PGP (1991) *Magn Reson Imaging* 9:559–568
151. Patten RM, Moss AA, Fenton TA, Elliott S (1992) *Journal of Magnetic Resonance Imaging* 2:25–34
152. Patten RM, Lo SK, Phillips JJ, Bowman SC, Glazer GM, Wall SD, Bova JG, Harris RD, Wheat RL, Johnson CD, Kressel HY, Stillman AE, Halvorsen RA, Moss AA (1993) *Radiology* 189:277–283
153. Kivelitz D, Gehl H-B, Heuck A, Krahe T, Taupitz M, Lodemann K-P, Hamm B (1999) *Acta Radiol* 40:429–435
154. Hirohashi S, Uchida H, Yoshikawa K, Fujita N, Ohtomo K, Yuasa Y, Kawamura Y, Matsui O (1994) *Magn Reson Imaging* 12:837–846
155. Malcolm PN, Brown JJ, Hahn PF, Stillman AE, Li KCP, Kawamura Y, Tanaka T, Noel JK, Molony BA, Johnson MF, Hildebolt CF (2000) *Journal of Magnetic Resonance Imaging* 12:702–707
156. Suto Y, Kamba M, Kato T (1995) *Br J Radiol* 68:1099–1102
157. Hirohashi S, Hirohashi R, Uchida H, Kitano S, Ono W, Ohishi H, Nakanishi S (1997) *Radiology* 203:281–285
158. Li KCP, Ang PGP, Tart RP, Storm BL, Rolfes R, Ho-Tai PCK (1990) *Magn Reson Imaging* 8:589–598
159. Kraus BB, Rappaport DC, Ros PR, Torres GM (1994) *Magn Reson Imaging* 12:847–858
160. Ogawa Y, Noda Y, Morio K, Nishioka A, Inomata T, Yoshida S, Toki T-I, Ogoshi S (1996) *Journal of Computer Assisted Tomography* 20:455–459
161. Unger EC, Fritz TA, Palestrant D, Meakem TJ, Granstrom P, Gatenby RA (1993) *Journal of Magnetic Resonance Imaging* 3:119–124
162. Aime S, Botta M, Fasano M, Terreno E (1993) *Spectrochim Acta, Part A* 49 A:1315–1322
163. Davies JA, Dutremez SG, Hockensmith CM, Keck R, Richardson N, Selman S, Smith DA, Ulmer CW, II, Wheatley LS, Zeiss J (1996) *Academic Radiology* 3:936–945
164. Tweedle MF (1997) *European Radiology* 7:S225–S230
165. Geraldles CFGC, Sherry AD, Brown RD, Koenig SH (1986) *Magn Reson Med* 3:242–250
166. Chang CA, Francesconi LC, Malley MF, Kumar K, Gougoutas JZ, Tweedle MF (1993) *Inorg Chem* 32:3501–3508
167. Yushmanov VE, Imasato H, Tominaga TT, Tabak M (1996) *J Inorg Biochem* 61:233–250
168. Balcom BJ, Fischer AE, Carpenter TA, Hall LD (1993) *J Am Chem Soc* 115:3300–3305
169. Gore JC, Kang YS, Schulz RJ (1984) *Phys Med Biol* 29:1189–1197
170. Vymazal J, Bulte JWM, Frank JA, di Chiro G, Brooks RA (1993) *Journal of Magnetic Resonance Imaging* 3:637–640
171. Fischer AE, Carpenter TA, Tyler JA, Hall LD (1995) *Magn Reson Imaging* 13:819–826
172. Potter K, Spencer RGS, McFarland EW (1997) *Biochim Biophys Acta* 1334:129–139
173. Fischer AE, Hall LD (1996) *Magn Reson Imaging* 14:779–783
174. Fischer AE, Balcom BJ, Fordham EJ, Carpenter TA, Hall LD (1995) *J Phys D:Appl Phys* 28:384–397

175. Fischer AE, Hall LD (1994) *Mag Reson Mater Phys Biol Med* 2:203–210
176. Päuser S, Keller K, Zschunke A, Mügge C (1993) *Magn Reson Imaging* 11:419–424
177. Tietze O, Reck G, Schulz B, Zschunke A, Keller K (1996) *J Prakt Chem/Chem-Ztg* 338:642–646
178. Kupka T, Dziegielewska JO, Pasterna G, Malecki JG (1992) *Magn Reson Imaging* 10:855–858
179. Bigham SL, Ballard JD, Giles KD, Clelland CS, Jeffcoat R, Griffin KS, Farley TD, Bushman DR, Wright JR (1990) *Physiol Chem Phys Med NMR* 22:63–72

Blood-Pool MRI Contrast Agents: Properties and Characterization

R. B. Clarkson

Department of Veterinary Clinical Medicine and the Illinois EPR Research Center,
University of Illinois, Urbana, IL 61801, USA
E-mail: clarkson@uiuc.edu

Unlike extracellular MRI contrast agents, which distribute non-specifically throughout the plasma and interstitial space of the body, blood-pool contrast agents (BPCA's) can remain largely in the vasculature throughout the period of an MRI examination. Vascular retention is achieved by the larger size of BPCA's, which also affects clearance times, rotational motion, and overall relaxivity. Nuclear magnetic relaxation dispersion (NMRD), NMR, and EPR techniques can provide details of BPCA behavior. Several different approaches for effective BPCA's currently are being developed, including polymeric and dendrimeric complexes of Gd^{3+} , low molecular weight Gd^{3+} complexes that reversibly bind to serum proteins, and ultra-small iron oxide particles. Applications of blood-pool agents include arterial phase and equilibrium phase MR angiography.

Keywords. Blood-pool contrast agents, Rotational motion, Relaxivity, Gd^{3+} chelates, Iron oxide particles, NMRD, EPR, NMR

1	Introduction	202
2	Types of Blood-Pool Contrast Agents	206
2.1	Gd^{3+} Chelates Covalently Attached to Proteins	206
2.2	Polymeric Gd^{3+} Chelates	206
2.3	Dendrimeric Gd^{3+} Chelates	209
2.4	Iron Oxide Particles	211
2.5	Low Molecular Weight Gd^{3+} Chelates Binding to Serum Proteins . .	212
2.6	Micelles and Liposomes	215
3	Physical Characterization of Protein-Associated BPCA's	216
4	Summary	230
5	References	232

List of Abbreviations

BBB	blood-brain barrier
BPCA	blood-pool contrast agent
BSA	bovine serum albumin
BWR	Bloch-Wangsness-Redfield
CNS	central nervous system
Da	Dalton
DOTA	1,4,7,10-tetrakis(carboxymethyl)-1,4,7,10- tetraazacyclododecane
DTPA	diethylene triamine pentaacetic acid
EPR	electron paramagnetic resonance
ESEEM	electron spin echo envelope modulation
HSA	human serum albumin
LODEPR	longitudinally-detected EPR
MR	magnetic resonance
MRI	magnetic resonance imaging
MW	molecular weight
NMR	nuclear magnetic resonance
NMRD	nuclear magnetic relaxation dispersion
PAMAM	poly(amidoamine)
PBL	Poupko-Barum-Luz
PCA	paramagnetic contrast agent
RIME	receptor-induced magnetization enhancement
USPIO	ultrasmall superparamagnetic iron oxide
ZFS	zero field splitting

1 Introduction

The use of paramagnetic contrast agents to improve the diagnostic specificity of MRI examinations has expanded rapidly in the last two decades. Gd(III)-DTPA was first introduced to clinical trials in Berlin in December, 1983 [1], and gained FDA approval in the United States in 1988. Since the first trials, literally hundreds of different chelates of Gd^{3+} , Mn^{2+} , Fe^{3+} and other paramagnetic metal ions have been synthesized and tested as potential paramagnetic contrast agents (PCAs), as have several superparamagnetic agents. In all the creative efforts in this field, the twin goals of higher contrast agent effectiveness (higher relaxivity) and greater patient safety (lower toxicity) have guided researchers.

The first successful compounds used in MRI contrast-enhanced imaging were small Gd^{3+} chelates, with molecular weights roughly in the range from 500–1000 g/mole. After intravenous administration, these compounds rapidly diffuse out of the vasculature into the extracellular space. The exception to this extravascular diffusion is in the brain, where an intact blood-brain barrier (BBB) prevents rapid movement out of the vessels. The great success that these small, extravascular agents have had in diagnosing lesions in the brain and CNS is due largely to the fact that any disease that disrupts or compromises the BBB

provides a route for PCA diffusion out of the vessels, with an accompanying diagnostic alteration in MRI image contrast.

While rapid extravascular diffusion is an advantage in diagnosing brain lesions, it comes with several serious drawbacks. The very ease of diffusion out of the circulation leads to a short half-life and rapid excretion, usually via the kidneys. After intravenous injection in man, for example, Gd-DTPA rapidly undergoes intravascular distribution and diffusion into the extracellular space. The early distribution phase is complete within a few minutes ($t_{1/2} \approx 10$ min), and the elimination phase has a half-life of about 1.5 hours [2]. The extremely hydrophilic character of Gd-DTPA keeps the agent from penetrating cellular membranes, and no binding to proteins is observed. This rapid exit from the circulation means that the contrast-enhanced phase of the MRI examination also is short, and that very little of the extracellular agent is available in the circulation for other diagnostic procedures, such as MR angiography. Clearly, it would be useful to have PCAs that are retained in the circulation for longer times.

Another disadvantage of the small, hydrophilic agents is that they tumble very rapidly in the extracellular fluid. In water at 25°C, for example, Gd-DTPA has a rotational correlation time (τ_R) of 58 ps as determined by the fitting of NMRD data [3], and 105 ps by EPR simulation in the VO^{++} -DTPA analog [4]. This very rapid motion dominates the relaxivity of the PCA in the frequency range of typical clinical interest (42–63 MHz). The reasons for this dominance of τ_R can be traced to the fact that small Gd^{3+} chelates like Gd-DTPA have a relaxivity at clinical frequencies that is determined predominantly by an inner sphere process; for Gd-DTPA at 50 MHz, Chen et al. calculate that the relaxivity in water is 43% inner sphere, 25% second sphere, and 32% outer sphere [4]. In turn, the inner sphere contribution to relaxivity is often modeled by the Solomon-Bloembergen equations [5, 6]

$$\frac{1}{T_1} = \frac{P_m q}{T_{1m} + \tau_m} \quad (1)$$

$$\frac{1}{T_{1m}} = \frac{2}{15} \frac{\gamma_I^2 g^2 \mu_B^2 S(S+1)}{r^6} \left[\frac{3\tau_1}{(1 + \omega_I^2 \tau_1^2)} + \frac{7\tau_2}{(1 + \omega_s^2 \tau_2^2)} \right] \quad (2)$$

$$\frac{1}{\tau_i} = \frac{1}{T_{ie}} + \frac{1}{\tau_m} + \frac{1}{\tau_R} \quad (3)$$

In these equations, the symbols have their customary meanings (see Toth et al. in this volume for an excellent review of the topic), and the correlation times given in Eq. (3) have the following typical values at 50 MHz in water: T_{1e} (electron spin-lattice relaxation time) ≈ 10 ns, T_{2e} (electron spin-spin relaxation time) ≈ 1 ns, τ_m (inner sphere water exchange correlation time) ≈ 130 ns [3], and $\tau_R \approx 60$ ps. These values, in the context of Eq. (1–3), show why rotational dynamics control relaxivity for such chelates.

One effect of this rapid rotational motion is the loss of relaxivity at clinical frequencies. Figure 1 shows a Nuclear Magnetic Relaxation Dispersion (NMRD)

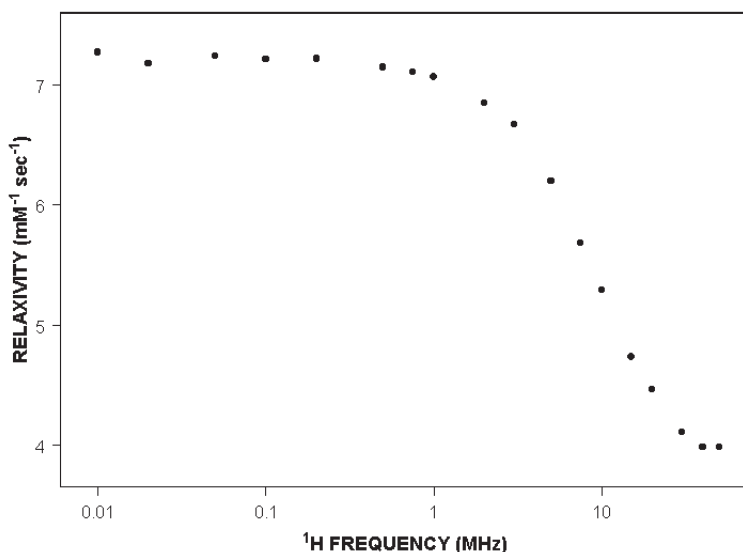


Fig. 1. Proton NMRD curve for Gd-DTPA in water at 24°C

curve for Gd-DTPA, which illustrates the problem caused by a rapid τ_R . Similar profiles are produced by virtually all low molecular weight agents. The same dynamic factor which causes the effectiveness of PCAs to fall off at higher frequencies also can restore relaxivity (r_1) in the clinical frequency range if τ_R can be slowed. This dependence of r_1 on τ_R is illustrated in Fig. 2. If the rotational motion of the agent can be slowed, effectiveness in the clinical frequency range will be restored, and even enhanced over values observed in fast-tumbling PCAs.

Blood pool contrast agents are designed to address both the need for longer vascular retention times and the desire for longer τ_R . First developed as Gd^{3+} complexes covalently bound to proteins like HSA or BSA [7] or to polymers like polylysine [8], the general class of agents has expanded to include complexes covalently and non-covalently bound to proteins, covalently bound to polymers and dendrimers, and micro-particles of iron oxide. All of these approaches have advantages that include high dose efficiency, prolonged tissue enhancement that eliminates the critical timing of images, the ability to gauge tissue blood volume and perfusion, and the ability to evaluate changes in capillary integrity [9]. The key physical characteristic that allows these agents to remain longer in the vasculature is to have a size greater than can easily pass out of capillaries. For example, glomerulus capillaries in the kidneys are fenestrated with pores 60–70 nm in diameter, each closed by a pore diaphragm. These capillaries can filter the plasma to remove any drug that has a molecular weight below about 20 kDa.

Above this weight, excretion also depends on the lipid solubility and polarity of the agent, as well as the pH of the environment [10]. Larger agents are partly or completely limited in diffusion through the endothelial membrane, but they

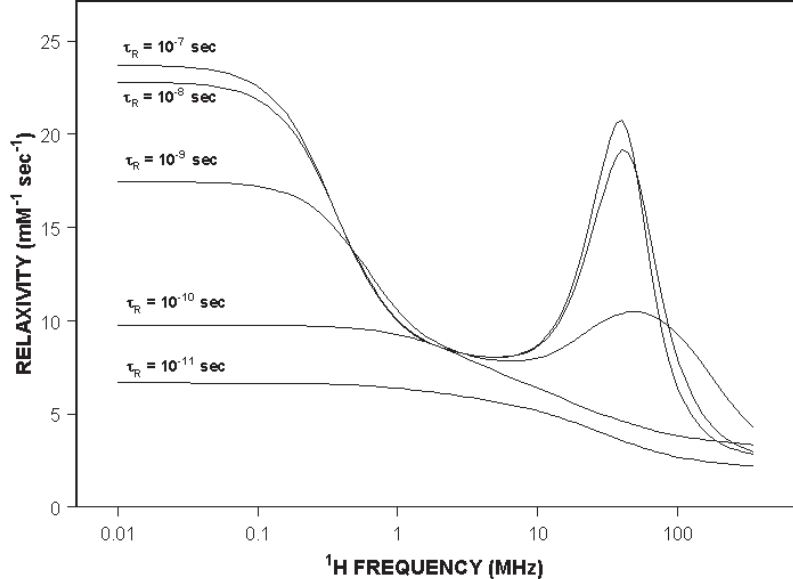


Fig. 2. Simulated dependence of relaxivity (r_1) on T_2

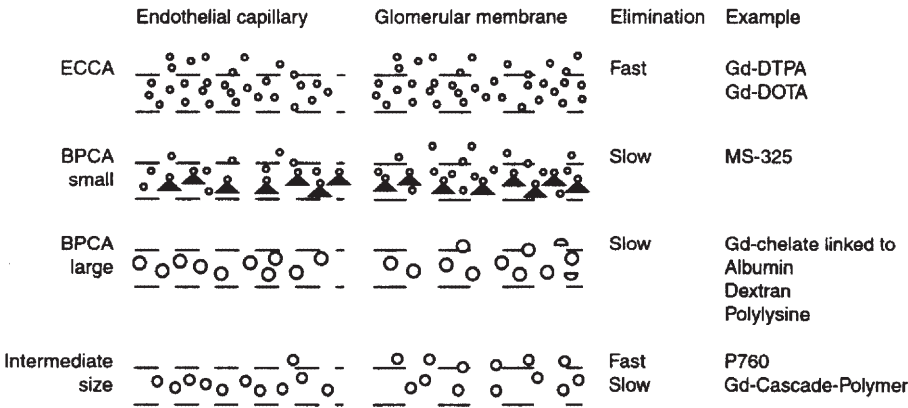


Fig. 3. Distribution and elimination of different sized PCAs. Note difference in permeability (pore size) of endothelial capillary and glomerular membrane ECCA = extracellular contrast agent; BPCA = blood-pool contrast agent. Adapted from [10] with permission

usually still are excreted by the kidneys. Molecules larger than about 70 kDa do not pass the glomerulus filter, but are metabolized before excretion [11]. Endothelial capillaries have a smaller permeability (pore size), and may not pass particles larger than 10–20 nm in diameter ($MW \leq 20$ kDa). A schematic of the distribution and elimination of different sized contrast agents is shown in Fig. 3 [10]; details of the diagram will be discussed in following sections.

2

Types of Blood Pool Agents

2.1

Gd³⁺ Chelates Covalently Bound to Proteins

One of the first attempts to slow the rotation of small Gd³⁺ chelates was to covalently attach them to proteins like HSA and BSA [7, 12–14]. DTPA chelates can be bonded to the protein by means of the reaction of DTPA-dianhydride with BSA or HSA in buffered aqueous solution. Resulting PCA/protein conjugates can be synthesized with up to about 30 Gd-DTPA ligands per protein, or up to 90 Gd³⁺/HSA with the chelate diethylenetriaminetetraacetic acid monoamide (DTTA-MA) [15]. A significant enhancement in the relaxivity/Gd³⁺ is observed in these protein conjugates, due to a longer τ_R produced by the slower tumbling of the chelate/protein system. For example, the relaxivity per Gd³⁺ (r_1) of the DTTA-MA/HSA conjugate is 14 mM⁻¹ s⁻¹ at 10 MHz [15], while the relaxivity of Gd-DTPA at the same frequency is about 3. This increase is by no means optimal (and may indicate both segmental rotational freedom of the protein linker and dipole-dipole interactions between neighboring Gd³⁺ ions), but the expected increase clearly is seen. For a less heavily loaded albumin, utilizing the cyclic anhydride of DTPA as a starting material, a relaxivity of about 20 mM⁻¹ s⁻¹/Gd³⁺ has been reported [13].

Albumin conjugates show a much longer contrast-enhancing effect, and prolonged intravascular retention [13]. Since HSA has a molecular weight of about 68 kDa, the chelate/protein conjugates can be considered large BPCAs, as seen in Fig. 3. Albumin-based macromolecular agents are not considered optimal for clinical development for several reasons. The consistency of the synthetic product is difficult to control. Cardiovascular toxicity may be a problem. Finally, there is a prolonged retention of gadolinium in the bone and liver for weeks to months after administration of a typical imaging dose.

2.2

Polymeric Gd³⁺ Chelates

Dextran [16] and polylysine-linked Gd-DTPA [17, 18] or Gd-DOTA [19] formed the basis for the first polymer-based BPCAs. The successes that these compounds have had in a variety of vascular and cardiac imaging applications has led to the development of a wide range of synthetic linear polymer-based agents that modify both the intravascular retention times and the relaxivity. Figure 4 illustrates the variation of r_1 relaxivity in three polylysine-Gd-DTPA compounds of differing molecular weight, compared with a monomeric Gd-DTPA preparation. Simulation of the NMRD curves gives approximate values of τ_R of 640 ps, 500 ps, 235 ps, and 70 ps for molecular weights of 50 kDa, 40 kDa, 2.3 kDa, and 0.7 kDa, respectively. If the behavior of these complex compounds can be approximated by a simple spherical Stokes-Einstein model for rotation in

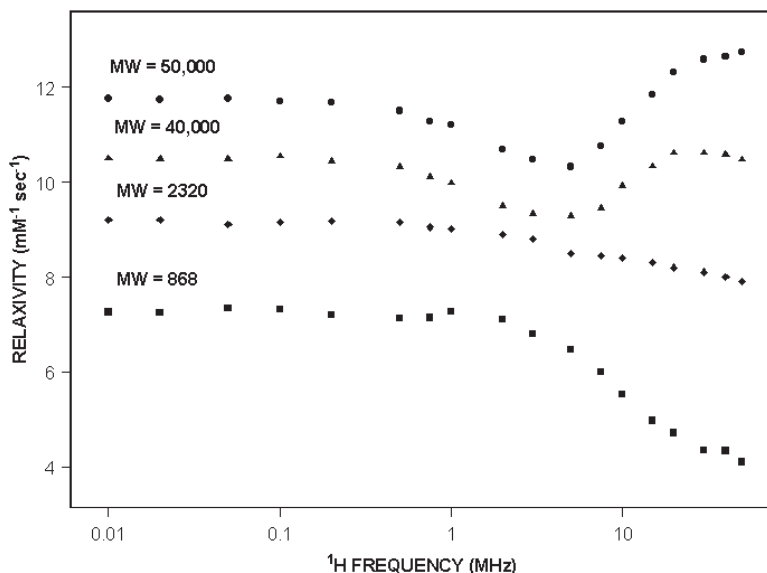


Fig. 4. NMRD curves for three polylysine-Gd-DTPA compounds (MW 50 kDa, 40 kDa, and 2.3 kDa), together with a Gd-DTPA preparation in water at 22°C. Compounds courtesy of H. J. Weinmann, Schering AG

solution, then the variation of τ_R with molecular weight will follow a relationship of the form:

$$\tau_m = \frac{4\pi R^3 \eta}{3k_B T} \quad (4)$$

Here, R is the radius of the sphere, η is the coefficient of viscosity, k_B is Boltzmann's constant, and T is temperature. Equation (4) implies that τ_R should vary linearly with volume, or mass, in the range where the Stokes-Einstein equation is valid. Figure 5 shows the roughly linear behavior of τ_R for these compounds, and illustrates why polymeric conjugates of Gd^{3+} chelates remain a very attractive method of modulating both τ_R and the intravenous retention time ($t_{1/2}$) of BPCAs.

Molecular weight alone is not an assurance that τ_R will increase in an optimal fashion. Local segmental flexibility can permit the Gd-chelate moiety to rotate rapidly while the overall motion of the polymer conjugate is much slower. In fact, many linear polymer systems show no appreciable increase in τ_R as molecular weights increase beyond 10 kDa, indicating that segmental flexibility dominates the motion of the paramagnetic ion. This can be seen by examining one common chemistry of attachment of a DTPA chelate to the polymer polylysine. As shown in Fig. 6, the entire carbon chain and amide linkage of DTPA allows for significant segmental flexibility, resulting in a τ_R value that is significantly shorter than the rotational correlation time for the polymer as a whole. Slower than

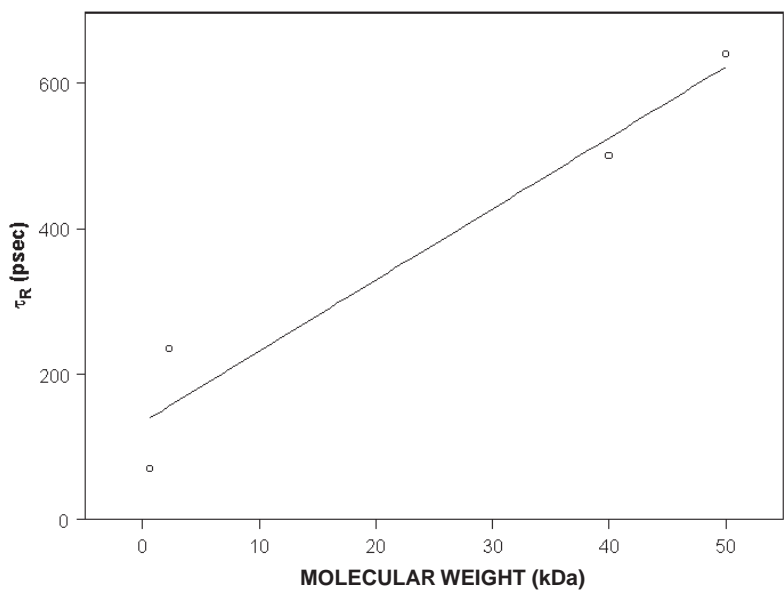


Fig. 5. Variation of τ_R with molecular weight for compounds in Fig. 4, illustrating the approximate Stokes-Einstein behavior

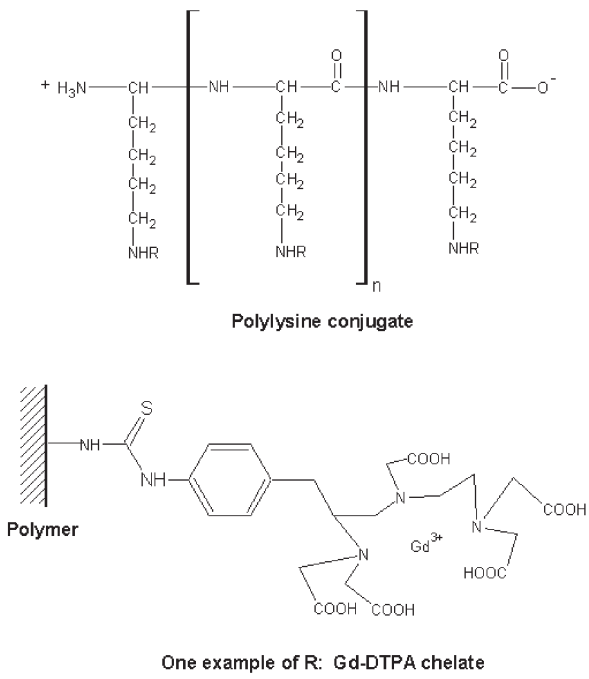


Fig. 6. Illustration of a method of attachment of Gd-DTPA to polylysine

optimal water exchange rates also have been implicated as a cause of lower than expected relaxivities in polymer conjugate systems [20].

Recently, polymeric Gd^{3+} chelates of varying molecular weights have been synthesized to control $t_{1/2}$ (the intravascular half-life) as well as τ_R [21]. A roughly linear relationship is seen for $t_{1/2}$ as a function of molecular weight. In general, blood pool retention is known to be affected by molecular weight (MW), size, shape and charge [22], so while the linear behavior of $t_{1/2}$ as a function of MW can be observed for members of a family of compounds with similar physical characteristics, it is not necessarily expected to hold when comparing polymeric conjugates based on different molecular structures.

In their comprehensive review of Gd^{3+} chelates as MRI contrast agents, Caravan et al. point out that macromolecular conjugates exhibit less complete elimination from the body, increasing the odds of cellular uptake and processing, leading potentially to the release of toxic byproducts, including free Gd^{3+} [20]. Moreover, large multivalent molecules are more likely to be antigenic than small molecules. There also is a concern that clinical doses of these materials will lead to hemodynamic abnormalities. In the case of Gd -DTPA-polylysine, typical doses of 0.05 and 0.15 mmole/kg showed no significant hemodynamic effects, although at higher doses (0.45 mmole/kg) a transient increase in blood pressure parameters and contractility was observed [23].

2.3

Dendrimeric Gd^{3+} Chelates

Cascade polymers, or dendrimers, differ from linear polymer systems in many ways. Dendrimers have much lower polydispersities [24]. They can be synthesized to have a higher number of reactive functional groups per unit mass and volume, and thus can serve as the vehicle to deliver attached paramagnetic ion chelates. Finally, they can be synthesized in concentric “generations” to achieve the appropriate size to achieve prolonged intravascular retention and slower rotation. Figure 7 illustrates one dendrimer system, based on the ammonia core poly(amidoamine) (PAMAM) cascade polymers, showing how it is synthesized in generations and derivatized with the chelate DTPA-TU [25]. The generation 2 system has a molecular weight of 8.5 kDa, while a generation 6 dendrimer has a molecular weight of 139 kDa.

Dendrimers can provide a macromolecular scaffold that is more nearly uniform in molecular weight than that achieved by linear polymers. They do not entirely solve the problems of segmental motion, however, and multiple τ_R values have been reported from the same structure [26]. Two classes of motion, attributed to “internal” and “terminal” carbons have been suggested, with τ_R (internal)/ τ_R (terminal) ≈ 100 for a generation 7 (MW = 87.3 kDa) poly(amidoamine) macromolecule. Wiener et al. suggest that the segmental motions that dominate relaxivity in the PAMAM dendrimer system are actually located in the interior of the polymer, and that the rotational motion of the whole system affects the apparent τ_R that is observed [25]. Bryant and co-workers have shown that in a PAMAM dendrimer system conjugated with a DOTA derivative and grown to high generation numbers ($G = 5, 7, 9, 10$), T_1 relaxivity does not con-

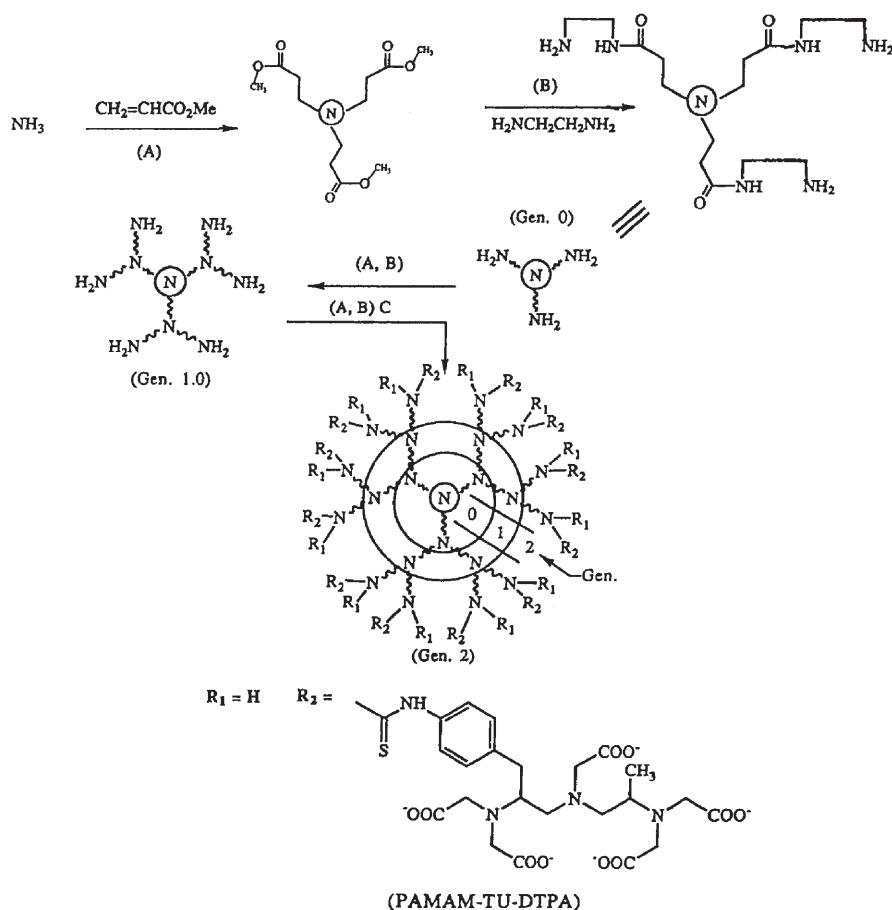


Fig. 7. General synthetic scheme for PAMAM dendrimer and its derivatization with DTPA-TU [25]. Used with permission

tinue to increase with macromolecular size, but reaches a plateau. Similar results were found for T_2 relaxivity; the effect is attributed to relaxivity limited by slow water exchange in the large dendrimer structures [27].

The synthesis and first animal model trials have been reported for dendrimer-based BPCAs that are designed to diffuse only very slowly through the vascular endothelium, while still being freely excreted by the kidneys. Based on a central core of trimesoyl triamide [28, 29], these materials are limited in size to about 18 kDa, and some versions are below 10 kDa in molecular weight. They have slower rotational dynamics, and hence improved relaxivity. These BPCAs remain in the vasculature long enough to conveniently perform MR angiographic procedures, while still being completely eliminated from the serum in 24 hours, reducing the risk of secondary metabolism and possible toxicity. While not a dendrimer, another macromolecular agent based on the chelate DOTA that

has been substituted with hydrophilic bulky groups, also is designed to achieve these advantageous values of longer τ_R and 24 hour excretion [30]. Again, molecular weights of 5.29 and 11.59 kDa are used to develop these properties in the agent. Clearly, the advantages of complete excretion in the span of one day will make this molecular weight range a popular one for the development of new BPCAs.

2.4

Iron oxide Particles

A quite different chemical and physical strategy is represented by nano-particles of iron oxide. Typical formulation consists of a magnetite (Fe_3O_4) core surrounded by a protective thin dextran coating [31, 32]. The magnetite core in one recently published study was reported to be less than 5 nm in size, while the overall particle size was about 21 nm; this is typical of materials termed Ultra-small Superparamagnetic Iron Oxide (USPIO) contrast agents [27]. The term superparamagnetic is applied to these systems. They exhibit a magnetic susceptibility that is intermediate between paramagnetic and ferromagnetic. The small size of the magnetite core gives rise to a magnetic moment that experiences a much smaller magnetic lattice anisotropy than is measured in larger crystalline systems. The very small magnetic anisotropy permits rapid thermal reorientation of the magnetization vector, giving rise to *superparamagnetic* behavior. Superparamagnetic systems behave more like paramagnetic ones, having a net magnetization that is proportional to the magnetic field at low fields, according to the form

$$\begin{aligned} M_S &= F_S N \mu_s L(x) \\ L(x) &= \coth(x) - 1/x \\ x &= \frac{\mu_s B}{kT} \end{aligned} \quad (5)$$

where N = total number of Fe atoms, F_S = number of magnetite cores divided by N , μ_s = the magnetic moment of the magnetite core, k = Boltzmann's constant, B = external magnetic field strength, and T = temperature. $L(x)$ is called the Langevin function, with the property that for $x \ll 1$, $L(x) = x/3$. Therefore M_S approaches zero as B approaches zero. Koenig and Kellar have considered the theory of NMRD profiles for superparamagnetic nano-particles [33]. They point out that higher field strengths result in a plateau in M_S called magnetic saturation, and this must be considered when analyzing the relaxivity of nano-particles at clinical frequencies. USPIO systems typically have values of μ_s that are much larger than μ measured for single paramagnetic ions, and that makes them powerful relaxation agents.

Proton relaxation is enhanced by the presence of these nano-particles in solution, although the mechanism of relaxivity is complex [33]. Bulte et al. suggest that for a particle preparation called MION-46L developed at the Center for Mol-

ecular Imaging Research, Massachusetts General Hospital and Harvard Medical School (Boston, MA), both T_1 and T_2 relaxivities are dominated by a combination of outer sphere contributions from large and small magnetite core superparamagnetism, as well as inner sphere contributions from residual paramagnetic Fe^{3+} , which may be on the surface of the cores or bound in the dextran coating [34]. In the preparation reported, approximately 41% of the total Fe atoms in the system are paramagnetic. In other systems, additional T_2^* effects due to susceptibility gradients around the particles have been noted [32]. Additional research is needed to fully clarify the situation.

One critical feature of USPIO contrast agents is their strong relaxation effects on T_2 as well as T_1 . While all paramagnetic and superparamagnetic agents affect both longitudinal and transverse relaxation, the potentially extremely strong effects of larger particles on T_2 can produce artifacts in MRI images. The ratio of T_2 to T_1 relaxivities, r_2/r_1 , is found to be a sensitive function of the size of the particle core: smaller cores have smaller r_2/r_1 ratios. Koenig and Kellar suggest that an optimum core size for these systems is between 6 and 10 nm; below 6 nm the relaxivity is too low, while larger than 10 nm the loss of MRI signal due to T_2 effects is too great [35]. Kollmann et al. reported relaxivity ratios (r_2/r_1) of 7 for a particle preparation with mean particle size of 60 nm, and 2 for a particle size of 20 nm. Measurements were made at 1.5 T; core magnetite diameters were not reported [36].

USPIO contrast agents are eliminated from the circulation by the reticuloendothelial system (RES), and often become sequestered in liver cells. Half-life in the circulation depends on the chemistry of preparation, and can range from hours [28] to weeks [37].

2.5

Low Molecular Weight Gd^{3+} Chelates Binding to Serum Proteins

All of the strategies thus far considered to develop MRI contrast agents with long intravascular retention times and slower rotational motion depended on synthesizing materials in a laboratory and injecting them into patients. The last category of PBCAs we will consider takes a different approach, termed by Lauffer "receptor induced magnetization enhancement" or RIME [38]. Here, a low molecular weight Gd^{3+} chelate is chemically designed to bind noncovalently to substrates like serum proteins. Once bound, the PCA-protein conjugate develops a higher concentration and longer intravascular retention than those of low molecular weight agents. The rotational motion of the Gd^{3+} ion also is slowed by its association with a high molecular weight molecule, and thus its relaxivity is substantially enhanced. In effect, the RIME-BPCA is assembled in vivo. The bound form of the agent is in equilibrium with a small amount of free agent, which acts like an extracellular agent, and is excreted renally over time. Thus, RIME agents avoid the problems of slow excretion often exhibited by covalently bound macromolecular systems, while enjoying longer intravascular retention and larger τ_R values.

Several chelates have been developed to exploit the RIME approach. These include $[\text{Gd}(\text{BOPTA})(\text{H}_2\text{O})]^{2-}$ (Multihance™, Bracco) [39], $[\text{Gd}(\text{EOB-DTPA})-$

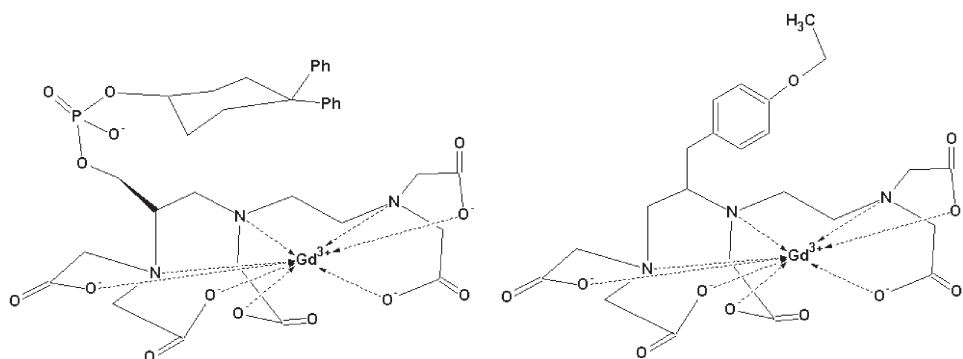


Fig. 8. Molecular structures for MS-325 (left) and $\text{Gd}(\text{EOB-DTPA})(\text{H}_2\text{O})^{2-}$ (right)

$(\text{H}_2\text{O})]^{2-}$ (EovistTM, Schering) [40–42], MP-2269 (Mallinckrodt) [43], B-21326/7 (Bracco) [44], and MS-325 (AngioMARKTM, EPIX) [45, 46]. Figure 8 shows the molecular structure of two of these agents, AngioMARK and Eovist. Both are based on the chelate DTPA, and both have additional functional groups that interact with serum proteins, particularly HSA. $\text{Gd}(\text{EOB-DTPA})$ currently is being evaluated as a liver contrast agent, targeting hepatocytes [42]. Because of its modest non-covalent association with HSA, it also acts as a BPCA, and provides a useful contrast to MS-325, which is structurally similar and binds strongly to albumin.

The mechanism of non-covalent binding of these agents to proteins is still a matter of research interest. Protein binding results similar to those obtained from the agents mentioned above have been obtained from alkyl-substituted DOTA complexes [47, 48], where the lipophilic side chain targets lipid binding sites on HSA. In addition to lipophilicity, however, other targeting mechanisms may play a role in the non-covalent attachment of RIME-BPCAs to serum proteins. Some agents, like MS-325 and EOB-DTPA, can bind at several sites on HSA: at high concentrations, as many as 20 ± 5 MS-325 molecules bind to a single HSA molecule [46].

Non-covalent attachment of low molecular weight chelates to proteins slows the tumbling rate of the paramagnetic agent (increases τ_R). While the parent chelate, GdDTPA , has a τ_R of between 60–100 ps, the derivatives MS-325 and EOB-DTPA have τ_R values of approximately 180 ps in HEPES buffer at 25°C. The increase in τ_R can be attributed to the addition of the substituents to the core chelate. When HSA is introduced, however, rotation is much more strongly affected. Toth et al. have studied the interaction of MP-2269 with 4% HSA in buffer [43]. They estimate a τ_R value of about 1 ns, 7 times longer than that of the unbound complex. A rotational correlation time of 30 ns is reported for the complex $[\text{Gd}(\text{PCTP-[13]})(\text{H}_2\text{O})]^{3-}$ bound to HSA at 25°C [49]. Chen et al. found a τ_R value of 9.8 ns for the VO^{++} analog of $\text{Gd}(\text{EOB-DTPA})$ bound to HSA [50], and a value of between 20–30 ns for the VO^{++} analog of MS-325 bound to HSA [51]. The longer values of τ_R result in an enhanced relaxivity, and thus the protein-bound complexes become more effective T_1 contrast agents. Furthermore, the

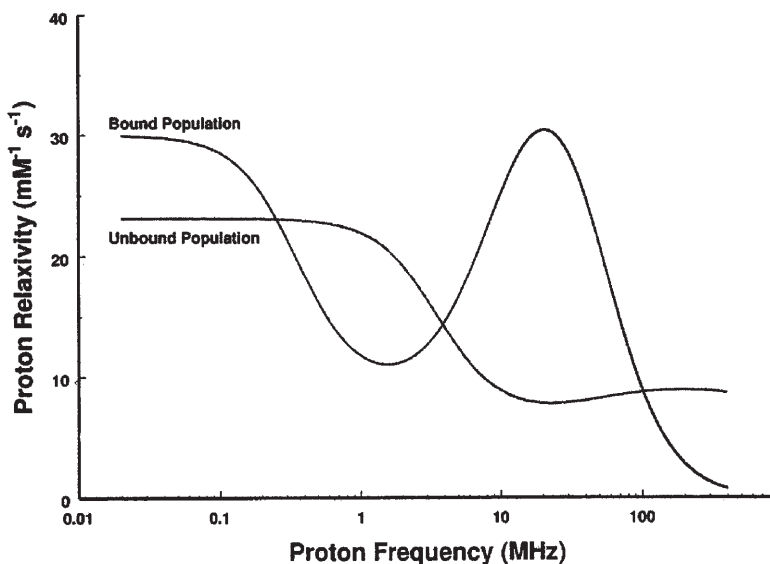


Fig. 9. The NMRD profile of the bound and the unbound populations of Gd(EOB-DTPA) in 4% HSA scaled to 1 mM [50]

effect of slower tumbling enhances relaxivity in the 40–60 MHz frequency range currently used in clinical MRI, thus helping to counter the fall-off in relaxivity exhibited by low molecular weight paramagnetic agents in this region. Figure 9 illustrates this point for Gd(EOB-DTPA) bound and unbound in a 4% HSA solution.

While differences in substituents on a core chelate may seem modest, the effects on protein binding can be very large. For example, MS-325 is reported to be 96.2% protein bound in human plasma at the clinical concentration of 0.1 mmole/L, and 94.3% bound in a 4.5% solution of HSA [46]. In contrast, Gd(EOB-DTPA) is only 10% bound in human plasma at a concentration of 1 mmole/L [40], and 11% bound in a 5% HSA solution with a Gd(EOB-DTPA) concentration of 1.5 mmol/L [50]. Thus, relatively modest changes in chelate structure can have large effects on protein binding, providing a route for “fine tuning” the MIME interaction for different applications.

Protein binding can also effect water exchange rates and electron spin relaxation in MIME-BPCAs. As τ_R becomes longer, its dominant effect in Eq. (3) above is lost, and the values of τ_M (water exchange correlation time) and τ_S (T_{1e} and T_{2e} , electron spin relaxation times) become important in controlling relaxivity. Toth et al. have studied MP- 2269 in the presence and absence of 20% w/v BSA (bovine serum albumin), making use of ¹⁷O NMR to measure water exchange rates [43]. They find no significant changes in τ_M when the agent binds to the albumin molecule. Aime et al. found that τ_M increased from 190 ns to 300 ns when Gd(BOM)₃DTPA bound to HSA, and that it increased from 250 ns to 390 ns when MS-325 bound to the protein [52]. These decreases in water exchange rates of about 50% when agents bind to HSA could result in lower-than- expected relax-

ivities, and the control of τ_M through careful chelate design currently is an active research area. Aime suggests that hydrophobic complex/protein interactions produce smaller changes in water exchange rates than purely electrostatic interactions [49, 52].

Changes in electron spin relaxation can affect relaxivities when chelates bind to proteins and rotational rates become slowed. For the $\text{Gd}(\text{BOM})_3\text{DTPA}$ system, Aime found that T_{1e} went from 15.3 ns to 57.9 ns when the complex bound to HSA, while for MS-325 T_{1e} went from 2.1 ns to 2.5 ns [52]. Both of these relaxation changes were calculated for a magnetic field value of 0.47 T from data obtained by ^{17}O NMR at 25°C. The authors advise caution in making use of data from their variable-temperature NMR studies, however, due to the possible heterogeneity of complex/protein binding sites. Here again, much research is still needed to clarify the relationships between chelate structure and environments that affect electron spin relaxation.

2.5

Micelles and Liposomes

A micelle is a colloidal aggregate of amphipathic (surfactant) molecules, which occurs at a well-defined concentration known as the critical micelle concentration. The typical number of aggregated molecules in a micelle (aggregation number) is 50 to 100. Figure 10 shows a two-dimensional cross section of a schematic micelle. Micelle size can be regulated by the structure of its molecular components to be from 5–10 nm up to 100 nm or larger. Thus, the micelle structure can provide a system for carrying paramagnetic contrast materials that will have long intravascular retention suitable for BPCA applications. The molecules that comprise the micelle may themselves be paramagnetic ion chelates with suitable hydrophobic chains [53], or the micelle can be formed independently and act as a vehicle to carry suitably hydrophobic contrast agent chelates [54]. The relatively large size of the micelle causes slow rotation, enhancing the relaxivity of these agents. Micelles can have r_1 values comparable to large macromolecular conjugates [55], without the problems of slow elimination from the body that often are encountered with polymer systems. Also, water exchange seems not to be affected by micellar organization, which may be loose enough to avoid obstructing the exchange process.

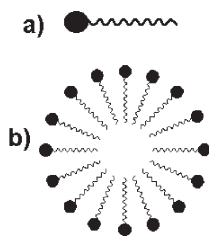


Fig. 10. a Molecule with ionic head (+ or -) and amphipathic chain. b 2-dimensional cross section of micelle formed from (a)

Liposomes are microscopic, fluid-filled vesicles whose walls are made of layers of phospholipids. Liposomes have been used to deliver certain vaccines, enzymes, or drugs (e.g., insulin and some cancer drugs) to the body. They have been filled with a variety of paramagnetic materials and can be synthesized with sizes greater than 10 nm, which keeps them in the circulation as BPCAs [56]. A typical preparation contains a range of sizes from 72–395 nm, containing 150 or 250 mM isotonic solutions of Gd-HP-DO3A (diluted ProHance™) [57]. Liposomes can be coated with a variety of materials for tissue targeting, including antibodies, and their phospholipid walls can be filled with lipophilic paramagnetic chelates to act as contrast agents [58]. A suitably synthesized Gd-DTPA derivative incorporated into cholesterol coated liposomes has successfully been used to study pulmonary perfusion by MRI [59]. The flexible chemistry of the surfaces of liposomes makes them a very interesting approach for targeted BPCAs.

3

Physical Characterization of Protein-Associated BPCAs

The development of advanced BPCAs, as well as their creative application, are guided by an understanding of relationships between molecular structure and contrast agent performance. There is still much to be learned about the ways in which structure affects relaxivity, as well as ways in which the biological environment modifies this performance. In earlier chapters in this book, Toth, Merbach and Helm have provided the theoretical framework for understanding relaxivity in terms of structure and dynamics, and Peters and Geraldes have considered how solution structures of the agents are related to their properties. BPCAs represent more complex systems, since they are designed to interact with other molecules and/or the biological environment, and their physical characterization presents experimental and theoretical challenges. In this section, several magnetic resonance methods that have proven useful in the characterization of RIME-type BPCAs will be discussed.

Because of their size, BPCAs have a slowed rotational motion. The long values of τ_R not only increase relaxivity, but also increase the importance of water exchange and electron spin relaxation as mechanisms controlling proton relaxation enhancement. Experimental methods have been developed to independently measure the *dynamic* parameters τ_R , τ_M , and τ_S (T_{1e} and T_{2e}), as well as to calculate these values from the simulation of NMRD curves. Because of possible alterations in the *structure* of BPCAs interacting with proteins and cells, it also may be important to measure the distribution of water proton- Gd^{3+} distances, r , and the actual effective number of inner sphere (and sometimes, second sphere) water molecules, q . In this section, results from several RIME-type BPCAs will be discussed, illustrating physical methods and pointing out areas for further research in this important class of agents.

3.1
Physical Methods

Table I lists some magnetic resonance methods that are applied in the physical characterization of BPCAs, and identifies the key physical parameters best studied by each technique.

Table 1. Magnetic resonance methods and parameters studied

Physical method	Parameters studied
Nuclear Magnetic Relaxation Dispersion (NMRD). The Koenig Relaxometer	Relaxivity as a function of field/frequency; through analysis by simulation models: r , q , τ_R , τ_M , τ_S for inner sphere, second sphere, and outer sphere water interactions. Also equilibrium constants for BPCA-protein and BPCA-cell interactions.
Multi-frequency EPR and High-Frequency EPR	T_{1e} , T_{2e} (τ_S); $g_{\text{effective}}$. Through analysis of the field/frequency dependence of electronic relaxation and $g_{\text{effective}}$: zero field splitting (ZFS, D , E , Δ^2), τ_V . Also details of BPCA-protein interactions, including BPCA fraction bound to protein.
Variable-temperature ^{17}O NMR	Water exchange rate ($1/\tau_M$), q , T_{1e} (through measurement of ^{17}O T_{2n}); τ_R (through measurement of ^{17}O T_{1n})
VO^{2+} substituted PCA (VO^{2+} substituted for Gd^{3+} , Mn^{2+} , etc.)	BPCA rotational motion, including specifics of anisotropic rotation ($\tau_{R(x,y,z)}$). Also details of BPCA-protein interactions.
Electron Spin Echo Envelope Modulation (ESEEM, pulsed EPR)	Distribution of water molecules interacting with BPCA: r .

3.1.1
Nuclear Magnetic Relaxation Dispersion (NMRD)

This technique measures proton T_1 over a range of frequencies from 0.01 MHz to 50 MHz, making use of a Koenig field-cycling relaxometer (see reference [60] for review of the technique). It still remains the best method of making an overall assessment of the behavior of a BPCA, and it measures the frequency dependence of contrast agent performance (relaxivity). Customarily, 15–20 frequency NMRD points are measured, spanning the entire frequency range of the instrument. The relaxometer follows the return to thermal equilibrium of the longitudinal magnetization by acquiring Hahn spin echos following a jump from the soak magnetic field (variable) to the observe field (constant at 7.5 MHz), resulting in a frequency scan data set that is virtually constant in signal-to-noise. Usually, 2 or 3 echos are recorded at different field jump times, and T_1 is calculated from a single exponential fit of the echo amplitudes. However, when more

detailed information is required, the machine can be programmed to take 15–20 echos at each frequency, giving a high-resolution measure of the longitudinal relaxation process. While such a high-resolution NMRD scan takes more time, it results in a data set that can be analyzed for multi-exponential T_1 processes. Because there often is a *distribution* of BPCAs between several environments, this more detailed (or 2-dimensional) approach is useful. An analysis approach, called CONTIN [61], which was developed for relaxometry by Springer and co-workers [62] from the original program for mathematical analysis of perturbation recovery data by Provencher, often is useful. This inverse Laplace transform analysis of the relaxation behavior of the proton spins allows the data to be analyzed for a distribution of relaxation times. Such a detailed study of relaxation dispersion behavior can reveal relaxivity distributions from water protons in differing environments, permitting the assessment of contributions to the overall relaxivity from bound and unbound BPCAs.

Cell suspensions containing agents like DTPA-EOB, with pronounced hepatocyte uptake, for example, exhibit multi-centered T_1 distributions, as Fig. 11 illustrates. In this figure, as the concentration of Gd(EOB-DTPA) is increased, the peak at short T_1 values moves to even shorter relaxation times, while the peak at longer T_1 values remains approximately constant. The peak at short T_1 values is assigned to water that is extracellular, while the peak at longer values is believed to arise from water within the hepatocytes. The familiar NMRD plots thus can be transformed into a plot having axes for T_1 , probability (frequency of occurrence), and BPCA concentration. Such 2-dimensional NMRD plots provide “cleaner” data by providing a truer picture of the distribution of relaxivity values, thus allowing more reliable computational modeling.

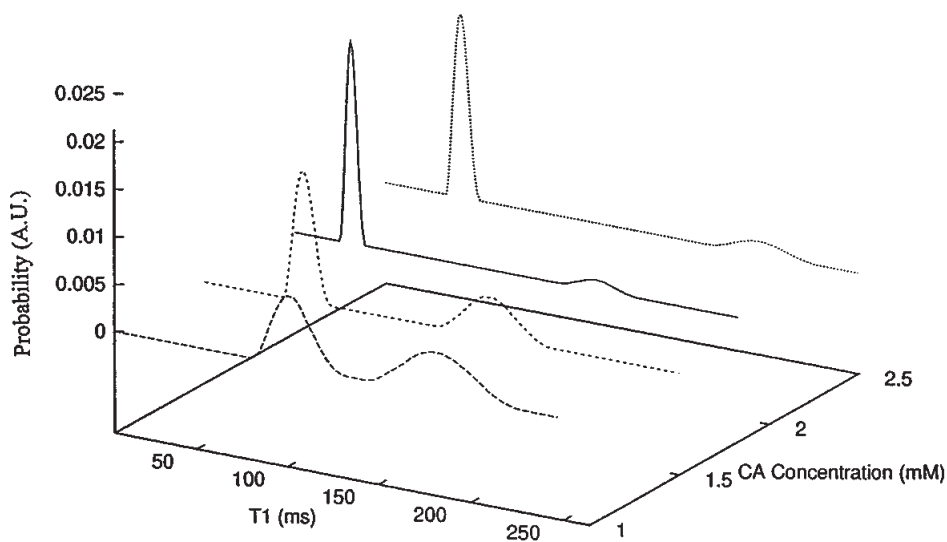


Fig. 11. Profiles taken at 10 MHz of 2-dimensional NMRD data sets, showing the distribution of proton T_1 values in a packed rat hepatocyte cell preparation with different concentrations of Gd(EOB-DTPA)

Analysis of NMRD data to obtain values for q , r , τ_R , τ_M , and τ_S is a complex process, complete with the problem of non-uniqueness of the best simulation parameters. New methods are being developed in which NMRD data is combined with data from other physical methods to assist in developing a best set of parameters [4, 63].

3.1.2

Multi-Frequency EPR

The main advantage of a multi-frequency study is that it provides information on the frequency dispersion of magnetic resonance parameters. This approach (dispersion), for example, is the power in NMRD studies. Several laboratories pioneered in the application of multi-frequency EPR as a route to a more accurate evaluation of key spectroscopic parameters (g , A , Q , D , E), as well as a more sensitive methodology for studying dynamical processes, where an interplay between the frequency dependence of the spin process and the frequency dependence of the EPR observation often can provide exceptionally detailed information [64, 65]. In order to take advantage of the method, the frequency dependence of spin systems must be understood. This has led to the development of several theoretical approaches for better analysis of multi-frequency data, and especially in BPCA research, for the analysis of the frequency dependence of $g_{\text{effective}}$, T_{1e} , T_{2e} , and the overall EPR line shape in frozen glasses and in room-temperature aqueous solutions.

3.1.2.1

Frozen Glassy Solutions

The technique involves adding a glass-forming solute (e.g. methanol, glycerol, salts) to an aqueous solution of BPCA, then carefully freezing the solution to a glass. Spectra are taken at temperatures between 77 K and 4.2 K. Spectra are analyzed by means of the eigenfield method developed by Belford [66], and a single set of spectral parameters is developed which best fits spectra taken at several experimental frequencies. For Gd^{3+} chelates, key variables obtained are $g_{\text{effective}}$, and the zero field parameters D and E .

3.1.2.2

Frequency Dependence of $g_{\text{effective}}$

Making use of a tracking NMR gaussmeter to measure field, and a digital frequency counter, g -factors ($g_{\text{effective}}$) can be measured to 6, and in some instances, 7 significant figures. This requires very careful technique, but the information obtained from such an approach justifies the effort, particularly in the case of Gd^{3+} chelates in aqueous solution, where a single resonance line shape is observed. Measuring $g_{\text{effective}}$ at multiple experimental frequencies and fields gives information on the frequency dependence of the effective g -factor, and hence a route to the determination of the magnitude of the ZFS in room temperature aqueous solutions.

In order to analyze these data, the frequency shift of $g_{\text{effective}}$ can be calculated by averaging over all orientations the anisotropic shift derived from a static spin Hamiltonian [67]. This treatment is based on the assumptions that molecular motion neither changes the spin precession rate nor perturbs the states and, thus, that the center of gravity of the spectrum is invariant even in presence of some motional averaging. For the allowed $|1/2\rangle \leftrightarrow \langle -1/2|$ transition under perturbation theory, with expressions valid up to the third order, this shift is given by [47]:

$$\Delta B = \frac{1}{20g\beta\omega_o} (4S(S+1) - 3) (2/3 D^2 + 2E^2) \quad (6)$$

so the shift is directly proportional to the ZFS term $(2/3 D^2 + 2E^2)$, which is usually denoted by the term Δ^2 . The result of Eq. 6 is identical to the shift expression for spin 5/2 that Baram et al. [68] derived by using the semiclassical stochastic Liouville general formalism in the limit when motional effects are negligible. For Gd(III) ion ($S = 7/2$), the field shift (Eq. 1) can be recast for an effective g -factor, g_{eff} , in terms of the squared ZFS matrix $\Delta^2 = D_{xx}^2 + D_{yy}^2 + D_{zz}^2$:

$$g_{\text{eff}} = g \left(1 - \frac{3\Delta^2}{\omega_o^2} \right) = g \left(1 - \frac{3\Delta_f^2}{\nu_o^2} \right) \quad (7)$$

where ν is the resonance frequency; Δ is in units of radians/s, while Δ_f is in units of Hertz (s^{-1}). Thus, the variation of $g_{\text{effective}}$ with experimental frequency, observed by multi-frequency EPR, can be analyzed to obtain Δ^2 . Figure 12 shows

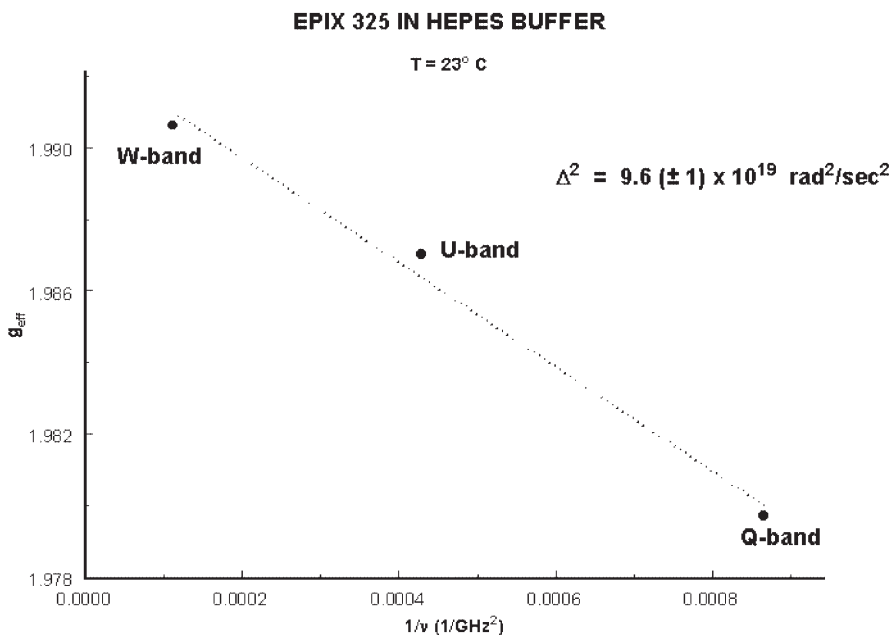


Fig. 12. Determination of Δ^2 by means of Eq. (7). The BPCA is MS-325

how the method is applied to MS-325 dissolved in HEPES buffer. Borel and co-workers also have considered this shift of g_{eff} with frequency, and have checked equation (1) for its region of validity ($\omega\tau_v > 1$) [69]. ZFS parameters obtain by exact consideration of the frequency shifts calculated from the imaginary part of the Redfield relaxation matrix, and the values obtained by Eq. (7) are in almost perfect agreement. This method, while approximate, is extremely accurate, and can quickly determine Δ^2 , and hence is very useful in these studies.

3.1.2.3

Frequency Dependence of Electron Spin Relaxation

Electron spin relaxation in aqueous solutions of Gd^{3+} chelates is too rapid to be observed at room temperature by the usual pulsed EPR methods, and must be studied by continuous wave (cw) techniques. Two EPR approaches have been used to study relaxation: studies of the line shape of the cw EPR resonance of Gd^{3+} compounds in aqueous solution, and more direct measurement of T_{1e} making use of Longitudinally Detected EPR (LODEPR) [70]. Currently, LODESR is available only at X-band, and the frequency dependence of relaxation is studied by following the frequency dependence of the cw EPR line shape, and especially of the peak-to-peak line width of the first derivative spectrum (ΔB_{pp}).

In some ways, measurement of the frequency dependence of the EPR line width ($1/T_{2e}$) is simpler than very accurate g-factor determination. A precise calibration of the magnetic field sweep used to acquire the spectrum is required, which is obtained using field standards like the hyperfine splitting in Fremy's salt, in conjunction with a tracking NMR Gaussmeter. Once the data are obtained at multiple EPR frequencies, they can be analyzed to determine Δ^2 and τ_v .

Powell et al. give an excellent review of several approaches to interpret the frequency dependence of T_{1e} and T_{2e} in these systems [71]. One convenient approach is that developed by Hudson and Lewis [72], who showed that the eigenvalues ξ_i of the relaxation matrix \mathbf{R} as defined in Bloch-Wangsness-Redfield (BWR) theory [73] are functions of τ_v and the experimental frequency ω , and are related to the relaxation time T_{2ei} of the i -th allowed electron spin transition by the expression:

$$\frac{1}{T_{2ei}} = -\Delta^2 \tau_v \xi_i \quad (8)$$

In this application of the BWR theory, Hudson and Lewis assume that the dominant line-broadening mechanism is provided by the modulation of a second rank tensor interaction (i.e., ZFS); higher rank tensor contributions are assumed to be negligible. \mathbf{R} is a 7×7 matrix for the $S = 7/2$ system, with matrix elements written in terms of the spectral densities $J(\omega, \tau_v)$ (see reference [65] for details). The intensity of the i -th transition also can be calculated from the eigenvectors of \mathbf{R} . In general, there are four transitions with non-zero intensity at any frequency, raising the prospect of a multi-exponential decay of the transverse magnetization. There is not a one-to-one correspondence between the

relaxation rates and the degenerate $|m_s\rangle \leftrightarrow |m_s \pm 1\rangle$ transitions, and generally one transition is predicted to have a T_{2ei} that is much longer than the other three. Particularly at frequencies greater than 35 GHz, the differences between the longest T_{2ei} and the other three values are predicted to be greater than a factor of 10, which suggests that in continuous wave EPR experiments, the spectrum of Gd(III) will consist of a narrow line superimposed on very much broader, weaker lines. The narrow line shape is likely to dominate any fitting of the spectrum by Lorentzian functions in an analysis to determine approximate values of T_{2e} . Below about 10 GHz (depending on the value of τ_v), only one transition has any appreciable intensity, but above that frequency, all four transitions contribute, and a multi-exponential behavior for T_2 is expected.

In order to calculate ΔB_{pp} , the EPR line shape must be calculated from T_{2e} values. Although one transition dominates the experimental shape, in order not to overlook real contributions from the other three transitions (and to avoid forcing Lorentzian behavior on non-Lorentzian lines), the values of T_{2ei} and the transition probabilities for all transitions in the system can be calculated as a function of magnetic field. In one approach, the time-dependent magnetization, $M(\omega, \Delta^2, \tau_v, t)$, then is calculated as a sum of all transitions, followed by a Fourier transformation of the magnetization function, and the peak-to-peak linewidth of the simulated first derivative spectrum then is determined [74]. The experimental data are fitted by allowing the values of Δ^2 and τ_v to vary, making use of a non-linear least squares procedure, and calculating eigenvalues of the R-matrix at each τ_v value. A field-independent relaxation rate, R_o , also is added to the fitting equation, which then becomes

$$M(\omega, \Delta, \tau_v, t) = \sum_{i=1}^7 I(\omega, \tau_v, i) \left[\exp \left(\frac{-t}{T_{2e}(\omega, \tau_v, \Delta^2, i) + \frac{1}{R_o}} \right) \right] \quad (9)$$

Here, $M(\omega, \Delta^2, \tau_v, t)$ is the magnetization in the x-y plane, $I(\omega, \tau_v, i)$ is the transition probability of a particular ($i = 1 \dots 7$) spin transition at the experimental frequency ω , and $T_{2e}(\omega, \tau_v, \Delta^2, i) = T_{2ei}$ of Eq. (8). The value of R_o is held constant for all calculations of a particular Gd³⁺ chelate. The exact mechanism(s) responsible for R_o is still the subject of investigation, and it may be the result of an approximation in this approach which will be discussed later. Figure 13 shows that this model accounts very well for the frequency dependence of the EPR line width in the MS-325 system. A similar agreement between experiment and calculation is obtained by this fitting procedure on most contrast agents in solution. Since the calculation of the T_{2ei} (and ultimately the measured parameter ΔB_{pp}) can be expressed as functions of Δ^2 and τ_v , the fitting of line width dispersion data provides another route to estimate the transient ZFS interaction parameters. For this system, best fit parameters are $\Delta^2 = 7.3 \times 10^{19} \text{ rad}^2/\text{s}^2$, $\tau_v = 29 \text{ ps}$, and $R_o = 1.7 \times 10^8 \text{ s}^{-1}$. Muller et al. have studied this system by multinuclear relaxometry, and they obtain $\tau_{SO} = 78$ or 101 ps (equivalent to $\Delta^2 = 2.4$ or $1.9 \times 10^{20} \text{ rad}^2/\text{s}^2$) and $\tau_v = 22$ or 33 ps [75]. The two values for each parameter result from two different assumed values for r .

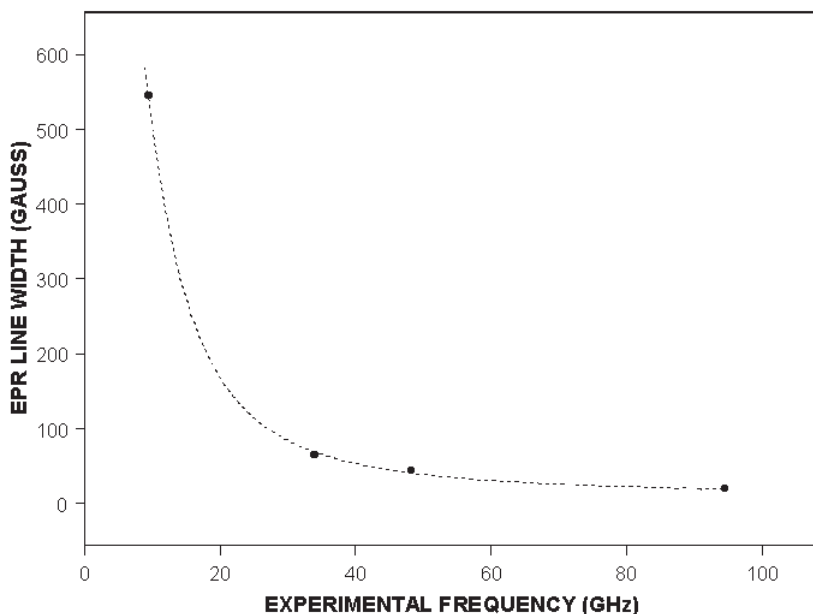


Fig. 13. Fitting the frequency dependence of the EPR line width of MS-325 in HEPES buffer at 23°C, making use of Eq. (9). Best fit parameters obtained from the data are: $\Delta^2 = 7.3 \times 10^{19} \text{ rad}^2/\text{s}^2$; $\tau_v = 2.9 \times 10^{-11} \text{ s}$; $R_o = 1.7 \times 10^8 \text{ s}^{-1}$

3.1.2.4

Total EPR Spectral Line Shape

The Hudson and Lewis (HL) approach to calculating spin relaxation makes use of the real part of the relaxation matrix \mathbf{R} from BWR theory. Poupko, Barum and Luz (PBL) made use of the complete (complex) matrix to calculate both the relaxation times and the frequency shifts of the four transitions that can contribute to a Gd^{3+} spectrum freely tumbling in aqueous solution [76], and Borel et al. recently applied the method to calculate the complete line shapes of Gd^{3+} contrast agents [69]. The complete PBL simulation does a better job of fitting the asymmetric line shapes that occur at certain frequencies for certain agents. For example, Fig. 14 illustrates the fitting of an X-band GdDTPA spectrum, taken in HEPES buffer. This asymmetric line is well-fitted by the PBL approach. While the detailed fitting of a spectrum taken at a single frequency might allow the determination of the ZFS parameters Δ^2 and τ_v , it is likely that the multi-frequency approach is more reliable, particularly when heterogeneous environments add complexity to the line shape. Also, the PBL and HL approaches use one time-varying ZFS, often called the *dynamic* ZFS, leading to the evaluation of two parameters, Δ^2 and τ_v . Recently, Bertini et al. have developed a theoretical treatment for $S = 1$ systems that include both a *dynamic* and a *static* ZFS term, each with its own correlation time [77].

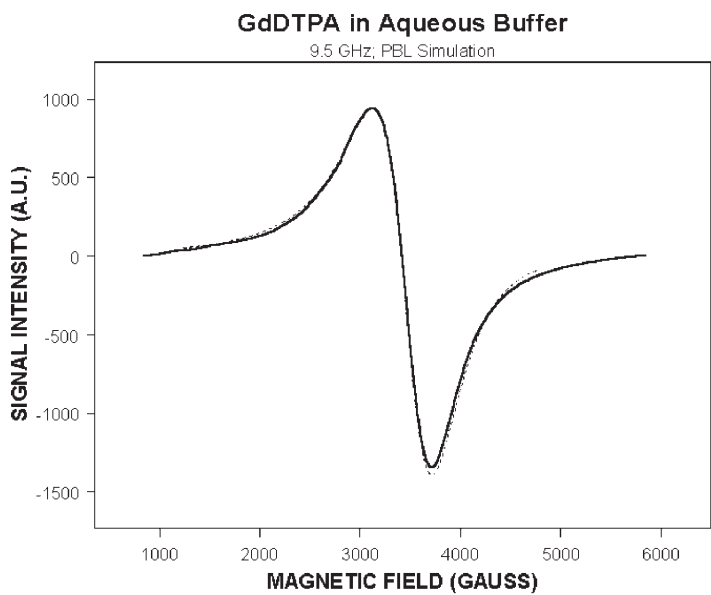


Fig. 14. Experimental EPR spectrum of GdDTPA at X-band (solid line), together with best fit using the PBL method (dashed line)

A new treatment for $S = 7/2$ systems has been undertaken by Rast and co-workers [78, 79]. They assume that in complexes with ligands like DTPA, the crystal field symmetry for Gd^{3+} produces a *static* ZFS, and construct a spin Hamiltonian that explicitly considers the random rotational motion of the molecular complex. They identify a magnitude for this static ZFS, called a_2 , and a correlation time for the rotational motion, called τ_r . They also construct a *dynamic or transient* ZFS with a simple correlation function of the form $(B_T)^2 e^{-t/\tau_v}$. Analyzing the two Hamiltonians (Rast's and HL), it can be shown that at the level of second order, Rast's parameter a_2 is exactly equivalent to the parameter Δ . The method has been applied to the analysis of the frequency dependence of the line width (ΔB_{pp}) of GdDTPA. These results are compared to a HL treatment by Clarkson et al. in Table 2.

Table 2. Comparison of results

Clarkson [74]			Rast [78]			
Δ^2	τ_v	τ_R^{-1}	$(a_2)^2$	$(B_T)^2$	τ_v	τ_r
rad ² /s ²	s	s	rad ² /s ²	rad ² /s ²	s	s
8×10^{19}	2.4×10^{-11}	1.1×10^{-10}	8×10^{19}	1.8×10^{19}	1.3×10^{-12}	3.9×10^{-10}

* Isotropic rotation correlation time measured for the VO²⁺-substituted DTPA complex [4].

In this comparison, it is exciting to see the exact correspondence between Δ^2 and $\langle a_2 \rangle^2$ that is predicted by theory. It also can be shown that $\Delta^2 = \langle a_2 \rangle^2 = 2/3D^2 + 2E^2$. Since D and E are the ZFS parameters determined by multi-frequency EPR in frozen glassy systems, a comparison with first measurements by this approach made by Kang et al. give $D = 1525$ MHz and $E = 440$ MHz [80]. Therefore, $2/3D^2 + 2E^2 = 7.6 \times 10^{19}$ rad²/s², again confirming that the Δ^2 term, determined either by powder simulation of frozen solutions, or by either of the solution methods (Eqs. 7 and 9), is the *static* ZFS in this system. It also should be noted that the field-independent relaxation rate R_0 , which is needed by the HL method to precisely fit the frequency dependence of the line width, is unnecessary in Rast's treatment, and may be an artifact of the approximate nature of the HL approach. Finally, the very close agreement between τ_R measured by a VO²⁺ substitution method and τ_r determined by Rast's approach hold out the hope that rotational rates may be determined from a correct analysis of the frequency dependence of spin relaxation in Gd³⁺ systems.

3.1.2.5

High-Frequency EPR

In addition to its importance in the context of multi-frequency methods, high frequency EPR ($\nu > 90$ GHz) has unique applications as a single frequency observation. For example, the effect of HSA protein binding on the static ZFS term in GdDTPA-EOB produces a small shift in the g -factor between the bound and unbound species. At 95 GHz, this shift is observed in the EPR spectrum of the system in buffer at room temperature. A deconvolution of the spectrum into bound and unbound contributions, followed by double integration, leads to a direct measure of the fraction of the agent bound to the protein, as shown in Fig. 15. Smirnova et al. [81] have tested this approach against the more time-consuming titration methods of NMRD, and found excellent agreement. When

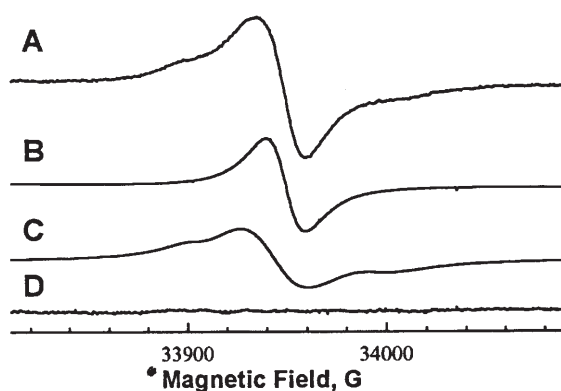


Fig. 15. 95 GHz EPR spectra of GdDTPA-EOB in a 20% HSA solution. A is the experimental spectrum. B is the deconvoluted unbound spectrum, C is the bound fraction, and D is the residual, showing the excellent fit to the model [81]

possible, this deconvolution also can provide line width information on PCAs partitioned between bound and unbound states, allowing us to determine Δ^2 and τ_v in the two environments simultaneously. High field EPR thus is an invaluable addition to our contrast agent research methods, particularly as we begin to study PCA-protein and PCA-cell interactions.

3.1.3

Variable Temperature ^{17}O NMR

The original work of Swift and Connick [82] paved the way for modern applications of this NMR method in paramagnetic contrast agent research. The Lausanne group of Merbach and co-workers have developed elegant applications of the method [83]. Most frequently, the difference between the transverse relaxation rates of ^{17}O in reference buffer ($1/T_{2A}$) and in solutions containing the BPCA ($1/T_2$) are measured as a function of temperature. The analysis fits the temperature dependence of the “reduced” transverse relaxation rate, $1/T_{2R}$, defined as:

$$\frac{1}{T_{2R}} = \frac{1}{P_m} \left[\frac{1}{T_2} - \frac{1}{T_{2A}} \right] \quad (10)$$

P_M is the mole fraction of water in the first hydration sphere of the complex. The procedure results in the determination of τ_M , the correlation time for water exchange from the first hydration sphere of the PCA, and can be very diagnostic in understanding the effects of chelate structure on water exchange, and hence PCA relaxivity. ^{17}O NMR also is useful in determining q , the number of inner sphere water molecules associated with any PCA. The method, developed by Alpoim et al., compares the chemical shift of ^{17}O in water induced by a known concentration of DyCl_3 to the shift induced by a known concentration of Dy^{3+} -substituted PCA [84]. The enhancement of ^{17}O relaxation by the paramagnetic ion also can be modeled to derive values for electronic relaxation rates, and from them, values for Δ^2 and τ_v . Measuring both T_{1n} and T_{2n} of ^{17}O at multiple frequencies can provide important new insights into rotational motion in BPCA systems [63].

3.1.3

VO^{2+} – Substituted BPCAs

This simple but highly effective method to measure the rotational motion of BPCAs was first demonstrated by Chen et al. [85]. It begins with a substitution of VO^{2+} for Gd^{3+} or Mn^{2+} in an agent, or the direct synthesis of VO^{2+} -labeled agents. Chen showed that the hydrodynamic radii of Gd and VO chelates are nearly identical, and that the VO^{2+} – substituted agent behaves in a manner nearly identical to that of the Gd chelate [85].

The purpose of the VO^{2+} -for- Gd^{3+} substitution is to introduce into the agent a paramagnetic species with well-resolved hyperfine structure and anisotropic g and A terms. The motionally modulated EPR spectrum of the tumbling VO^{2+}

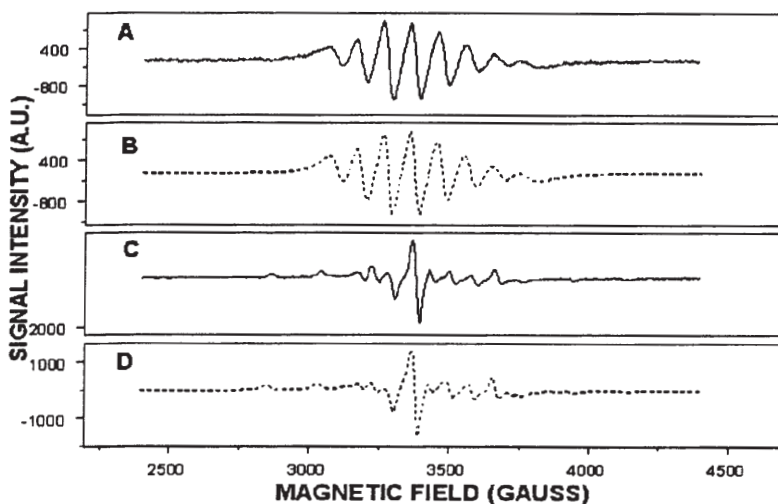


Fig. 16. Use of VO^{2+} labeling to determine change in t_R when MS-325 binds to HSA. A is spectrum in buffer, B is simulation ($\tau_R = 1.8 \times 10^{-10}$ s), C is spectrum in HSA, D is simulation [$\tau_R(1) = 6.7 \times 10^{-10}$ s (56%); $\tau_R(2) = 1.6 \times 10^{-8}$ s (44%)]

ion has been analyzed by Schneider and Freed [86], utilizing a stochastic Liouville matrix approach of Meirovitch et al. [87], and is published as a program called EPRL. Chen et al. developed a more general form of EPRL, in that it includes nonsecular \mathbf{g} matrix and \mathbf{A} matrix term in the spin Hamiltonian [4]. Inclusion of nonsecular terms makes it possible to avoid the high-field approximation inherent in the EPRL programs. This is an essential feature for simulating vanadyl ion spectra at X-band, given that the large hyperfine interaction in the ion is quite significant compared with the electronic Zeeman interaction at that frequency. Another advantage of Chen's method is that it yields accurate rotational line widths over a wider range of motions than EPRL, specifically for very fast motions when $(\tau_R)^{-1}$ approaches the electronic Larmor frequency. The program can make use of several different models of microscopic diffusion, and can treat the data as if there were one or two species present. Finally, the calculation can fit the spectra with an isotropic or an anisotropic rotational model, providing a route to study the behavior of BPCA complexes interacting in protein and cellular environments. Figure 16 illustrates an application of the approach, measuring the change in τ_R when MS-325 binds to HSA. Although almost all of the PCA is known to be bound to the protein, there are two rotational regimes which are only apparent through the VO^{2+} labeling method, and which cannot be accounted for by a single species with anisotropic rotation. In this way, details of BPCA-protein interactions can be studied by means of VO^{2+} -labeling.

3.1.4

Electron Spin Echo Envelope Modulation (ESEEM)

ESEEM techniques provide a way to measure hyperfine interactions with great precision, even in disordered systems. An analysis of hyperfine couplings can, in turn, provide information about electron-nuclear distances (often with precision equal to or better than x-ray crystallographic data), and hence of molecular structure. The technique has been called “EPR-detected NMR”, and can provide information about the positions of atoms surrounding the central metal ion. This is currently of interest, since it can map the distribution of water molecules, and how these distributions are affected by chelate structure and protein interactions. ESEEM will help test various molecular modeling approaches being developed for Gd^{3+} chelates by providing direct measurements of water distributions surrounding a PCA, which can be compared to theoretical predictions from the molecular modeling methods (see, for example, Ref [88]). Validation of good molecular modeling techniques is vital for more advanced rational design of PCAs for MRI. ESEEM is a phenomenon observed in electron spin echo experiments. The experiment requires a pulsed EPR spectrometer, and is almost always carried out at low temperatures to maximize T_{1e} and T_{2e} . Good reviews of the methodology and instrumentation are available in the literature [89, 90]. Because spin echo envelope modulation potentially can arise from any electron-nucleus hyperfine interaction, the task in BPCA research is to attempt to simplify the data by isotopic enrichment. As with solid-state NMR, there are many pulse sequences available to develop one- and two- dimensional ESEEM data. New techniques for the determination of water distance distributions (see for example a recent article by Astashkin and Raitsimring [91]) are making this a very exciting time for this research. Recently, Dikanov et al. were successful in applying a four-pulse, 2-dimensional ESEEM technique, called HYSCORE (hyperfine sublevel correlation spectroscopy) to the study of GdDTPA , for the first time resolving ^{14}N - Gd couplings [92]. If the primary crystal field effects that produce the magnitude of the ZFS in these complexes are due to N - Gd interactions, then it should be possible to correlate the ZFS parameters D and E (or Δ^2) with HYSCORE data, providing a direct spectroscopic examination of one of the primary factors controlling PCA effectiveness in slow-tumbling environments. Figure 17 illustrates the new HYSCORE data.

In a recent paper, Borel et al. have used an electrostatic force field model to calculate the interactions of Gd chelates with solvent water molecules [88]. Clearly, such modeling is a direct step toward the goal of rational PCA design, and the detailed molecular dynamics calculations of BPCA-water interactions are helping to clarify relationships between chelate structure and BPCA relaxivity. Figure 18 shows the radial distribution function that Borel et al. calculate for the hydrogens and oxygens in water surrounding $\text{Gd}(\text{DTPA})$ and $\text{Gd}(\text{DTPA-BMA})$.

Clarkson et al. used ^2H ESEEM to study the $\text{Gd}(\text{DTPA})$ system. They determined water deuteron- Gd^{3+} distances of 2.8 Å (inner sphere) and 3.9 Å (second sphere), with 7 D_2O molecules associated with the second sphere [93]. The distributions in Figure 18 show a significant number of protons with an H - Gd

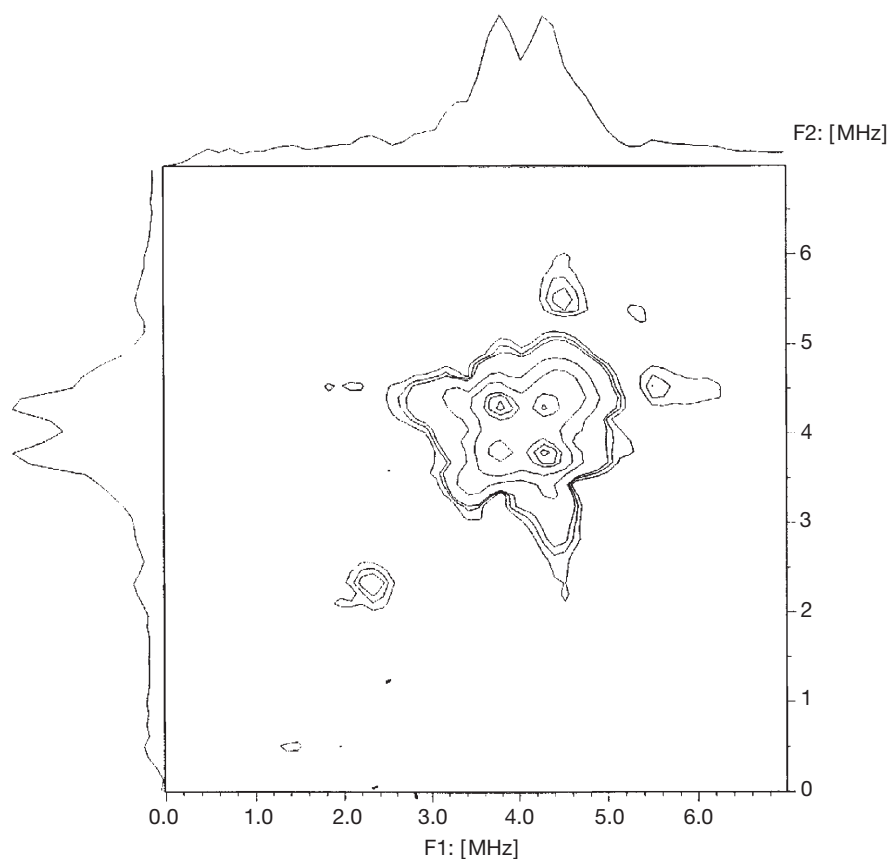


Fig. 17. First HSCORE data from GdDTPA at 4 K, 3502 G. The correlated cross peaks, with splittings from 0.6–1.0 MHz, may reveal ^{14}N -Gd couplings that can be probed [92]

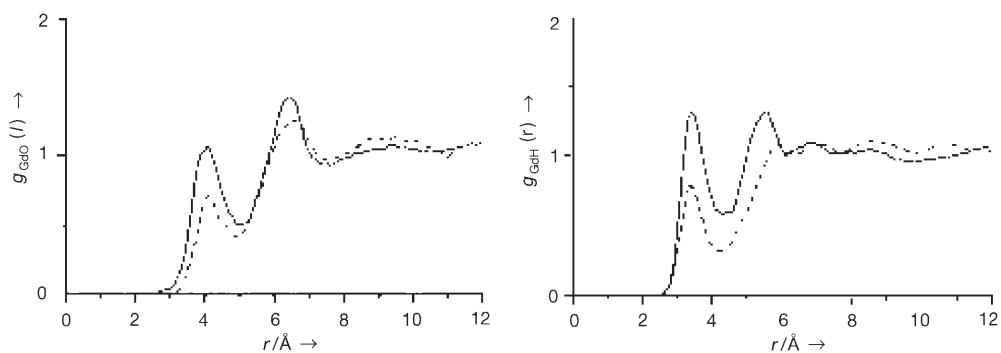


Fig. 18. The radial distribution function for water O atoms (left) and H atoms (right) around Gd of $[\text{Gd}(\text{dtpa})(\text{H}_2\text{O})]^{2-}$ (solid line) and $[\text{Gd}(\text{dtpa-bma})(\text{H}_2\text{O})]$ (dashed line) [88]

distance $< 3 \text{ \AA}$, and the molecular model predicts 6.8 water molecules in the second sphere. While more work needs to be done, the good agreement between ESEEM and molecular dynamics calculations is encouraging. Not only will combinations of theoretical and experimental methods provide a rigorous test of modeling strategies, but the combined approach also will advance ESEEM as an important structural tool for BPCA research, with many advantages over single crystal X-ray structure determinations. Information gained from the combined approach should allow the detailed determination the effects of chelate structure on Gd^{3+} -nuclear distances, and how those distances relate to ZFS parameters, water coordination, and protein interaction effects.

4

Summary

BPCAs have been developed using a wide range of approaches. The goals of long intravascular retention times, complete clearance, and, when possible, enhanced relaxivity have been addressed by covalent linkage of Gd^{3+} chelates to large molecular weight polymers, proteins, and dendrimers; by the use of nano-particles of superparamagnetic iron oxide; by nano-sized micelles and liposomes made of or filled with Gd^{3+} compounds; and by non-covalent association of lipophilic Gd^{3+} chelates to serum proteins. Other paramagnetic ions (notably Mn^{2+} and Fe^{3+}) also have been used. Table 3 lists the relaxivities of a selection of BPCAs based on these various approaches.

The characterization of BPCAs by magnetic resonance methods has advanced our understanding of relationships between chelate structure and contrast agent performance. Such methods can report on both the dynamic (τ_R , τ_M , and τ_S (T_{1e} and T_{2e})) and the structural parameters (r and q). Furthermore, they can help to assess the effects of the biological environment on BPCA performance. This capability is especially important for understanding RIME-type agents, which are specifically designed to interact with serum proteins, as well as other agents targeting tissues and cells. New instrumental methods like ESEEM, and new theoretical models, like that of Rast et al. [79], are providing details of contrast agent behavior that are useful in the design of even more effective materials for various MRI applications.

It sometimes is possible to measure the same parameter by several different physical methods. This helps to improve the accuracy by which the variable is known, and can also serve as a check on the models being used to interpret the data. For example, data for the zero field parameters of MS-325 in HEPES buffer and in HSA solutions are given in Table 4.

While there is general agreement between the various methods, some variation in the values of Δ^2 and τ_V are noted. Additional research will be needed to better understand the reasons for these variations, which may in part be due to the approximate nature of the models used in the calculations.

While it is beyond the scope of this review to discuss in detail the current medical applications of BPCAs, some of the general areas of research should be mentioned.

Table 3. Relaxivities for selected BPCAs

Contrast agent	Conditions (values for 20 MHz unless noted)	Relaxivity (r_1) $s^{-1} mM^{-1}$	Ref.
<i>Extracellular agents</i>			
Gd(DTPA)	1 mM, 25°C	4.3	94
Gd(DOTA)	1 mM, 25°C	4.2	94
<i>Macromolecular covalent conjugates</i>			
GdDTPA-polylysine	48.7 kDa, 39°C	13.1	8
GdDTPA-albumin	90 kDa, 25°C	14	15
<i>Dendrimers</i>			
Gadomer 17	17.453 kDa, 39°C	17.3	29
<i>Micelles</i>			
Gd-HHD-DO3A	39°C	9.2	53
<i>Liposomes</i>			
Gd-HP-DO3A	250 mM ProHance™, 242 ± 5 nm; 37°C	$r_1 = 0.27$; $r_2 = 0.69$	57
	72 ± 6 nm; 37°C	$r_1 = 1.13$; $r_2 = 1.19$	57
<i>Superparamagnetic nano-particles</i>			
Magnetite	4.6 ± 1.2 nm (core size); 37°C	$r_1 = 34.8$; $r_2 = 16.5$ [$s^{-1} mM(Fe)^{-1}$]	31
<i>Non-covalent protein conjugates</i>			
MS-325	0.1 mM in HEPES buffer; 25°C	7.7	52
	0.1 mM in 1.7 mM HSA; 25°C	38	52
Gd (EOB-DTPA)	1 mM in HEPES buffer; 25°C	8	50
	37°C	6.52	42
	1.5 mM in 18% HSA; 20°C	18	50
Gd-(R)-EOB-DTPA	1 mM; 4% HSA; 37°C	9	95
Gd-(S)-EOB-DTPA	1 mM; 4% HSA; 37°C	13	95
Gd (EOB-DTPA)	rat liver; 39°C	16.6	40

Currently, BPCAs are being used to assess perfusion in areas of ischemia and provide information about capillary permeability in areas of reperfusion. They are applied to show the extent of tumor neovascularity and associated permeability changes. Finally, they are useful in studies requiring prolonged imaging, including MR angiography. New applications are being added continually, and this list mentions only some of the areas currently being studied. Several articles and reviews of medical applications of BPCAs should be consulted for further information [28, 97–102].

Table 4. Zero Field Parameters for MS-325

Sample conditions	Method ^a	Δ^2 (10^{19} rad ² /s ²)	τ_V (ps)	Ref.
0.1 mM MS-325 in HEPES buffer	T_{2e}	7.3	29	96
same	g_{eff}	9.6		96
10 mM MS-325 in HEPES buffer	^{17}O NMR	2.5	1.7	52
12.5 mM in water	^{17}O NMR	21	18.7	75
1 mM MS-325 in water at 25°C	^1H NMRD	2.2 ^b 2.5	22 ^b 33	75
0.1 mM MS-325 in 4.5% HSA	T_{2e}	7.4	20	96
same	g_{eff}	8.0		96
10 mM MS-325 in 3 mM HSA	^{17}O NMR	1.0	6.7	52

^a T_{2e} = multi-frequency EPR measurement of line widths; g_{eff} = multi-frequency EPR measurement of $g_{effective}$; ^{17}O NMR = measurement of transverse relaxation of ^{17}O ; ^1H NMRD = measurement of proton T_1 relaxation dispersion with relaxometer.

^b First values based on NMRD simulation assuming $r = 0.295$ nm, second values $r = 0.31$ nm.

Acknowledgement. Partial support for this work was provided through grants from the National Institutes of Health (R01-GM42208, P41-RR01811 and R01-RR01811). Some facilities were provided by the Illinois EPR Research Center, an NIH-funded Resource Center. Gd(III) complexes were provided by Dr. B. Radüchel and colleagues, Schering, AG, Berlin, Germany and Dr. Peter Caravan, EPIX Pharmaceuticals, Cambridge, MA. Prof. R. L. Belford, Prof. Peter Petillo, Prof. Mark J. Nilges, and Mr. Hoon Kang, University of Illinois at Urbana/Champaign, and Professors Alex and Tanya Smirnov, North Carolina State University, Raleigh are thanked for valuable discussions.

5 References

- Bydder G (1990) In: Bydder G et al. (eds) Contrast Media in MRI. Medicom, Bussum, p xix
- Weinmann H-J, Press WR, Radüchel B, Platzek J, Schmitt-Willich H, Vogler H (1990) In: Bydder G et al. (eds) Contrast Media in MRI. Medicom, Bussum, p 19
- Powell DH, Ni Dhubhghaill OM, Pubanz D, Helm L, Lebedev Y S, Schlaepfer W, Merbach AE (1996) J Am Chem Soc 118:9333
- Chen JW, Belford RL, Clarkson RB (1998) J Phys Chem 102:2117
- Solomon I (1955) Phys Rev 99:559
- Bloembergen NJ (1957) J Chem Phys 27:572
- Lauffer RB, Brady TJ (1985) J Magn Reson Imaging 3:11
- Schuhmann-Giampieri G, Schmitt-Willich H, Frenzel T, Press WR, Weinmann H J (1991) Invest Radiol 26:969
- Brasch RC (1992) Radiology 183:1
- Kroft LJM, de Roos A (1999) J Magn Reson Imaging 10:395
- Arthurson G, Wallenius G (1964) Scand J Clin Lab Invest 1:76
- Lauffer RB, Brady TJ, Brown RD III, Baglin C, Koenig SH (1986) Magn Reson Med 3:541
- Schmiedl U, Ogan M, Paajanen H, Marotti M, Crooks LE, Brito AC, Brasch RC (1987) Radiology 162:205

14. Sherry AD, Cacheris WP, Kuan K T (1988) *Magn Reson Med* 8:180
15. Sleiving PF, Watson AD, Rockledge SM (1990) *Bioconjugate Chem* 1:65
16. Wang SC, Wikstrom MG, White DL, Klaveness J, Holtz E, Rongved P, Moseley ME, Brasch RC (1990) *Radiology* 175:483
17. Kornguth S, Anderson M, Turski P, Sorenson J, Robins H I, Cohen J, Rappe A, Markley J (1990) *Am J Neurorad* 11:313
18. Marchal G, Bosmans H, Van Hecke P, Speck U, Aerts P, Vanhoenacker P, Baert A L (1990) *Am J Roentgen* 155:407
19. Curtet C, Maton F, Havet T, Slinkin M, Mishra A, Chatal JF, Muller RN (1998) *Invest Radiol* 33:752
20. Caravan P, Ellison J J, McMurry TJ, Lauffer RB (1999) *Chem Rev* 99:2293
21. Ladd DL, Hollister R, Peng X, Wei D, Wu G, Delecki D, Snow RA, Toner JL, Kellar K, Eck J, Desai VC, Raymond G, Kinter LB, Dessler TS, Rubin DL (1999) *Bioconjugate Chem* 10:361
22. Petrak K, Goddard P (1989) *Adv Drug Delivery Rev* 3:191
23. Knollman FD, Sorge R, Mühler A, Mäurer J, Muschick P, Böck J C, Felix R (1997) *Invest Radiol* 32:755
24. Tomalia DA, Naylor AM, Goddard WA (1990) *Angew Chem Int Ed Engl* 29:138
25. Wiener EC, Auteri FP, Chen JW, Brechbiel MW, Gansow OA, Schneider DS, Belford RL, Clarkson RB, Lauterbur PC (1996) *J Am Chem Soc* 118:7774
26. Meltzer AD, Tirrell DA, Jones AA, Inglefield PT, Hedstrand DM, Tomalia DA (1992) *Macromolecules* 25:4541
27. Bryant LH Jr, Brechbiel MW, Wu C, Bulte JW, Herynek V, Frank JA (1999) *J Magn Reson Imag* 9:348
28. Clarke SE, Weinmann H-J, Dai E, Lucas AR, Rutt BK (2000) *Radiology* 214:787
29. Dong Q, Hurst DR, Weinmann H-J, Chenevert TL, Londy FJ, Prince MR, (1998) *Invest Radiol* 33:699
30. Marchand B, Douek P C, Benderbous S, Corot C, Canet E (2000) *Invest Radiol* 35:41
31. Shen T, Weissleder R, Papisov M, Bogdanov AJr, Brady TJ (1993) *Magn Reson Med* 29:599
32. Røhl L, Østergaard L, Simonsen CZ, Vestergaard-Poulsen, P, Sørensen L, Bjørnerud A, Brileys Sæbø K, Gyldensted C (1999) *Acta Radiol* 40:282
33. Koenig SH, Kellar KE (1995) *Magn Reson Med* 34:227
34. Bulte JWM, Brooks RA, Moskowicz BM, Bryant LH Jr, Frank JA (1999) *Magn Reson Med* 42:379
35. Koenig SH, Kellar KE (1998) *Acad Radiol* 5(suppl 1):S200
36. Knollmann FD, Bock JC, Rautenberg K, Beier J, Ebert W, Felix R (1998) *Invest Radiol* 33:637
37. Sayegh Y, Pochon S, Vallée J-P, Becker M, Lazeyras F, Tournier H, Hyacinthe R, Fouillet X, Terrier F (2001) *Invest Radiol* 36:15
38. Lauffer RB (1991) *Magn Reson Med* 22:339
39. Uggeri F, Amie S, Anelli P L, Botta M, Brochetta M, de Haen C, Ermondi G, Grandi M, Paoli P (1995) *Inorg Chem* 34:633
40. Schuhmann-Giamperi G, Schmitt-Willich H, Press W-R, Negishi C, Weinmann H-J, Speck U (1992) *Radiology* 183:59
41. Vander Elst L, Maton F, Laurent S, Seghi F, Chapelle F, Muller R N (1997) *Magn Reson Med* 38:604
42. Lewin M, Clément O, Belguise-Valladier P, Tran L, Cuénod C-A, Siauve N, Frija G (2001) *Invest Radiol* 36:9
43. Toth E, Connac F, Helm L, Adzamlı K, Merbach AE (1998) *J Biol Inorg Chem* 3:606
44. Cavagna FM, Maggioni F, Castelli PM, Daprà M, Imperatori L G, Lorusso V, Jenkins BG (1997) *Invest Radiol* 12:780
45. Parmalee DJ, Walovitch RC, Ouellet HS, Lauffer RB (1997) *Invest Radiol* 12:741
46. Lauffer RB, Parmalee DJ, Dunham SU, Ouellet HS, Dolan RP, Witte S, McMurry TJ, Walovitch RC (1998) *Radiology* 207:529
47. Smirnova TI, Smirnov AI, Belford RL, Clarkson RB (1998) *J Am Chem Soc* 120: 5060

48. Smirnova TI, Smirnov AI, Belford RL, Clarkson RB (1999) *Magn Reson Materials Phys Biol Med* 8: 214
49. Aime S, Botta M, Crich SG, Giovenzana GB, Pagliarini R, Piccinini M, Sisti M, Terreno E (1997) *J Biol Inorg Chem* 2:470
50. Chen JW, Belford RL, Clarkson RB (2001) *J Phys Chem* (submitted)
51. Chen JW, Konda-Sundheim R, Belford RL, Clarkson RB (2001) to be published
52. Aime S, Chiaussa M, Digilio G, Gianolio E, Terreno E (1999) *J Biol Inorg Chem* 4:766
53. Gløgaard C, Hovland R, Fossheim, SL, Aasen AJ, Klaveness J (2000) *J Chem Soc Perkin Trans 2* 1047
54. Torchilin VP, Trubetskoy VS (1997) *Polym Prepr (Am Chem Soc, Div Polym Chem)* 38: 545
55. Andre JP, Toth E, Fischer H, Seelig A, Macke HR, Merbach AE (1999) *Chem Eur J* 5: 2977
56. Torchilin V, Babich J, Weissig V (2000) *J Liposome Res* 10: 483
59. Fossheim SL, Fahlvik AK, Klaveness, Muller RN (1999) *Magn Reson Imaging* 17:83
58. Nævestad A, Fossheim S, Fahlvik AK (1999) *Trends in Contrast Media*, Springer, Heidelberg, pp. 171–181.
59. Suga K, Mikawa M, Ogasawara N, Okazaki H, Matsunaga N (2001) *Invest Radiol* 36: 136
60. Rinck PA, Fischer HW, Vander Elst L, Van Haverbeke Y, Muller R N (1988) *Radiology* 168: 843
61. Provencher S W (1982) *Comput Phys Commun* 27: 229
62. Labadie C, Lee J-H, Vetek G, Springer CS Jr (1994) *J Mag Res Series B* 105:99
63. Dunand FA, Tóth E, Hollister R, Merbach AE (2001) *J Biol Inorg Chem* 6:247
64. Belford RL, Clarkson RB (1993) In: Botto R, Sanada Y (eds) *Techniques in Magnetic Resonance for Carbonaceous Solids*, ACS Advances in Chemistry Series 229, American Chemical Society, Washington, p 107
65. Powell DH, Merbach AE, Gonzalez G, Bruecher E, Micskei K, Ottaviani MF, Koehler K, von Zelewsky A, Grinberg O Ya, Lebedev Ya S (1993) *Helv Chim Acta* 76: 2129
66. Belford RL, Davis PH, Belford GG, Lenhardt TM (1974) *ACS Symposium Series* 5, American Chemical Society, Washington, p 40
67. Alexander S, Luz Z, Naor Y, Poupko R (1977) *Mol Phys* 33:1119
68. Baram A, Luz Z, Alexander S (1973) *J Chem Phys* 58: 4558
69. Borel A, Toth E, Helm L, Jánosy A, Merbach AE (2000) *Phys Chem Chem Phys* 2: 1311
70. Atsarkin AV, Demidov VV, Vasneva GA, Odintsov BM, Belford, RL, Platzek J, Clarkson, RB (2001) *J Phys Chem A* 105:9323
71. Powell DH, Ni Dhubghaill OM, Pubanz D, Helm L, Lebedev YS, Schlaepfer W, Merbach AE (1996) *JAm Chem Soc* 118:9333
72. Hudson A, Lewis JWE (1970) *Trans Faraday Soc* 66:1297
73. Slichter CP (1980) *Principles of Magnetic Resonance*. Springer, Berlin Heidelberg New York
74. Clarkson RB, Smirnov AI, Smirnova TI, Belford RL (2001) In: Merbach A, Toth E (eds) *The Chemistry of Contrast Agents in Medical Magnetic Resonance Imaging*, Chapter 9. Wiley, New York p 383
75. Muller R N, Radüchel B, Laurent S, Platzek J, Piérart C, Mareski P, Vander Elst L (1999) *Eur J Inorg Chem* 2:1949
76. Poupko R, Barum A, Luz Z (1974) *Mol Phys* 27:1345
77. Bertini I, Kowalewski J, Luchinat C, Nilsson T, Parigi G (1999) *J Chem Phys* 111:5795
78. Rast S, Fries PH, Belorizky (2000) *J Chem Phys* 113:8724
79. Rast S, Borel A, Helm L, Belorizky E, Fries PH, Merbach AE (2001) *JAm Chem Soc* 123: 2637
80. Kang H, Belford RL, Clarkson RB (2001) (to be published)
81. Smirnova TI, Smirnov AI, Belford RL, Clarkson RB (2001) (to be published)
82. Swift TJ, Connick RE (1962) *J Chem Phys* 37: 307
83. Micskei K, Helm L, Brücher E, Merbach AE (1993) *Inorg Chem* 32:3844
84. Alpoim MC, Urbano AM, Geraldés CFGC (1992) *J Chem Soc Dalton Trans* 463
85. Chen JW, Auteri FP, Budil DE, Belford RL, Clarkson RB (1994) *J Phys Chem* 98: 13452

86. Schnieder DJ, Freed JH (1989) In: Berliner LJ, Reuben J (eds) *Biological Magnetic Resonance*, vol 8. Academic Press, New York, p 1
87. Meirovitch E, Ignier E, Ignier D, Moro G, Freed JH (1982) *J Chem Phys* 77: 3915
88. Borel A, Helm L, Merbach AE (2001) *Chem Eur J* 7:600
89. Van Doorslaer S, Schweiger A (2000) *Naturwissenschaften* 87: 245
90. Deligiannakis Y, Louloudi M, Hadjiliadis N (2000) *Coord Chem Rev* 204:1
91. Astashkin AV, Raitsimring AM (2000) *J Mag Res* 143: 280
92. Dikanov S, Belford RL, Clarkson RB (2001) to be published
93. Clarkson RB, Hwang J-H, Belford RL (1993) *Magn Reson Med* 29:521
94. Aime S, Botto M, Panero M, Grandi M, Uggeri F (1991) *Magn Reson Chem* 29:923
95. Vander Elst L, Chapelle F, Laurent S, Muller RN (2001) *J Biol Inorg Chem* 6:196
96. Smirnova TI, Smirnov AI, Belford RI, Clarkson RB (2001) to be published
97. Weishaupt D, Ruhm SG, Binkert CA, Schmidt M, Patak MA, Steybe F, McGill S, Debatin JF (2000) *Am J Roentgen* 175:189
98. Grist TM, Korosec FR, Peters DC, Witte S, Walovitch RC, Dolan RP, Bridson WE, Yucel EK, Mistretta CA (1998) *Radiology* 207: 539
99. Steinbach GC, Baker KG, Lim GL, Mattrey RF, Arellano RS (1994) *Artif Cells, Blood Substitutes, Immobilization Biotechnol* 22: 1501
100. Saeed M (1999) *Drugs of Today* 35:879
101. Kauczor HU (1998) *Invest Radiol* 33:606
102. Mahfouz AE, Hamm B, Taupitz M (1997) *Eur Radiol* 7:507

Author Index Volume 201–221

Author Index Vols. 26–50 see Vol. 50

Author Index Vols. 51–100 see Vol. 100

Author Index Vols. 101–150 see Vol. 150

Author Index Vols. 151–200 see Vol. 200

The volume numbers are printed in italics

Albert M, see Dax K (2001) 215:193–275

Angyal SJ (2001) The Lobry de Bruyn-Alberda van Ekenstein Transformation and Related Reactions. 215: 1–14

Astruc D, Blais J-C, Cloutet E, Djakovitch L, Rigaut S, Ruiz J, Sartor V, Valério C (2000) The First Organometallic Dendrimers: Design and Redox Functions. 210:229–259

Augé J, see Lubineau A (1999) 206:1–39

Baars MWPL, Meijer EW (2000) Host-Guest Chemistry of Dendritic Molecules. 210:131–182

Ballauff M (2001) Structure of Dendrimers in Dilute Solution. 212:177–194

Baltzer L (1999) Functionalization and Properties of Designed Folded Polypeptides. 202:39–76

Bartlett RJ, see Sun J-Q (1999) 203:121–145

Bertrand G, Bourissou D (2002) Diphosphorus-Containing Unsaturated Three-Membered Rings: Comparison of Carbon, Nitrogen, and Phosphorus Chemistry. 220:1–25

Betzemeier B, Knochel P (1999) Perfluorinated Solvents – a Novel Reaction Medium in Organic Chemistry. 206:61–78

Blais J-C, see Astruc D (2000) 210:229–259

Bogár F, see Pipek J (1999) 203:43–61

Bourissou D, see Bertrand G (2002) 220:1–25

Brand SC, see Haley MM (1999) 201:81–129

Bray KL (2001) High Pressure Probes of Electronic Structure and Luminescence Properties of Transition Metal and Lanthanide Systems. 213:1–94

Briicher E (2002) Kinetic Stabilities of Gadolinium(III) Chelates Used as MRI Contrast Agents. 221:103–122

Brunel JM, Buono G (2002) New Chiral Organophosphorus catalysts in Asymmetric Synthesis. 220:79–106

Buchwald SL, see Muci A R (2002) 219:131–209

Bunz UHF (1999) Carbon-Rich Molecular Objects from Multiply Ethynylated π -Complexes. 201:131–161

Buono G, see Brunel JM (2002) 220:79–106

Cadierno V, see Majoral J-P (2002) 220:53–77

Carmichael D, Mathey F (2002) New Trends in Phosphametallocene Chemistry. 220:27–51

Chamberlin AR, see Gilmore MA (1999) 202:77–99

Chow H-F, Leung C-F, Wang G-X, Zhang J (2001) Dendritic Oligoethers. 217:1–50

Clarkson RB (2002) Blood-Pool MRI Contrast Agents: Properties and Characterization. 221:201–235

Cloutet E, see Astruc D (2000) 210:229–259

Cooper DL, see Raimondi M (1999) 203:105–120

Cornils B (1999) Modern Solvent Systems in Industrial Homogeneous Catalysis. 206:133–152

Crooks RM, Lemon HI BI, Yeung LK, Zhao M (2001) Dendrimer-Encapsulated Metals and Semiconductors: Synthesis, Characterization, and Applications. 212:81–135

Croteau R, see Davis EM (2000) 209:53–95

- Curran DP, see Maul JJ (1999) 206:79–105
- Davis EM, Croteau R (2000) Cyclization Enzymes in the Biosynthesis of Monoterpenes, Sesquiterpenes and Diterpenes. 209:53–95
- Davies JA, see Schwert DD (2002) 221: 165–200
- Dax K, Albert M (2001) Rearrangements in the Course of Nucleophilic Substitution Reactions. 215:193–275
- de la Plata BC, see Ruano JLG (1999) 204:1–126
- de Meijere A, Kozhushkov SI (1999) Macrocyclic Structurally Homoconjugated Oligoacetylenes: Acetylene- and Diacetylene-Expanded Cycloalkanes and Rotanes. 201:1–42
- de Meijere A, Kozhushkov SI, Khlebnikov AF (2000) Bicyclopropylidene – A Unique Tetra-substituted Alkene and a Versatile C₆-Building Block. 207:89–147
- de Meijere A, Kozhushkov SI, Hadjiaraoglou LP (2000) Alkyl 2-Chloro-2-cyclopropylideneacetates – Remarkably Versatile Building Blocks for Organic Synthesis. 207:149–227
- de Raadt A, Fechter MH (2001) Miscellaneous. 215:327–345
- Desreux JF, see Jacques V (2002) 221: 123–164
- Diederich F, Gobbi L (1999) Cyclic and Linear Acetylenic Molecular Scaffolding. 201:43–79
- Diederich F, see Smith DK (2000) 210: 183–227
- Djakovitch L, see Astruc D (2000) 210:229–259
- Donges D, see Yersin H (2001) 214:81–186
- Dormán G (2000) Photoaffinity Labeling in Biological Signal Transduction. 211: 169–225
- Dorn H, see McWilliams AR (2002) 220: 141–167
- Drabowicz J, Mikołajczyk M (2000) Selenium at Higher Oxidation States. 208:143–176
- Ehse A, Romero A, Peruzzini M (2002) Metal-Mediated Degradation and Reaggregation of White Phosphorus. 220:107–140
- Eder B, see Wrodnigg TM (2001) The Amadori and Heyns Rearrangements: Landmarks in the History of Carbohydrate Chemistry or Unrecognized Synthetic Opportunities? 215: 115–175
- Famulok M, Jenne A (1999) Catalysis Based on Nucleic Acid Structures. 202:101–131
- Fechter MH, see de Raadt A (2001) 215:327–345
- Ferrier RJ (2001) Substitution-with-Allylic-Rearrangement Reactions of Glycol Derivatives. 215:153–175
- Ferrier RJ (2001) Direct Conversion of 5,6-Unsaturated Hexopyranosyl Compounds to Functionalized Glycohexanones. 215:277–291
- Frey H, Schlenk C (2000) Silicon-Based Dendrimers. 210:69–129
- Frullano L, Rohovec J, Peters JA, Geraldes CFGC (2002) Structures of MRI Contrast Agents in Solution. 221: 25–60
- Fugami K, Kosugi M (2002) Organotin Compounds. 219: 87–130
- Fuhrhop J-H, see Li G (2002) 218: 133–158
- Furukawa N, Sato S (1999) New Aspects of Hypervalent Organosulfur Compounds. 205: 89–129
- Gamelin DR, Giidel HU (2001) Upconversion Processes in Transition Metal and Rare Earth Metal Systems. 214:1–56
- Garcia R, see Tomas C (2002) 218:115–132
- Geraldes CFGC, see Frullano L (2002) 221: 25–60
- Gilmore MA, Steward LE, Chamberlin AR (1999) Incorporation of Noncoded Amino Acids by In Vitro Protein Biosynthesis. 202:77–99
- Glasbeek M (2001) Excited State Spectroscopy and Excited State Dynamics of Rh(III) and Pd(II) Chelates as Studied by Optically Detected Magnetic Resonance Techniques. 213:95–142
- Glass RS (1999) Sulfur Radical Cations. 205:1–87
- Gobbi L, see Diederich F (1999) 201:43–129
- Gouzy M-F, see Li G (2002) 218: 133–158
- Gries H (2002) Extracellular MRI Contrast Agents Based on Gadolinium. 221: 1–24
- Giidel HU, see Gamelin DR (2001) 214: 1–56
- Guga P, Okruszek A, Stec WJ (2002) Recent Advances in Stereocontrolled Synthesis of P-Chiral Analogues of Riophosphates. 220:169–200
- Hackmann-Schlichter N, see Krause W (2000) 210:261–308

- Hadjiraoglou LP, see de Meijere A (2000) 207:149–227
- Hausler H, Stitz AE (2001) D-Xylose (D-Glucose) Isomerase and Related Enzymes in Carbohydrate Synthesis. 215:77–114
- Haley MM, Pak JJ, Brand SC (1999) Macrocyclic Oligo(phenylacetylenes) and Oligo(phenyl-diacetylenes). 201:81–129
- Hartmann T, Ober D (2000) Biosynthesis and Metabolism of Pyrrolizidine Alkaloids in Plants and Specialized Insect Herbivores. 209:207–243
- Haseley SR, Kamerling JP, Vliegthart JFG (2002) Unravelling Carbohydrate Interactions with Biosensors Using Surface Plasmon Resonance (SPR) Detection. 218:93–114
- Hassner A, see Nambhothiri INN (2001) 216:1–49
- Helm L, see Tóth E (2002) 221:61–101
- Hemscheidt T (2000) Tropane and Related Alkaloids. 209:175–206
- Hergenrother PJ, Martin SF (2000) Phosphatidylcholine-Preferring Phospholipase C from *B. cereus*. Function, Structure, and Mechanism. 211:131–167
- Hermann C, see Kuhlmann J (2000) 211:61–116
- Hirsch A, Vostrowsky O (2001) Dendrimers with Carbon Rich-Cores. 217:51–93
- Hiyama T, Shirakawa E (2002) Organosilicon Compounds. 219:61–85
- Houseman BT, Mrksich M (2002) Model Systems for Studying Polyvalent Carbohydrate Binding Interactions. 218:1–44
- Hricovíiová Z, see Petruš L (2001) 215:15–41
- Igau A, see Majoral J-P (2002) 220:53–77
- Iwaoka M, Tomoda S (2000) Nucleophilic Selenium. 208:55–80
- Iwasawa N, Narasaka K (2000) Transition Metal Promoted Ring Expansion of Alkynyl- and Propadienylcyclopropanes. 207:69–88
- Imperiali B, McDonnell KA, Shogren-Knaak M (1999) Design and Construction of Novel Peptides and Proteins by Tailored Incorporation of Coenzyme Functionality. 202:1–38
- Jacques V, Desreux JF (2002) New Classes of MRI Contrast Agents. 221:123–164
- James TD, Shinkai S (2002) Artificial Receptors as Chemosensors for Carbohydrates. 218:159–200
- Jenne A, see Famulok M (1999) 202:101–131
- Kamerling JP, see Haseley SR (2002) 218:93–114
- Kashemirov BA, see Mc Kenna CE (2002) 220:201–238
- Kato S, see Murai T (2000) 208:177–199
- Khlebnikov AF, see de Meijere A (2000) 207:89–147
- Kirtman B (1999) Local Space Approximation Methods for Correlated Electronic Structure Calculations in Large Delocalized Systems that are Locally Perturbed. 203:147–166
- Kleij AW, see Kreiter R (2001) 217:163–199
- Klein Gebbink RJM, see Kreiter R (2001) 217:163–199
- Klopper W, Kutzelnigg W, Müller H, Noga J, Vogtner S (1999) Extremal Electron Pairs – Application to Electron Correlation, Especially the R12 Method. 203:21–42
- Knochel P, see Betzemeier B (1999) 206:61–78
- Kosugi M, see Fugami K (2002) 219:87–130
- Kozhushkov SI, see de Meijere A (1999) 201:1–42
- Kozhushkov SI, see de Meijere A (2000) 207:89–147
- Kozhushkov SI, see de Meijere A (2000) 207:149–227
- Krause W, Hackmann-Schlichter N, Maier FK, Müller R (2000) Dendrimers in Diagnostics. 210:261–308
- Kreiter R, Kleij AW, Klein Gebbink RJM, van Koten G (2001) Dendritic Catalysts. 217:163–199
- Kuhlmann J, Herrmann C (2000) Biophysical Characterization of the Ras Protein. 211:61–116
- Kunkely H, see Vogler A (2001) 213:143–182
- Kutzelnigg W, see Klopper W (1999) 203:21–42
- Lawless LJ, see Zimmermann SC (2001) 217:95–120
- Leitner W (1999) Reactions in Supercritical Carbon Dioxide (scCO₂). 206:107–132
- Lemon III BL, see Crooks RM (2001) 212:81–135

- Leung C-F, see Chow H-F (2001) 217: 1–50
- Levitzki A (2000) Protein Tyrosine Kinase Inhibitors as Therapeutic Agents. 211: 1–15
- Li G, Gouzy M-F, Fuhrhop J-H (2002) Recognition Processes with Amphiphilic Carbohydrates in Water. 218: 133–158
- Li X, see Paldus J (1999) 203: 1–20
- Linclau B, see Maul JJ (1999) 206: 79–105
- Lindhorst TK (2002) Artificial Multivalent Sugar Ligands to Understand and Manipulate Carbohydrate-Protein Interactions. 218: 201–235
- Lindhorst TK, see Rockendorf N (2001) 217: 201–238
- Lubineau A, Augé J (1999) Water as Solvent in Organic Synthesis. 206: 1–39
- Lundt I, Madsen R (2001) Synthetically Useful Base Induced Rearrangements of Aldonolactones. 215: 177–191
- Loupy A (1999) Solvent-Free Reactions. 206: 153–207
- Madsen R, see Lundt I (2001) 215: 177–191
- Maier FK, see Krause W (2000) 210: 261–308
- Majoral J-P, Igau A, Cadierno V, Zablocka M (2002) Benzyne-Zirconocene Reagents as Tools in Phosphorus Chemistry. 220: 53–77
- Manners I (2002), see McWilliams AR (2002) 220: 141–167
- March NH (1999) Localization via Density Functionals. 203: 201–230
- Martin SF, see Hergenrother PJ (2000) 211: 131–167
- Mathey F, see Carmichael D (2002) 220: 27–51
- Maul JJ, Ostrowski PJ, Ublacker GA, Linclau B, Curran DP (1999) Benzotrifluoride and Derivates: Useful Solvents for Organic Synthesis and Fluorous Synthesis. 206: 79–105
- McDonnell KA, see Imperiali B (1999) 202: 1–38
- Mc Kenna CE, Kashemirov BA (2002) Recent Progress in Carbonylphosphonate Chemistry. 220: 201–238
- McWilliams AR, Dorn H, Manners I (2002) New Inorganic Polymers Containing Phosphorus. 220: 141–167
- Meijer EW, see Baars MWPL (2000) 210: 131–182
- Merbach AE, see Tóth E (2002) 221: 61–101
- Metzner P (1999) Thiocarbonyl Compounds as Specific Tools for Organic Synthesis. 204: 127–181
- Mezey PG (1999) Local Electron Densities and Functional Groups in Quantum Chemistry. 203: 167–186
- Mikołajczyk M, see Drabowicz J (2000) 208: 143–176
- Miura M, Nomura M (2002) Direct Arylation via Cleavage of Activated and Unactivated C-H Bonds. 219: 211–241
- Miyaura N (2002) Organoboron Compounds. 219: 11–59
- Miyaura N, see Tamao K (2002) 219: 1–9
- Moller M, see Sheiko SS (2001) 212: 137–175
- Morales JC, see Rojo J (2002) 218: 45–92
- Mrksich M, see Houseman BT (2002) 218: 1–44
- Muci AR, Buchwald SL (2002) Practical Palladium Catalysts for C-N and C-O Bond Formation. 219: 131–209
- Müllen K, see Wiesler U-M (2001) 212: 1–40
- Muller G (2000) Peptidomimetic SH2 Domain Antagonists for Targeting Signal Transduction. 211: 17–59
- Muller H, see Kloppe W (1999) 203: 21–42
- Muller R, see Krause W (2000) 210: 261–308
- Murai T, Kato S (2000) Selenocarbonyls. 208: 177–199
- Muscat D, van Benthem RATM (2001) Hyperbranched Polyesteramides – New Dendritic Polymers. 212: 41–80
- Nakayama J, Sugihara Y (1999) Chemistry of Thiophene 1,1-Dioxides. 205: 131–195
- Namboothiri INN, Hassner A (2001) Stereoselective Intramolecular 1,3-Dipolar Cycloadditions. 216: 1–49

- Narasaka K, see Iwasawa N (2000) 207: 69–88
- Nishibayashi Y, Uemura S (2000) Selenoxide Elimination and [2,3] Sigmatropic Rearrangements. 208:201–233
- Nishibayashi Y, Uemura S (2000) Selenium Compounds as Ligands and Catalysts. 208:235–255
- Noga J, see Kloppe W (1999) 203:21–42
- Nomura M, see Miura M (2002) 219: 211–241
- Nubbemeyer U (2001) Synthesis of Medium-Sized Ring Lactams. 216: 125–196
- Nummelin S, Skrifvars M, Rissanen K (2000) Polyester and Ester Functionalized Dendrimers. 210: 1–67
- Ober D, see Hemscheidt T (2000) 209:175–206
- Okruszek A, see Guga P (2002) 220:169–200
- Osanai S (2001) Nickel (II) Catalyzed Rearrangements of Free Sugars. 215:43–76
- Ostrowski PJ, see Maul JJ (1999) 206:79–105
- Pak JJ, see Haley MM (1999) 201:81–129
- Paldus J, Li X (1999) Electron Correlation in Small Molecules: Grafting Cl onto CC. 203:1–20
- Paulmier C, see Ponthicux S (2000) 208:113–142
- Penadés S, see Rojo J (2002) 218:45–92
- Peruzzini M, see Ehses M (2002) 220:107–140
- Peters JA, see Frullano L (2002) 221: 25–60
- Petrui L, Petrušová M, Hricová Z (2001) The Břilik Reaction. 215: 15–41
- Petršová M, see Petrui L (2001) 215:15–41
- Pipck J, Bogár F (1999) Many-Body Perturbation Theory with Localized Orbitals – Kapuy's Approach. 203:43–61
- Ponthicux S, Paulmier C (2000) Selenium-Stabilized Carbanions. 208: 113–142
- Raimondi M, Cooper DL (1999) Ab Initio Modern Valence Bond Theory. 203:105–120
- Reinhoudt DN, see van Manen H-J (2001) 217: 121–162
- Renaud P (2000) Radical Reactions Using Selenium Precursors. 208:81–112
- Richardson N, see Schwert DD (2002) 221: 165–200
- Rigaut S, see Astruc D (2000) 210:229–259
- Riley MJ (2001) Geometric and Electronic Information From the Spectroscopy of Six-Coordinate Copper(II) Compounds. 214:57–80
- Rissanen K, see Nummelin S (2000) 210:1–67
- Røeggen I (1999) Extended Geminal Models. 203:89–103
- Rockendorf N, Lindhorst TK (2001) Glycodendrimers. 217:201–238
- Rohovec J, see Frullano L (2002) 221: 25–60
- Rojo J, Morales JC, Penadés S (2002) Carbohydrate-Carbohydrate Interactions in Biological and Model Systems. 218:45–92
- Romerosa A, see Ehses M (2002) 220:107–140
- Ruano JLG, de la Plata BC (1999) Asymmetric [4+2] Cycloadditions Mediated by Sulfoxides. 204: 1–126
- Ruiz J, see Astruc D (2000) 210:229–259
- Rychnovsky SD, see Sinz CJ (2001) 216: 51–92
- Salaiin J (2000) Cyclopropane Derivates and their Diverse Biological Activities. 207:1–67
- Sanz-Cervera JF, see Williams RM (2000) 209:97–173
- Sartor V, see Astruc D (2000) 210:229–259
- Sato S, see Furukawa N (1999) 205:89–129
- Scherf U (1999) Oligo- and Polyarylenes, Oligo- and Polyarylenevinyls. 201:163–222
- Schlenk C, see Frey H (2000) 210:69–129
- Schwert DD, Davies JA, Richardson N (2002) Non-Gadolinium-Based MRI Contrast Agents. 221: 165–200
- Sheiko SS, Moller M (2001) Hyperbranched Macromolecules: Soft Particles with Adjustable Shape and Capability to Persistent Motion. 212:137–175
- Shen B (2000) The Biosynthesis of Aromatic Polyketides. 209:1–51
- Shinkai S, see James TD (2002) 218:159–200
- Shirakawa E, see Hiyama T (2002) 219: 61–85

- Shogren-Knaak M, see Imperiali B (1999) 202:1–38
- Sinou D (1999) Metal Catalysis in Water. 206:41–59
- Sinz CJ, Rychnovsky SD (2001) 4-Acetoxy- and 4-Cyano-1,3-dioxanes in Synthesis. 216:51–92
- Skrifvars M, see Nummelin S (2000) 210:1–67
- Smith DK, Diederich F (2000) Supramolecular Dendrimer Chemistry – A Journey Through the Branched Architecture. 210:183–227
- Stec WJ, see Guga P (2002) 220:169–200
- Steward LE, see Gilmore MA (1999) 202:77–99
- Stocking EM, see Williams RM (2000) 209:97–173
- Stütz AE, see Hausler H (2001) 215:77–114
- Sugihara Y, see Nakayama J (1999) 205:131–195
- Sun J-Q, Bartlett RJ (1999) Modern Correlation Theories for Extended, Periodic Systems. 203:121–145
- Sun L, see Crooks RM (2001) 212:81–135
- Surján PR (1999) An Introduction to the Theory of Geminals. 203:63–88
- Tamao K, Miyauchi N (2002) Introduction to Cross-Coupling Reactions. 219:1–9
- ten Holte P, see Zwanenburg B (2001) 216:93–124
- Thiem J, see Werschkun B (2001) 215:293–325
- Thutewohl M, see Waldmann H (2000) 211:117–130
- Tiecco M (2000) Electrophilic Selenium, Selenocyclizations. 208:7–54
- Tomoda S, see Iwaoka M (2000) 208:55–80
- Tóth E, Helm L, Merbach AE (2002) Relaxivity of MRI Contrast Agents. 221:61–101
- Tomas C, Garcia R (2002) Interaction Forces with Carbohydrates Measured by Atomic Force Microscopy. 218:115–132
- Ublacker GA, see Maul JJ (1999) 206:79–105
- Uemura S, see Nishibayashi Y (2000) 208:201–233
- Uemura S, see Nishibayashi Y (2000) 208:235–255
- Valdemoro C (1999) Electron Correlation and Reduced Density Matrices. 203:187–200
- Valério C, see Astruc D (2000) 210:229–259
- van Benthem RATM, see Muscat D (2001) 212:41–80
- van Koten G, see Kreiter R (2001) 217:163–199
- van Manen H-J, van Veggel FCJM, Reinhoudt DN (2001) Non-Covalent Synthesis of Metallo-dendrimers. 217:121–162
- van Veggel FCJM, see van Manen H-J (2001) 217:121–162
- Vliegthart JFG, see Haseley SR (2002) 218:93–114
- Vogler A, Kunkely H (2001) Luminescent Metal Complexes: Diversity of Excited States. 213:143–182
- Vogtner S, see Kloppe W (1999) 203:21–42
- Vostrowsky O, see Hirsch A (2001) 217:51–93
- Waldmann H, Thutewohl M (2000) Ras-Farnesyltransferase-Inhibitors as Promising Anti-Tumor Drugs. 211:117–130
- Wang G-X, see Chow H-F (2001) 217:1–50
- Weil T, see Wiesler U-M (2001) 212:1–40
- Werschkun B, Thiem J (2001) Claisen Rearrangements in Carbohydrate Chemistry. 215:293–325
- Wiesler U-M, Weil T, Müllen K (2001) Nanosized Polyphenylene Dendrimers. 212:1–40
- Williams RM, Stocking EM, Sanz-Cervera JF (2000) Biosynthesis of Prenylated Alkaloids Derived from Tryptophan. 209:97–173
- Wirth T (2000) Introduction and General Aspects. 208:1–5
- Wrodnigg TM, Eder B (2001) The Amadori and Heyns Rearrangements: Landmarks in the History of Carbohydrate Chemistry or Unrecognized Synthetic Opportunities? 215:115–175
- Yersin H, Donges D (2001) Low-Lying Electronic States and Photophysical Properties of Organometallic Pd(II) and Pt(II) Compounds. Modern Research Trends Presented in Detailed Case Studies. 214:81–186
- Yeung LK, see Crooks RM (2001) 212:81–135

Zablocka M, see Majoral J-P (2002) 220: 53–77

Zhang J, see Chow H-F (2001) 217: 1–50

Zhao M, see Crooks RM (2001) 212: 81–135

Zimmermann SC, Lawless LJ (2001) Supramolecular Chemistry of Dendrimers. 217: 95–120

Zwanenburg B, ten Holte P (2001) The Synthetic Potential of Three-Membered Ring Aza-Heterocycles. 216: 93–124